# THÈSE POUR OBTENIR LE GRADE DE DOCTEUR DE L'UNIVERSITÉ DE MONTPELLIER

**En Electronique**

**École doctorale : Information, Structures, Systèmes**

**Unité de recherche UMR 5214, Institut d'Electronique et des Systèmes**

# Direct measurements of electric field at interfaces of medium thickness solid samples using thermal pulses and coupled temperature/space charge responses


**Présentée par Sneha Satish HEGDE**
**Le 16 Décembre 2022**

**Sous la direction de**
**Petru NOTINGHER et Jean-Charles LAURENTIE**


**Devant le jury composé de**

| | |
|---|---|
| **Pascale GALL BORRUT, Professeur, Université de Montpellier** | **Présidente** |
| **Laurent BERQUEZ, Professeur, Université de Toulouse** | **Rapporteur** |
| **Thierry PAILLAT, Professeur, Université de Poitiers** | **Rapporteur** |
| **Stéphane HOLÉ, Professeur, Sorbonne Université** | **Examinateur** |
| **Céline CORBRION, Maître de Conférences, Sorbonne Université** | **Examinatrice** |
| **Petru NOTINGHER, Professeur, Université de Montpellier** | **Directeur de thèse** |
| **Jean-Charles LAURENTIE, Maître de Conférences, Université de Montpellier** | **Co-encadrant** |


UNIVERSITÉ DE MONTPELLIER
l'Europe s'engage en Occitanie
UNION EUROPÉENNE
La Région Occitanie Pyrénées - Méditerranée
Projet cofinancé par le Fonds Européen de Développement Régional

# *Acknowledgements*

First and foremost, I would like to extend my sincerest appreciation to the esteemed members of the jury for their valuable time, effort and expertise in evaluating my work. Their valuable suggestions and feedback have been instrumental in the completion of my PhD research. I am truly honored to have had the opportunity to present my work to such a distinguished panel of experts and for the opportunity to have received their guidance. I would like to thank each of them, Pascale GALL BORRUT, Laurent BERQUEZ, Thierry PAILLAT, Stéphane HOLÉ, and Céline CORBRION for their active participation and dedication to my PhD defence. Their support and encouragement throughout this process have been greatly appreciated.

This research would not have been possible without the financial support provided by the University of Montpellier, as well as the co-financing provided by the European Regional Development Fund.

I am truly grateful to my PhD advisor, Petru NOTINGHER, for his unwavering support during my thesis. As a newbie to the dielectrics domain, I had many questions and doubts, but he never judged me and always provided me with patient answers, even until the day before my PhD defense. His expertise and guidance were invaluable in helping me understand the complexities of this field. His willingness to go above and beyond to provide me with the support I needed is deeply appreciated. I cannot thank him enough for his support and for believing in my capabilities to achieve my goals. I am grateful for his mentorship and for helping me throughout this journey.

I would like to express my deepest gratitude to my co-supervisor, Jean-Charles LAURENTIE for his invaluable guidance, support, and encouragement throughout the course of this research. His expertise and insight have helped to shape the direction and outcome of this work.

I would like to express my heartfelt gratitude to Stéphane HOLÉ in particular for his invaluable support and assistance during the final and most crucial phase of my research. His generosity in allowing us to use the experimental bench and all of the necessary equipment at ESPCI in Paris was critical to the success of my experiments. I would also like to thank him for his prompt assistance and for his willingness to help whenever we needed it. I am truly grateful for the opportunity to have had the benefit of working in his lab.

When I first arrived in Montpellier to begin my PhD, I was filled with uncertainty and doubt. The new language and the fact that I was entering a field where there were few women like myself made me feel out of place. But thanks to the support and guidance of my lab members, particularly Olivier, Ben, Guillaume, Xav, Mourad, Abdellah, Yao, I was able to overcome these challenges and find my footing. They welcomed me into their lab and helped me learn French, and through our shared experiences, I have formed friendships that will last a lifetime. These friends have been with me every step of the way during my PhD journey, from the beginning to the end. The transformation I have undergone during my PhD, both personally and professionally, has made all the uncertainty and hard work worth it.

During the final year of my PhD, which can be a stressful time, I had the most enjoyable experience, all thanks to the wonderful group of people I met at LMGC. Despite coming from different labs, they never made me feel like an outsider. They were a constant source of support and helped me stay grounded during difficult times, and they have accepted me for who I am. I cannot thank them enough for all the good times and memories we shared over the last year. I would like to give a special thanks to Pankaj, Pierro, Jojo, Nathan, Lea, Agathe, Emy, Toto, Xavier, Will, Sam, Max, Cami, Theo, Chenghe, Clement, and Seby, you guys are the best!

I just want to give a big shoutout to my parents for always believing in me and giving me the trust and support I needed. Their faith in me allowed me to take on new challenges and grow in ways I never thought possible. They were always there to support me and push me forward, even though it was hard to communicate while I was studying abroad. I'm so grateful for everything they've done for me and for always having faith in me to achieve my goals.

I also want to thank my grandparents and the rest of my family for always being there for me during my PhD journey. They've always believed in me and been a constant source of motivation. They were always understanding and patient during the tough times, and always there to celebrate my wins and lift me up during setbacks. I'm so lucky to have such a loving and supportive family, they've been the foundation of my life and I'll always be thankful to them.

This journey would have been much harder without the support of my friends who are like family. I am forever grateful to my best friends Hazel and Joyce for being there for me through thick and thin, and to the rest of the JIGGA family. Their presence in my life has been precious, and I cannot express enough gratitude for all they have done. I am deeply grateful for their friendship and love, and I cannot thank them enough. I love you all.

Lastly, I would like to extend my heartfelt thanks to all those who were present, physically or virtually, on such an important day. Seeing the support and encouragement of my loved ones was incredibly uplifting and helped boost my confidence. I am truly grateful to each and every one of you for being a part of my journey.

Thank you all!

# *Table of Contents*


*General Introduction..... 1*

*Chapter 1: HVDC, insulators and space charge measurements ..... 7*

**1.1 Introduction ..... 8**

**1.2 Electric power transmission, high voltage dc current (HVDC) systems and associated components ..... 9**

1.2.1 Electric power transmission and HVDC ..... 9

1.2.2 Components of HVDC systems ..... 11

1.2.2.1 Power converters and semiconducting devices ..... 11

1.2.2.2 Switchgears ..... 13

1.2.2.3 Insulated cables and accessories ..... 14

1.2.3 Problematics related to the development of HVDC links ..... 16

**1.3 Charge-related phenomena in insulating materials ..... 17**

1.3.1 Polarization ..... 17

1.3.1.1 Polarization mechanisms ..... 19

1.3.1.1.1 Electronic polarization ..... 19

1.3.1.1.2 Atomic or ionic polarization ..... 20

1.3.1.1.3 Orientation (dipolar) polarization ..... 20

1.3.1.1.4 Space charge or interfacial polarization ..... 20

1.3.2 Dielectric losses & spectrum ..... 20

1.3.3 Charge Transport ..... 22

1.3.3.1 Electrode-controlled conduction mechanisms ..... 23

1.3.3.1.1 Schottky effect ..... 24

1.3.3.1.2 Fowler-Nordheim Tunnelling ..... 24

1.3.3.1.3 Thermo-ionic field emission ..... 25

1.3.3.2 Volume-controlled conduction mechanisms ..... 25

1.3.3.2.1 Poole-Frenkel effect ..... 25

1.3.3.2.2 Ohmic conduction ..... 26

1.3.3.2.3 Space-Charge limited conduction ..... 26

1.3.3.2.4 Hopping ..... 28

1.3.3.2.5 Ionic transport ..... 28

1.3.3.2.6 Grain-boundary limited conduction ..... 28

1.3.4 Space charge and aim of the thesis ..... 29

1.3.4.1 Space charge accumulation ..... 29

1.3.4.2 Consequences of space charge and aims of the thesis ..... 31

**1.4 Space Charge Measurement Methods ..... 34**

1.4.1 Non-resolutive methods ..... 35

1.4.1.1 The Thermally Stimulating Discharge Currents Method (TSDC or TSC) ..... 35

1.4.1.2 The Mirror Method ..... 36

1.4.1.3 Decay of Surface Potential ..... 37

1.4.1.4 Dielectric Spectroscopy ..... 38

1.4.1.5 Capacitance-Voltage (C-V) technique ..... 38

1.4.2 Resolutive methods ..... 38

1.4.2.1 Etching method ..... 38

1.4.2.2 Stimuli Methods ..... 39

1.4.2.2.1 Pressure methods ..... 39

1.4.2.2.2 Thermal methods ..... 43
1.4.3 Aspects regarding resolution ..... 56
1.4.4 Synthesis and discussion with respect to the aim of the work ..... 61
**1.5 Conclusion ..... 63**
***Chapter 2: Simulations ..... 65***
**2.1. Introduction ..... 66**
**2.2. General parameters ..... 66**
**2.3. Thermal Simulations ..... 67**
2.3.1. Equations and conditions ..... 67
2.3.2. Results and analysis ..... 69
**2.4. Electrical Simulations ..... 73**
2.4.1. Equations and parameters ..... 73
2.4.2. Results and analysis ..... 75
**2.5. Conclusions ..... 79**
***Chapter 3: Experimental Results ..... 81***
**3.1. Introduction ..... 82**
**3.2. Samples ..... 82**
3.2.1. Materials, structures and dimensions ..... 82
3.2.2. Electrodes / Temperature sensors ..... 84
**3.3. Experimental setup ..... 86**
3.3.1. Instrumental chain and measurement cell ..... 86
3.3.2. Conditioning circuit ..... 88
3.3.3. Measurement protocol ..... 90
**3.4. Primary results ..... 91**
**3.5. Decoupling and analysis of temperature and charge signals ..... 94**
3.5.1. Temperature signals ..... 94
3.5.1.1. Decoupling procedure ..... 94
3.5.1.2. Qualitative analysis ..... 94
3.5.2. Charge signals ..... 95
3.5.2.1. Decoupling procedure ..... 95
3.5.2.2. Qualitative analysis ..... 96
3.5.2.2.1. LDPE samples with Pt electrodes ..... 96
3.5.2.2.2. XLPE samples coated with carbon-black electrodes and Pt electrodes ..... 99
3.5.3. Conclusion ..... 102
**3.6. In-depth signal analysis. Determination of temperature distributions and of interface fields ..... 102**
3.6.1. General considerations ..... 102
3.6.2. Expressions of the temperature and charge signals with respect to the measured signals and the components of the conditioning circuit ..... 104
3.6.3. Temperature across the sample ..... 108
3.6.3.1. Surface Temperature ..... 108
3.6.3.1.1. Equations ..... 108
3.6.3.1.2. Results and analysis ..... 109

3.6.3.2. Volume Temperature ..... 112
3.6.3.2.1. Equations ..... 112
3.6.3.2.2. Results and analysis ..... 113
3.6.4. Determination of interface fields ..... 116
3.6.4.1. Charge signals and dependence of the field across the sample ..... 116
3.6.4.2. Calibration signals and determination of the coefficient α ..... 117
3.6.4.3. Determination of interface fields ..... 119
**3.7. Conclusions ..... 122**
***Conclusions & Perspectives ..... 125***
***Bibliography ..... 139***

# *Table of Figures*

Figure 1.1 Principle diagram of an ac grid, majorly used today in electrical power generation, transmission and distribution ..... 9
Figure 1.2 Comparison of costs between HVAC and HVDC Transmission Systems ..... 10
Figure 1.3 HVDC transmission system converter technologies [8] ..... 11
Figure 1.4 Schematic diagram design of MV SiC MOSFET power module [21] ..... 13
Figure 1.5 Offshore platform configuration of a DC GIS [23] ..... 14
Figure 1.6 HVDC cables with different insulation systems [1] : Mass impregnated non draining (a), oil-filled (b), polypropylene-paper laminate (c) and extruded polyethylene (d) . 15
Figure 1.7 Basic design of a joint for polymeric cables [31] ..... 16
Figure 1.8 Schematic representation of the different types of polarization mechanisms ..... 19
Figure 1.9 Dielectric constant vs frequency (log scale) showing various mechanisms [36] ... 22
Figure 1.10 Schematic diagram of energy band gap in solids ..... 22
Figure 1.11 Conduction mechanisms in dielectrics ..... 23
Figure 1.12 Comparison of energy band diagram representation of thermoionic emission, thermoionic-field emission, field emission in a MIS structure ..... 23
Figure 1.13 Energy band diagram representation of (a) Poole-Frenkel effect in MIS structure, (b) Ohmic conduction in MIS structure ..... 26
Figure 1.14 Current Density vs voltage graph for an ideal case of SCLC [43] ..... 27
Figure 1.15 Energy band diagram representation of ionic conduction (a) without the applied electric field and (b) with the applied electric field [37] ..... 28
Figure 1.16 Schematic diagram of state density in dielectric materials (a Deep and shallow traps one-level model ) (b) Symbolic representation of shallow and deep traps for electrons and holes [55] ..... 29
Figure 1.17 (a) Homocharge and (b) Heterocharge at the electrodes ..... 30
Figure 1.18 Electric field distortion due to the space charge distribution ..... 31
Figure 1.19 DC volume resistivity of LDPE vs temperature and electric field [65] ..... 32
Figure 1.20 Space charge density distributions for an epoxy insulating sample after conditioning for 4h at 25 °C and 105 °C [62] ..... 33
Figure 1.21 Most popular space charge measurement methods ..... 34
Figure 1.22 The principle of the thermally stimulated discharge currents (TSDC) ..... 36
Figure 1.23 The principle of the mirror method ..... 37
Figure 1.24 Schematic diagram for the PEA method [88] ..... 40
Figure 1.25 On the PWP method [94]: (a) principle of the method using a laser for the generation of the pressure pulse, (b) form of signals obtained without internal charges and (c) with internal charges ..... 41
Figure 1.26 Experimental setup for the LIPP method [58] [98] ..... 41
Figure 1.27 Experimental setup of PIPP method ..... 42
Figure 1.28 Schematic diagram of the PIPS method [58] ..... 42
Figure 1.29 Diagram related to the determination of the expression on the current response of an insulating sample submitted to a temperature variation on one of its faces [111] ..... 44
Figure 1.30 TSM setup in short – circuit condition. ..... 47

Figure 1.31 Diagram of TPM setup for two configurations: (a) Sample with two metallized electrodes , (b) Sample metallized on only one face [130]. ..... 48
Figure 1.32 Electrical analog circuit used in Collin's "deconvolution" process [124] ..... 52
Figure 1.33. Schematic diagram of the experimental set up for the LIMM [154] ..... 56
Figure 1.34 Spatial resolution for acoustic methods (a) and thermal methods (b) [156] ..... 57
Figure 1.35 Illustration of the definition of the two types of spatial resolution [157] ..... 58
Figure 1.36 TPM for different sample configurations [159] ..... 58
Figure 1.37 Schematic diagram for diffusion of heat using femtosecond laser ..... 60
Figure 2.1 Domain of study ..... 66
Figure 2.2 Thermal stimulus considered in the simulations as applied to the surface of the sample ..... 68
Figure 2.3 Temperature variation across LDPE samples with respect to time and depth coordinates for Q=214 mJ, $t_{pulse}$=10 µs and $x_o$=0.1 nm: (a) 50 µm-thick insulating sample, (b) 100 µm-thick insulating sample ..... 70
Figure 2.4 Temperature variation with respect to time at different depth coordinates x from the excited surface for $t_{pulse}$= 0.1 ms: (a) Q = 1 mJ, (b) Q = 5 mJ ..... 70
Figure 2.5 Temperature variation with respect to time at different depth coordinates x from the excited surface for $t_{pulse}$= 1 µs: (a) Q = 1 mJ, (b) Q = 5 mJ ..... 71
Figure 2.6 Temperature distribution in the depth at several instants t after the application of the thermal stimulus: (a) Q = 5 mJ, $t_{pulse}$= 5 ns, (b) Q = 676 mJ, $t_{pulse}$= 0.1 ms ..... 71
Figure 2.7 Temperature variation with respect to time at different depth coordinates x for $t_{pulse}$=5 ns and: (a) Q = 1 mJ, (b) Q = 5 mJ ..... 71
Figure 2.8 Temperature variation for $t_{pulse}$=5 ns and Q=0.1 mJ: (a) at different depth coordinates x with respect to time, (b) across the sample at different moments t ..... 72
Figure 2.9 Diagram of the sample with respect to the charge position ..... 73
Figure 2.10 Examples of charges $Q_i$ placed in the sample at the depth $x_i$ and of influence charges $Q_{i1}$ and $Q_{i2}$ at electrodes: (a) $x_i$=10 µm, 50 µm-thick insulating sample, (b) $x_i$=50 µm, 100 µm-thick insulating sample ..... 74
Figure 2.11 Electric field values and distributions induced by the charge $Q_i$ placed at different positions $x_i$ with respect to the left electrode (x=0): (a) 50 µm-thick insulating sample, (b) 100 µm-thick insulating sample The bold curves correspond to the charge positions from Figure 2.10. ..... 74
Figure 2.12 Simulated thermal pulse current responses in a 50µm-thick sample for $t_{pulse}$=5 ns: (a) Q=1 mJ, (b) Q=5 mJ ..... 75
Figure 2.13 Simulated thermal pulse current responses in a 50µm-thick sample for Q = 5 mJ and: (a) $t_{pulse}$ = 1 µs, (b) $t_{pulse}$ = 0.1 ms ..... 75
Figure 2.14 Influence of the semicon electrode thickness $x_0$ on the thermal pulse current response for a 50 µm-thick sample when the charge is placed at the interface ($x_i$=0), $t_{pulse}$ = 1 µs and Q = 5 mJ ..... 76
Figure 2.15 Influence of the semicon electrode thickness $x_0$ on the thermal pulse current response for a 50 µm-thick sample when the charge is placed at the interface ($x_i$=0), $t_{pulse}$=5 ns and: (a) Q = 1 mJ, (b) Q = 5 mJ ..... 76
Figure 2.16 Simulated thermal pulse voltage response for Q=1 mJ and $t_{pulse}$=5 ns and zoom in area of the first microsecond ..... 77

Figure 2.17 Simulated thermal pulse voltage response for Q = 5 mJ, $t_{pulse}$=5 ns and zoom in the area of the first microsecond ..... 78
Figure 2.18 Influence of the semicon electrode thickness $x_0$ on the thermal pulse voltage response for $t_{pulse}$=5 ns and: (a) Q = 1 mJ, (b) Q = 5 mJ ..... 78
Figure 2.19 Influence of the semicon electrode thickness $x_0$ on the thermal pulse voltage response when $t_{pulse}$=1 µs and Q=5 mJ ..... 78
Figure 3.1 Structure of the Pt-coated LDPE samples ..... 82
Figure 3.2 Structure of the carbon-black XLPE samples with Pt layers for the surface temperature measurements ..... 83
Figure 3.3 Reflectivity versus wavelength of various typical metals at normal incidence (Φ=0) [168] ..... 83
Figure 3.4 (a) Diagram of the e-beam evaporation process, (b) E-beam thermal evaporator chamber ..... 85
Figure 3.5 Steps taken to make the electrode deposition ..... 85
Figure 3.6 Schematic diagram of the experimental setup using TPM ..... 87
Figure 3.7 Test cell and details ..... 88
Figure 3.8 Diagram of the temperature measurement circuit ..... 90
Figure 3.9 Primary temperature signals measured without applying voltage for different currents( IT) fed to the electrode(a) 50 µm-thick sample ($R_e$=30 Ω), (b) 100 µm-thick sample ($R_e$=53 Ω) ..... 91
Figure 3.10 Primary temperature signals measured on samples submitted to different voltages and fed with an electrode current of +/- 20mA: (a) 50 µm-thick sample ($R_e$=56 Ω), (b) 100 µm-thick sample ($R_e$=39 Ω) ..... 92
Figure 3.11 Primary charge signals measured without applying voltage on a: (a) 50 µm-thick sample ($R_e$=30 Ω), (b) 100 µm-thick sample ($R_e$=53 Ω) ..... 92
Figure 3.12 Primary charge signals measured on a 50 µm-thick sample submitted to different voltages for feeding currents of +/- 20mA ($R_e$=56 Ω) ..... 92
Figure 3.13 Primary signals measured on a 100 µm-thick sample in volt-off conditions: (a) Temperature signals ($R_e$=53 Ω), (b) Charge signals ..... 93
Figure 3.14 Primary charge signals measured on a 100 µm-thick sample for a feeding current of +/- 20mA ($R_e$=39 Ω) for different applied voltage ..... 94
Figure 3.15 Bolometric signals measured on a: (a) 50 µm-thick sample ($R_e$=56 Ω), (b) 100 µm-thick sample ($R_e$=39 Ω) ..... 95
Figure 3.16 Charge signals issued by a (a) 50 µm-thick sample ($R_e$=56 Ω), (b) 100 µm-thick sample ($R_e$=39 Ω) ..... 97
Figure 3.17 Charge signals related to low field polarization in a 50 µm-thick sample ..... 97
Figure 3.18 Illustration of the symmetry of charge signals when positive and negative voltages are applied to a 50 µm-thick sample ..... 98
Figure 3.19 Signals related to the internal field in a 50 µm-thick sample (a) Face A, (b) Face B ..... 98
Figure 3.20 Signal related to the internal field in a 100 µm-thick sample (a) Face A, (b) Face B ..... 99
Figure 3.21 Charge signals issued from a 160 µm-thick sample with semicon electrodes: (a) Face A ($R_e$=58 Ω), (b) Face B ($R_e$=55 Ω) ..... 99

Figure 3.22 Signals related to the interface field in a 160 µm-thick sample with semicon electrodes: (a) Face A ($R_e$=58 Ω), (b) Face B ($R_e$=55 Ω) ..... 100
Figure 3.23 Primary charge signal measured on the semiconducting samples in volt-off conditions ..... 101
Figure 3.24 Electrical diagram of temperature and charge measurement circuit..... 102
Figure 3.25 Simplified equivalent circuit at high frequencies ..... 103
Figure 3.26 Equivalent circuit when $I_T = 0$ ..... 104
Figure 3.27 Equivalent circuit when $V_{TPM}$=0..... 104
Figure 3.28 Surface temperature variations of the thermally excited faces of 50 µm-thick (a) and 100 µm-thick (b)LDPE sample coated with Pt electrodes in volt-off conditions ..... 110
Figure 3.29 Surface temperature variations of the thermally excited faces of a 50 µm-thick LDPE sample coated with Pt electrodes and submitted to different voltages: (a) Face A, (b) Face B..... 110
Figure 3.30 Surface temperature variations of the thermally excited faces of a 100 µm-thick LDPE sample coated with Pt electrodes and submitted to different voltages: (a) Face A, (b) Face B..... 111
Figure 3.31 Surface temperature variations of the thermally excited faces of a 160 µm-thick XLPE sample provided with semicon and Pt electrodes: (a) Face A, (b) Face B..... 111
Figure 3.32 Temperature variations with time at different depths from the excited electrodes of a 50 µm-thick LDPE sample: (a) Excitation applied to Face A, (b) Excitation applied to Face B. Measurement campaign 1. Volt-off conditions..... 113
Figure 3.33 Temperature distributions across a 50 µm-thick LDPE sample at different moments after thermal excitation of Face A (a) and Face B (b). Measurement campaign 1. Volt-off conditions. ..... 113
Figure 3.34 Temperature variations with time at different depths from the excited electrodes of a 50 µm-thick LDPE sample: (a) Excitation applied to Face A, (b) Excitation applied to Face B. Measurement campaign 2. Volt-off conditions..... 114
Figure 3.35 Temperature distributions across a 50 µm-thick LDPE sample at different moments after thermal excitation of Face A (a) and Face B (b) of. Measurement campaign 2. Volt-off conditions. ..... 114
Figure 3.36 Temperature variations with time at different depths from the excited electrodes of a 160 µm-thick XLPE sample provided with carbon-black electrodes: (a) Excitation applied to Face A, (b) Excitation applied to Face B. Volt-off conditions..... 114
Figure 3.37 Temperature distributions across a 160 µm-thick XLPE sample provided with carbon-black electrodes at different moments after thermal excitation of Face A (a) and Face B (b) of. Volt-off conditions. ..... 115
Figure 3.38 Volt-on and volt-off TPM signals issued by a 50 µm sample: Thermal stimulus applied on Face A (a) and on Face B (b)..... 116
Figure 3.39 Volt-on and volt-off TPM signals issued by a 100 µm sample: Thermal stimulus applied on Face A (a) and on Face B (b)..... 116
Figure 3.40 Calibration signals and volt-off signals corresponding to a 50 µm sample: Stimulus applied on Face A (a) and on Face B (b). The dotted curves correspond to signals recalculated after determining the value of α. ..... 118

Figure 3.41 Calibration signals and volt-off signals corresponding to a 100 μm sample: Stimulus applied on Face A (a) and on Face B (b). The dotted curves correspond the signals recalculated after determining the value of α. ..... 118
Figure 3.42 Quantity E(t) as an image of the electric field at the interface zone of a 50 μm-thick LDPE sample with Pt electrodes ..... 121
Figure 3.43 Quantity E(t) as an image of the electric field at the interface zone of a 100 μm-thick LDPE sample with Pt electrodes ..... 121
Figure 3.44 Quantity E(t) as image of the electric field at the interface zone of a 160 μm-thick XLPE sample with semicon electrodes and Pt layers deposited on the semicon electrodes, i.e. at the Pt/semicon interface. A value of α equal to the one determined for LDPE has been considered. ..... 122

# *Table of Tables*

Table 1.1 Overview of relationship between current density and voltage ..... 27
Table 1.2 Overview of the spatial resolution for different space charge measurement techniques [157] ..... 59
Table 1.3 Characteristics of space charge measurement methods [36] ..... 62
Table 2.1 Simulation parameters for the insulating layers ..... 67
Table 2.2 Energies and pulse durations used in the simulations and maximum temperature elevation near the thermally excited electrode. In the greyed areas, the values exceed 50 K. 69
Table 3.1 Components of the measurement circuit ..... 89
Table 3.2 Significance of notations used for measurements ..... 90
Table 3.3 Coefficient $\alpha$ determined from different calibration signals issued by a 50 µm-thick LDPE sample with Pt electrodes ..... 119

# *List of Abbreviations*

| Abbreviation | Meaning |
|---|---|
| AIS | Air Insulated Switchgear |
| Ar | Argon |
| ATWM | Alternative Thermal Wave Method |
| Au | Gold |
| $C_6H_6$ | Benzene |
| $CH_4$ | Methane |
| Cr | Chromium |
| CSC | Current Source Converter |
| C-V | Capacitance-Voltage |
| CVD | Chemical Vapour Deposition |
| DS | Dielectric Spectroscopy |
| EAR | Electro Acoustic Reflectometry |
| FEP | Fluorinated Ethylene Propylene |
| FLAMM | Focused Laser Acoustic Modulation Method |
| FLIMM | Focused Laser Intensity Modulation Method |
| F-N | Fowler-Nordheim |
| FTE | Field-Enhanced Thermoionic Emission |
| GaN | Gallium Nitride |
| GIS | Gas Insulated Switchgear |
| $H_2O$ | Water |
| HCl | Hydrochloric Acid |
| HDPE | High Density Polyethylene |
| HF | High Frequency |
| HPOF | High Pressure Oil Filled |
| HVAC | High Voltage Alternating Current |
| HVDC | High Voltage Direct Current |
| IC | Integrated Circuits |
| IGBT | Insulated Gate Bipolar Transistor |
| IPL | Inverse Power Law |
| KCl | Potassium Chloride |
| LCC | Line Commutated Converter |
| LDPE | Low Density Polyethylene |
| LF | Low Frequency |
| LIMM | Laser Intensity Modulation Method |
| LIPP | Laser Intensity Pressure Pulse |
| MEMS | Micro Electro Mechanical Systems |
| MIS | Metal Insulator Semiconductor |
| MIND | Mass Impregnated Non Draining |
| MMC | Modular Multi-Level Converter |
| MOSFET | Metal Oxide Semiconductor Field Effect Transistor |

| | |
|---|---|
| MV | Medium Voltage |
| NaCl | Sodium Chloride |
| $NH_3$ | Ammonia |
| OC | Ohmic Conduction |
| OF | Oil Filled |
| PEA | Pulsed Electro Acoustic |
| PE | Polyethylene |
| PECVD | Plasma Enhanced Chemical Vapour Deposition |
| PET | Polyethylene Terephthalate |
| P-F | Poole-Frenkel |
| PIPP | Piezoelectrically Induced Pressure Pulse |
| PIPS | Piezoelectrically Induced Pressure Step |
| PI | Polyimide |
| PMMA | Polymethyl Methacrylate |
| PPL | Polypropylene Paper Laminate |
| Pt | Platinum |
| PTFE | Polytetrafluoroethylene |
| PVC | Polyvinyl Chloride |
| PVDF | Polyvinylidene Fluoride |
| PWP | Pressure Wave Propagation |
| SCLC | Space Charge Limited Conduction |
| SCOF | Self-Contained Oil Filled |
| Si | Silicon |
| SiC | Silicon Carbide |
| Ti | Titanium |
| TSM | Thermal Step Method |
| TPM | Thermal Pulse Method |
| TPT | Thermal Pulse Tomography |
| TSC | Thermally Stimulated Current |
| TSDC | Thermally Stimulated Discharge Current |
| TSPC | Thermally Stimulated Polarization Current |
| VSC | Voltage Source Converter |
| XLPE | Cross Linked Polyethylene |

# General Introduction

The industrial growth of emerging countries, as well as the need to take strong action against pollution-causing factors, are now driving changes in the architecture of electrical power networks, allowing them to meet the needs of the present and future. As a result, there is a continuous increase in the number of high-powered "clean" energy production facilities (hydraulic, solar, wind) located at more and more remote locations from the consumption centers. High voltage transmission networks, which have been established and developed over more than a century, are the primary means by which electrical energy, which is essential to society's activities, is delivered to users. To support this energy transition and meet future needs, new means of energy transport are needed.

The majority of electrical energy is now transmitted via alternating current (AC) transmission networks. However, the development of "super-grids," which are meant to transport this energy over very long distances, is inextricably linked to the development of high voltage direct current (HVDC) equipment. Thus, beyond a certain distance, which can range from a few dozens to several hundred kilometers, direct current (DC) transmission is economically superior to AC transmission. Furthermore, DC allows for the connection of networks that are not synchronized or have different frequencies, via conversion stations based on power electronics. Finally, because capacitive effects limit the use of high-voltage AC cables to several dozens of kilometers, DC networks are particularly well suited to transmission by submarine and land cables over very long distances. HVDC power transmission is important in today’s global power grid and will continue to be important in the future, particularly for the high-voltage, large-capacity, long-distance power transmission [1]. Forecasts require a sharp rise in capacity (6 GW over 3,000 km instead of 2 GW over 600 km today), hence the need to triple the present voltages. For this purpose, it is necessary to develop new cables and accessories, with polymer insulations. The main obstacle to this development is related to the development of materials and structures with properties adapted to the constraints of the HVDC.

The reliability of HVDC components is related to the appearance, under the effect of the strong thermoelectric DC stress, of electric charge zones in the insulations. These "space charges" (so-called because they accumulate in insulating spaces) prematurely age the materials and can make them break down unexpectedly, putting networks out of service. The control of these charges being the key to the required technological leap, their measurement is decisive for designing, qualifying and monitoring DC insulation systems. This requires space charge measurement techniques with high sensitivity, spatial resolution and applicability, particularly at interfaces, which are the weak points of any insulating system, as they are usually the places enduring the higher stress.

The measurement of space charge has been a subject of study for several decades and several non-destructive methods based on the application of non-homogeneous acoustic or thermal stimuli to insulating samples have been set-up. Among them, the thermal methods, like the Thermal Pulse Method (TPM), Thermal Step Method (TSM) and the Laser Intensity Modulation Method (LIMM), proved to be the most sensitive, and have been used extensively in different configurations and on various thicknesses. Thus, as the amount of available energy is very high in the case of the TSM, this method has been mainly used for samples of medium and strong thickness (> 100 µm), while the TPM and the LIMM have been mainly used on

much thinner samples (often below 20 µm), particularly for the study of electrets, as the amount of heat which can be transferred to the sample in a short period of time must be limited to avoid overheating of the excited surface, which may cause damages to the sample. In turn, methods like the TPM allow a higher resolution near the thermally excited surface. On the other hand, these methods may offer the possibility of a deeper scan of the sample, provided that the heating conditions are well known and mastered.

The transient electrical responses resulting from the application of a thermal stimulus to a sample containing electrical charges are expressed as integrals in space, the cores of which are products of the spatio-temporal temperature distribution and the spatial distribution of the electric field. Sensitivity and resolution therefore depend, on one hand, on the intensity of the stimulus diffusing into the studied structure (and therefore, above all, on the efficiency of the thermal transfer, as the temperature rise cannot be too high to avoid thermo-stimulated discharge phenomena or alteration of the state of the materials), and, on the other hand, on the knowledge of the spatio-temporal distribution of the temperature. The calculation of this distribution involves solving the heat equation with boundary conditions that depend on the shape and amplitude of the stimulus. The precise evaluation of these conditions can be tricky, either because of the difficulty of perfectly controlling the liquid/solid heat exchange in the case of a temperature step stimulus (applied with a heat transfer liquid in direct contact with the electrode or with a metallic exchange surface), or, in the case of radiative heating, because of the impossibility of knowing precisely the energy absorbed by the electrode.

Although calibration processes with known electric fields can significantly reduce uncertainties, obtaining micrometric resolutions in medium-thickness structures and sub micrometric resolutions in thinner samples and at interfaces requires a very good knowledge of the surface temperature, the best way to obtain it being a direct measurement. At this level, the challenges lie in the experimental implementation and instrumentation to generate and acquire the signals with sufficient dynamics, as well as in the separation afterwards of the reciprocal contribution of the two types of signals, which may be coupled through the measurement circuit and the sample.

The possibility of simultaneously acquiring, in a TPM experiment, bolometric signals from the excited electrode and the space charge signal over the entire sample has already been demonstrated experimentally on samples with thicknesses of several microns [2]. Nevertheless, this technique has been employed very little on thicker samples, whereas it seems to offer sufficient possibilities for use on films of several tens of microns and even beyond, and most certainly for the measurement of interface fields in such samples. On the other hand, while the feasibility of coupled temperature/charge measurements has been proven, and the importance of having the true temperature distribution demonstrated, such signals have not been yet quantitatively exploited to determine the temperature distributions across the samples and the electric field values near the thermally excited electrodes.

This work thus has two objectives. The first is to approach the measurement of interface electric fields in samples with thicknesses of the order of 50-100 µm-thick and electrodes of several tens of mm in diameter, in order to be able to characterize objects with microscopic structures close to those that can be found in electrical engineering components. In addition, this may

allow TSM/TPM cross-measurements, which would ensure a better characterization throughout the entire thickness. The second objective is to be able to fully exploit the temperature and charge data, and thus to determine the quantitative values of the electric fields at the interfaces.

This thesis is divided into three chapters, each of them with its own role and content. Chapter 1 presents first an overview of the subject that forms the basis of the work, focusing on the objectives, issues and problematics related to the use of insulating materials in HVDC systems. The main charge-related phenomena encountered in insulating materials (polarization, injection, conduction and trapping) are then discussed in order to put into focus the mechanisms and consequences of the creation of space charge zones in polymeric insulations subjected to high thermo-electrical stress. The various existing techniques for measuring space charge distribution are then described. They are then analyzed in relation to the work's objectives, and a synthesis of all these methods is provided. Finally, the TPM, whose use on medium thickness insulating samples is the subject of this thesis, is discussed in detail.

In Chapter 2, results of thermal and electrical numerical simulations are presented. The aim of the numerical study, the parameters and the equations used are first detailed. In the “thermal simulation” part which follows, the analysis focuses on estimating the temperature variations at the surface and in the bulk of polyethylene samples provided with metallic and semicon electrodes and also, to assess the effects of pulses of different energies and durations and to determine their limits for heating as much as possible the samples without damaging them. These results are then used in electrical signal simulations for assessing the space charge responses which may be expected when applying different thermal pulses to samples containing fields of several kV/mm.

The third chapter of the manuscript is dedicated to the experimental results obtained by applying thermal stimuli of heat-pulse type to polyethylene samples with thicknesses of 50 µm to 160 µm. The first section is devoted to the preparation of the samples, in accordance with the requirement of the experimental work and available technology. The samples and the electrodes, that served both as temperature sensors and contacts for the space charge signal, are first shown. The measurement cell and the acquisition circuit are then described, followed by illustrations and discussions of typical acquired signals. The procedure for decoupling charge and temperature responses from primary signals is presented, followed by a qualitative analysis to highlight, in particular, the interface responses. The final section of this chapter is concerned with a detailed analysis of the measured signals, taking into account the entire acquisition chain, allowing the temperature distribution across the samples and the amplitude of the interface fields to be determined.

The conclusion and the different perspectives opened by this work are summarized at the end of the thesis.

# Chapter 1: HVDC, insulators and space charge measurements

## 1.1 Introduction

High Voltage Direct Current (HVDC) cables are critical components in the design of future electrical power transmission networks that must be capable of transporting high power over long distances. The ongoing expansion of HVDC networks, induced by a continuous increase in global energy needs, increasing distance between the production sites and consumption centers, and the development of renewable energies, necessitates an increase in HVDC cable production capacities today, specifically by developing highly reliable insulation systems based on polymers (mainly chemically cross-linked PE). This necessitates that the design account for the impacts of strong DC electric fields, high temperatures, and thermal gradients, which is the framework for the research presented in this thesis.

This chapter describes the conditions that prompted our research. Particular attention is paid to the issues and challenges associated with HVDC networks, insulators, physical phenomena that occur when high electric fields are applied to dielectrics, and methods for measuring electric charges present in insulating spaces ("space charges").

First, we will look at electric power transmission and the advantages of employing HVDC over large distances rather than HVAC. The structure and operation of HVDC cables are then examined. Power converters, semiconducting devices, cables, accessories, and switchgears continue to be major roadblocks in the development of HVDC systems and are addressed in detail. The following section identifies and discusses the barriers to the development of HVDC links.

Second, we review the charge-related phenomena in the insulating materials. The objective of this section is to set the groundwork for comprehending the circumstances that cause high electrical stress zones inside insulators. Polarization, injection, transport, and trapping processes are described and connected to material structure. The concept of space charge is addressed, and the effects of space charge are explored. These impacts are highlighted within the scope of the study, emphasizing one of the key goals of our work, which is to contribute to the advancement of space charge characterization techniques capable of probing at the best interfaces between insulating, conducting, and semi-conducting materials, allowing for the most precise measurement and survey of space charge and electric fields.

In the final section of the chapter, we evaluate the state of the art of existing space charge measuring techniques and analyze them in light of the thesis's aims and specific context in order to determine the next steps to be taken.

## 1.2 Electric power transmission, high voltage dc current (HVDC) systems and associated components

### 1.2.1 Electric power transmission and HVDC

The transmission of electric power from the production plants and its distribution toward the final consumer is presently done mostly in alternative current (ac). In contrast, power transmission in high voltage dc current (HVDC) mode, even if used since the beginning of electricity transmission, at the end of the 1800's, it is still very limited. This historical situation is particularly due to the facility to raise and lower the values of alternative voltages with the aid of transformers, whereas for many years the costs related to ac/dc and dc/dc conversion has been significant, letting HVDC transmission reserved for particular cases.

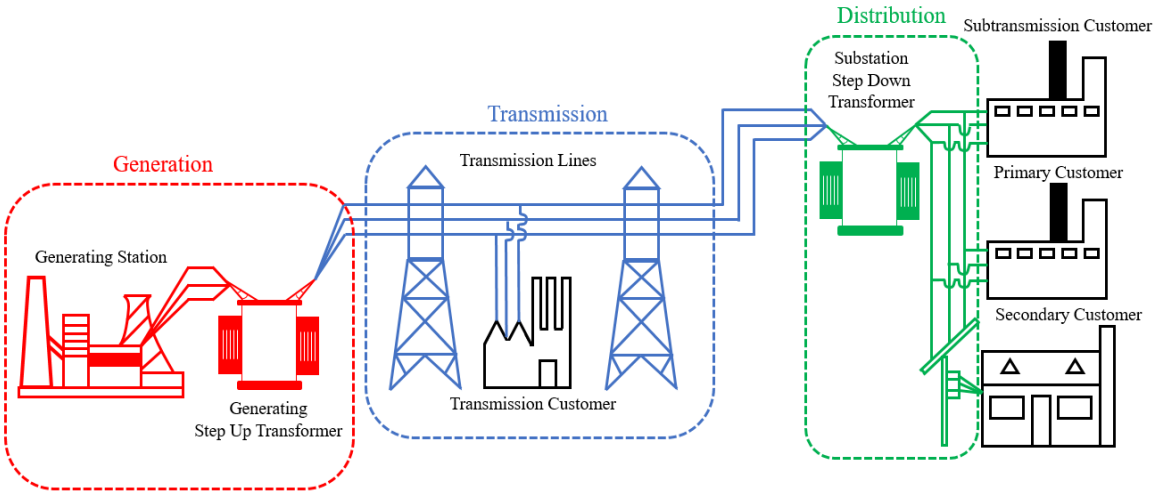


*Figure 1.1 Principle diagram of an ac grid, majorly used today in electrical power generation, transmission and distribution*

However, the evolution of the industrial growth during the last decades has led to a continuously increased consumption of electric power and triggered the constraints of producing "clean" energy. This growing need for "green" energy requires new power plants, more facilities in transmission and interconnection systems, and more decentralized power grids, at optimum costs. In the same time, the decrease of the cost and the increase of the reliability of power semiconducting devices now allows to consider manufacturing and use of static high power converters at a much larger scale than before. All these reasons favor more and more the development of direct current transport networks. Thus, HVDC transmission of electricity up to 600–800 MW across distances of roughly 300 km has already been accomplished using underwater cables, and links of up to 1000 km and above are now being planned [1, 3, 4].

With the maturity of thyristor and transistor technology since the 1960's, which has progressively increased component reliability and reduced the difficulty and the cost of building conversion stations, the number of HVDC systems has expanded continuously [5]. HVDC transmission by cable has been particularly enhanced in subsea applications, used to connect offshore platforms and windmill farms to land, or to transmit electricity over long distances at

sea, where overhead lines cannot be used. The connection between islands and mainland is also one of the main applications of HVDC transmission technology. HVDC overhead lines are also considered, especially for very high power links (projects up to 12 GW are under way [3, 4]).

The major constraint of the ac transmission over long distances is the limited transmission capacity and transmission distance due to the significant inductive (mainly in overhead lines) and capacitive (mainly in cables) aspects. Depending on the needed transmission capacity and loss evaluation of the system in addition to the operating voltage and frequency, with the corresponding reactive compensations the attainable transmission distance for a HVAC cable will be in the range of 40-100 km (usually 70 km at 220 kV, 40 km at 380 kV) [6, 7]. Also, it is not feasible to directly connect two systems with different frequencies, unless a couple of ac/dc and dc/ac converters is used, with the associated costs. Effects of the line inductance and/or capacitance have to be compensated along the ac link, which increases the overall ac transmission cost. Hence, a HVDC transmission system can be more economical compared to its ac counterpart when a bulk power is to be transported over very long distances. In addition to the economic and environmental benefits, HVDC transmissions offer other technical advantages such as lower losses, black-start possibilities, improved system stability, transmission capacity and enhanced reliability. At the moment, an overhead HVDC line is in general cheaper than a HVAC one for transmission of more than 1 GW on distances greater than 600 km, also known as the "break-even distance" (Figure 1.2). In terms of cable links, for distances of 40–50 km and above, HVDC is often more convenient [8].

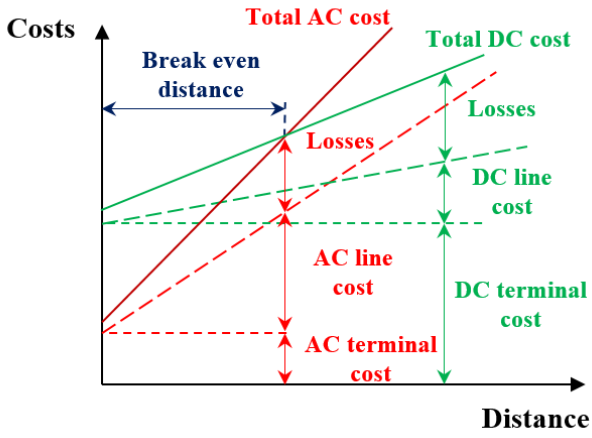


*Figure 1.2 Comparison of costs between HVAC and HVDC Transmission Systems*

Thus, despite the high cost of converter stations, HVDC projects offer important benefits over ac systems. For dc transmission, two conductors are required, with respect to three in ac transmission. Because a dc line can supply equivalent amounts or even larger amounts of power with only two sets of conductors rather than three, the towers don't have to be as huge, resulting in lower transmission costs. On the other hand, in dc transmission there is no inductance, no surges and no skin effect – so conductors with a smaller cross section can be used at equivalent level of transmitted power. Moreover, at the same voltage level, a dc system has usually less potential stress than an ac one; therefore, less insulation is required for a dc cable, which reduces its price. In the case of overhead lines, Corona losses are much lower in dc then in ac.

However, despite all the advantages of a HVDC transmission system over a HVAC one, there are counterparts related to the specificity of the constraints encountered in HVDC systems that must be mastered at the design level of the components that they embed.

## 1.2.2 Components of HVDC systems

### *1.2.2.1* Power converters and semiconducting devices

In current HVDC transmission systems, two fundamental converter technologies are employed: conventional line-commutated current source converters (CSC's) and self-commutated voltage source converters (VSC's). Figure 1.3 (a) depicts a traditional HVDC converter station with CSC's, whereas Figure 1.3 (b) depicts a VSC-equipped HVDC converter station.

The prevailing current source HVDC scheme, also known as the line commutated CSC's, is a traditional technology which has been extensively and reliably used for power transmission for many years. Since the commutation process is dependent on the voltages and impedances of the AC system, these devices using thyristors are also known as Line Commutated Converters (LCC) [9], and require a synchronous voltage source. To eliminate the ac side harmonics, ac transformers are coupled to the thyristors (Figure 1.3 (a)). A single thyristor may carry up to 6.25 kA and block voltages up to 10 kV in such a system [10]. A twelve-pulse arrangement is commonly used, with numerous twelve-pulse converter units linked in series, which can boost the voltage rating even further. As a result, among the available HVDC converter technologies, the LCC system has the greatest voltage and power rating.

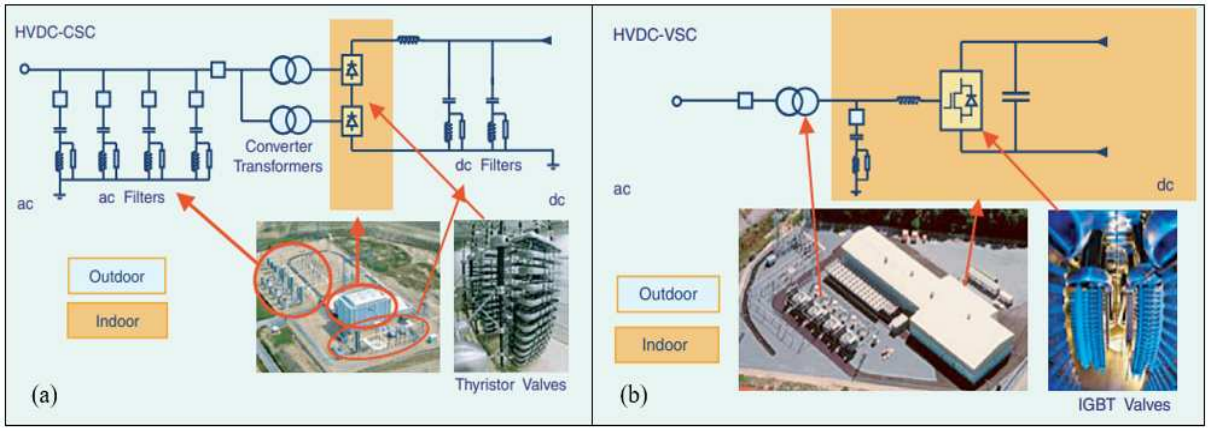


*Figure 1.3 HVDC transmission system converter technologies [8]*

LCC systems reverse the power flow by switching the dc voltage polarity while keeping a constant current. In comparison to other methods, this methodology provides a high level of dependability and requires less maintenance. In addition, when compared to VSC systems, LCC converters presently have reduced station losses and costs. Hence, LCC is the most efficient method of transmitting large amounts of power across high voltage transmission lines [10, 11].

In a VSC, insulated gate bipolar transistors (IGBT) are used, as shown in Figure 1.3 (b). Two-level or three-level converters are employed. The two-level converter is the fundamental building component of the VSC-HVDC architecture [12, 13]. It is similar to a six-pulse bridge,

except that instead of thyristors, IGBTs with inverse-parallel diodes are used, and the LCC's dc smoothing reactor is replaced by a dc capacitor. This technology's current can be turned on and off at any time, regardless of the ac voltage, and it even generates its own ac voltages in the event of a black start [14]. VSCs use pulse width modulation (PWM) to work at a high frequency, allowing the amplitude and phase angle of the converter to be adjusted simultaneously while the voltage remains constant [15]. VSCs offer a great degree of flexibility, with the ability to control both active and inherent reactive power, making it more suitable in urban power networks [16].

The two-level VSC draws its name from the fact that it features complementarily operated switching devices that create two levels of voltage ($+V_{dc}/2$ and $-V_{dc}/2$) at the converter's ac output terminal. Only one switching device may be used at a time in this complimentary action, and the other is switched off. When both switching devices are turned on at the same time, the capacitor across the dc connection will undergo short circuit, potentially destroying the converter switches owing to excess current. Each semiconductor switch in this configuration can endure the full voltage stress passing through the line [17]. The multilevel converter is the result of an endeavor to eliminate low harmonic distortion while also having a high efficiency. In contrast to a LCC, in a VSC the power flow can be reverted by reverting the sense of the current, allowing to avoid voltage polarity switching, which may be a hard constraint for polymer-insulated high voltage cables.

Due to its characteristics, VSC technology is considered as the best option for transporting intermittent renewable energy, such as that produced by wind and solar farms either offshore or onshore [10].

In order to obtain dc/dc converters of high power and high voltages, the tendency is to increase the operating frequency in order to lower the size of the converter [18]. For CSCs, silicon (Si) based thyristors have traditionally been utilized. Similarly, for VSCs, Si insulated-gate bipolar transistors (IGBTs) have been the most popular choice. Modular Multi-Level Converter (MMC) topologies have had a considerable influence on a variety of power electronic applications, owing to lower converter losses as compared to two or three level VSC [19]. Because of the improved physical features of the silicon carbide (SiC) material in contrast to Si, SiC based semiconductor devices are now recognized to offer greater efficiency performance, as well as a decrease in the cost of the total system, across a wide range of power electronics applications. Metal–oxide–semiconductor field-effect transistors (MOSFETs) made of SiC are now becoming more widely accessible in industry, allowing for the development of high-performance dc/dc converters based on modular designs [18].

Figure 1.4 represents the diagram of a power module for a medium voltage (MV) SiC MOSFET. Thanks to technical advancements over the last ten years, wide band gap semiconductors are now accessible, with better properties compared to Si devices, such as higher blocking voltage, higher thermal conductivity, higher temperature, and higher switching frequency. Gallium nitride (GaN) and SiC devices have made the most progress in terms of commercial availability and also considering the level of sophistication of their technical processes. SiC, on the other hand, is better suited to high-power and high-voltage applications

due to its thermal characteristics and the difficulty of producing the high-quality bulk substrates necessary for GaN vertical devices [20].

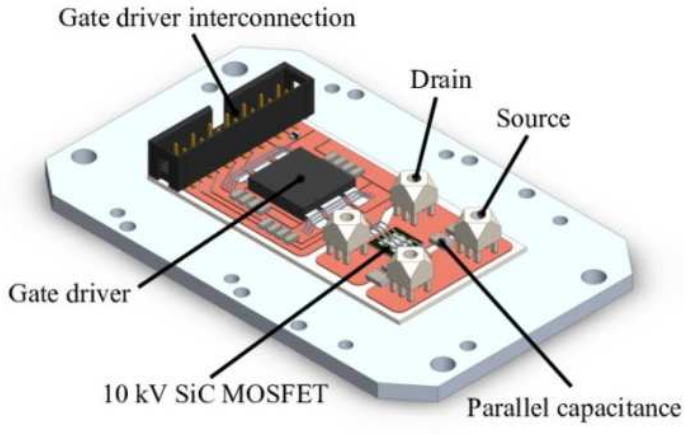


*Figure 1.4 Schematic diagram design of MV SiC MOSFET power module [21]*

The SiC MOSFET-based converters would enable for a reduction in switching losses and an increase in the switching frequency of HVDC power systems, resulting in a reduction in passive components [18].

All these semiconducting devices require, during the manufacturing process, the setup of passivation layers to electrically insulate the different parts of the dies. Oxide and nitride layers are commonly deposited to generate the passivation layers. In other cases, plasma enhanced chemical vapour deposition (PECVD) is used to create the oxide and nitride layers [22]. These insulating areas endure very high thermal and electrical stress and are fundamental for the device reliability.

### *1.2.2.2 Switchgears*

Control, protection, and isolation of electrical equipment and circuits are the tasks that a switchgear performs. There are two types of switchgears: Air Insulated Switchgears (AIS) and Gas Insulated Switchgears (GIS). The advantage of the use of a GIS is mainly its compacity.

Ac GIS are used as much as possible on the ac parts of a grid as they are well-mastered and less complex, because the passage through zero of the current in ac facilitates considerably the arc extinction; however, the use of dc GIS cannot always be avoided, and it increases continuously. Dc GIS are currently designed for applications with limited area, such as onshore and offshore HVDC converter stations, and transition stations between different transmission media. Figure 1.5 shows the offshore platform configuration of a dc GIS. DC GIS take up to 95 % less space than technically identical AIS. As a result, the HVDC offshore converter platform's footprint may be reduced by up to 10 %, while the footprint of transition stations can be lowered by up to 90 %, like those for lengthy DC cable lines [23].

A GIS includes both solid and gas insulating media. Specific constraints must be taken into account when designing dc GIS, as the electric field distribution in ac is governed by permittivity, whereas the electrical conductivity determines the electric field distribution in dc

[24]. As a result, key variables determining the dc field distribution are the surface conductivity of the gas/solid interfaces, the volume conductivity of the solid insulating parts and the strong non-linear conductivity of the gas. Thus, charge build-up may occur at the gas-solid interface, which is the insulator's surface, due to the discontinuous change in conductivity. This charge, governed by solid-state conduction, gas ion drift, or insulator surface conductance [25], is an important factor to be assessed and mastered.

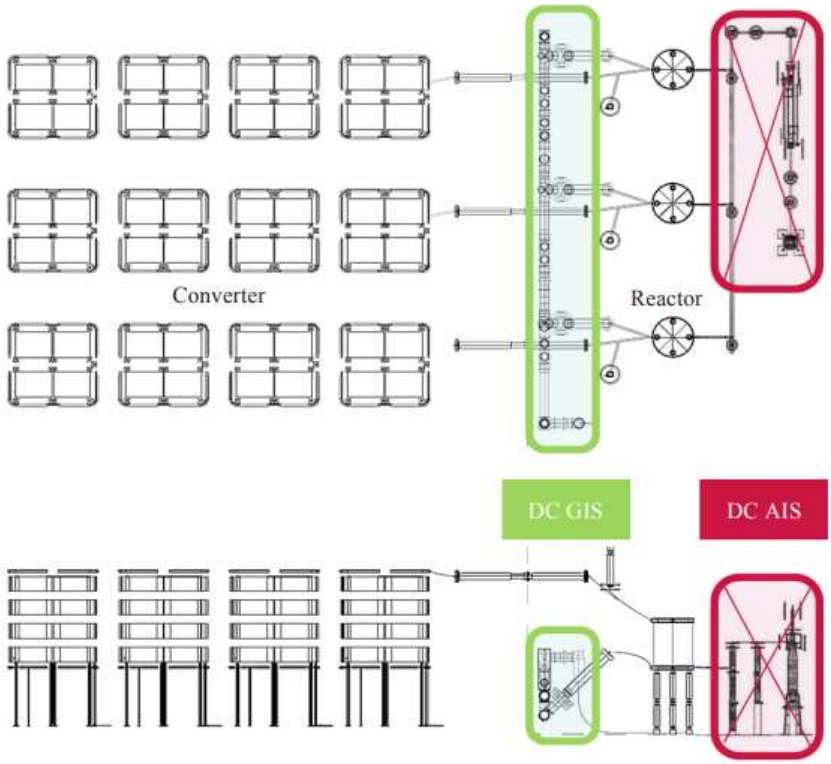


*Figure 1.5 Offshore platform configuration of a DC GIS [23]*

### *1.2.2.3 Insulated cables and accessories*

As evoked previously, using HVDC transmission for subterranean or offshore cable networks may result in significant cost reductions for installed cables and losses. These savings, depending on the power level to be transferred, can balance the converter station expenses for distances of 40–50 km or more [8]. Offshore applications are one of the most important and critical applications for HVDC. Thus, for distances greater than tens of kilometers and with the transmission capacity ranging from hundreds to thousands megawatts, especially for bipolar systems, HVDC is the favored technology for subsea applications. The used cables must be able to withstand not only the thermal and electrical stress, but also the mechanical stress related to the installation process and to the hydraulic pressure of water; there are also possibilities of damage due to tides, anchors, fishing equipment and other factors [26, 27]. In the same time, such cables are also used for terrestrial links, which are more and more present.

Two types of insulation are encountered in HVDC cables: oil-impregnated paper and synthetic ("dry") materials. Based on this, there are different types of HVDC cables, as shown in Figure 1.6 [1] [26, 27, 28, 29]:

- Mass impregnated non draining (MIND) cables (Figure 1.6 (a))
- Oil Filled (OF) cables
    - Self-contained OF (SCOF) cables (Figure 1.6 (b))
    - High pressure OF (HPOF) cables
- Polypropylene-paper laminate (PPL) cables (Figure 1.6 (c))
- Polymer-insulated (or extruded insulation) cables (Figure 1.6 (d))

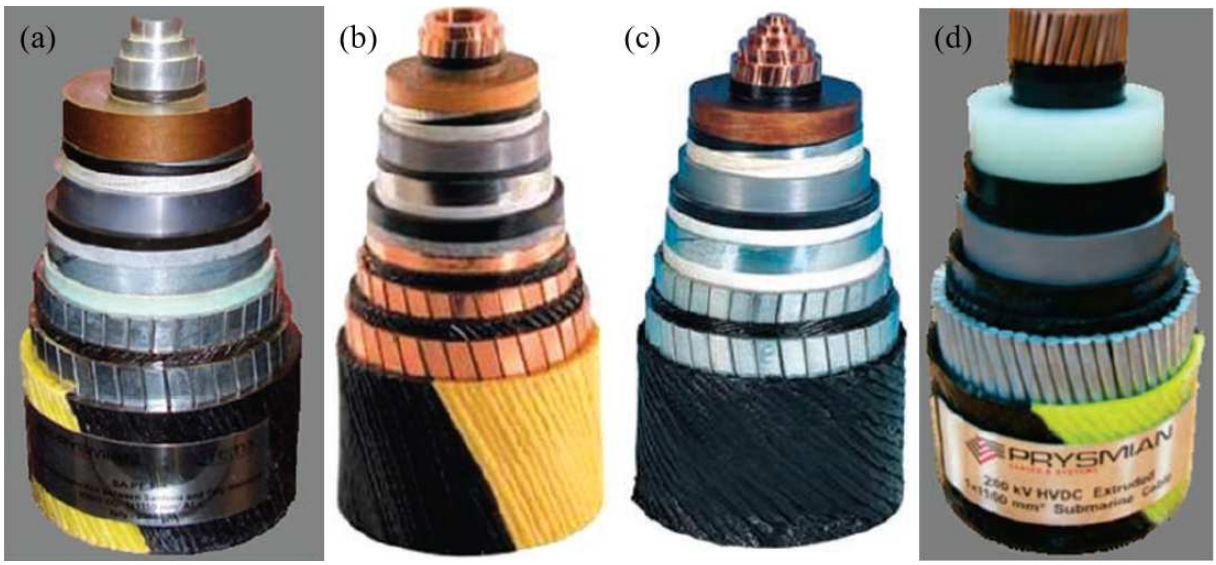


*Figure 1.6 HVDC cables with different insulation systems [1] : Mass impregnated non draining (a), oil-filled (b), polypropylene-paper laminate (c) and extruded polyethylene (d)*

Except the PPL, the technologies used for oil-impregnated paper cables are nowadays mature. Their use for many years in HVDC links has been made possible thanks to their significant reliability. Available both for submarine and underground use, each technology has its own advantages (possibility of transporting significant power for OF and practically unlimited length for MIND) and drawbacks (limited length and complex maintenance for OF due to the oil pressure mastering, power limitation for the MIND because of the thermal limit of the insulation at 55 °C). Also, both MIND and OF share the drawbacks of potential environmental problems related to the use of oil and of relatively high costs. In addition, such cables take time to be produced, and their jointing is difficult; this is not really a problem for submarine cables where the number of joints can be limited, but may become a huge one for long landlines.

The cables with extruded insulation have been used in HVAC since the 1960's, but their use in HVDC has been limited for a long time due to the reliability problems that may encounter the used insulations (mainly polyethylene) under high dc fields and temperature. The growing demand of eco-friendly insulations able to operate at high temperatures arouses today the setup of extruded HVDC cables with continuously increasing capacities. Thus, synthetic insulators can be used at higher temperatures (up to 90 °C), their dielectric losses are lower, their maintenance is reduced, their weight is lower, they are much easier to joint and they also have lower production costs. However, materials with insulating properties appropriate to the constraints under high dc field and temperature must be designed and used instead of the classical ac insulators.

On the other hand, it is impossible to produce pieces of dozens or hundreds of kilometers of HVDC land cables (and even submarine ones), as, because their weight and dimensions, such lengths cannot be transported on their installation sites. For this reason, with respect to their weight and volume, pieces of one to two kilometers are produced in practice for landlines and jointed at the installation. When using prefabricated joints according to the model shown in the figure below, the jointing time of extruded cable systems is significantly reduced [30]. However, testing and service experience show that the most crucial components for transmission system dependability are the joints and accessories, as they include and must match many layers of materials with different properties, and the number of joints may be enormous, especially in lengthy subterranean HVDC systems.

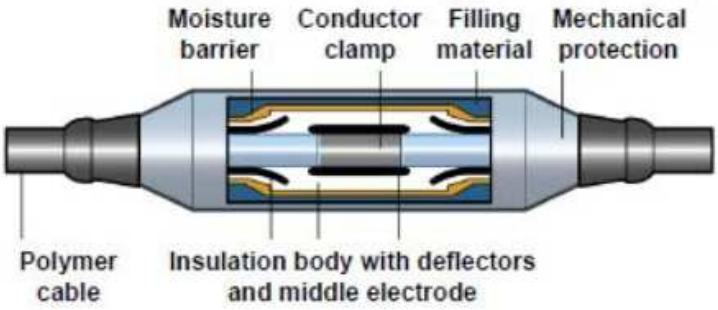


*Figure 1.7 Basic design of a joint for polymeric cables [31]*

In average, there is a cable joint to be installed about every kilometer, i.e. a 300 km landline would include ~300 joints. With such numbers, and taking into account the consequences of the breakdown of a joint which may put out a power link of several hundreds of MW or more during hours or days, it is obvious that the reliability of the joints and accessories are one of the most important matters to be dealt with in HVDC transmission.

## 1.2.3 Problematics related to the development of HVDC links

During many years, power electronics has been a major break for the expansion of HVDC links. Although the cost of power conversion stations still remains high, the recent development of bi-directional high voltage/high current devices as the aforementioned ones solved a major part of the problems posed by the diode and thyristor technologies.

The main bottlenecks to the development of HVDC networks remain the cables, the accessories and the switchgears. Thus, it is necessary to set up materials and structures (often multilayered) with properties adapted to the specific constraints induced by this type of networks, namely high dc electric fields and thermal gradients. The major problem is related to the establishment, under such stress, of electrically charged areas in the dielectrics and at their interfaces. These charge accumulations (called “space charges” as they are distributed in insulating spaces) overstress locally the materials and may make them age prematurely and/or initiate untimely breakdown. It is therefore essential to be able to determine the fields produced by these charges in order to anticipate their effect and thus to guarantee the performance of power infrastructures using synthetic insulations.

Our thesis work is situated at this level, concerning the measurement of space charges in insulating materials for HVDC components. The knowledge of the materials and fabrication processes should then allow to control space charge accumulation, both in the bulk of the dielectrics and at the different interfaces of the insulating systems.

Approaching these problematics necessitates the knowledge and the consideration of phenomena susceptible to take place in insulating materials under high electric field and of their effects (space charge accumulation in particular), which will be reviewed in the next section.

## 1.3 Charge-related phenomena in insulating materials

### 1.3.1 Polarization

The notion of polarization is related to the presence of bonded charges, i.e. dipoles. A dipole is defined as an association of two charges of opposite sign $(+Q\ and\ -Q)$, separated by a distance '$r$'. They are characterized by their dipolar moment $\vec{p} = q\vec{r}$, which is a vector oriented toward the positive charge across the center of gravity of the two charges.

When an electric field is applied to the material, either permanent dipoles are oriented more or less parallel to the field lines ("orientation polarization") or new dipoles are induced by local displacement of the barycenter of the positive and negative charges of the atoms and molecules ("distortion polarization"). If $\vec{M}$ is the equivalent dipole moment, i.e. the sum of all the projection of the dipole moments in the field direction, the polarization vector $P$ is defined as

$$\vec{P} = \frac{\vec{M}}{V}\ [C/m^2] \qquad Eq\ 1.1$$

where $V$ is the volume of the dielectric.

There is a local electric field $\overrightarrow{E_l}$ in a dielectric due to the influence of the external field $\vec{E}$ and the existence of dipoles. This local field creates a dipole moment $\vec{p} = \alpha\vec{E_l}$, at the level of each molecule, and $\alpha$ is referred to as the molecule's polarizability. We define the polarization vector $\vec{P}$ at the macroscopic level as the volume density $\frac{d\vec{p}}{dv}$ of dipole moments produced or orientated by the field. If we multiply the concentration of these dipoles by $N$, we get:

$$\vec{P} = \frac{d\vec{p}}{dv} = N\,\vec{p} = N\alpha\,\overrightarrow{E_l} \qquad Eq\ 1.2$$

In vaccum the electric displacement $\vec{D}$ (charge density displaced under the effect of the applied field) and the applied electric field are proportional: $\vec{D} = \varepsilon_0\vec{E}$, where $\varepsilon_0$ is called permittivity of vaccum. In a polarized material (other than vaccum), the effect of the polarization must be considered, and one gets:

$$\vec{D} = \varepsilon_0\,\vec{E} + \vec{P} \qquad Eq\ 1.3$$

In linear and homogeneous dielectric, the polarization is proportional to the field:

$$\vec{P} = \varepsilon_0 \chi \vec{E} \qquad \textit{Eq 1.4}$$

where $\chi$ is the electrical susceptibility of the material, so:

$$\vec{D} = \varepsilon_0 \vec{E} + \varepsilon_0 \chi \vec{E} = \varepsilon_0 (1 + \chi) \vec{E} = \varepsilon_0 \varepsilon_r \vec{E} \qquad \textit{Eq 1.5}$$

where $\varepsilon_r = (1 + \chi)$ is called the relative permittivity of the material. As it can be seen, the relative dielectric permittivity ($\varepsilon = \varepsilon_0 \varepsilon_r$) is a quantitative measure of the polarization of the material.

With respect to their structure, dielectrics can be distinguished into two types:

- Polar dielectrics: They possess polar molecules, which have their positive and negative charge centers of gravity separated. As a result, even in the absence of an applied electric field, these molecules exhibit permanent dipole moments. When an external field is applied, these dipole moments, which were initially oriented randomly, orient themselves mostly in the direction of the external field. This is known as orientation polarization. The dipole moment increases in proportion to the difference in electronegativity of the atoms that make up the molecule [32]. Some examples of polar dielectrics include $H_20$, $NH_3$, HCl, PMMA, PVC, PET etc.

- Non-polar dielectrics: Because of the symmetrical distribution of positive and negative charges of their molecules, which causes the centers of their charge distributions to coincide, non-polar dielectric molecules do not have a persistent dipole moment. When an electric field is applied, the charge barycenters are separated, with positive charges concentrating on one side and negative charges concentrated on the other. Non-polar dielectrics include $C_6H_6$ and $CH_4$, polyethylene, polypropylene.

### *1.3.1.1 Polarization mechanisms*

There are four different types of mechanisms through which electrical polarization can arise Figure 1.8: (a) Electronic polarization, (b) Ionic polarization, (c) Orientation or Dipolar polarization, (d) Space charge or Interfacial polarization.

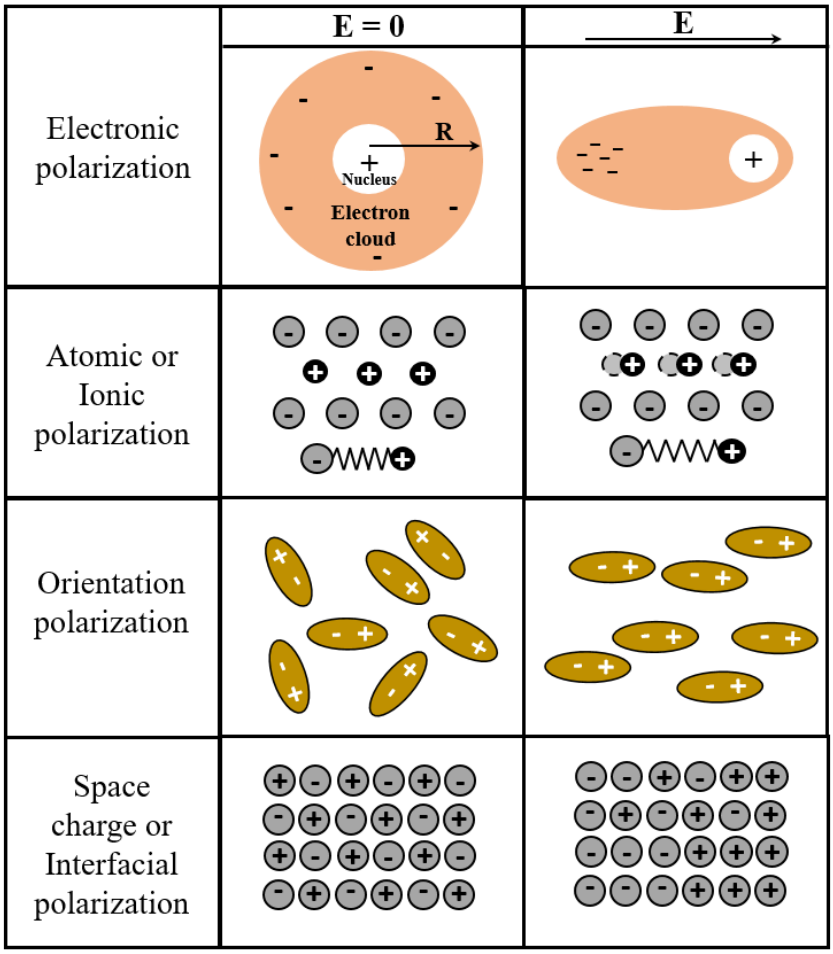


*Figure 1.8 Schematic representation of the different types of polarization mechanisms*

#### *1.3.1.1.1 Electronic polarization*

Each atom or ion has a positively charged nucleus surrounded by a cloud of negatively charged electrons. When there is no externally applied electric field, the charge center of this cloud and the center of the atom's nucleus coincide. If the atom is subjected to an external electric field, the trajectories of the electrons are quickly displaced, as if the electronic "cloud" would have moved. As the volume of an atom is $4\pi R^3$, where $R$ its radius, the electronic polarization can be written as:

$$P = 4\pi\epsilon_0 R^3 E N_{dm} \qquad Eq\ 1.6$$

With $N$ the number of atoms per unit volume. The electronic polarization occurs very fast ($10^{-15}$ s) and disappears as fast when the external field is turned off.

#### *1.3.1.1.2 Atomic or ionic polarization*

Ionic crystal elements, like NaCl or KCl, exhibit this form of polarization. Because the charge of the negative ions is very close to that of the positive ions, in the absence of an external electric field there is no permanent dipole moment inside these materials. When an external field is applied, the ions are shifted from their equilibrium positions. The molecules are distorted, resulting in induced polarization, or a net average dipole moment, as shown in Figure 1.8. The setup time of ionic polarization is of the order of $10^{-13}$ s.

#### *1.3.1.1.3 Orientation (dipolar) polarization*

Orientation polarization (or dipole, or Debye polarization [33]) is characteristics to materials which possess molecules with permanent dipole moments. In the absence of an electric field, the dipole moments are oriented randomly by thermal agitation, resulting in a net zero dipole moment for the material. When an external electric field is set, the molecule begins to rotate in order to align itself with the field, as shown in the Figure 1.8. After the removal of the electric field, the dipoles can remain aligned in this way for a long time, depending on their mass and the "viscosity" of the material, as well as on the temperature.

Orientation polarization is slow, as usually it involves big molecules or supramolecular structures, with time constants which may vary from $10^{-9}$ s to several seconds.

#### *1.3.1.1.4 Space charge or interfacial polarization*

Interfacial polarization is also known as the Maxwell-Wagner-Sillars-effect [32]. It occurs in heterogeneous materials in the frequency range below 10 Hz, as shown in the Figure 1.9. When an external field is applied, it causes the separation of mobile positively and negatively charged particles, resulting in a build-up of charge at the boundaries between the materials, and/or the material and electrodes. Such polarization occurs in polymer matrix composites, particularly when a conductive reinforcing phase is present, in semi-crystalline polymers (due to the co-existence of amorphous and crystalline phases), and in all the materials due to the presence of impurities or even additives [34, 35].

### 1.3.2 Dielectric losses & spectrum

Dielectric loss corresponds to the power dissipated in a dielectric by the charge displaced during the polarization process. When a field is applied to the dielectric, the dipoles tends to align or to be induced with a delay more or less important with respect to their size and links to the structure of the material. If the applied field is harmonic, the result is a phase shift between polarization and applied field, which reflects the active power dissipated in the dielectric and corresponds to the appearance of a current component in phase with the applied ac voltage. The effect of conduction is added to the previous phenomenon.

To illustrate this, let us recall the expression of the current density ($J$):

$$J(t) = \sigma E(t) + \frac{\partial D(t)}{\partial t} \qquad \textit{Eq 1.7}$$

where $\sigma$ is the electrical conductivity. In ac, the previous equation becomes, in complex representation:

$$J(\omega) = \sigma E(\omega) + j\omega D(\omega) \qquad \textit{Eq 1.8}$$

with $j = \sqrt{-1}$, $\omega = 2\pi f$ the angular frequency and $f$ the frequency of the applied field. By using the definition of the dielectric displacement $D$, one gets:

$$J(\omega) = \sigma E(\omega) + j\omega[\varepsilon_0 E(\omega) + \varepsilon_0 E(\omega)x(\omega)] \qquad \textit{Eq 1.9}$$

$$J(\omega) = \{\sigma + j\omega\varepsilon_0[\,1 + x'(\omega) - jx''(\omega)]\}E(\omega) \qquad \textit{Eq 1.10}$$

where $x', x''$ are the real and imaginary components of the electric susceptibility. From a physical point of view, the real part corresponds to the effect of polarization ($x' = x$), whereas the imaginary part $x''$ accounts for the energy dissipated in this process.

The previous relationship can also be written as:

$$J(\omega) = [\sigma + \omega\varepsilon''(\omega) + j\omega\varepsilon'(\omega)]E(\omega) \qquad \textit{Eq 1.11}$$

$$\textit{with } \varepsilon_0[\,1 + x'(\omega) - jx''(\omega)] = \varepsilon'(\omega) - j\omega\varepsilon''(\omega) = \varepsilon(\omega) \qquad \textit{Eq 1.12}$$

where $\varepsilon' = \varepsilon_0\varepsilon_r'$ ánd $\varepsilon'' = \varepsilon_0\,\varepsilon_r''$ have the same physical meanings as $x'$ and $x''$. The loss factor is defined as:

$$tan\delta = \frac{\varepsilon''}{\varepsilon'} = \frac{\varepsilon_r''}{\varepsilon_r'} \qquad \textit{Eq 1.13}$$

where $\delta$ is the loss angle (the phase shift between voltage and current).

The power dissipated per unit volume is then given by

$$P_v = \varepsilon_0\varepsilon_r''\omega E^2 = \varepsilon_0\varepsilon_r'\omega E^2 tan\delta \qquad \textit{Eq 1.14}$$

So far, we have considered the case of a single type of dipoles (so a unique type of polarization). In reality, the structure of most of the dielectrics makes that several types of polarization may coexist (for instance, electronic polarization is present in all the materials). By varying the frequency and by measuring the real and imaginary components of the permittivity, one gets spectra like the one illustrated below, where the effects of the different polarization mechanisms occurring in the material may be underlined.

Spectra like the one presented below can be drawn for any material, with respect to its particular structure, which defines the presence of more or less relaxation peaks and the transition frequencies.

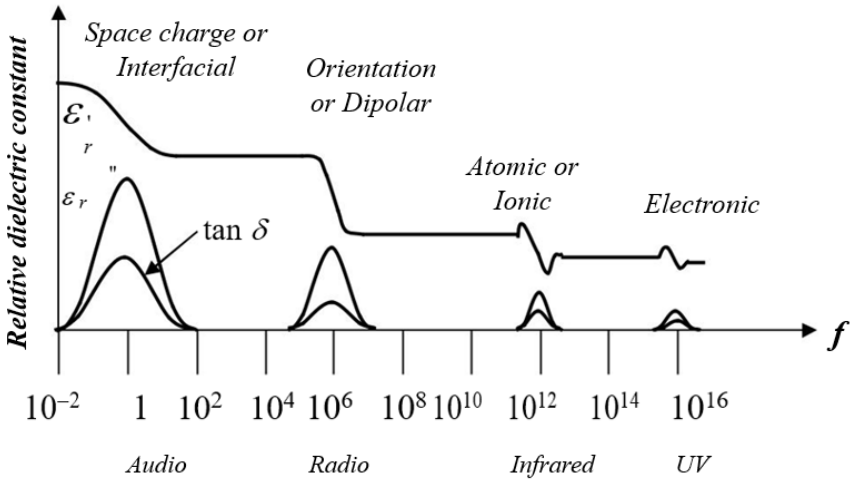


*Figure 1.9 Dielectric constant vs frequency (log scale) showing various mechanisms [36]*

Indeed, because of their inertia, the largest dipoles progressively cease following the field fluctuations as the frequency increases, resulting in these spectra. Each time a relaxation occurs, the actual permittivity drops (since the dipoles are no longer oscillating, they no longer attract charges at electrodes) and losses peak. The relaxations at the lowest frequencies correspond to orientation (or dipolar), interfacial (or space charge relaxations), whereas the peaks linked to ionic or electronic polarization appear in the high frequency range, given the size of the different charged species that a dielectric can contain and their mobilities, as shown in the Figure 1.9.

### 1.3.3 Charge Transport

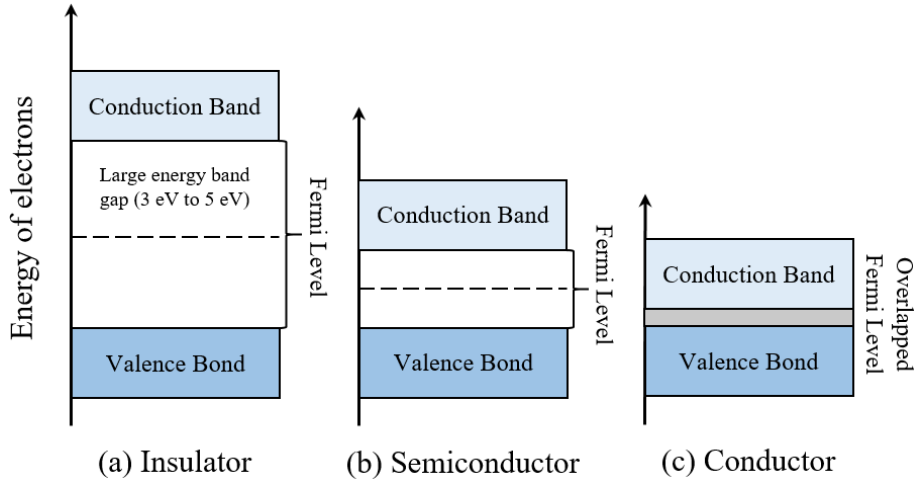


*Figure 1.10 Schematic diagram of energy band gap in solids*

Charge transport mechanisms in dielectric are essential for these materials to be used successfully. Dielectric materials have a poor electrical conductivity and a huge energy band gap often higher than 3 eV, as presented in the Figure 1.10. Because of this, no electrons can reach the conduction band at ordinary temperatures, which make them insulators. In conductors, such as metals, the valence band overlaps the conduction band, whereas it is separated by a small gap in semiconductors, the presence of doping substance (even in a very small quantity)

in such small gaps can drastically boost conductivity. Almost all insulators are dielectrics (vacuum is the exception) [37].

There are two kinds of charge transport in insulators as shown in Figure 1.11. Some mechanisms are dependent on the electrical characteristics of the electrode/dielectric contact. These mechanisms are called electrode-limited, interface-limited or injection-limited mechanisms. Other mechanisms are dependent on the dielectric bulk properties: these processes are referred to as bulk-limited or volume-limited conduction mechanisms [38, 39, 40, 41].

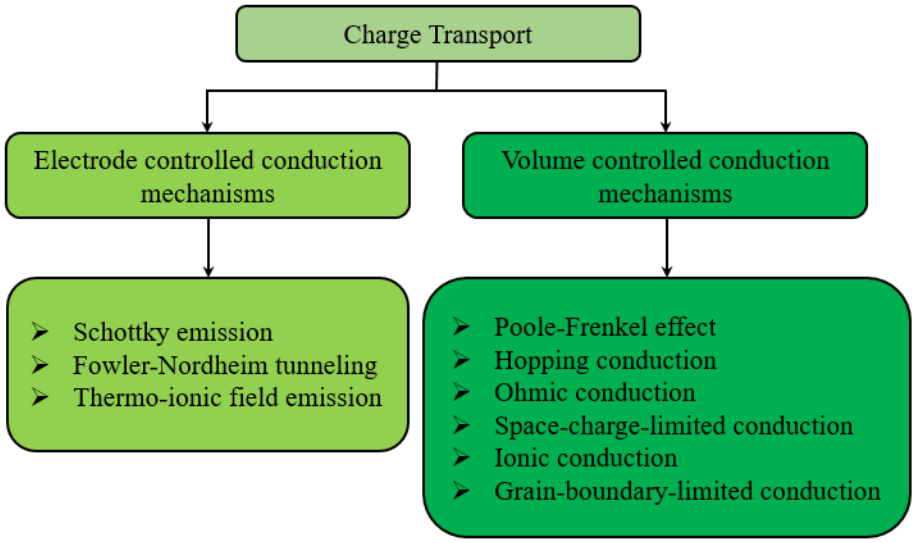


*Figure 1.11 Conduction mechanisms in dielectrics*

### *1.3.3.1 Electrode-controlled conduction mechanisms*

Electrode-controlled mechanisms are classified into three types: Schottky effect, Fowler-Nordheim tunneling and Thermo-ionic field emission.

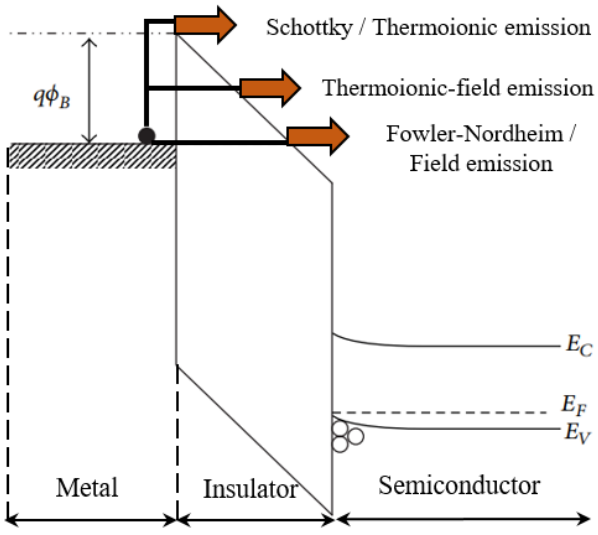


*Figure 1.12 Comparison of energy band diagram representation of thermoionic emission, thermoionic-field emission, field emission in a MIS structure*

#### *1.3.3.1.1 Schottky effect*

The Schottky effect or field enhanced thermionic emission is named after the German physicist Walter H. Schottky. In this phenomenon, the electrons from the metal will overcome the potential barrier at the interface of the metal-dielectric to migrate to the dielectric if they can gain enough energy via thermal activation, when the field barrier between the electrode and the insulator is lowered by the field at the interface. This is illustrated in the Figure 1.12 for a Metal-Insulator-Semiconductor (MIS) structure, where $E_F$ is the Fermi energy, $E_C$ and $E_V$ are the conduction band and valence band energy.

Due to the presence of the image force acting on the electron to be injected, an external electric field can diminish the height of the barrier at the boundary [42]. The current density expression due to the Schottky emission is given by: [37]

$$J = AT^2 \, exp\left[\frac{-q(\emptyset_B - \emptyset_Z)}{kT}\right] \qquad \textit{Eq 1.15}$$

with $\emptyset_z = \sqrt{\frac{qE}{4\pi\varepsilon_r\varepsilon_0}}$, the barrier height *Eq 1.16*

and $A = \frac{4\pi q k^2 m}{h^3}$ *Eq 1.17*

where $A$ is the Richardson constant, $T$ is the absolute temperature, $q$ is the electronic charge, $q\emptyset_B$ is the barrier height (i.e. offset of the conduction band), $E$ is the electric field at the interface, $k$ is the Boltzmann's constant, $m$ is the electron mass, $h$ is the Planck's constant, $\varepsilon_0$ is the vacuum constant and $\varepsilon_r$ is the relative permittivity. It is a highly temperature-dependent phenomenon, very common at fields > 1 kV/mm and temperatures above 40 ° in a wide range of materials.

#### *1.3.3.1.2 Fowler-Nordheim Tunnelling*

The Fowler-Nordheim tunnelling is named after physicists Ralph H. Fowler and Lothar Wolfgang Nordheim. Figure 1.12 shows the schematic diagram of Fowler – Nordheim (F-N) tunnelling in a MIS structure.

F-N tunnelling occurs when the applied electric field is strong enough (higher than $10^8$ $Vm^{-1}$) [43, 44], so the electron wave function can pierce past the triangle potential barrier (assuming that the barrier is sufficiently thin [45]) to reach the dielectric's conduction band. The expression for the F-N tunnelling is given by [37]:

$$J = \frac{q^3E^2}{8\pi hq\emptyset_B} exp\left[\frac{-8\pi(2qm_T)^{\frac{1}{2}}}{3hE}\emptyset_B{}^{\frac{3}{2}}\right] \qquad \textit{Eq 1.18}$$

Where $m_T$ is the effective dielectric tunnelling mass and the rest of the notations are same as previously. It is interesting to note that F-N tunneling is not temperature-dependent, which hopefully aids to its recognition in practice.

#### *1.3.3.1.3 Thermo-ionic field emission*

Thermionic-field emission is a kind of emission that falls somewhere between field and Schottky emission. In this case, the tunnelling electrons should have an energy somewhere between the metal's Fermi level and the dielectric's conduction band edge. Figure 1.12 shows the schematic representation of the energy band diagram of the thermoionic field emission and also shows the comparison between three different electrode-limited conduction mechanisms. The equation for the current density owing to thermoionic-field emission is [37, 46]:

$$J = \frac{q^2\sqrt{m}(kT)^{\frac{1}{2}}E}{8h^2\pi^{\frac{5}{2}}}\ exp\left(-\frac{q\emptyset_B}{kT}\right) exp\left[\frac{h^2q^2E^2}{24m(kT)^3}\right] \qquad Eq\ 1.19$$

### *1.3.3.2 Volume-controlled conduction mechanisms*

Bulk conduction mechanisms can be categorized into six types: Poole-Frenkel effect, ohmic conduction, hopping conduction, space-charge limited conduction, Ionic conduction and grain boundary limited conduction. Steady-state electrical analysis of actual insulators frequently concludes that bulk-limited conduction may contribute for a significant, if not major, portion of leakage current [45]. The electrical characteristics of the dielectric itself determine the bulk-limited conduction processes. The trap energy level in the dielectric layers is the most essential characteristics in this sort of conduction process.

#### *1.3.3.2.1 Poole-Frenkel effect*

Poole-Frenkel (P-F) effect is a model developed by H.H. Poole, then, the work on the extended theory was done by Yakov Frenkel [47]. This model describes the trap-assisted electron transport mechanism in an electrical insulator. In the case of an electron trapped in a trapping center, an applied electric field across the dielectric can diminish the electron's Coulomb potential energy. The decrease in potential energy may improve the chances of an electron being thermally stimulated out of the trap and into the dielectric's conduction band [48, 49]. Figure 1.13 (a) represents the energy band diagram of the Poole-Frenkel effect in a MIS structure. The current density *J* due to the P-F effect is given by [1]:

$$J = q\mu N_c E exp\left[\frac{-q(\emptyset_T - \sqrt{\frac{qE}{\pi\varepsilon_i\varepsilon_0}})}{kT}\right] \qquad Eq\ 1.20$$

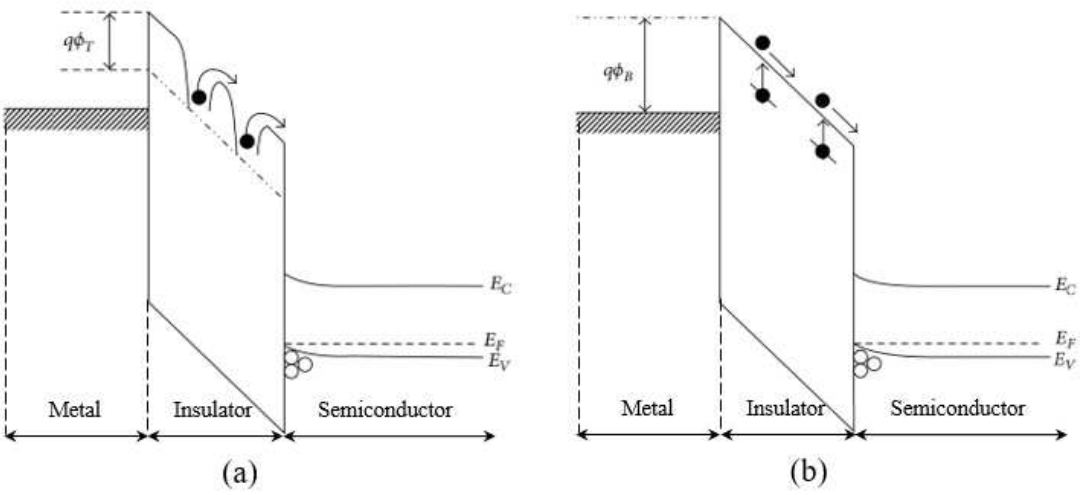


*Figure 1.13 Energy band diagram representation of (a) Poole-Frenkel effect in MIS structure, (b) Ohmic conduction in MIS structure*

#### *1.3.3.2.2 Ohmic conduction*

Ohmic conduction (OC) is due to intrinsic positive and negative carriers which may exist in their valence and conduction bands. The two models that are commonly used to describe ohmic conduction in insulating materials are trap-free and trap-limited ohmic conduction [43]. Figure 1.13 (b) is the energy band diagram representation of the Ohmic conduction in MIS structure. When no electric field is applied, the thermal energy of electrons in the conduction band and of the holes in the valence band of a solid allows them to travel freely in all directions, according to the trap-free ohmic conduction model. As a result, these electrons collide at random with lattice thermal vibrations, crystal defects and voids. The flow of electrons is isotropic and without a predominant speed as a result of these random collisions. As a result, their net speed is nil, whereas in the presence of an electric field, electrons are propelled in the opposite direction of the electric field from one collision to the next [1]. Due to electrons, the charge mobility produces an electric current, of density [43]:

$$J = q_e n_e \mu_e E \qquad \textit{Eq 1.21}$$

where $q_e$ is the electric charge of an electron, $n_e$ is the number of electrons per unit volume, $\mu_e$ is the mobility of electrons and $E$ is the applied electric field. This is of course the equation which stands for metals, but which in insulators is valid for very low fields only, if ever.

#### *1.3.3.2.3 Space-Charge limited conduction*

Space-charge limited conduction (SCLC) is a conduction mechanism which is highly dependent on the insulation thickness. Although the initial quantity of free charge may be minimal, more free charge may be injected under high field, potentially leading to a considerable charge build-up within the insulation. As a result, at least in the initial step, more charge may enter the dielectric than leave it. Future displacement of the charge injected from the electrodes into the bulk material may be problematic in a later stage, resulting in the creation of space-charge

distributions at the electrodes and inside the bulk, which limit further charge motions. Figure 1.14 shows the current density vs voltage in a log-log coordinate system for an ideal case of SCLC. For the trap-free dielectric, the equation for the metal current density is [43, 1]:

$$J = n_o e\mu \frac{V}{d} + \frac{9\varepsilon\mu V^2}{8d^3} \qquad \textit{Eq 1.22}$$

where the first term is the ohmic term and the second one is referred to as Mott-Gurney Law term.

For dielectrics with traps, all the injected electrons contribute to the space charge and a part of them also contributes to the current, even though it may be of very small order of magnitude. In this case, the space charge limited current density is:

$$J = \theta \frac{9\varepsilon\mu V^2}{8d^3} \qquad \textit{Eq 1.23}$$

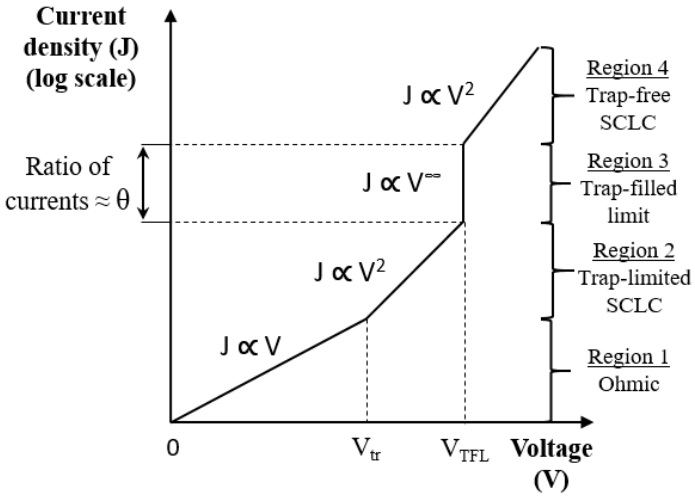


*Figure 1.14 Current Density vs voltage graph for an ideal case of SCLC [43]*

In Figure 1.14, $V_{tr}$ is the transition voltage an, $V_{\mathrm{TFL}}$ is the trap filled limit voltage. From the Table 1.1, log(J) vs log(V) shows four correlations between the current density and voltage which are labelled in terms of the different regions from 1 to 4.

*Table 1.1 Overview of relationship between current density and voltage*

| Region | Region Limits | Slope |
|---|---|---|
| 1 | $0 < V < V_{tr}, J \propto V$ | Slope = 1 |
| 2 | $V_{tr} < V < V_{\mathrm{TFL}}, J \propto V^2$ | Slope = 2 |
| 3 | $V = V_{\mathrm{TFL}}, J \propto V^{\infty}$ | Slope = ∞ |
| 4 | $V > V_{\mathrm{TFL}}, J \propto V^2$ | Slope = 2 |

#### *1.3.3.2.4 Hopping*

The tunnelling action of the trapped electrons from one trap site to another in dielectric films causes the hopping conduction mechanism, for which the current density is [1, 50, 51]:

$$J = qanv\, exp\left[\frac{qaE}{kT} - \frac{E_a}{kT}\right] \qquad Eq\ 1.24$$

where $a$ is the mean hopping distance, $n$ is the electron concentration in the dielectric's conduction band, $v$ is the frequency of thermal vibration of electrons at trap sites and $E_a$ is the activation energy (i.e. the energy level from trap states to the bottom of the conduction band).

#### *1.3.3.2.5 Ionic transport*

Ionic conduction is the movement of ions in the presence of an electric field, which is due to the existence of lattice flaws in the dielectric. Energetically, this can be viewed as a leap of an ion over a potential barrier from one defect site to another. The energy representation of the ionic movements without the application of electric field is shown in the Figure 1.15 (a), while Figure 1.15 (b) illustrates the ionic movement with an electric field [1]. The expression for the ionic current density is:

$$J = J_0\, exp\left[-\left(\frac{q\emptyset_B}{kT} - \frac{Eqd}{2kT}\right)\right] \qquad Eq\ 1.25$$

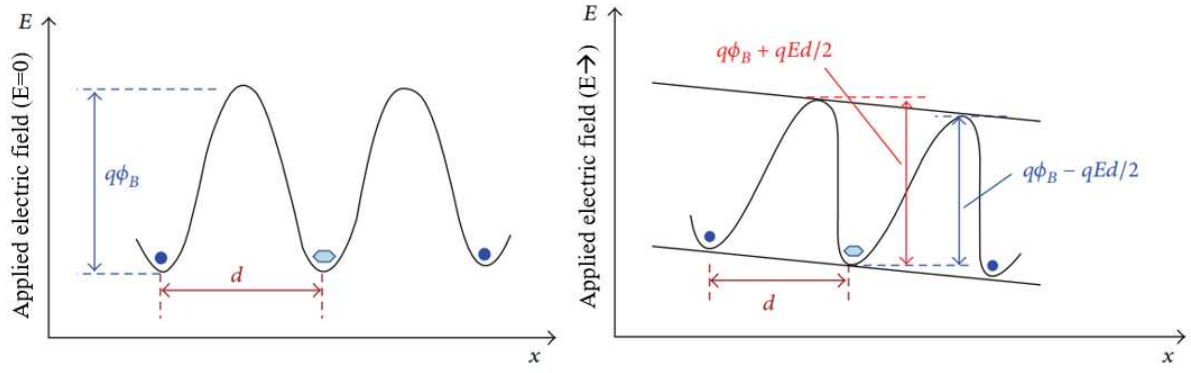


*Figure 1.15 Energy band diagram representation of ionic conduction (a) without the applied electric field and (b) with the applied electric field [37]*

where $J_0$ is a constant, $q\emptyset_B$ is the potential barrier height and $d$ is the distance between two close jumping sites. It is to note that, ions being big and rare in polymers like PE at usual temperature ionic conduction is generally much lower than electronic conduction.

#### *1.3.3.2.6 Grain-boundary limited conduction*

The grain borders of a polycrystalline dielectric material may have a substantially greater resistance than the grains themselves. As a result, the electrical characteristics of grain boundaries may be used to restrict the conduction current. The grain-boundary-limited

conduction mechanism is used in this scenario [52, 53]. A potential energy barrier ($\Phi_B$) is built by the grain [1]:

$$\Phi_B = q\emptyset_B = \frac{q^2 n_b^2}{2\varepsilon N} \qquad Eq\ 1.26$$

Where $n_b$ is the trap density, $\varepsilon$ is the relative dielectric constant and $N$ is the concentration of the dopant.

## 1.3.4 Space charge and aim of the thesis

### *1.3.4.1 Space charge accumulation*

As presented before, under the effect of electric field and temperature, charge carriers may be injected in an insulator from the electrodes and/or move with the assistance of the traps existing in the material. Some of them may be trapped for longer or shorter periods, giving birth to local accumulation of charge commonly called "space charge". The space charge distribution in a material at a given moment results from a balance between injection and transport of extrinsic charges, to which add the intrinsic charges.

Localized states might operate as recombination centers or traps. Traps return carriers to transport states, allowing them to contribute to transportation, for example, through carrier hopping, whereas band-like mobility is aided by delocalized states rather [54].

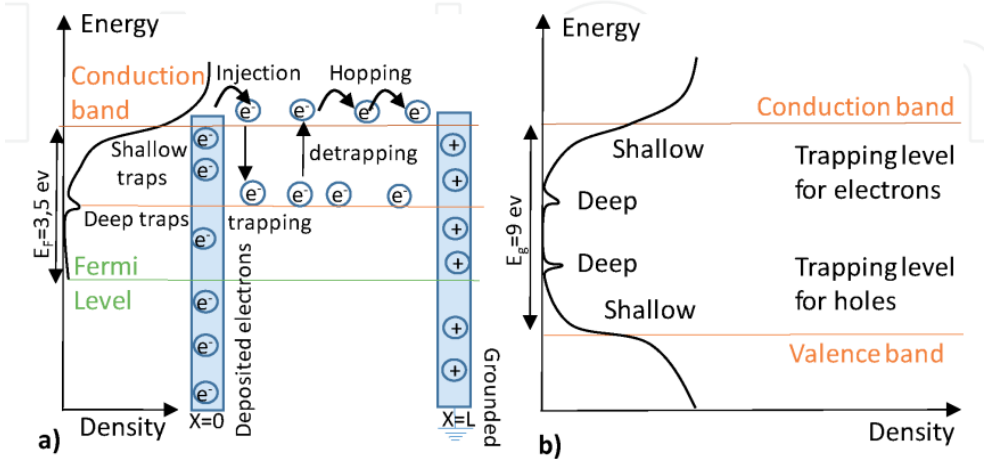


*Figure 1.16 Schematic diagram of state density in dielectric materials (a Deep and shallow traps one-level model ) (b) Symbolic representation of shallow and deep traps for electrons and holes [55]*

Traps are commonly divided into two types: shallow and deep, as shown in Figure 1.16. Using Fermi and demarcation levels, traps/recombination centers and shallow/deep traps may be statistically distinguished in the energy space. Figure 1.16 (a) represents the one-level model for the deep and shallow traps and Figure 1.16 (b) shows the model of deep and shallow traps for electrons and holes which are associated to physical and chemical defects [55]. Shallow traps are those that occur within a range of roughly 1 eV from the band boundaries and are caused mostly by the physical defects such as structural instability. Deep traps and

recombination centers, on the other hand, are often found outside of the 1 eV range, and their formation is more closely linked to chemical impurities and defects. The estimation of the trapping time $(t)$ can be made with [54]:

$$t = v_0^{-1}\, exp\left(\frac{E_{Trap}}{kT}\right) \qquad Eq\ 1.27$$

where $v_0$ is the hopping frequency, $E_{Trap}$ is the trap depth, $k$ is the Boltzmann constant and $T$ is the temperature. The depth or potential well of the traps is determined by the thermal agitation of ions about their mean position, the random orientation of dipoles, and the imperfections in the molecular structure [56]. As a result, the above calculation of trap depth can provide a good indicator of how defects and impurities irrespective of whether they are physical or chemical (eg. Hopping states or states for space charges), can impact conductivity.

Commercially available materials or samples already contain impurities which might be due to dislocations, contaminants, and chemical and physical flaws or abnormalities, which will affect the insulating material locally. Ionization of particular chemical species is frequently connected with the production of space charge in a polymer. Concentration of such impurities have been estimated to be as high as 4 mol% [57].

Crosslinking, melting, softening, and permeation processes in polymers have all been found to cause charge accumulation. Despite the fact that various steps are taken to decrease accumulated charges, some charges may persist even after shipping. As a result, when such materials are employed, the residual charge may disrupt the normal field distribution profile [58]. The injected charges and/or the charges already existing in the material must be trapped for space-charge accumulation to occur. Consequently, the phenomena are dependent on the availability and type of traps.

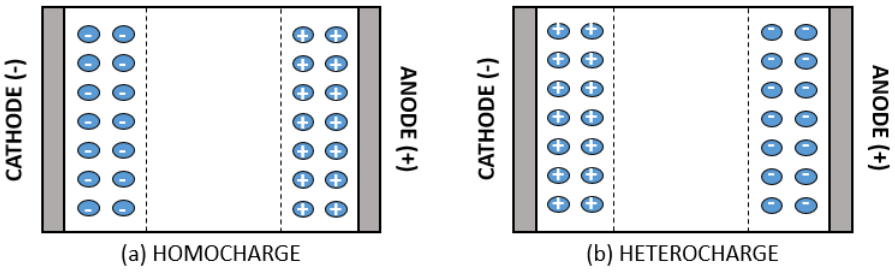


*Figure 1.17 (a) Homocharge and (b) Heterocharge at the electrodes*

Two types of space charge distributions may be detected in relation to the charge trapped in the region of the electrodes [59]: homocharge and heterocharge (Figure 1.17). The homocharge has the same polarity as the adjoining electrode, whereas heterocharge has the opposite polarity to that of the neighboring electrode. Charge from a semiconducting layer, for example, may be pumped into XLPE cable insulation quicker than it can be carried away, in this situation, 'Homocharge' occurs when negative space charge accumulates near the negative electrode and positive space charge accumulates near the positive semicon. However, charge may be carried away quicker than it could be injected, resulting in 'heterocharge' distribution [60]. The electric field at the electrode interfaces grows lower than the uniform field $E_0$ (where $E_0 = V_0/d$), but in

the bulk there is a much higher field, assuming homocharges are injected from both electrodes as depicted in the Figure 1.18 (a). On the contrary, for heterocharges, the electric field value is higher near the electrodes and it decreases in the bulk, as shown in Figure 1.18 (b).

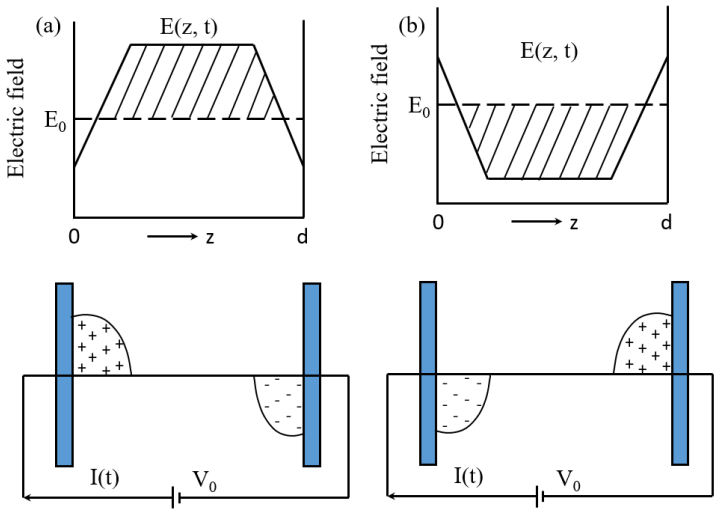


*Figure 1.18 Electric field distortion due to the space charge distribution*

### *1.3.4.2 Consequences of space charge and aims of the thesis*

In order to increase the employment of HVDC links, a significant effort is made today for setting up HVDC cables, accessories and switchgears. For these components, the main problematics related to reliability is the appearance, under the effect of high DC fields and temperatures, of space charge areas.

Indeed, local field re-enforcement due to space charge accumulation can significantly reduce the lifetime of the material, by oversolliciting it locally beyond the design stress. In order to illustrate the long term effects of stable accumulation of space charge, we may consider the example of a cable insulation designed to support 50 kV/mm during 40 years (as targeted for future HVDC cables), in which the trapped charges induce a localized increase of the field of 10 kV/mm, i.e. the maximum field would be locally 60 kV/mm instead of 50 kV/mm. If we take for the material lifetime ($t_{BD}$) a field dependent inverse power law, as in ac ($t_{BD} \sim E^{-n}$), with $n = 15$ (common value for polyethylene insulated ac cables), we get a lifetime of 2.6 years instead of 40 years without space charge. Even if the real effect is probably lower (the CIGRE Technical Brochure 496 [61] suggests $n = 10$ in dc, but this value is still under debate due to the still insufficient knowledge of long-term behavior of such insulators under such electric fields), it comes out clearly that the accumulation of space charge must be mastered and the real field in the insulation known.

In case of ac insulating systems, because of the polarity reversal which occurs several dozens of times per second, space charge accumulation is reduced, as most of the charges injected in one half-cycle are rejected in the next one. In the same way, charge transport is reduced. In

contrast, in HVDC cables, accessories and switchgears, the mechanisms described previously in this chapter favor injection, dissociation and accumulation of space charges, with their undesired effects. To that is added the contribution of the temperature gradient, which inevitably sets up in the insulation during the functioning of the insulating systems.

Thus, if we take the case of a cable, the Joule effect provoked by the current circulating through the cable core during service makes the temperature of the insulating regions close to the core higher than that of the regions close to the outer jacket [62]). This thermal gradient can be as high as 20 °C in the case of the strong thicknesses needed for HVDC applications.

A similar phenomenon occurs in the case of the solid insulators used in switchgears. This phenomenon exists both in ac and in dc, however, it does not affect the "Laplace" capacitive field distribution in ac, because this former is governed by the permittivity of the insulator, which varies with the temperature and electric field.

In contrast, in the case of HVDC components, the electric field distribution is governed by resistivity, which highly varies with temperature and electric field, due to the charge transport phenomena in the dielectric evoked and which, as it is shown by the corresponding relationships, are highly non-linear with respect to these parameters. A common approximation for the volume resistivity variation with field *E* and temperature *T*, as proposed by Eoll [63, 64] is:

$$\rho(E,T) = \rho_0 \, exp[-\propto T - \beta E] \qquad Eq\ 1.28$$

with $\rho_0$ is the volume resistivity at the reference temperature. For most polymers, the value of the coefficients $\alpha, \beta$ are such that the sensitivity drops are of one magnitude order every 10 °C to 20 °C and by a factor of 2 or more every 10 kV/mm.

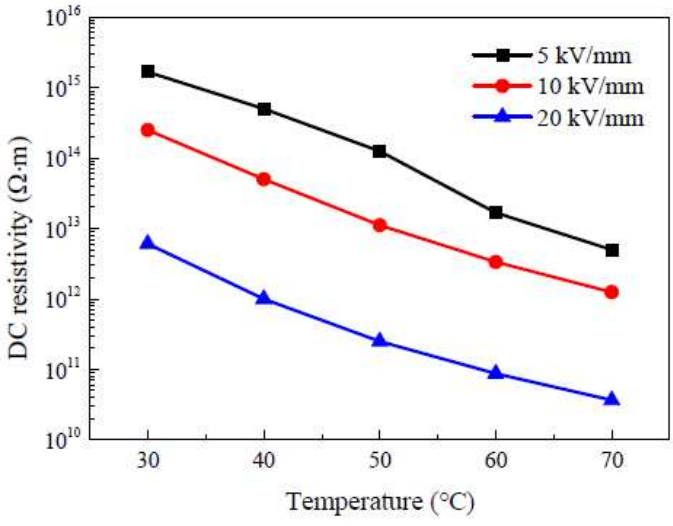


*Figure 1.19 DC volume resistivity of LDPE vs temperature and electric field [65]*

Even in the absence of charge injection, the resistivity gradients lead to the inversion of the field separately with respect to the capacitive case, i.e. the field becomes higher under the outer regions and lower near the inner regions. The distribution of space charge density was measured

for various temperature and electric field conditioning states. Figure 1.20 shows some of the outcomes. At 25 °C and an electric field stress of less than 2 kV/mm, the space charge density is near to zero. As the temperature and electric field increase, so does the formation of hetero-charges around the electrodes. A higher charge density was discovered with a conditioning temperature of 105 °C, close to the glass transition temperature of the epoxy system, especially at high electric field strength. Given that molecule mobility increases with temperature and electric field, the charge distribution is ascribed to a combination of polarization gradient and intrinsic charge carrier displacement to the opposite polarity electrode [62].

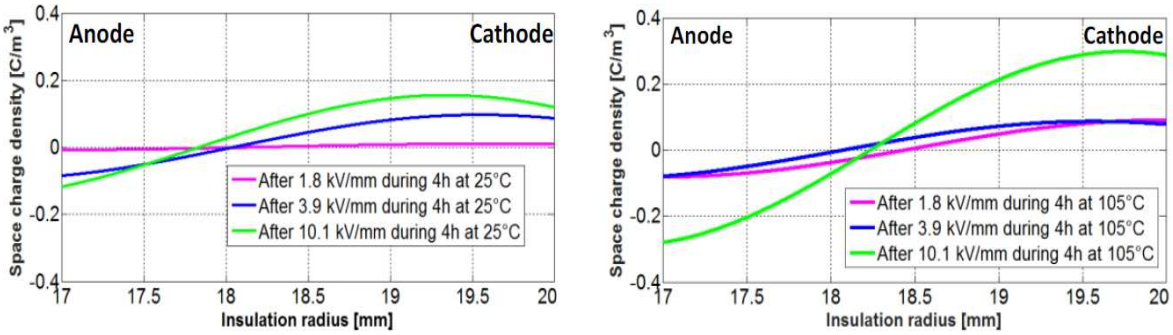


*Figure 1.20 Space charge density distributions for an epoxy insulating sample after conditioning for 4h at 25 °C and 105 °C [62]*

If significant charge accumulation equally occurs, the space charge distribution can become very distorted and lead to premature aging and early breakdown.

The constraints considered by industry for future HVDC equipment may be as high as several dozens of kV/mm at temperature pop up to 90 °C. At this level of stress, the effects of injection, conduction and accumulation of charges become significant, and the stakes related to their knowledge and control are particularly high. Because of significant number of physical parameters related to injection, conduction and trapping in the materials, which are very difficult to estimate, and of the inhomogeneity of the materials at a microscopic level, it is generally impossible to predict the repartition of the internal electric field. As far as of today, simulations do not allow to reproduce experimental results in a satisfactory manner. This is even more true when multilayer structures are involved. The best (and the most often the only) manner to approach these charge accumulation is the direct measurement. This requires space charge measurement techniques, in terms of sensitivity, spatial resolution and applicability, particularly at the interface, which are the weak point of any insulating system, as they are the places where usually the higher constraints occur.

Thus, the aim of this work is to contribute to the progress of space charge characterization techniques able to probe at the best the interfaces between insulating, conducting and semi-conducting materials, in order to allow the measurement and the survey of the space charge and electric fields at this level with the highest precision.

In order to approach as much as possible the phenomena occurring in HVDC insulating layers and to be as representative as possible to the structure of such layers, by keeping the thickness as low as possible for sensitivity reasons, we chose to use as study objects insulating films of

polyethylene (50 to 100 µm) coated with metallic and semi-conducting electrodes. The thickness homogeneity of thick samples (comparable to the "grain" of HVDC insulation) is of the order of 1 to 2 µm.

Several techniques, based on different principles and applicable to different materials and thicknesses, have been developed during the last decades to measure the space charges. These techniques are described and analyzed in the following section.

## 1.4 Space Charge Measurement Methods

Since the 1970's, there has been development of many space charge measurement techniques, which are commonly classified into "destructive" and "non-destructive". The destructive ones are so called not necessarily because they destroy the sample (even that some of them, like the etching method, really do), but, for the most of them, because at the end of the measurement a part or, more frequently, the entire stored charge is evacuated. Thus, destructive methods do not allow to study the evolution of the electric charge with time. Non-destructive measurement methods do not affect the accumulated charges and usually allow to determine their distribution throughout the sample. For this reason, it is possible to monitor the charge distribution evolution [58, 66, 67, 68]. The most popular non-destructive and destructive charge measurement methods are listed in Figure 1.21 and will be described in more detail herein after.

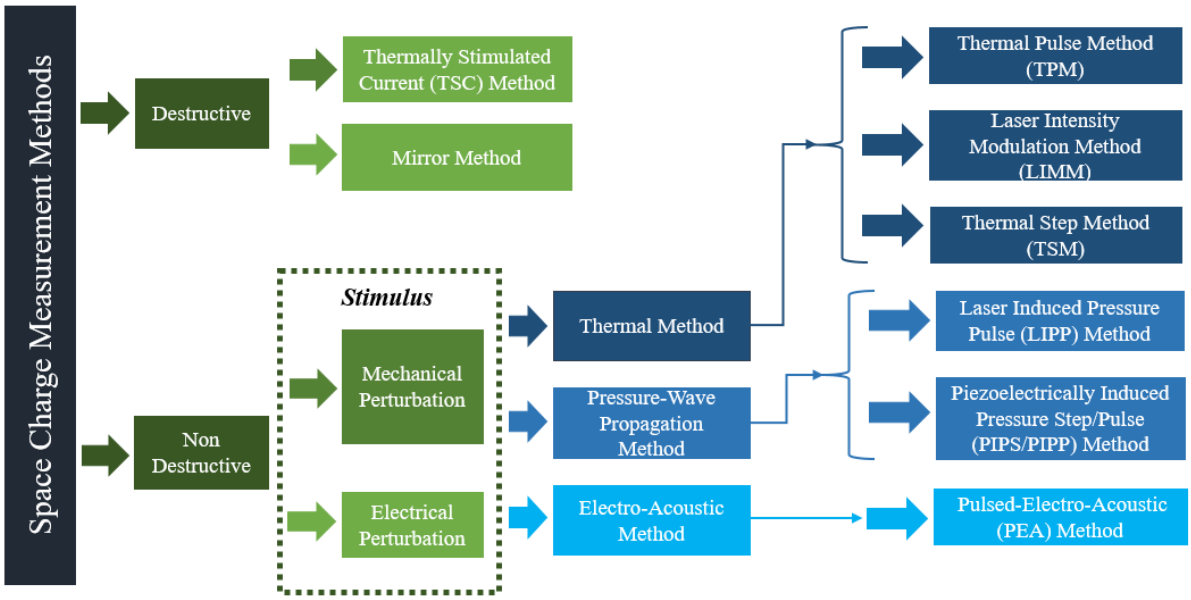


*Figure 1.21 Most popular space charge measurement methods*

On the other hand, non-destructive and destructive methods can be spatially resolutive or not. Most of the destructive methods are not spatially resolved, while non-destructive methods usually are; however, what gives the "resoluteness" of a method is the principle on which it is based. Between the resolutive methods, the most used (as also non-destructive) are the so-called "stimuli" methods, which rely on an excitation of the sample by an external stimulus of electrical, mechanical or thermal origin. The stimulus, if it disturbs locally the equilibrium of the sample leading to an electrical or mechanical response related to the charge distribution, is

set low enough to avoid triggering sample discharge, so the electrical state of the sample is not changed after a measurement, thus allowing sample monitoring over time.

### 1.4.1 Non-resolutive methods

Such techniques allow to obtain information on the charges in the dielectrics without providing their spatial distribution. Among the most used, there are:

- The Thermally Stimulating Discharge Currents Method (TSDC or TSC)
- The Mirror Method
- The Surface Potential Decay Method
- The Dielectric Spectroscopy (DS)
- The Capacitance-Voltage (C-V) technique

#### *1.4.1.1 The Thermally Stimulating Discharge Currents Method (TSDC or TSC)*

Set up in the 1970's [69], the TSDC is a very popular method for studying dielectrics, its principle being summarized in Figure 1.22. A thermally stimulated discharge electrical response is measured in the external circuit while the sample containing non-bonded charge or polarization (due to bonded charges) is subjected to a rise of temperature in short-circuit or open circuit. Usually (and particularly in the case of the study of dipolar dielectrics) short-circuit TSDC is employed, whereas for nonpolar dielectrics open-circuit TSDC is sometimes preferred [70, 71].

The TSDC technique involves beforehand the conditioning of the sample by a static field at the desired temperature, or its charging by other means (e.g., irradiation). In the case of a thermos-electrical conditioning, during the poling stage the sample is subjected to a voltage *Vc* at a temperature *Tc* (Figure 1.22). With respect to the applied field, the temperature and the structure of the material, dipolar entities are oriented or separated in the dielectric and/or development of injection, conduction and charge trapping phenomena occurs. The sample is then cooled down to a temperature $T_1$ at which the external field is removed. The sample is then short-circuited. After a stabilization period at constant temperature, a linear increase of the temperature of the dielectric (considered as constant in the whole sample) of a few degrees/minute allows the relaxation of the charge from the sample, which results in the appearance of a current in the external circuit. This current exhibits one or more peaks, characteristics of the different depolarization and/or discharge phenomena. Usually, the peaks corresponding to the lower temperatures are related to dipolar relaxation, whereas the higher temperature peaks correspond to the detrapping of space charge.

It is important to underline that, in contrast to what it may be believed, the current measured in a TSDC experiment is not a conduction current - it is a displacement current due to the transport between electrodes, during the heating process, of influence charges which previously had set up at electrodes in the virtue of the electrostatic influence. Influence charges are put into

movement from one electrode to the other to re-establish the electrostatic balance of the sample while the bulk unbonded and bonded charges changes position under the effect of the temperature, and the measured TSDC signal is provoked by these movements of the influence charges; in this sense, the physics of the TSDC is very close to the one of many stimuli methods that will be addressed in the following sections.

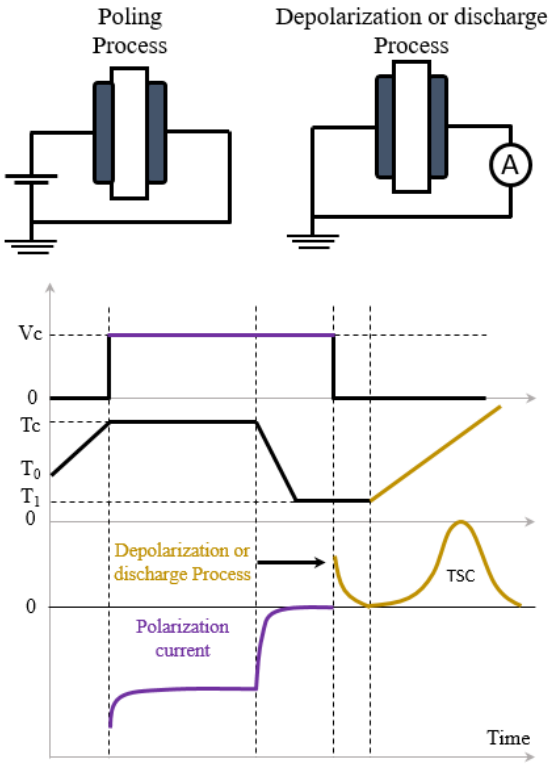


*Figure 1.22 The principle of the thermally stimulated discharge currents (TSDC)*

This means that, in the case of bonded charge (polarization), TSDC fully allows to determine the equivalent charge of the dipoles, as while they disorient, they mandatorily provoke movements of influence charges. In contrast, if close enough to each other, stored charges of opposite sign can recombine without giving any signal in the external circuit. Consequently, a TSDC experience does not necessarily allow to calculate the entire amount of stored charge and may be unsensitive to charges distributed in the sample in ways that allows them to easily recombine with close counterparts of opposite sign.

To summarize, the TSDC allow to obtain the activation energies and the equivalent charge of the dipolar species, or a more or less fraction of the trapped charges and the corresponding activation energies. They do not allow to determine the positions of the charges within the dielectric.

### *1.4.1.2 The Mirror Method*

The effect of “electrostatic mirror”, demonstrated by Le Gressus et al [72], is particularly used for studying the trapping properties of oxides and polymers. Considerable work was performed

in order to extract details regarding the electrical characteristics of the insulators and to understand the associated charge trapping and detrapping mechanisms [72, 73, 74, 75, 76].

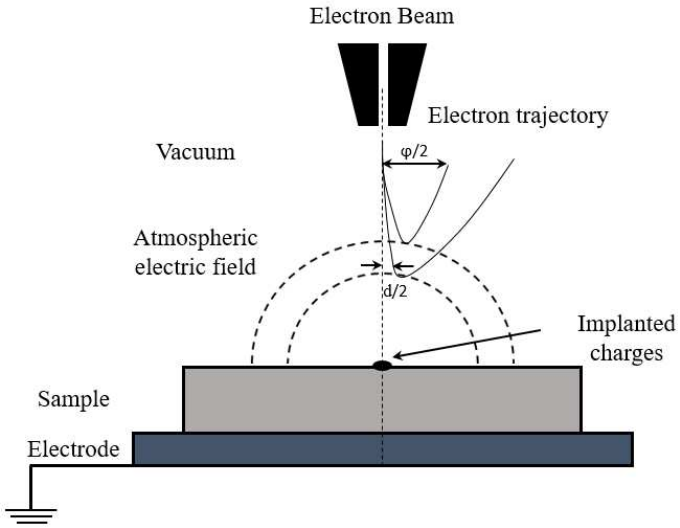


*Figure 1.23 The principle of the mirror method*

The operating principle is to inject electrical charges in the dielectric by using a high energy electron beam (accelerated under voltages from 5 to 40 kV), in a first step, as shown in the Figure 1.23. The electron beam from the microscope is well focused and its direction is fixed. The charges from the beam trapped in the sample give rise to an electric field in the dielectric and in its environment. In the observation phase, a low energy electron beam (accelerating voltages between 200 and 5 kV) is used, its trajectory being deviated due to the presence of the implanted charges. After performing analysis on these beam deviations, information related to the trapped charge, as the total charge injected and its extension, is obtained [76].

It may be argued that the mirror technique is destructive as the implantation of charges modifies the state of the material; however, it can rather be qualified as an intrusive method, which, if it indirectly gives information about the area where the implanted charges are trapped, it does not really provide spatial resolution.

### *1.4.1.3 Decay of Surface Potential*

The principle of this method appeared in the 1970's and promoted particularly, among others, by Coelho [77, 78], Adamec and Calderwood [79] and later by Molinié et al [80, 81], is to follow the decay of the surface potential of a sample previously charged (by a corona discharge, a thermo-electric conditioning, contact charging, an electron beam…). This measurement, made with an electrostatic probe, allows to provide information on the transport mode (in bulk or on the surface) of the charges deposited on the surface and on their mobilities. The quantification of the space charge in the dielectric is made possible with the aid of more or less complex mathematical treatment, which may also allow estimating charge centroids, without providing a real charge distribution.

#### *1.4.1.4 Dielectric Spectroscopy*

This is a very classical and extremely used widely method, mainly for the determination of the electric permittivity and loss factor of a dielectric with respect to frequency, temperature and sometimes applied voltage [82]. It lies in the application to the sample of a sinusoidal voltage of a given frequency and amplitude and by measuring the amplitude and the phase of the current absorbed by the sample. The value of the phase shift $\varphi$, lower than $\pi / 2$ because of the dissipation of energy by the movement of dipoles and unbonded charge which tend to follow the oscillations of the harmonic field, is determined. As the material can be modeled as a parallel RC circuit (for instance, $R = d/(S*\sigma)$ and $C = \varepsilon_0\varepsilon_r'S/d$ in the case of a flat sample, with $S$ its surface et $d$ its thickness), by determining the complex impedance of the sample, one may calculate its conductivity $\sigma$ and its relative permittivity $\varepsilon_r'$, then the loss factor:

$$\tan(\delta) = \tan(\pi/2 - |\varphi|) = \varepsilon_r'' / \varepsilon_r' \qquad \textit{Eq I.34}$$

By varying the frequency and the temperature, the spectra of $\varepsilon_r'$, $\varepsilon_r''$ and $tan\delta$ can be determined. Although it does not provide information about the quantity or the distribution of the charges in the sample, the analysis of the dielectric spectra and of their time evolution allows identifying mechanisms of polarization and movement of charges in the material [82].

#### *1.4.1.5 Capacitance-Voltage (C-V) technique*

The capacitance-voltage technique [83] consists of measuring the variation, at a given frequency, of the capacitance of a sample during a dc voltage sweep. Widely used in microelectronics, this non-destructive technique allows to obtain information on the charge present in thin films and in electronic structures. However, it does not provide the spatial distribution of the electric charge across the entire insulating layer; only the centroid of the charges close to the semiconductor interface can be located, and the method is mainly suited for metal-oxide-semiconductor (MOS) structures. Moreover, the obtained results are highly dependent on the physical modelling of the characterized sample.

### 1.4.2 Resolutive methods

#### *1.4.2.1 Etching method*

For dielectric layers thinner than 100 nm (i.e. in the microelectronic industry), the space charge distribution in compatible samples can be obtained by the etch-off technique [83, 84]. The idea is to progressively etch the sample from top to bottom, by keeping measuring the potential across the sample. The charge concentration in the depth direction can then be calculated by deriving twice the potential with respect to the measurement direction. The obvious drawback is that at the end the sample is completely destroyed, preventing a follow-up of the charge distribution, and such a technique has a very limited application.

#### *1.4.2.2 Stimuli Methods*

The stimuli methods are non-destructive techniques allowing to access the charge distribution across insulating materials [68]. The stimuli, which are slight perturbations applied to the samples for revealing the charges, are of electrical, mechanical or thermal nature [67, 68, 85]. They are usually classified into pressure methods (if the stimulus is mechanical or exploit a mechanical coupling, i.e., elastic waves) and thermal methods (when the stimulation is provoked through the use of heat).

##### *1.4.2.2.1 Pressure methods*

This family of methods rely on the propagation of acoustic waves. Among the most popular ones, one may quote the Pulsed Electroacoustic (PEA) method and the Pressure Wave Propagation (PWP) method with its variants.

**a. The Pulsed Electro Acoustic (PEA) Method**

This approach, proposed in the middle of the 1980's by Takada and based on electric pulse stimulations of the sample and detection of acoustic waves [86, 87], is historically the newest and actually the most popular method for space charge measurements. Its working principle uses the compression of the material by Coulomb forces and the technique is referred to as the Pulsed Electro Acoustic (PEA) method. The idea at the basis of the technique is shown in the schematic diagram from Figure 1.24.

Thus, an external electric pulse is applied to the sample containing space charges. The electrostatic forces which are created under the effect of the applied field and the trapped charges cause localized strains, which give birth to elastic waves propagating from the charges that are proportional to their values. These waves move at the speed of sound over the insulator and are detected by a piezoelectric transducer installed on the other electrode. Since the duration of wave propagation inside the sample is related to the position of the charge which generated it and, consequently, to the spatial resolution, the piezoelectric membrane thickness plays a very important role in the accuracy of the measurement; as a result, a balance is set between the necessity for adequate spatial resolution and the signal amplitude generated by the piezoelectric layer. On the other hand, the output signal must be deconvoluted and calibrated in order to get the space charge distribution, particularly because of absorption and acoustic reflections.

The structure of the measurement cell has not changed much over time, with the exception of the size and material of the components used, as well as of the thickness of the specimen to be evaluated [88, 89]. The preceding concepts apply to any insulating structure, meaning that homogeneous samples and structures having physical characteristics that change with the depth-coordinate can be characterized; however, in the former case, particular care must be taken to overtake the problems related to reflections. Y. Tanaka *et al*. [90] made vary the size

and the type of various PEA cell components, such as the pulse generator characteristics, in order to increase the measurement resolution.

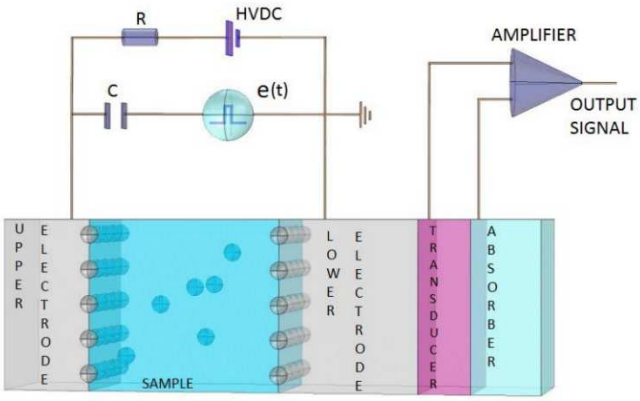


*Figure 1.24 Schematic diagram for the PEA method [88]*

As a result, for samples with a thickness of 25 to 100 µm, spatial resolutions of the order of 10 µm, constant in volume, are claimed. The sensitivity is of the order of 10 mC/m$^3$. As the signals are fast-varying and consequently decoupled from low frequency responses that are characteristics for high field dielectric phenomena, the PEA method presents the advantage to allow measurements in the presence of thermal stress and under applied dc or ac voltage.

### b. Pressure Wave Propagation (PWP) Method

Older than the PEA, the Pressure Wave Propagation (PWP) method, presented in Figure 1.25, was proposed by Laurenceau in 1976 [91, 92]. Thus, when a pressure wave travels across the sample to be tested, the charges encountered successively are mechanically displaced. This leads to the perturbation of the electrostatic equilibrium of the sample, which triggers the redistribution of the influence charges at electrodes, resulting in the appearance of a current.

Laurenceau's idea was that if a pressure wave is used to displace the charges in the material, the measured signal's time dimension matches the material's spatial dimension [93]. In other words, with a pressure pulse, the signal obtained in the external circuit is an image of the charge distribution, as time and position are related through the sound velocity, $x = v_s t$. Figure 1.25 (b) and (c) illustrate the shape of the current signal in a sample in voltage-on conditions for the cases when it does not contain any space charge and when space charges ("internal charges") are present in the bulk.

Since the original publication on PWP, there have been development of several approaches for generating the pressure wave in the sample: shock tubes, piezoelectric transducers and lasers with short rise times. The technique is known as the laser-induced-pressure-pulse (LIPP) method when a laser is used to create the pressure pulse. If the pressure pulse is created with a piezoelectric transducer, the method is named the Piezoelectrically-Induced-Pressure-Pulse (PIPP) method. If a pressure step is generated by the same means, the method is called the Piezoelectrically-induced-pressure-step (PIPS) technique.

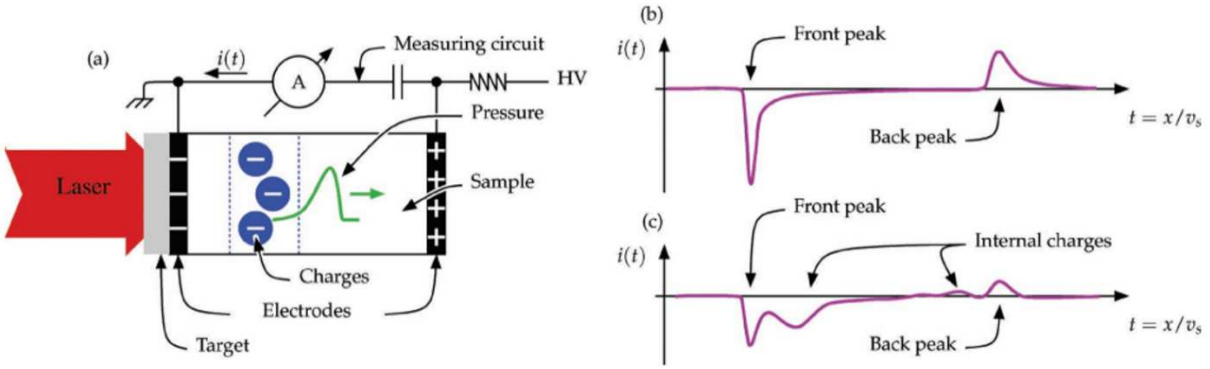


*Figure 1.25 On the PWP method [94]: (a) principle of the method using a laser for the generation of the pressure pulse, (b) form of signals obtained without internal charges and (c) with internal charges*

Sessler and Gerhard [95, 96, 97, 98] were among the first to use a Laser-induced pressure pulse (LIPP) (Figure 1.26) to investigate space-charge and polarization characteristics of different types of materials charged through electron beams, corona discharges or liquid contacts. The energy of the laser is absorbed by the target (electrode), which causes a fast expansion of the electrode, resulting in a powerful pressure step. The expression of the measured current $I(t)$, where the overall characteristics of the material are taken into account, is [99]:

$$I(t) = X_s C_0 G(\varepsilon_r) \int_0^d E(x) \frac{\partial p(x,t)}{\partial t} dx \qquad Eq\ 1.29$$

where $X_s$ is the sample compressibility, $C_0$ is the sample capacitance, $G(\varepsilon_r)$ is the ratio of the non-compressed and compressed sections of the sample's relative permittivity, $d$ is the thickness of the sample, $E$ is the electric field distribution and $p(x,t)$ is the pressure profile with respect to the sample depth co-ordinate $x$ at any instant $t$.

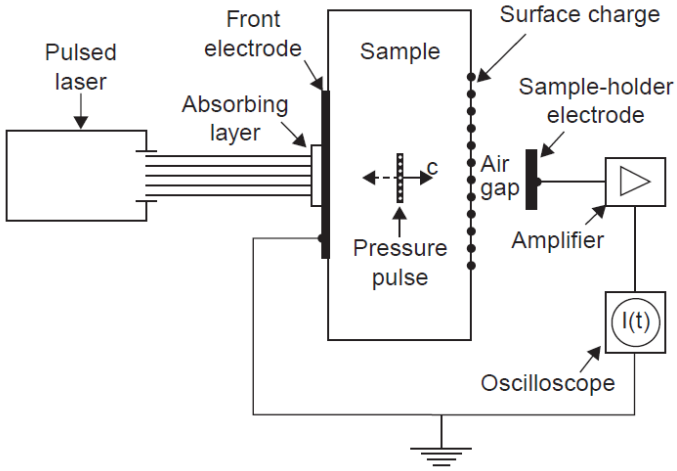


*Figure 1.26 Experimental setup for the LIPP method [58] [98]*

In the case of the Piezoelectrically Induced Pressure Pulse, voltage pulse is applied to a piezo electric transducer in order to create the stimulus (Figure 1.27) [100, 101, 102].

The current can be expressed as [103]:

$$I(t) = \frac{C_0}{Y}(1 + A)\int_0^d [E(x,t)]\frac{\partial p(x,t)}{\partial t}dx \qquad Eq\ 1.30$$

where $C_0$ is the capacity of the cell's suspension, $Y$ is the young's modulus, $A$ is related to properties of cells suspension, $d$ is the depth of the cell's suspension, $E(x,t)$ is the electric field intensity in cells suspension, $p(x,t)$ points the profile pressure of the $x$ position where the cell supposed stays. This method is used to measure polarization and space charge distribution in the samples of thickness between 50 and 1000 µm [88].

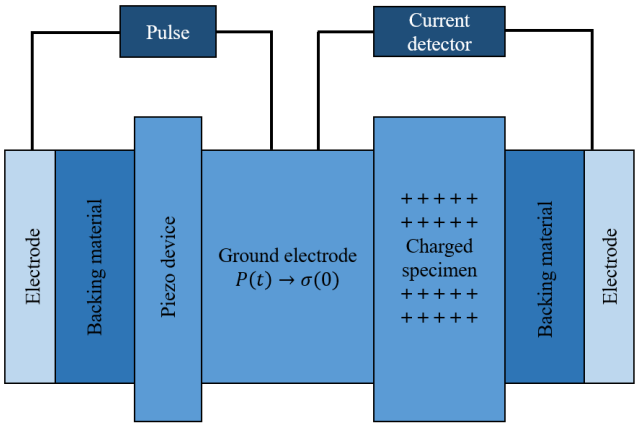


*Figure 1.27 Experimental setup of PIPP method*

The Piezoelectrically Induced Pressure Step (PIPS) [104, 105, 106] relies on the transient response of a piezoelectric crystal plate to generate pressure steps. Figure 1.28 shows the schematic diagram of the PIPS method.

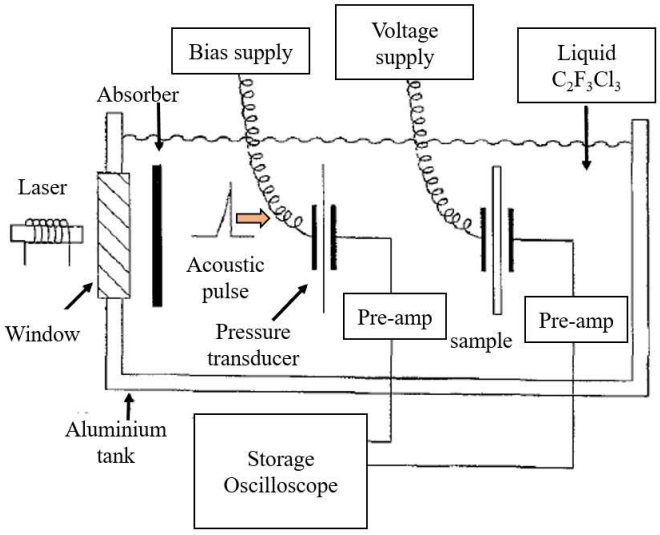


*Figure 1.28 Schematic diagram of the PIPS method [58]*

A relay-triggered discharge of a 50 Ω coaxial wire produces a 100 ns square pulse with an amplitude of 400 to 600 V. A piezo electric quartz plate with a thickness of 3 mm and a diameter of 25 mm is driven using a positive and negative voltage step sequence. To efficiently transfer the ensuing pressure steps to the sample, a 100 to 200 nm thick silicon oil layer is utilized and a conductive rubber disc contacts the non-metalized surface of the sample. Between the rubber

electrode and the grounded quartz metallization facing the sample, the sample's reaction is sensed. The current response signal *I(t)* can be written as [106]:

$$I(t) = \frac{AV}{L}\left[(1+\gamma)\left(\sigma_s + \int_0^d \rho(x)dx\right) - ed - \gamma P(d)\right] \qquad Eq\ 1.31$$

where $A$ and $L$ are the area and thickness of the sample, $V$ is the velocity amplitude of the step wave, $\gamma$ is the relative electrostriction coefficient and $\sigma_s$ is the static counter charge per area on the sample's grounding electrode, $e$ is the piezoelectric constant, $P(d)$ is the persistent polarization and $d$ the thickness of the sample.

Whatever the variant, the PWP method is particularly adapted to continuous media because the reflection of the pressure wave at interfaces, which makes the interpretation of the obtained signals delicate. The signals are very fast because of the sound of speed in solids (e.g., ~2000 m/s for polymers and ~5700 m/s for silicon dioxide) and complex devices may be needed. The spatial resolution of these techniques can be as low as 10 µm with a sensitivity of the order of 10 mC/m$^3$.

#### *1.4.2.2.2 Thermal methods*

The principle of the thermal methods is similar to the one of the pressure wave methods, excepting that the sample stimulation is due to a temperature rise at one electrode instead of a pressure pulse or step. The diffusion of heat induces inhomogeneous expansion of the sample in the depth direction, which slightly displaces the space charges, and inhomogeneous variation of permittivity. Consequently, changes in the influence charges at electrodes occur, and a transient signal (current or voltage) appears in the external circuit, with respect to the connection of the two electrodes (short-circuit or open-circuit). The type of thermal stimulus, which is directly related to the amplitude of the perturbation and to the amount of heat which diffuses in the sample, has a major impact on the measurable thickness.

With respect to the form of the thermal stimulus, the main techniques are based on the application of a heat pulse, a temperature step or a modulated thermal wave.

### a. The Thermal Step Method (TSM)

The idea of the TSM [66, 107, 108], proposed by Toureille in 1988, is to apply a temperature step on one of the electrodes of the sample.

The case of the current response given by a thermally excited insulating flat sample has been addressed in many papers (e.g. [85, 109, 110, 111]. We present here the detailed approach proposed in [111] for the TSM, which is in fact a general approach for any thermal method where a transient current is measured, because the expression of the thermal stimulus is not used in the calculations.

Thus, let us consider an insulating sample with a thickness ($L$) and a surface ($S$) and two conducting electrodes on the abscissa $x = 0$ and $x = L$, respectively (Figure 1.29). (The thickness of the sample is noted $L$ in this section in order to avoid confusion with the symbols used for the derivatives). $\varepsilon$ is the sample's permittivity which varies with respect to the thickness of the sample and is represented as $\varepsilon(x)$.

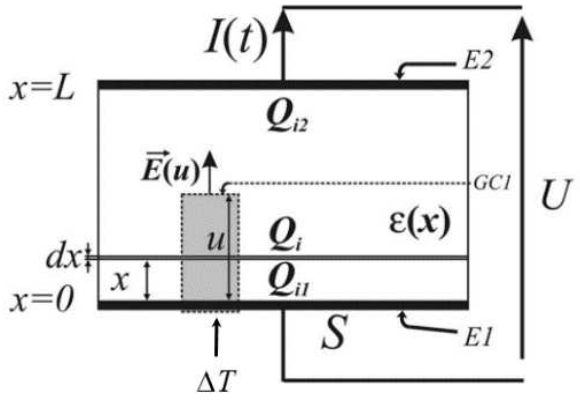


*Figure 1.29 Diagram related to the determination of the expression on the current response of an insulating sample submitted to a temperature variation on one of its faces [111]*

In a plane parallel to the electrodes, the electric field is considered to be constant, since the material is assumed to be infinitely flat (i.e., $L \ll \sqrt{S}$). $Q_i$ is the space charge value which is assumed to be constant during the experiment and equally distributed throughout an infinitely thin layer of thickness $(dx)$. '$U$' is the voltage drop across the sample. Since the system which consists of sample, electrode, and conducting wire is in electrostatic equilibrium, the charge $Q_i$ located in the bulk of the insulator at the abscissa $x$ produces charges, such as $Q_{i1}$ and $Q_{i2}$, at the electrodes, according to the principle of electrostatic influence:

$$Q_i + Q_{i1} + Q_{i2} = 0 \qquad \textit{Eq 1.32}$$

Let us consider the case of a cylindrical surface GC1 with bases parallel to electrodes, with the top base of this Gauss cylinder situated at an arbitrary coordinate (u) above the space charge $Q_i$ $(u > x)$. By applying Gauss's theorem to GC1, it comes out:

$$E(u) = \frac{Q_{i1}+Q_i}{S\varepsilon(u)} \quad for\ x < u < L \qquad \textit{Eq 1.33}$$

The application of Gauss's theorem to a cylinder comparable to GC1 but with the upper base between $Q_{i1}$ and $Q_i$ (i.e. at a coordinate u<x) yields:

$$E(u) = \frac{Q_{i1}}{S\varepsilon(u)} \quad for\ 0 < u < x \qquad \textit{Eq 1.34}$$

The electric field circulation across the sample is given by:

$$\int_0^L E(u)du = U \qquad \textit{Eq 1.35}$$

From Eq (1.33) to Eq (1.35), we get

$$\int_0^{\mathrm{L}} \mathrm{E(u)du} = \int_0^{\mathrm{x}} \frac{Q_{i1}}{S\varepsilon(u)}\mathrm{du} + \int_x^{\mathrm{L}} \frac{\mathrm{Q_{i1}} + \mathrm{Q_i}}{\mathrm{S\varepsilon(u)}}\mathrm{du} = \mathrm{U}$$

$$Q_{i1} = \frac{SU}{\int_0^L \frac{1}{\varepsilon(u)}du} - \frac{Q_i \int_x^L \frac{1}{\varepsilon(u)}du}{\int_0^L \frac{1}{\varepsilon(u)}du} = -\frac{Q_i \int_x^L \frac{1}{\varepsilon(u)}du - SU}{\int_0^L \frac{1}{\varepsilon(u)}du} \quad \textit{Eq 1.36}$$

In first order, the new permittivity and elementary displacement may be represented as $\varepsilon(u)[1+\alpha_\varepsilon(u)\Delta T(u,t)]$ and $du[1+\alpha_x(u)\Delta T(u,t)]$, where the ratio of fluctuation in material permittivity as a function of temperature $\alpha_\varepsilon(u)$ is given by $\alpha_\varepsilon(u) = \left(\frac{1}{\varepsilon}\right)\left[\frac{\partial\varepsilon}{\partial\Delta T(u,t)}\right]$ and it's coefficient of thermal expansion $\alpha_x(u)$ is given by $\alpha_x(u) = (1/u)[\partial u/\partial\Delta T(u,t)]$. As a result, $\frac{du}{\varepsilon(u)}$ becomes

$$\frac{du}{\varepsilon(u)} = \frac{1+(\alpha_x(u)-\alpha_\varepsilon(u))\Delta T(u,t)-A}{1-B} \quad \textit{Eq 1.37}$$

where $A = \alpha_{\mathrm{x}}(\mathrm{u})\alpha_{\varepsilon}(\mathrm{u})\Delta\mathrm{T}^2(\mathrm{u},\mathrm{t}), B = \alpha_{\varepsilon}^2(\mathrm{u})\Delta\mathrm{T}^2(\mathrm{u},\mathrm{t})$

Since $\alpha_x$ and $\alpha_\varepsilon$ are both lower than $10^{-4}$ in practice and $\Delta T$< 30K, we have $A \ll 1$ and $B \ll 1$. Finally, by setting $\alpha_x(u) - \alpha_\varepsilon(\mathrm{u}) = \alpha(\mathrm{u})$, one obtains $\frac{du}{\varepsilon(u)} = du[1+\alpha(u)\Delta T(u,t)/\varepsilon(u)$. With these observations Eq (1.36) becomes

$$Q_{i1} = -Q_i \frac{\left[\int_x^L \frac{du}{\varepsilon(u)} + \int_x^L \frac{\alpha(u)\Delta T(u,t)}{\varepsilon(u)}du\right]\left[\int_0^L \frac{du}{\varepsilon(u)} - \int_0^L \frac{\alpha(u)\Delta T(u,t)}{\varepsilon(u)}du\right]}{\left[\int_0^L \frac{du}{\varepsilon(u)}\right]^2 - \left[\int_0^L \frac{\alpha(u)\Delta T(u,t)}{\varepsilon(u)}du\right]^2} + SU\frac{\left[\int_0^L \frac{du}{\varepsilon(u)} - \int_0^L \frac{\alpha(u)\Delta T(u,t)}{\varepsilon(u)}du\right]}{\left[\int_0^L \frac{du}{\varepsilon(u)}\right]^2 - \left[\int_0^L \frac{\alpha(u)\Delta T(u,t)}{\varepsilon(u)}du\right]^2} \quad \textit{Eq 1.38}$$

By using the inequalities as mentioned in detail [111], Eq (1.38) can be written as follows:

$$Q_{i1} = -Q_i\left[\frac{\int_x^L \frac{du}{\varepsilon(u)}}{\int_0^L \frac{du}{\varepsilon(u)}} + \frac{\left[\int_x^L \frac{\alpha(u)\Delta T(u,t)}{\varepsilon(u)}du\right]}{\int_0^L \frac{du}{\varepsilon(u)}} - \frac{\left[\int_x^L \frac{du}{\varepsilon(u)}\right]\left[\int_0^L \frac{\alpha(u)\Delta T(u,t)}{\varepsilon(u)}du\right]}{\left[\int_0^L \frac{du}{\varepsilon(u)}\right]^2}\right] + SU\frac{\left[\int_0^L \frac{[1-\alpha(u)\Delta T(u,t)]du}{\varepsilon(u)}\right]}{\left[\int_0^L \frac{du}{\varepsilon(u)}\right]^2} \quad \textit{Eq 1.39}$$

The variation of the influence charges causes the measured current in the external circuit, which is expressed as $I(x,t) = -\frac{\partial Q_{i2}}{\partial t} = \frac{\partial Q_{i1}}{\partial t}$. By deriving Eq (1.44), we obtain:

$$I_{(x,t)} = -Q_i f(x,t) - SUP(t) \quad \textit{Eq 1.40}$$

where $f(x,t)$ and $P(t)$ are given by

$$f(x,t) = \left(\frac{1}{\int_0^L \frac{du}{\varepsilon(u)}}\right)\left[\int_x^L \frac{\alpha(u)}{\varepsilon(u)}\frac{\partial\Delta T(u,t)}{\partial t}du\right] - \left(\frac{\left[\int_x^L \frac{du}{\varepsilon(u)}\right]}{\left[\int_0^L \frac{du}{\varepsilon(u)}\right]^2}\right)\left[\int_0^L \frac{\alpha(u)}{\varepsilon(u)}\frac{\partial\Delta T(u,t)}{\partial t}du\right] \quad \textit{Eq 1.41}$$

$$P(t) = \int_0^L \frac{\alpha(u)}{\varepsilon(u)}\frac{\partial\Delta T(u,t)}{\partial t}du\left[\int_0^L \frac{du}{\varepsilon(u)}\right]^{-2} \quad \textit{Eq 1.42}$$

In the general case of a space charge distribution of density ρ(x), i.e. $Q_i = \rho(x)dv = S\rho(x)dx$, with dv is the volume element, one gets:

$$I(t) = -\int_V^0 Q_i f(x,t) - SUP(t) = S\int_0^L \rho(x)f(x,t)dx - SUP(t) \quad \textit{Eq 1.43}$$

where V is the volume of the specimen. The current expression is expressed as follows, by employing the Poisson's equation $\rho(x) = \frac{d}{dx}[\varepsilon(x)E(x)]$ into it and by performing integration by parts :

$$I(t) = -S\left[[\varepsilon(x)E(x)f(x,t)]_0^L - \int_0^L \varepsilon(x)E(x)\frac{\partial f(x,t)}{\partial x}dx\right] - SUP(t) \qquad Eq\ 1.44$$

Since $f(0,t) = f(L,t) = 0, \forall t$, the expression of current (Eq (1.44)) is simplified to

$$I(t) = S\int_0^L \varepsilon(x)E(x)\frac{\partial f(x,t)}{\partial x}dx - SUP(t) \qquad Eq\ 1.45$$

The integral formula is used for determining $\partial f(x,t)/\partial x$, and $\varepsilon(x)$ which is substituted in Eq (1.45) leading to :

$$I(t) = -\frac{S}{\int_0^L \frac{du}{\varepsilon(u)}}\int_0^L \alpha(x)E(x)\frac{\partial \Delta T(x,t)}{\partial t}dx + S\left[\int_0^L E(x)dx\right]P(t) - SUP(t) \qquad Eq\ 1.46$$

with the change in variables $u = x, du = dx$, and because $\int_0^L E(x)\,dx = U$, it comes out that:

$$I(t) = -\frac{S}{\int_0^L \frac{dx}{\varepsilon(x)}}\int_0^L \alpha(x)E(x)\frac{\partial \Delta T(x,t)}{\partial t}dx \qquad Eq\ 1.47$$

The sample capacitance (C) being the quantity before the integral sign, one finally gets:

$$I(t) = -C\int_0^L \alpha(x)E(x)\frac{\partial \Delta T(x,t)}{\partial t}dx \qquad Eq\ 1.48$$

In the case when $\alpha$ does not vary in the x-direction (i.e., a monolayer insulating sample with two conducting electrodes), the equation reads:

$$I(t) = -\alpha C\int_0^L E(x)\frac{\partial \Delta T(x,t)}{\partial t}dx \qquad Eq\ 1.49$$

It is to note that in the above approach no distinction was made between "real" (non-bonded) charge and bonded charge, i.e. the field distribution under the integral is the result of both space charge and polarization.

In the case of the Thermal Step Method, the thermal stimulus is a temperature step applied at $t = 0$ on the "lower" electrode (at $x = 0$), i.e.:

$$\Delta T(0,t) = T_1 - T_0 \qquad Eq\ 1.50$$

where $T_1$ is the temperature to which the thermally stimulated electrode is sharply raised (or lowered) from $t = 0$ to the end of the measurement.

Extracting the electrical field (and then the charge distribution through the Poisson's equation) from the current integral requires mathematical treatment. Several algorithms have been proposed since the 1990's through Fourier analysis, successive differentiations and matrix inversion [67, 107, 109, 112, 113].

Figure 1.30 illustrates the experimental setup of the TSM in short circuit conditions. In practice the Thermal Step is created by a cold or warm liquid circulating within a radiator in contact

with the sample, and the electrodes are connected through a current amplifier. The latter is connected to a computer, which records the current and does the numerical data processing. After performing a measurement, the sample can be reheated using a warm liquid, and the experiment can be repeated. With respect to other thermal methods, as the amount of heat transferred to the material is quite important, the TSM suits well medium and thick samples (usually, between 100 µm and 25 mm, with resolutions down to several µm with respect to the thickness), but applications have been made down to thicknesses of 100 nm (with a very low spatial resolution in this case). The TSM can be applied both to flat and cylindrical structures (cables). The duration of the measurement is between 100 ms and 100 min.

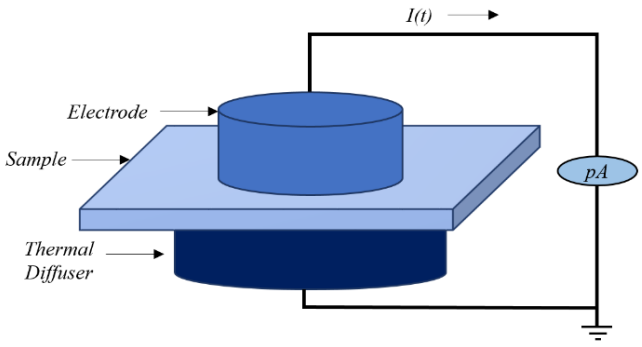


*Figure 1.30 TSM setup in short – circuit condition.*

## b. The Thermal Pulse Method (TPM)

The TPM is the most ancient stimulus method and at the origin of all the thermal methods. The problematics of non-destructive measurement methods of electric charge in insulating solids has started to receive attention in the middle of the 1970's, driven by the study of electrets, and underwent significant development afterwards. The original problem was to determine the distribution of fixed charges and permanently aligned dipoles in thin films (dozens of microns). Probably inspired by works done with thermal pulses in the domain of pyroelectric optical-radiation detectors [114], R. E. Collins was the first to propose the use of a thermal pulse for probing the amount of single-signed charges and their mean position in a 25 µm thin FEP sample in 1975 [115]. Collins's idea was to make the sample absorb a short heat pulse which, in contrast to the thermally stimulated currents, would not discharge the sample, but only slightly displace the trapped charges temporarily, giving birth to a transient signal. He quickly generalized the principle for the analysis of the spatial distribution of the charge in an electret [116].

As opposed to a setup proposed by Sessler *et al* at the same time [117], which claimed a resolution of 1 µm in a similar sample by scanning the material with an electron beam used as a virtual electrode, Collins's "thermal pulse" principle had the enormous advantage of being completely repeatable and non-destructive [118], allowing the monitoring of the electrical condition of the samples. Consequently, this principle was quickly adopted by others and researches using thermal pulses for probing spatial charge distribution and/or polarization over

the thickness of dielectric materials with thicknesses of 10 to 30 µm have been developed in the next decades [118, 119, 120, 121, 122, 123, 124].

From the end of the 1980's, the use of the TPM has also been extended to cable insulation specimens, in the frame of the study of the ageing of insulating materials for HVAC and HVDC applications. Thus, space charges induced in XLPE specimens cut from AC cables aged under various circumstances were investigated (for instance, 220 µm thick sample obtained by scraping the insulation using a machining tool called lathe were used for examinations [125]). Suzuoki *et al* [126] investigated the space charge in HDPE using a modified TPM. The Suzuoki approach used the same fundamental premise as Collins, though it used the current response during a protracted, step-like heat pulse. It is to note that Collins's idea gave birth to a broader family of thermal methods, such as the (F)LIMM and the TSM presented in this chapter, with applicability to thicker samples, to multi-layer structures and directly to components.

In the 2000's, Mellinger *et al* revised the TPM for 2D and 3D (Thermal-Pulse Tomography, TPT) measurements [127, 128]. Particularly, they showed a resolution of 38 µm in the lateral direction on an irradiated polytetrafluoroethylene (PTFE) sheet with a thickness of 17 µm and a resolution in the thickness direction of less than 0.5 µm [128].

### *i. Equations and implementation*

Classical TPM setups are basically illustrated in Figure 1.31 [116, 129, 130]. The sample of thickness *d,* considered as containing "real" charges of volume density $\rho(x)$ and a polarization $P(x)$, is heated by radiation ("incident light", e.g. a light pulse) on the top electrode (at $x = 0$).

In open circuit (zero external field), the potential difference across the sample reads [116]:

$$V_0 = \frac{1}{\varepsilon_0 \varepsilon_r} \int_0^d [x\rho(x) + P(x)]dx \qquad Eq\ 1.51$$

where $\varepsilon_r$ is the material's dielectric constant and $\varepsilon_0$ the permittivity of the free space ($\varepsilon = \varepsilon_0 \varepsilon_r$).

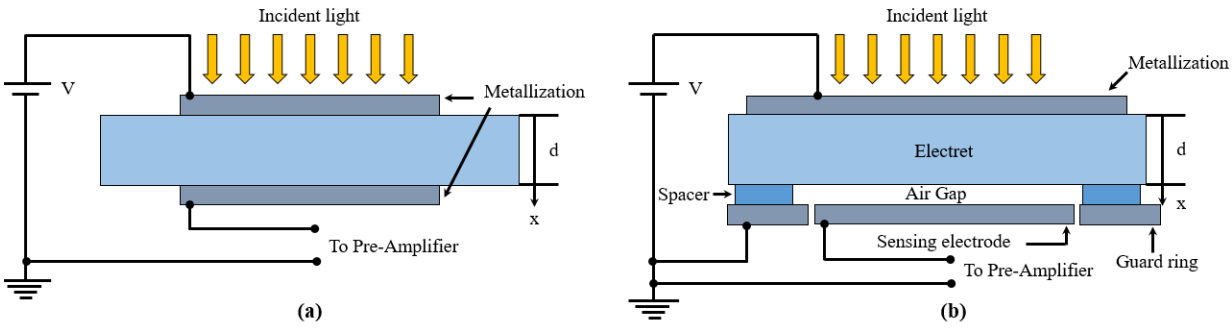


*Figure 1.31 Diagram of TPM setup for two configurations: (a) Sample with two metallized electrodes , (b) Sample metallized on only one face [130].*

Following absorption of heat at $x = 0$, the voltage variation $\Delta V(t)$ measured by the pre-amplifier is:

$$\Delta V(t) = \frac{1}{\varepsilon_0 \varepsilon_r} \int_0^d \left\{ \left[ \alpha \rho(x) - \beta \frac{dP(x)}{dx} \right] \int_0^x \Delta T(x') dx' \right\} dx \qquad Eq\ 1.52$$

where $\alpha = \alpha_x - \alpha_\varepsilon$ and $\beta = \alpha_P - \alpha_x - \alpha_\varepsilon$, with $\alpha_P = \left(\frac{1}{xP}\right) dP/dT$.

In the case of a non-polar sample, $P = 0$ and:

$$\Delta V_\rho(t) = \frac{\alpha_x - \alpha_\varepsilon}{\varepsilon_0 \varepsilon_r} \int_0^d \left[ \rho(x) \int_0^x \Delta T(x', t) dx' \right] dx \qquad Eq\ 1.53$$

By using Poisson's equation $\rho(x) = \varepsilon_0 \varepsilon_r \partial E / \partial x$ in the above relationship and by integrating it by parts taking into account that the electric field is nil on the electrodes, we get:

$$\Delta V_\rho(t) = -(\alpha_x - \alpha_\varepsilon) \int_0^d E(x) \Delta T(x, t) dx \qquad Eq\ 1.54$$

where *E* is the field of the unpolarized sample.

If the internal space charge density $\rho(x)$ and internal distribution of polarization $\frac{dP(x)}{dx}$ are both equal and opposite for a sample with internal field zero, $\rho(x) = +\frac{dP(x)}{dx}$ and $\Delta V(t)$ is given by:

$$\Delta V_p(t) = \frac{\alpha_p}{\varepsilon_0 \varepsilon_r} \int_0^d P(x) \Delta T(x, t) dx \qquad Eq\ 1.55$$

If no difference can be made between non-bonded charge and bonded charge, it comes out that:

$$\Delta V(t) = -\alpha \int_0^d E(x) \Delta T(x, t) dx \qquad Eq\ 1.56$$

with *E* accounting for the effects of unbonded charge and polarization gradient.

In the case of the measurement of a transient current (sample in short-circuit with respect to the measurement instrument), the signal reads, as shown in the TSM section [108]:

$$I(t) = -\alpha C \int_0^d E(x) \frac{\partial \Delta T(x,t)}{\partial t} dx \qquad Eq\ 1.57$$

In general, for short times the influence charges have not enough time to move from an electrode to the other, so the recorded signal should be a voltage one. For longer times the charges have the time to move between electrodes, so a current signal is expected. The response given by the sample can be generalized, as the variation of the influence charges is:

$$Q_{i2}(t) = C \left[ \Delta V(t) + \int_0^d \alpha E(x) \Delta T(x, t) dx \right], \qquad Eq\ 1.58$$

A short-circuit condition corresponds to $\Delta V = 0$, so:

$$Q_{i2}(t) = C \int_0^d \alpha E(x) \Delta T(x, t) dx \qquad Eq\ 1.59$$

The current response is the charge variation with time:

$$I(t) = -\frac{\Delta Q_{i2}}{\Delta t} = -\frac{dQ_{i2}}{dt} \qquad Eq\ 1.60$$

Consequently:

$$I(t) = -\alpha C \int_0^d E(x) \frac{\partial T(x,t)}{\partial t} dx \qquad \textit{Eq 1.61}$$

In open circuit $Q_{i2}(t) = 0$, so:

$$0 = C \left[ \Delta V(t) + \int_0^d \alpha E(x) \Delta T(x,t) dx \right] \qquad \textit{Eq 1.62}$$

$$\Delta V(t) = -\alpha \int_0^d E(x) \Delta T(x,t) dx \qquad \text{Eq 1.63}$$

In practice, with respect to its own capacitance and to the electrical characteristics of the components from the measurement circuit, the measured signal may be a voltage or a current one [131]. The way in which the data are regarded being essential for the subsequent treatment, it is important to assess if the measured signal is a current or a voltage response. This is not always easy without a thorough analysis of the measurement circuit, which is often more complex that the basic one illustrated above and contains additional resistive and capacitive elements for various reasons. Some tricks to test experimentally whether one or the other condition applies during a measurement are given in [132]. However, the limit between "short time" and "long time" is relative and it is not always possible to fully separate the two cases, i.e. the measured signal can be assimilated to a voltage signal for some time, and to a current signal afterwards. In this situation, a thorough analysis of the circuit elements and the consideration of its full transfer function may be necessary to correctly interpret the signal, as we will show in Chapter 3.

### *ii. Some aspects related to the determination of the charge distribution*

The non-homogeneous displacement and permittivity variation of the material when the heat progresses in the sample being the effect of a diffusive process instead of a propagative one, the expressions of the experimental signals presented are Fredholm equations of the first kind, where the field and the temperature distributions at a given time are multiplied under the integral sign. To obtain spatial information about the space charge, appropriate treatment of the signal (commonly called "deconvolution" even if the concerned expressions are not strictly convolution products) is necessary. Collins proposed a method based on the discretization of the sample in a finite number of layers, each layer having a thermal equivalent circuit and bearing a discrete charge density, and where the charge distribution was determined by iteratively adjusting the value of each layer to fit the experimental signal [124]. DeReggi *et al* [118] set up analytical formulations based on Fourier series to determine the charge distribution across the sample and illustrated it on a polyvinylidene difluoride copolymer electret. Such approaches, based on the Fourier analysis of the heat equation, are still used. Mopsik and DeReggi claimed that if precautions are taken both theoretically and practically, the precision with which the distribution may be estimated under their experimental circumstances (25 µm film and 60 µs light pulse) is limited solely by experimental accuracy, not by the computational technique [119]. They employed their approach to investigate the poling behavior of different polymeric samples [118, 119, 120, 121]. Gerhard-Multhaupt and others continued to develop and to use the TPM during the 1990's for the investigation of electrets [122, 123].

In a first approach, proposed by Collins [124], an equivalent thermal circuit of the sample was used. A discrete model was set up to model the sample, in which the material is divided into *N* parts parallel to the surface. Each part has its own thermal resistance and thermal capacity. As illustrated in Figure 1.32, an electrical analog network is built with the thermal capacities and resistances of all the pieces, and with charges distributed in each discrete slab, allowing to calculate the temperature and to assess the measured signal by iterations when varying the charge of each slab.

It is mentioned in Collins's study [124] that it is not required to know the exact temperature variations caused by the heat pulse. The time scales of the analog model and the actual sample must, however, be connected in a recognized fashion. This can be approximated by comparing known values of the physical and thermal characteristics of the sample to the electrical analog model's measured component values. Alternatively, a more precise direct measuring approach, as described below, can be utilized.

Since this model is discrete, it is an approximation of the real sample, hence the findings must be understood accordingly. It is obvious that the model's validity improves as the value of *N* rises. *N = 20* was the value chosen in the Collin's study and it also shows that when compared to other aspects, the inaccuracies contributed by this source are thought to be minor. Heat losses from the sample due to thermal conduction via the air between the sample and the sensing electrode may be readily included by connecting a resistor $R_l$ of appropriate value at the RC network's corresponding end as shown in the Figure 1.32. Furthermore, an additional capacitor $C_m$ at the input point can replicate the metallizing's thermal inertia. The values of these components are derived using the system's known physical properties. Their impact can be non-negligible.

Collins approached the charge distribution using an analog simulator. Summation approximations are used to substitute the integrals in Eq (1.64). A discrete series of *N* charge layers $\rho_i$ at coordinates $x_i = \left(i - \frac{1}{2}\right) d/N$ with $i = 1,2, \ldots N$, replaces the continuous charge distribution. Similarly, another integral function for the temperature distribution up to point $x$ is also replaced by a summation up to the corresponding layer $x_i$ [58]. The total of all the above summation functions w.r.t the temperature functions which corresponds to the charge at the given layer, produces an experimentally determined voltage value $\Delta V(t)$ as follows:

$$\Delta V(t) = \sum_{i=1}^{N} \rho_i \left( \sum_{j=1}^{i} \Delta T_j \right) \qquad \textit{Eq 1.64}$$

As a result, this "deconvolution" procedure entails selecting a discrete charge distribution $\rho_1, \ldots, \rho_N$ and determining the form of the $\Delta V(t)$ function that this distribution creates. After that, the distribution is manually iterated and $\Delta V(t)$ calculations are revised until the experimental data coincides with the assumption. Collins indicated at that time that the charge distributions cannot be produced in a unique way with such an approach [129], as slight variation of the charge distributions can generate findings that are virtually identical or fall within the experimental error range. The efficiency of this approach therefore hinges on getting experimental data of sufficient precision to be able to compute the charge distribution to within tolerable limits. It is also important that the charge distributions that are formed be physically

sound, so the human factor cannot be completely eliminated from the deconvolution process [124]. Many of Collins's conclusions still hold today, even if they have been revisited, reinterpreted or formalized differently.

DeReggi et al. [118, 119] showed that the electrical response can be studied using Fourier series, making the study far more quantitative than Collins. They also demonstrated that the analysis can be enhanced by pulsing a sample alternately on both sides and combining the data to better isolate the exponential components that occur in the electrical response expression. Based on the width of the light pulse, they were able to graphically identify the first four Fourier coefficients of the polarization distribution of a TFE-$VF_2$ copolymer sample and estimated that roughly 10-15 coefficients could be acquired for actual samples as thin as 25 μm [119]. The estimated resolution was of the order of 2.5 μm.

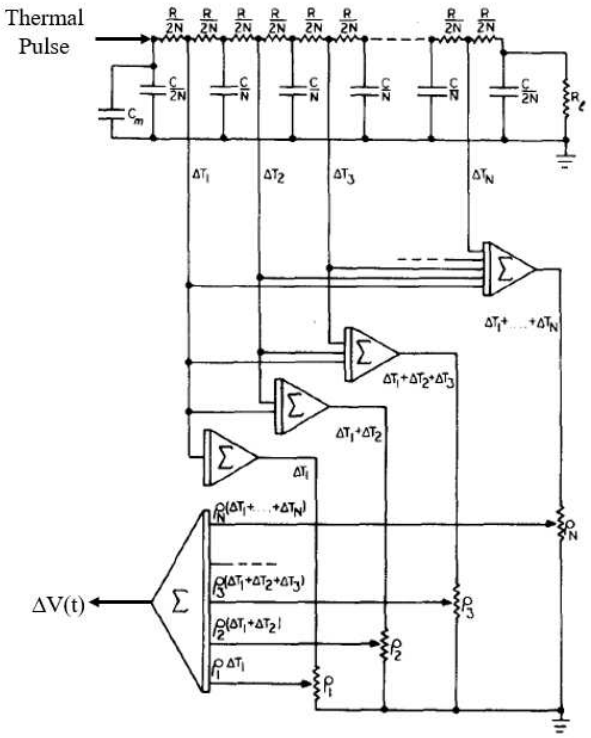


*Figure 1.32 Electrical analog circuit used in Collin's "deconvolution" process [124]*

DeReggi's idea was to use the general solution of the heat equation to develop a deconvolution procedure. Thus, the temperature at the surface of the sample (i.e. $x = 0$) after a transmission of heat during $t_{pulse}$, which is taken as time origin ($t = 0$), can be written as:

$$T(x,0) = T_1 + \Delta T(x,0) \qquad \textit{Eq 1.65}$$

where $T_1$ is the sample's uniform temperature before applying the pulse and $\Delta T(x,0)$ represents the deviation from $T_1$. In actuality, $\Delta T(x,0)$ is a tightly localized function with a width $\xi \ll d$ that extends from $x = 0$. The temperature at a given coordinate $x$ inside the sample at $t > 0$ is then given by

$$T(x,t) = T_1 + \Delta T(x,t) \qquad \textit{Eq 1.66}$$

where $\Delta T(x,t)$ is expressed as [133]:

$$\Delta T(x,t) = a_0 + \sum_{n=1}^{\infty} a_n \cos\left(\frac{n\pi x}{d}\right) exp\left(\frac{-tn^2}{\tau_1}\right) \quad \textit{Eq 1.67}$$

where $\tau_1 = \frac{d^2}{k\pi^2}$, k is the thermal diffusivity where

$$a_0 = d^{-1}\int_0^d \Delta T(x,0)dx = \lim_{t\to\infty} \Delta T(x,t) \quad \textit{Eq 1.68}$$

and

$$a_n = \frac{2}{d}\int_0^d \Delta T(x,0)\cos\left(\frac{n\pi x}{d}\right)dx, n = 1,2,\ldots \quad \textit{Eq 1.69}$$

In the particular case where $\Delta T(x,0) \to \delta(x)$, all the $a_n$'s are

$$a_n = 2a_0, n = 1,2,\ldots \quad \textit{Eq 1.70}$$

For a general function $\Delta T(x,0)$:

$$\Delta T(0,t) = a_0 + \sum_{n=1}^{\infty} a_n exp\left(\frac{-tn^2}{\tau_1}\right) \quad \textit{Eq 1.71}$$

and

$$\Delta T(d,t) = a_0 + \sum_{n=1}^{\infty}(-1)^n a_n exp\left(\frac{-tn^2}{\tau_1}\right) \quad \textit{Eq 1.72}$$

It is to note that thermal diffusivity measurements rely generally on the equations Eq (1.66) and Eq (1.67) [134]. DeReggi pointed out that, by measuring the transient resistance of one or both electrodes, the dimensionless ratios $\Delta T(0,t)/a_0$ and $\Delta T(d,t)/a_0$ may be derived. Then, without knowing the precise geometry of the light pulse, the $a_n/a_0$ and $\tau_1$ may be calculated.

The voltage variation due to the non-bonded charge when the sample is thermally excited reads, by substituting Eq (1.67) in Eq (1.56):

$$\Delta V_p(t) = \frac{(\alpha_x - \alpha_\varepsilon)}{\varepsilon_0\varepsilon_r}\left[a_0A_0 + \frac{d}{n}\sum_{n=1}^{\infty}\frac{a_nA_n}{n} exp\left(\frac{-tn^2}{\tau_1}\right)\right] \quad \textit{Eq 1.73}$$

where

$$A_0 = \int_0^d x\rho(x)\,dx \quad \textit{Eq 1.74}$$

and

$$A_n = \int_0^d \rho(x)\sin\left(\frac{n\pi x}{d}\right)\,dx,\ n = 1,2,\ldots \quad \textit{Eq 1.75}$$

and Eq (1.73) can be written as

$$\Delta V_p(t) = \frac{(\alpha_p + \alpha_x - \alpha_\epsilon)}{\varepsilon_0\varepsilon_r}\left[a_0B_0 + \frac{d}{n}\sum_{n=1}^{\infty} a_nB_n exp\left(\frac{-tn^2}{\tau_1}\right)\right] \quad \textit{Eq 1.76}$$

where

$$B_0 = \int_0^d P(x)\,dx \quad \textit{Eq 1.77}$$

and

$$B_n = \int_0^d P(x)\, cos\left(\frac{n\pi x}{d}\right)\, dx,\ n = 1,2,\ldots \qquad Eq\ 1.78$$

The terms $a_0$, $A_n$ and $B_n$ are coefficients of Fourier series expansions for $\Delta T(x,0), \rho(x)$ and $P(x)$ respectively.

The experimental signal is thus composed of exponentially declining components with relaxation durations of $\tau_1/n^2$. The electrical response is measured in the above described model, and the result are combinations of the Fourier coefficients. The non-bonded charge case produces Fourier coefficient combinations as follows: $(a_n/a_0)\ (A_n/A_0)\ (d/\pi)$, whereas the polarization case yields $(a_n/a_0)\ (B_n/B_0)$. The approximation of $(a_n/a_0) \cong 2$ can be derived for sufficiently small pulse duration ($t_r \ll \tau_1/n^2$ up to the highest required value of n). A separate measurement of the electrodes transient resistance can be used to obtain $a_n/a_0$ if necessary. (This is an idea which have already been evoked by DeReggi at that time, but which has not been really considered until several years ago) Thus, up to the terms with n of order $N = (\tau_1/t_r)^{\frac{1}{2}}$, the Fourier coefficients of the space charge distribution, $A_n/A_0$, or $B_n/B_0$ may be calculated. The thermal pulse experiment after DeReggi has a spatial resolution of around $d/N$ [118].

If the direction of the thermal excitation is changed [in which case $a_n$ becomes $(-1)^n a_n$] or if the sample is reverted [in which case $A_n$ and $B_n$ become $-(-1)^n A_n$ and $-(-1)^n B_n$], equations Eq (1.68) and Eq (1.71) gain alternating signs. The even and odd Fourier coefficients can be determined individually by taking the sum and difference of the two signals if separate response signals are acquired by thermally pulsing adjacent surfaces in turn. The distribution of the response is symmetric or asymmetric, based on a visual comparison of the two signals. The graphical analysis for the even and odd responses have been explained in detail in DeReggi's study [118]. It has also been shown that samples under various poling conditions, other copolymer samples and homopolymer (Polyvinylidene fluoride) samples can display approximately uniform polarization [135]. The reaction is virtually step-like in such circumstances, and $B_n/B_0 = 0$ for all *n* values. DeReggi, Mopsik and their team expanded this approach to other cases of electrets and developed full deconvolution algorithms using calibration procedures [119, 136].

It is interesting to note that DeReggi's approach was then used for developing signal processing for other thermal methods, like the TSM and LIMM. However, this technique has limitations as it assumes a constant spatial resolution across the sample thickness, which is not really the case. Further analysis and more elaborated techniques, like regularization [137] and scaling transformations, were proposed at the end of the 80's by Leal-Ferreira [138] and Coufal *et al.* [139] in order to obtain an approximation of the desired charge or polarization profiles. These ideas were further developed by Ploss *et al* [140] Ploss [141] and Bauer [110, 142] (they are not detailed here, as there will not be used in the subsequent work). All these analyses show clearly that the resolution of the thermal pulse method is very high near the excited electrode, but decreases in the bulk. This makes the TPM a good choice for assessing very thin samples and interfaces.

In recent years, attention has been given to real-time measurements of the electrode temperature, which is an important issue. Indeed, if the amount of heat transported by the laser beam to the sample surface is usually well known, the real surface temperature can be calculated only through hypothesis concerning the reflectance of the electrode, which is poorly known. Consequently, the values of the temperature at the electrode are usually not known with enough accuracy. If this still allows to obtain charge and field profiles, this do often not allow to give the real values of the field and charge, and for this reason many results obtained by the TPM (and by other thermal methods using non-contact stimuli) are often expressed in arbitrary units. Calibration procedures can be used [136], but advances made since 2015 [143, 144, 145] have shown that it is possible to measure simultaneously the surface temperature and the charge signal, which should hopefully allow to reach directly the values of the electric field near the interface and increase the precision in the bulk, but which has never been done so far. This is the approach that we will develop in the experimental part of this work, with samples of thicknesses of 50 µm to 160 µm.

## c. Laser Intensity Modulation Method

The functioning principle of these methods is similar to the TSM and the TPM. However, the amplitude of the thermal stimulus is sinusoidally at several frequencies. In short-circuit conditions, the expression of the current with respect to the frequency *f* reads [146]:

$$I(f) = j2\pi f \frac{S}{d} \int_0^d \rho(x) T(x,f) dx \qquad \textit{Eq 1.79}$$

The most known technique of this type is the Laser Intensity Modulation Method (LIMM) [147, 148, 149, 150], proposed in the mid-1980's by S. B. Lang and D.K. Das-Gupta. The diagram of the experimental setup is shown in Figure 1.33. The test sample is set in a temperature-controlled chamber with optical windows. The surface of the sample is subjected to a laser beam whose intensity is sinusoidally modulated with the help of an acousto-optic modulator or a modulator built in the laser. In order to extract the LIMM signal at a even frequency from noise, a lock-in amplifier is used. The energy of the laser beam is absorbed by the front electrode and the sinusoidally fluctuating temperature waves cross the sample. Hence, the interaction between the spatially distributed polarization, fluctuating temperature and space charge creates a sinusoidal current response that is measured. Measurements are performed over a wide range of frequencies, spaced logarithmically. Each value obtained through the temperature distribution produces a unique current; thus, from the knowledge of the temperature distribution and the obtained current, the charge and polarization distributions in the sample are calculated.

The FLIMM (Focused Laser Intensity Modulation Method) and FLAMM (Focused Laser Acoustic Modulation Method) [151, 152] use the same principle, but the laser beam is focused, and its displacement allows a 3D cartography of the sample. The ATWM (Alternative Thermal Wave Method) [153] works on the same principle as the LIMM, but the temperature is modulated with a Peltier module. For the methods using modulated thermal waves, in order to ensure a good in-depth resolution, it is necessary to use a relatively wide frequency span, which

may induce a significant measurement duration (1 to 100 minutes with respect to the used scan range). They are thus particularly used to study slowly evolving phenomena in thin samples (e.g. study of polarization and electrets). The spatial resolution of such methods is of the order of 1 to 10 µm (near the sample surface), with a sensitivity of the order of 10 mC/m$^3$.

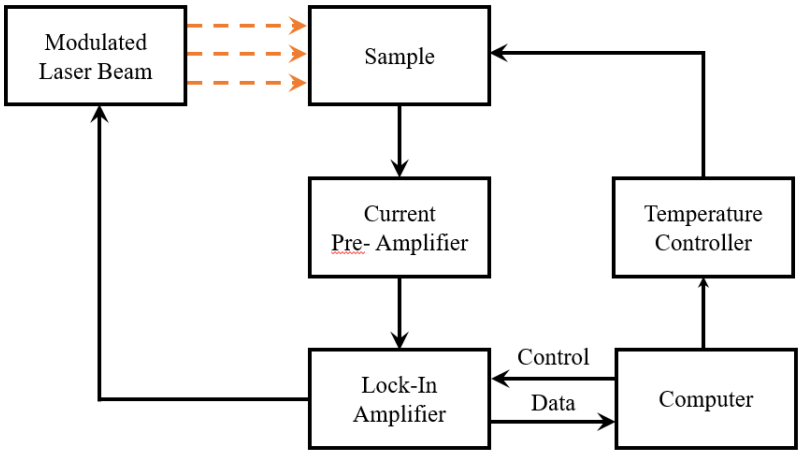


*Figure 1.33. Schematic diagram of the experimental set up for the LIMM [154]*

### 1.4.3 Aspects regarding resolution

Intuitively, the spatial resolution corresponds to the "width" of the thinnest "line" in the distribution represented in a precise manner in the measured profile, or to the smallest distance separating two distinguishable objects [155]. For transient perturbations the best resolution without reducing the signal to noise ratio is associated with the shortest distance on which the perturbation varies from 10 to 90% of its amplitude. Figure 1.34 illustrates the definition of the spatial resolution of the pressure and thermal methods [156].

In the case of the propagation of elastic waves, that is to say for the pressure wave propagation and for the pulsed electroacoustic methods, the rising edge of symmetrical pulses is equivalent to the duration $\tau$ of the elastic pulse at half amplitude times the sound velocity $v_s$, as shown in Figure 1.34. If $f_{max}$ is the bandwidth, the resolution $R$ reads:

$$R = v\tau = \frac{v}{2f_{max}} \qquad Eq\ 1.80$$

In the case of the thermal methods, the resolution $R$ is related to the material's thermal diffusivity $D$ and the time $t$:

$$R = 2.35\sqrt{Dt} = 2.35\sqrt{\frac{D}{2f_{max}}} \qquad Eq\ 1.81$$

Thus, at 50% of the amplitude, the position $x_{50}$ is $1.66(Dt)^{1/2}$, as shown in Figure 1.34 (b); the resolution depends linearly to this position roughly as $R \approx \sqrt{2}\, x_{50}$. These expressions allow to make estimations on the available resolutions for given bandwidths without considering the aspects related to the signal-to-noise ratio. However, as pointed by Holé in [157], the largest

excitation bandwidth does not always lead to the best resolution; the signal amplitude under the noise level in the frequency domain can sometimes make the difference. The variation between signals induced by slightly different charge distributions can be used to define the spatial resolution in the same way for any measurement technique, by considering the level of noise. There are two types of spatial resolution to consider: positioning resolution and discerning resolution.

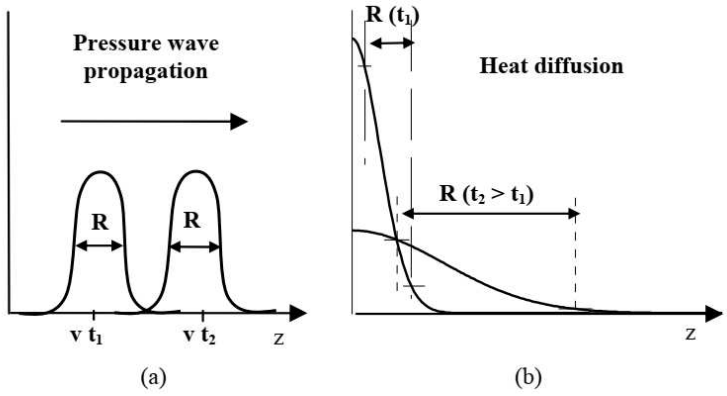


*Figure 1.34 Spatial resolution for acoustic methods (a) and thermal methods (b) [156]*

As shown in Figure 1.35, positioning resolution is related to the precision of a charge's location inside the material, whereas the second type of resolution is related to the potential to discriminate between two separate charges. For the positioning resolution, the position of two charges cannot be differentiated if the signals generated by a charge at one position is not sufficiently distinct from the signal generated by the same charge at a slightly different position. On the other hand, if the difference among these signals is large enough, the two charge locations may be distinguished (Figure 1.35 1(a) and 1(b)). For a given signal to noise ratio, position resolution may thus be defined as the smallest charge displacement between two measurements that alters the signal by the noise level. If the distinction between the two signals is less than the noise level, it is impossible to determine where the charge from the signal is positioned at $x_0$ or at $x_0+\delta x_0$; if the distinction between the two signals is greater than the noise level, it is feasible to determine where the charge from the signal is positioned, and if the distinction between the two signals is below the noise threshold, $\delta x_0$ is the minimum distance between the two positions that can be detected, and hence it is the position resolution (Figure 1.35 1(c), 1(d) and 1(e)).

Similarly, for the discerning resolution, if the signal produced by two separate charges is not significantly different from the signal produced by a single charge, the gap between the two charges is too tiny to differentiate them. On the other hand, if the difference between these signals is large enough, the two charges may be distinguished (Figure 1.35 2(a) and 2(b)). For a given signal to noise ratio, the discerning (or distinguishing) resolution is defined as the shortest distance between two identical charges producing a signal that varies by the noise level from the signal produced by a single charge at the same mean position, but with twice the amplitude. It is impossible to tell if there are one or two charges if the difference between the two signals is less than the noise level. Otherwise, it is possible to determine whether there are one or two charges (Figure 1.35 2(c) and 2(d)). In the case where the difference is less than the

noise level, $\delta x_0$ is the smallest distance between the charges to be distinguished, and hence it is the discerning resolution (Figure 1.35 2(e)).

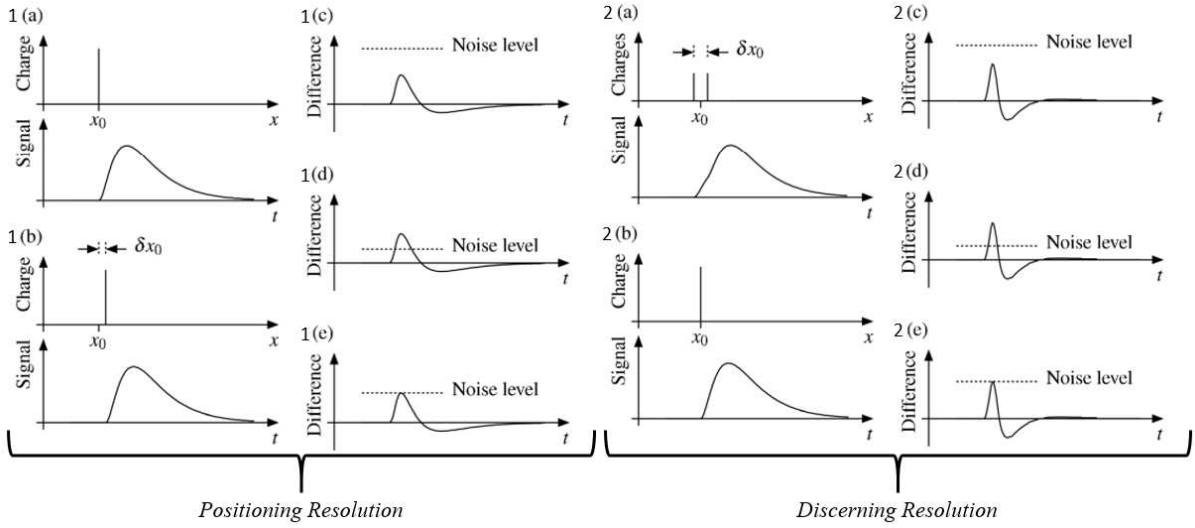


*Figure 1.35 Illustration of the definition of the two types of spatial resolution [157]*

Because the noise level is employed as the detection limit in these two types of spatial resolution, a reference to the signal to noise ratio is required. Any other restriction, such as the signal level itself, might be utilized instead. This would only scale the resolution for all the measuring methods in the same way. The advantage of employing the noise level is that it should provide the highest spatial resolution from the processed signal because it is the lowest discernible signal change.

An overview of the positioning and discerning resolutions has been summarized in Table 1.2, as calculated for stimuli of different nature and profile by Hole et al [157]. As it can be seen, the methods based on thermal diffusion act differently from those based on elastic wave propagation. In fact, the spatial resolution decreases as the position of the charge changes within the sample whereas it is practically constant at all positions in the case of pressure wave method and electro-acoustic method. The sensitivity of the heat step [158] and heat modulation [150] techniques do not diminish with charge position (Table 1.2). As a result, these thermal approaches are better suited for thicker materials and achieve nearly the same resolution results.

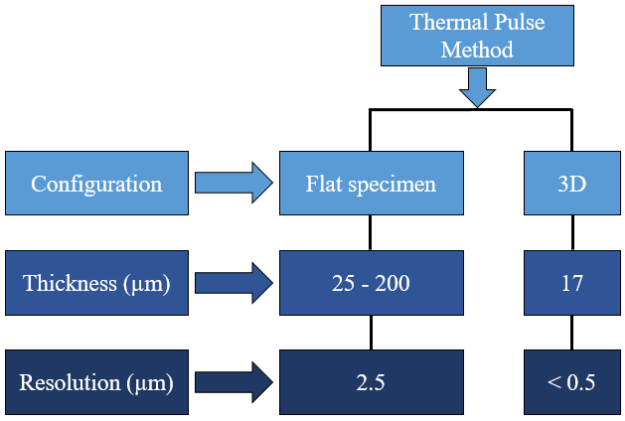


*Figure 1.36 TPM for different sample configurations [159]*

It is clear that the best resolution can be acquired with thermal methods, in the vicinity of the thermally excited electrode. Taking data from both the sides of the samples enhances the resolution. Resolutions can be as low as 100 nm when using an extremely closely concentrated laser pulse (for example, a femtosecond laser).

However, the measurement system bandwidth has to be as high as feasible in order to get a satisfactory resolution. At the moment, both at the level of the perturbation and at the level of the measurement system, such bandwidth can be of the order of a few hundreds of MHz However, going to the sub-THz bandwidth is required to get a spatial resolution in the nanometer range, thus this isn't enough [156]. The tests may be carried out without any mechanical contact with the material thanks to the use of femtosecond laser pulses. This might be a crucial feature since IC's and MEMS are delicate devices, and any physical contact could jeopardize their proper functionality. In the Figure 1.36, the thickness direction is referred to by the resolution value. For a sample with a width of few millimeters, the resolution in the lateral direction is of the order of 38 μm [159, 160]. Because of heat wave dampening in thicker materials, this approach guarantees great resolution (< 1 μm) (Figure 1.36) and is particularly useful for the analysis of thin samples (< 100 μm).

*Table 1.2 Overview of the spatial resolution for different space charge measurement techniques [157]*

| *Measurement technique* | *Positioning resolution* | | *Discerning resolution* | |
|---|---|---|---|---|
| Heat pulse | $\frac{0.31x}{SNR}$ | $\frac{0.31x^3}{x_0^2 SNR_0}$ | $\frac{0.75x}{\sqrt{SNR}}$ | $\frac{0.75x^2}{x_0\sqrt{SNR_0}}$ |
| Heat step | $\frac{2.07x}{SNR}$ | $\frac{2.07x}{SNR_0}$ | $\frac{2.94x}{\sqrt{SNR}}$ | $\frac{2.94x}{\sqrt{SNR_0}}$ |
| Heat modulation | $\frac{1.92x}{SNR}$ | $\frac{1.92x}{SNR_0}$ | $\frac{2.72x}{\sqrt{SNR}}$ | $\frac{2.72x}{\sqrt{SNR_0}}$ |
| Temperature step | $\frac{0.52x}{SNR}$ | $\frac{0.52x^2}{x_0 SNR_0}$ | $\frac{1.14x}{\sqrt{SNR}}$ | $\frac{1.14x^{3/2}}{\sqrt{x_0 SNR_0}}$ |
| Pressure or voltage pulse | $\frac{0.98v_s\tau}{SNR}$ | $\frac{0.98v_s\tau}{SNR_0}$ | $\frac{1.68v_s\tau}{\sqrt{SNR}}$ | $\frac{1.68v_s\tau}{\sqrt{SNR_0}}$ |
| Pressure or voltage step | $\frac{0.98v_s\tau}{SNR}$ | $\frac{0.98v_s\tau}{SNR_0}$ | $\frac{2.24v_s\tau}{\sqrt{SNR}}$ | $\frac{2.24v_s\tau}{\sqrt{SNR_0}}$ |

It is important to induce very short duration temperature fluctuations in order to achieve a resolution in the nanoscale range using thermal methods. Dagher *et al* [156] have also proposed the use of a femtosecond laser for the temperature variations with a rapid speed.

When a high-power Titanium and Sapphire based femtosecond laser pulse hits a metallic target like for, e.g., aluminium, photon electron interaction excites some of the target's electrons. The energy of these electrons is swiftly transferred to the lattice when they thermalize. Because the laser pulses are so brief, and if the target absorbs the photons across a thin enough layer, the ensuing temperature increase only reaches a few nanometers into the target. Figure 1.37 shows how this works and ultrafast temperature fluctuations can be created in this fashion. The thermo-elastic regime cannot be exploited to create longitudinal elastic waves in the direction of sample thickness by employing longer laser pulses, such as picosecond. Instead, an ablation protocol can be utilized, although it is harmful. The entire test may be carried out efficiently by utilizing a femtosecond laser that emits pulses at a frequency on the order of 100 MHz, even if an averaging approach is utilized to enhance the signal to noise ratio. A potential resolution of roughly 60 nm in SiO2 could thus be achieved using the thermal and pressure wave propagation techniques. In order to efficiently assess the charge signal, the electric field created by the sample owing to the perturbation must be computed while taking into consideration all of the sample's features, such as electrode thickness or induced electric current.

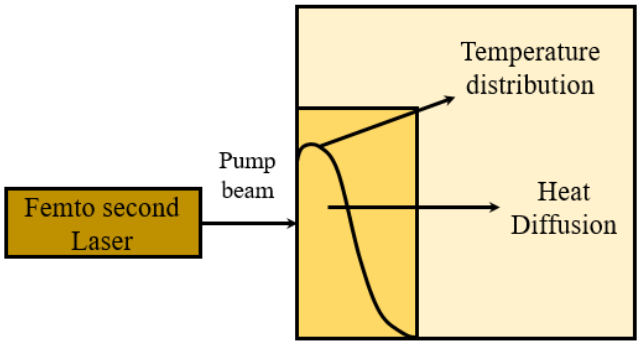


*Figure 1.37 Schematic diagram for diffusion of heat using femtosecond laser*

In the case of elastic methods, evolutions have been proposed recently with the aim of reaching micronic and submicronic resolutions [161]. Hamidouche [162, 163, 164] proposed a new approach called Electro Acoustic Reflectometry (EAR). With respect to classical pressure methods, EAR is different in two aspects: the type of the excitation signal and the way the released elastic signal is measured. In fact, to overcome the limitation on the size of the excitation bandwidth encountered with elastic methods (PWP, PEA), EAR method works in frequency domain. That is, the excitation signal is sinusoidal, and it is swept over the frequency range of choice. Therefore, the size of the excitation bandwidth is under control and can be adjusted as needed. If charges are present inside the material, they will respond to this excitation signal by emitting elastic waves at the frequencies corresponding to the elastic resonances of the material. So, part of the input electrical energy is transformed into elastic energy at those frequencies. From microwave standpoint, the input signal is not totally reflected by the sample since part of the energy is converted into elastic energy. Consequently, the reflected signal contains the signature of the elastic signal. Generally, the generated elastic signal in a given

material holds the information about space charge distribution. With the EAR method, this elastic signal can be deduced from the reflected electrical signal, then the information about space charge distribution can be recovered. Thus, the EAR method can be summarized in three main steps: first, measurement of the reflected electrical signal, second, extraction of the elastic signal from the electrical signal and finally, transforming the extracted elastic signal into time domain using an inverse Fourier transform. Finding the space charge distribution as a function of position along the thickness of the material is a matter of mapping time instants into space positions using sound velocity in the material. Results claiming a resolution of 1.2 µm in a 9 µm-thick PVDF sample have been reported [162], which make this technique a very promising one, provided that adequate solutions to the problems related to the compensation of the intrinsic capacitance of the sample (which, combined to the input impedance of the measurement system, hinders the detection of resonances above the GHz level), are found [164].

Finally, it must not be forgotten that, whatever the method, the resolution increases with the decrease of the thickness and the increase of the stimulus magnitude. Thus, submicronic resolutions can be reachable only on very thin samples (< 50 µm), which must be homogeneous at and below the micron scale. However, increasing the resolution in thicker structures (above 50 µm) is also of interest, as the homogeneity degree of such structures is generally higher than 1 µm due to the manufacturing process.

### 1.4.4 Synthesis and discussion with respect to the aim of the work

As presented, each space charge measurement method has its own features, determined by the nature of the used stimulus and by the conversion chain utilized to obtain the signal. Table 1.3 summarizes the data available in the literature on the characteristics of the different space charge distribution measurement techniques. For the reasons presented in section 1.3.4, the samples to be studied in the present work would be metallized and carbon-black coated medium thickness polyethylene samples (50 to 150 µm) on which the aim is to evaluate as directly and as precisely as possible the interface fields. Knowing that for such samples the material "grain" is of the micron order, aiming below the micron has no real physical sense, as the homogeneity of the material does not match for claiming higher resolutions.

As it comes out from the bibliographic review, the thermal methods are the most sensitive ones and those for which resolutions of the micron order can be expected near the sample surface, so they are naturally the most suited for the given specifications. Samples with thicknesses ranging from 10 µm to 150 µm have been used with the TPM, LIMM and FLIMM methods and thicknesses between 100 µm and to 30 mm have been characterized by the TSM. It has been shown recently that positioning resolutions between 2 and 5 µm and discerning resolutions below 10 µm are at reach with the TSM, with enhanced thermal step setups on 100 µm XLPE samples coated with 30 µm carbon black electrodes, at the carbon black/polymer interface [36].

*Table 1.3 Characteristics of space charge measurement methods [36]*

<table>
<tr><td></td><td colspan="3">Thermal Methods</td><td colspan="2">Pressure Wave Propagation Methods</td><td>Electro Acoustic Methods</td></tr>
<tr><td>Method</td><td>TPM</td><td>LIMM</td><td>TSM</td><td>LIPP</td><td>PIPS/PIPP</td><td>PEA</td></tr>
<tr><td>Perturbation</td><td colspan="3">Diffusion of heat</td><td colspan="2">Elastic waves</td><td>Electrical pulses</td></tr>
<tr><td>Mode of generation</td><td>Short laser pulse compared to the thermal relaxation time</td><td>Amplitude modulated laser beam at different frequencies</td><td>Temperature step applied on one of the electrodes</td><td>Short pulsed laser compared to the acoustic transit time</td><td>Pressure generated by the piezo effect on a crystal</td><td>Electric pulse voltage applied between the electrodes</td></tr>
<tr><td>Response</td><td colspan="5">Electrical displacement quantity (voltage or current variation)</td><td>Acoustic wave (Converted into voltage by a piezoelectric transducer)</td></tr>
<tr><td rowspan="2">Estimated resolution</td><td>Very good near the surface (< 1 μm)</td><td>Good near the surface (1 – 10 μm)</td><td>Good near the surface (several μm)</td><td colspan="3" rowspan="2">10 – 100 μm before deconvolution<br>≤ 10 μm after deconvolution<br>Good in the volume, less near the surface</td></tr>
<tr><td colspan="3">Decreases in the volume</td></tr>
<tr><td>Sensibility</td><td colspan="3">1 – 10 mC/m$^3$</td><td colspan="3">10 – 100 mC/m$^3$</td></tr>
<tr><td>Measurement time</td><td>Short (1μs – 1s)</td><td>Long (1 – 100 min)</td><td>Medium to Long (100 ms – 100 min)</td><td colspan="3">Short (1 μs – 10 μs)</td></tr>
<tr><td>Samples</td><td colspan="2">Thin Films (10 μm – 150 μm)</td><td colspan="2">Films, Plates, Cables (100 μm – 30 mm)</td><td>Thick films, Plates, Cables (100 μm – 30 mm)</td></tr>
<tr><td>Application domain</td><td colspan="2">Structures and thin films</td><td colspan="4">Films, Insulating structures, Plates, Cables, Capacitors</td></tr>
</table>

Progress in this area with the TSM is related to the increase and control of the thermal step steepness, to the improvement of the thermal transfer from the coolant liquid to the sample (i.e., the design of the radiator), and, last but not least, to the knowledge of the interface temperature (on which research is currently under way).

In the case of the TPM, there have been many results reporting micrometric resolutions on samples of several dozens of microns, even if the results are often given in arbitrary values, as the real electrode temperature is difficult to be approached accurately. With the aid of calibration procedures and μs-large laser pulses, Mopsik, DeReggi and their co-workers [125, 136, 165] presented at the end of the 1980's convincing values and distributions of electric field in polyethylene samples with thicknesses of 50 μm and above (even if micrometric resolutions were not claimed). Because of the development of new methods like the PEA and the TSM and their applicability to medium and strong insulating thicknesses and to components including them, few attention has been made since to the application of the TPM on such samples.

However, the use of the TPM is of interest on medium thickness samples, especially for determining the interface fields, as the resolution of the TPM near the interface is the best from all the methods, and the non-contact mode of application of the stimulus is a significant asset for characterizing samples under electro-thermal or other types of stress. In the same time, the progress made lately on the measurement of the electrode temperature, for which it has been experimentally proven that it can be acquired simultaneously with the charge signal [143, 144, 145] thus allowing a more precise knowledge of the thermal stimulus, open new possibilities. These aspects will be the subject of the rest of this thesis.

## 1.5 Conclusion

In this chapter, with the aid of a bibliographic review, we have detailed the problems and challenges that led to the origin of this thesis and served as the foundation for our work.

Firstly, the issues related to the electric power transmission were addressed. The technical and economic advantages that makes DC transmission a vector of choice over AC transmission, for the future of electricity transmission over long distances, were presented.

The problematics related to the development of HVDC networks using land or submarine cables were then presented. It was shown that a key problem is the establishment, under strong electrical and thermal gradients, of space charge zones in the insulation, which affect its performance and can decrease its lifetime. The physical mechanisms and phenomena related to the occurrence of space charges were reviewed.

In order to analyze and control space charges, it is necessary to be able to quantify and localize them: this is the subject of our work, which aims to improve the measurement of these charges in materials and structures. The various existing techniques were thus reviewed and analyzed in relation to the objectives of the thesis, namely the evolution and the improvement of a measurement technique enabling highly accurate detection of space charges. We chose as study objects medium thickness insulating films of polyethylene (50 μm to 160 μm) coated with

metallic and semi-conducting electrodes, to approach as closely as possible the phenomena occurring in HVDC insulating layers and to be as representative as possible of the structure of such layers by keeping the thickness as low as possible for sensitivity reasons. The principle of the thermal pulse method appeared to be a potential candidate for achieving these objectives, and the implementation of an optimized measurement set up based on this principle will be the subject of the remainder of the thesis.

After having laid, in this part of the manuscript, the foundations for the understanding of our subject, the study by simulation of the various related problems and the search for solutions are addressed in the following chapter.

# Chapter 2: Simulations

# 2.1. Introduction

The analysis of the electric field in a sample with a stimulus method requires the knowledge of the evolution of the stimulus with respect to time and space. In the case of a homogeneous sample receiving on one face a rectangular heat pulse of known duration, the heat distribution in the bulk can be calculated by solving analytically the heat equation.

In order to approach the temperature variation, we have carried out a study by stimulation on medium thickness insulating samples under conditions consistent with the thesis's objective. The aim was to assess conditions for experiments on polyethylene sample of several dozens of microns and provided with metallic and semicon electrodes. Thus, we simulated the diffusion of heat across uncoated and carbon-black coated medium thickness polyethylene flat samples to which thermal pulses are applied on one face, to determine the shapes of the temperature distributions and to evaluate under what conditions measurable signals can be obtained without affecting the sample state.

In a first step, the increase of the surface temperature and the distribution of the temperature in the bulk were calculated to determine the maximum temperature of the sample and the temperature penetration depth when pulses of different energies are used, and to estimate the maximum amount of heat that can be brought under different conditions without damaging the material. Electrical simulations were then carried out for estimating the thermal pulse signals issued by samples containing electric fields of several kV/mm, to analyse their measurability with state-of-the-art instrumentation and to aid afterwards to the interpretation of the experimental results.

# 2.2. General parameters

The simulations were made in an unidimensional configuration representing a flat polyethylene slab of thickness $50\ \mu m \leq d \leq 100\ \mu m$ to which a quantity of heat $Q[J]$ is brought on one face at the time $t = 0$ (Figure 2.1).

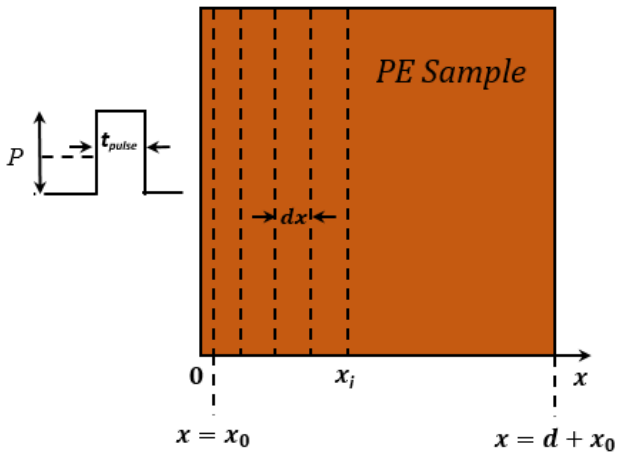


*Figure 2.1 Domain of study*

It is considered that the surface *S*, which totally absorbs the heat, is a disc of diameter $\phi = 50\ mm$. The thermal stimulus is assimilated to a rectangular pulse of power *P* and duration $t_{pulse}$ applied at $x = 0$. An additional thickness $x_0 \in [0.1\ nm; 40\ \mu m]$ is added to account for the thermal interface and/or for thickness of the semicon electrode when studied. The calculation domain contains an electric field issued by the presence, in the bulk of the sample, of a small layer of charge of density $\rho$ extended over a small distance *dx* (details are given in section 2.4.2 herein after).

The physical parameters used for the simulations, given in the [166], were those of polyethylene.

*Table 2.1 Simulation parameters for the insulating layers*

| Parameter | Value | Unit |
|---|---|---|
| Mass Density ($Mv$) | 975 | $kg/m^3$ |
| Specific heat ($Cp$) | 1550 | $Jkg^{-1}K^{-1}$ |
| Thermal conductivity (λ) | 0.4 | $Wm^{-1}K^{-1}$ |
| Dielectric constant ($\varepsilon_r$) | 2.3 | |
| $\alpha$ - constant ($\alpha = \alpha_x - \alpha_\varepsilon$) | 5 x $10^{-4}$ | $K^{-1}$ |

# 2.3. Thermal Simulations

## 2.3.1. Equations and conditions

The heat diffusion across the calculation domain was considered as in an infinite semi-plane (the validity of this hypothesis was checked a posteriori).

In this conditions, by taking the case of the rectangular power step applied at the surface at $t = 0$, as shown in Figure 2.2, and assuming that the heated surface is instantly thermalized, the temperature variation at a coordinate *x* from the surface is, at an instant $t > 0$ [157]:

$$\Delta T_1(x,t) = \frac{2w_0}{Z}\frac{te^{\frac{-x^2}{4Dt}}}{\sqrt{\pi t}} - \frac{w_0 x}{\lambda}\left[1 - erf\left(\frac{x}{\sqrt{4Dt}}\right)\right] \qquad \textit{Eq 2.1}$$

where $Z = \sqrt{M_v C_p \lambda}$ , with $M_v$ the volume mass of the sample, $C_p$ its specific heat , λ its thermal conductivity and *D* its thermal diffusivity. The quantity $w_0 = q_0/t_{pulse}$ $[W/m^2]$ is the surface power density, with $q_0 = Q/S$ $[J/m^2]$ the energy per surface unit. Obviously, $S = (\pi \Phi^2)/4$ $[m^2]$, where $\Phi$ is the diameter of the electrode.

By applying the same heat step at a time $t_{pulse}$ (Figure 2.2), the temperature variation of the sample reads [157]:

$$\Delta T_2(x,t) = \frac{2w_0}{Z}\frac{(t-t_{pulse})e^{\frac{-x^2}{4D(t-t_{pulse})}}}{\sqrt{\pi(t-t_{pulse})}} - \frac{w_0 x}{\lambda}\left[1 - erf\left(\frac{x}{\sqrt{4D(t-t_{pulse})}}\right)\right] \qquad Eq\ 2.2$$

The variation of the temperature inside the sample generated by a heat pulse of duration $t_{pulse}$ (which corresponds to the hatched surface from the figure below and which is the thermal stimulus in the case of a thermal pulse voltage response) can be calculated as the difference of the two previous quantities (*i.e.,* by the subtraction of Eq. 2.2 from Eq. 2.1):

$$\Delta T(x,t) = \Delta T_1(x,t) - \Delta T_2(x,t) \qquad Eq\ 2.3$$

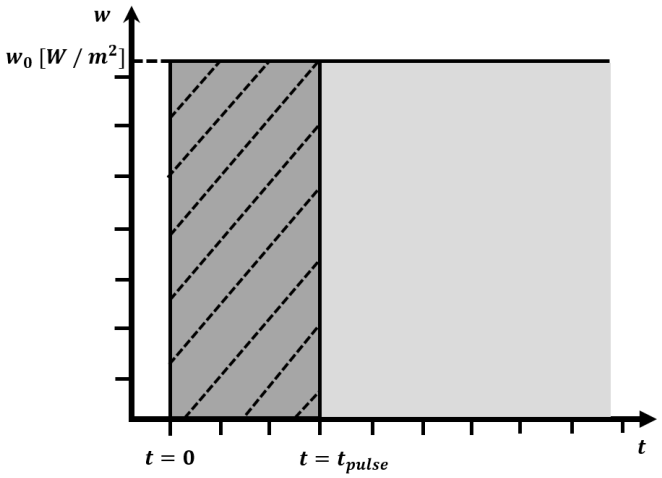


*Figure 2.2 Thermal stimulus considered in the simulations as applied to the surface of the sample*

leading to [166]:

$$\Delta T(x,t) = \frac{2w_0}{Z}\frac{te^{\frac{-x^2}{4Dt}}}{\sqrt{\pi t}} - \frac{w_0 x}{\lambda}\left[1 - erf\left(\frac{x}{\sqrt{4Dt}}\right)\right] - \frac{2w_0}{Z}\frac{(t-t_{pulse})e^{\frac{-x^2}{4D(t-t_{pulse})}}}{\sqrt{\pi(t-t_{pulse})}} + \frac{w_0 x}{\lambda}\left[1 - erf\left(\frac{x}{\sqrt{4D(t-t_{pulse})}}\right)\right] \qquad Eq\ 2.4$$

The derivative of the temperature raise $\Delta T(x,t)$ with respect to time, which is the thermal stimulus in the case of a thermal pulse current response, is then:

$$\frac{\partial \Delta T(x,t)}{\partial t} = \frac{w_0}{Z}\left(\frac{e^{\frac{-x^2}{4Dt}}}{\sqrt{\pi t}} - \frac{e^{\frac{-x^2}{4D(t-t_{pulse})}}}{\sqrt{\pi(t-t_{pulse})}}\right) \qquad Eq\ 2.5$$

The thermal simulations have been performed up to depth coordinates of several dozens of microns, beyond which the temperature variation with time approaches 0. A small additional thickness $x_0 = 0.1\,nm$ has been placed before the sample to account for a thermal interface encountered by the heat before entering the insulator. For the sake of simplicity, $x_0$ is not shown in the following graphical representations (*i.e.*, except otherwise stated, $x = 0$ corresponds in the next figures to the beginning of the insulator, which bears the electric field).

### 2.3.2. Results and analysis

Temperature distributions have been computed for a span of pulse durations going from 5 ns to 0.1 ms, as shown in Table 2.2. The associated energies from the table correspond to values for which the increase of the temperature near the heated surface would not exceed 50 K (corresponding to a maximum temperature of the sample of 70°C, at which LDPE softens, considering an initial temperature of 20 °C).

*Table 2.2 Energies and pulse durations used in the simulations and maximum temperature elevation near the thermally excited electrode. In the greyed areas, the values exceed 50 K*

| ***Pulse energy Q*** | **Maximum temperature rise** | | | | | |
|---|---|---|---|---|---|---|
| | *Pulse duration $t_{pulse}$* | | | | | |
| | *5 ns* | *14 ns* | *150 ns* | *1 µs* | *10 µs* | *0.1 ms* |
| 1 mJ | 10.4 K | 5.65 K | 1.9 K | 0.74 K | 0.23 K | 0.074 K |
| 5 mJ | 52.0 K | 28.25 K | 9.5 K | 3.70 K | 1.15 K | 0.37 K |
| 12 mJ | | | 22.8 K | 8.88 K | 2.76 K | 0.89 K |
| 32 mJ | | | | 23.68 K | 7.36 K | 2.37 K |
| 42 mJ | | | | 31.08 K | 9.66 K | 3.11 K |
| 67 mJ | | | | 49.58 K | 15.41 K | 4.96 K |
| 214 mJ | | | | | 49.22 K | 15.83 K |
| 676 mJ | | | | | | 50.02 K |

An example of spatio-temporal distribution of the temperature, corresponding to a pulse width of 10 µ$s$ and an energy of 214 mJ, is given in Figure 2.3. As it can be seen, the thermal stimulus advances fast in the material, but its amplitude also decreases quickly, so if the neighbourhood of the interface is subjected to temperature variations of several dozens of Kelvin, the regions broadly beyond 30 – 40 µ$m$ are subjected to very small temperature variations. This validates the thermal model of the infinite semi-plane for samples with thicknesses of 50 to 100 µ$m$, but also indicates that the electric field detection sensitivity should be feeble for depth coordinates above the cited values.

Temperature variations with respect to time at several depth coordinates after excitations with long pulses (which flash lamps are able to deliver) are plotted in Figure 2.4 and Figure 2.5. The slope of the plots let recognise the pulse duration, which correspond to the temperature rise time near the interface (the maximum temperature at the interface being reached at the end of the heating time), then the temperature decreases slowly. It comes out that, for a pulse of 0.1 ms, the maximum temperature variation at a depth of 20 µ$m$ is of the order of 10 % of its counterpart of the interface, and less than 3 % of the latter at 50 µ$m$. This indicates that with such pulses a depth of 50 µ$m$ can be reasonably scanned and the first 20 µ$m$ well resolved, provided that the temperature raise and the existing field in the sample are high enough to yield signals measurable by the used instrumentation, with the appropriate dynamics. It is to note that this does not mean that the field existing beyond the 20-50 µ$m$ depths does contribute to a thermal pulse signal, particularly if this field has a high value, but that the distribution in this areas will

be poorly resolved, as a high value of the field will be multiplied by a low value of the stimulus, significantly increasing the difficulty of stabilizing the solutions of the integral equations.

On the other hand, when the duration of the pulse decreases, the temperature variation concentrates more and more in the vicinity of the interface, with higher temperature raises for identical or lower energies (Figure 2.5 and Figure 2.6). This illustrates, as discussed in the bibliographic chapter, that with short pulses it is possible to scan thoroughly the regions near the interface: the shorter the pulse, the closest to the interface the scanned region, and the highest the resolution.

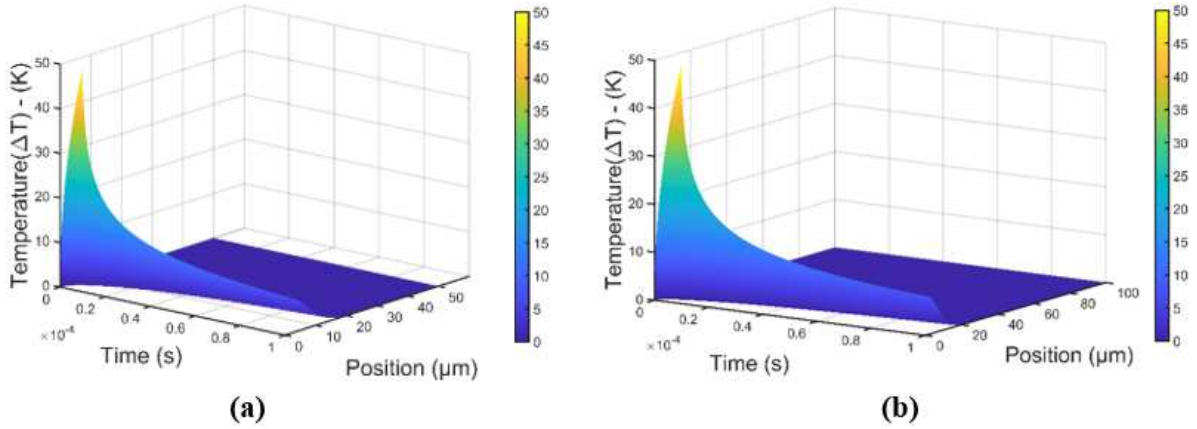


*Figure 2.3 Temperature variation across LDPE samples with respect to time and depth coordinates for Q=214 mJ, $t_{pulse}$=10 μs and $x_o$=0.1 nm: (a) 50 μm-thick insulating sample, (b) 100 μm-thick insulating sample*

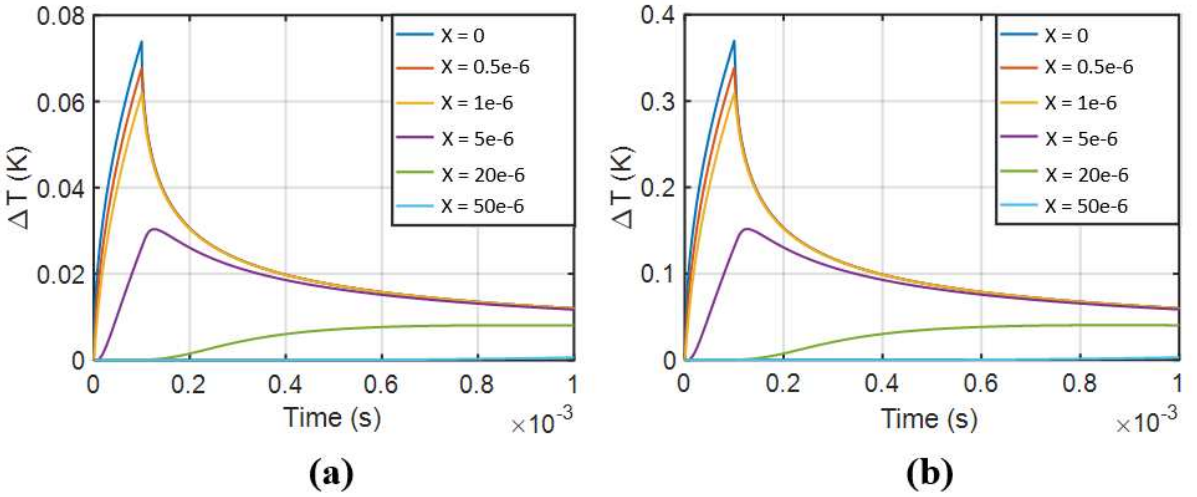


*Figure 2.4 Temperature variation with respect to time at different depth coordinates x from the excited surface for $t_{pulse}$= 0.1 ms: (a) Q = 1 mJ, (b) Q = 5 mJ*

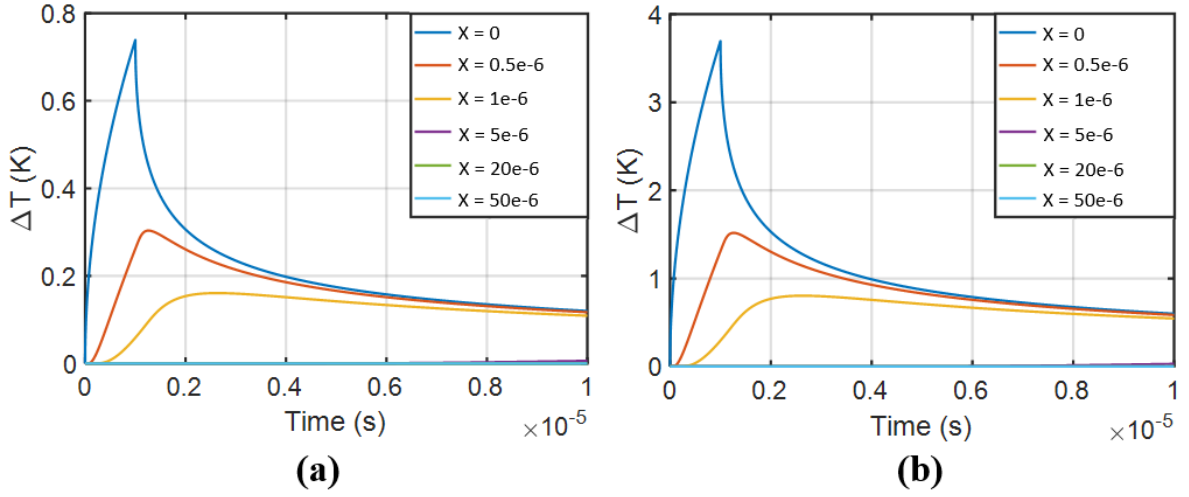


*Figure 2.5 Temperature variation with respect to time at different depth coordinates x from the excited surface for $t_{pulse}$= 1 µs: (a) Q = 1 mJ, (b) Q = 5 mJ*

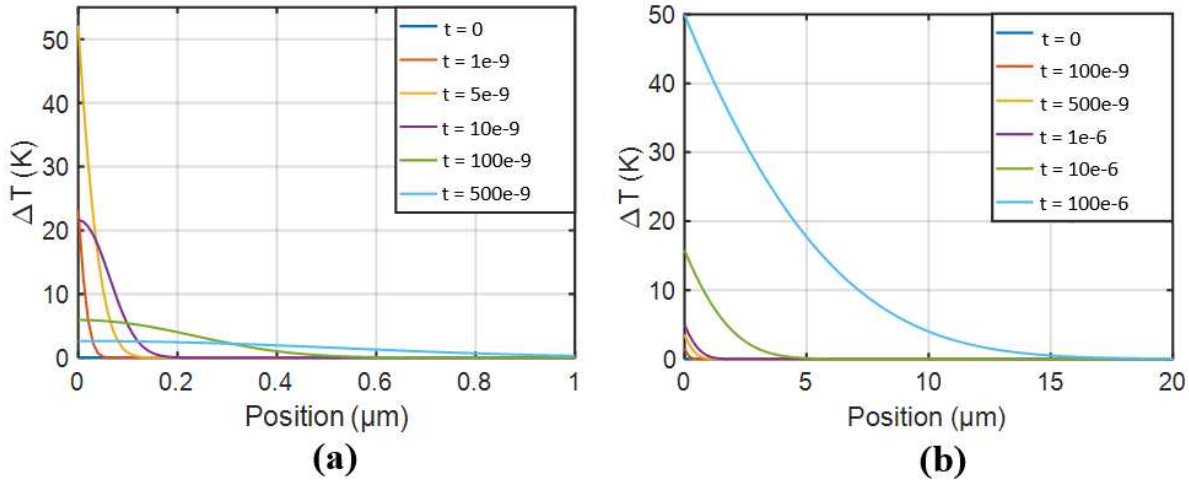


*Figure 2.6 Temperature distribution in the depth at several instants t after the application of the thermal stimulus: (a) Q = 5 mJ, $t_{pulse}$= 5 ns, (b) Q = 676 mJ, $t_{pulse}$= 0.1 ms*

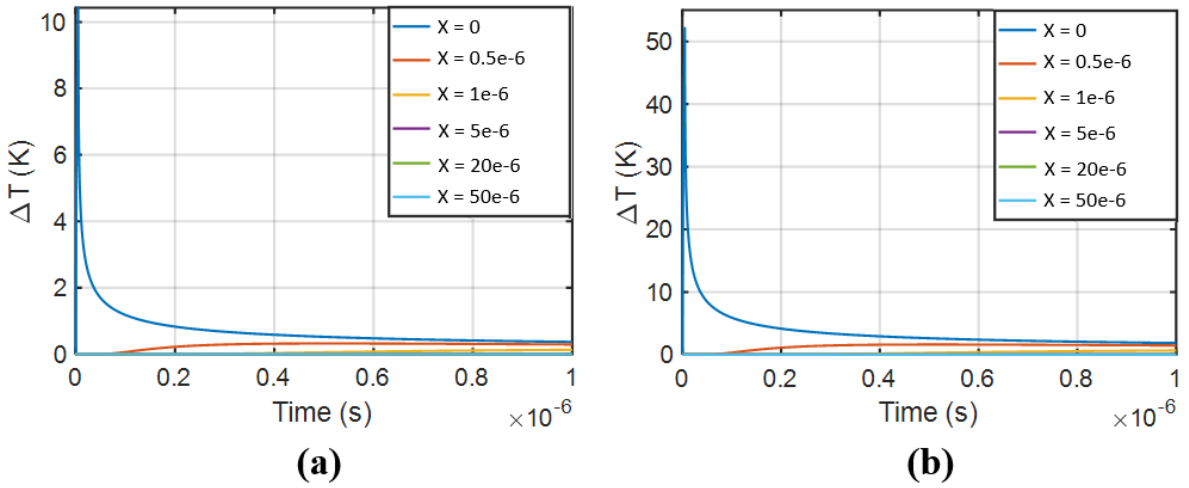


*Figure 2.7 Temperature variation with respect to time at different depth coordinates x for $t_{pulse}$=5 ns and: (a) Q = 1 mJ, (b) Q = 5 mJ*

Thus, if an energy of 1 to 5 mJ is absorbed by the surface on a duration of 5 ns (excitation which can be easily supplied by using, for instance, a nanosecond laser), a temperature raise of 10 K to 50 K can be achieved near the interface (Figure 2.6 (a) and Figure 2.7). In this cases, the well resolved depth would not exceed 2 µm in polyethylene, as the thermal stimulus decreases of more than 95 % beyond the micron. If lower energies are absorbed (ex. 0.1 mJ - Figure 2.8), the temperature increase may fall below 1 K, and the depth contributing in a major manner to the thermal pulse signal would be of the order of 1 µm.

These results are clearly in accordance with the studies indicating that submicronic resolutions can be achievable with thermal methods. In order for such measurements to have a physical meaning, the degree of homogeneity of the material must be higher than the targeted resolution. Materials for electrical engineering applications are mostly homogenous at the micron level, so going beyond this limit requires adequate samples.

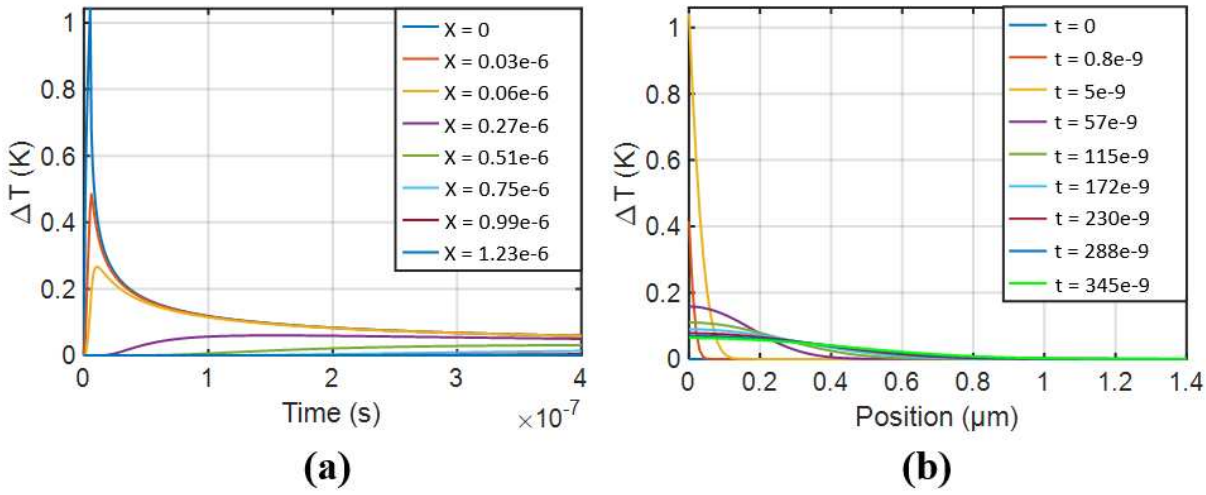


*Figure 2.8 Temperature variation for $t_{pulse}$=5 ns and Q=0.1 mJ:*
*(a) at different depth coordinates x with respect to time, (b) across the sample at different moments t*

It is also to note that the temperature increase of 50 K, which has been considered above as a limit not to be exceeded, has been set with respect to the thermal behaviour of a polymeric material like polyethylene. However, reaching a temperature as high as 70 °C may result in charge detrapping, with respect to the trap depths, so in reality detrapping and dipolar disorientation in the studied material must be carefully considered when applying high thermal stimuli.

To summarize, the presented results show that the interface of a polyethylene sample can in principle be scanned at the micron level with nanosecond heat pulses, while pulses of longer durations (above 10 µs) allow depth scans up to several dozens of µm, provided that the temperature raise and the values of the field in the sample are high enough to give birth to measurable signals. This aspect is addressed in the following section.

# 2.4. Electrical Simulations

## 2.4.1. Equations and parameters

Transient electrical responses issued by a sample of thickness *d*, of constant permittivity $\varepsilon$ and containing an electric field $E(x)$, when submitted to a heat pulse on one of its faces, have been calculated by considering that the sample possesses, at a depth $x_i$ from the heated face (electrode), a zone of thickness *dx* containing a volume charge density $\rho$ $[C/m^3]$ (Figure 2.9). The presence of this space charge induces at electrodes influence charges, namely $Q_{i1}$ and $Q_{i2}$ (Figure 2.10). If the quantity *dx* is very small, the space charge placed at $x_i$, of value $Q_i = \rho S dx$ is very slim, and the influence charge $Q_{i1}$ can be calculated in short circuit conditions from Eq. 1.36, where $\varepsilon(u) = \varepsilon$, $U = 0$, $x = x_i$ and $L = d$:

$$Q_{i1} = -Q_i \frac{d - x_i}{d} \qquad Eq\ 2.6$$

The second influence charge $Q_{i2}$ is then:

$$Q_{i2} = -Q_i \frac{x_i}{d} \qquad Eq\ 2.7$$

The application of Gauss's theorem gives the field on both sides of the space charge:

$$E_1(x) = \frac{Q_{i1}}{\varepsilon S}\ for\ x \in [0, x_i) \qquad Eq\ 2.8$$

$$E_2(x) = -\frac{Q_{i2}}{\varepsilon S}\ for\ x \in (x_i + dx, d] \qquad Eq\ 2.9$$

Examples of field distributions induced by a charge placed at different positions $x_i$ between the electrodes are given in Figure 2.11. These distributions were used to simulate thermal pulse signals. The value of the space charge ($\rho = 123\ C/m^3$, $dx = 1\ \mu m, i.e.\ Q_i = 0.24\ \mu C$) has been chosen to yield electric fields in the range of several kV/mm, which is the order of magnitude one would like to detect in practice.

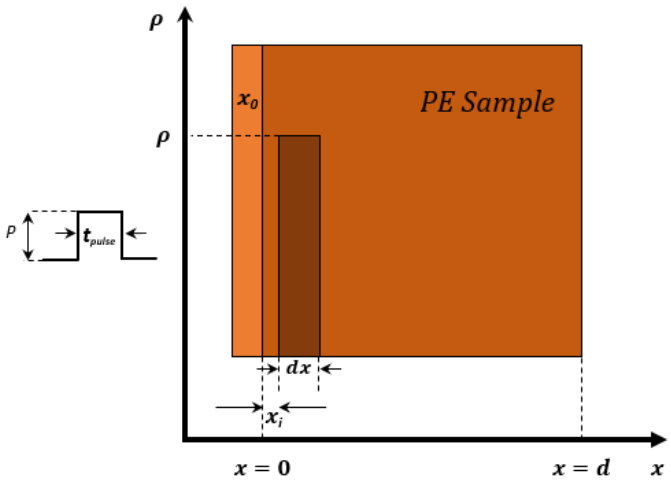


*Figure 2.9 Diagram of the sample with respect to the charge position*

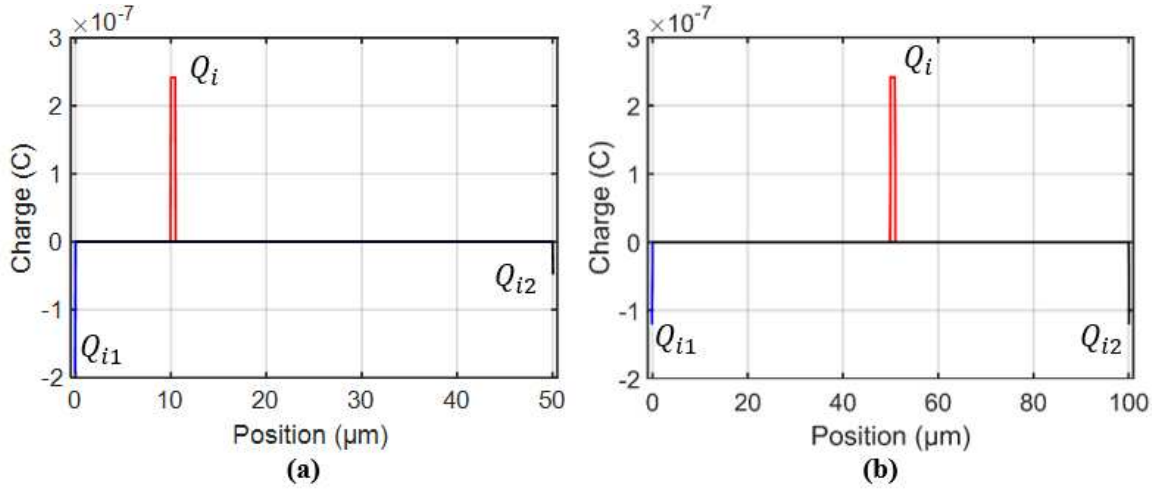


*Figure 2.10 Examples of charges $Q_i$ placed in the sample at the depth $x_i$ and of influence charges $Q_{i1}$ and $Q_{i2}$ at electrodes: (a) $x_i$=10 µm, 50 µm-thick insulating sample, (b) $x_i$=50 µm, 100 µm-thick insulating sample*

To simulate transient thermal pulse signals, it was considered that the thermal excitation is applied on the left side of the sample, before the thickness $x_0$ which correspond to the thermal interface (or to the electrode thickness, when considered, *i.e.* when semicon electrodes are present; otherwise, $x_0 = 0.1\ nm$). The electric field on $x_0$ is obviously nil. In all the graphical representations of the field and charge distributions, $x = 0$ is considered to be the beginning of the insulating (field-containing) region and $x_0$ is not shown. However, the temperature in the sample was calculated by taking into account that the heat pulse has been applied at a distance $x_0$ from the field-containing thickness, as for the temperature simulations from the previous section.

Thermal step responses were computed both in current and voltage mode. After calculating the temperature distribution in the sample as shown in the previous section, the current signals were calculated with Eq. 1.49 and the voltage signals with Eq. 1.57, by considering electric field distributions from the panel presented in Figure 2.11.

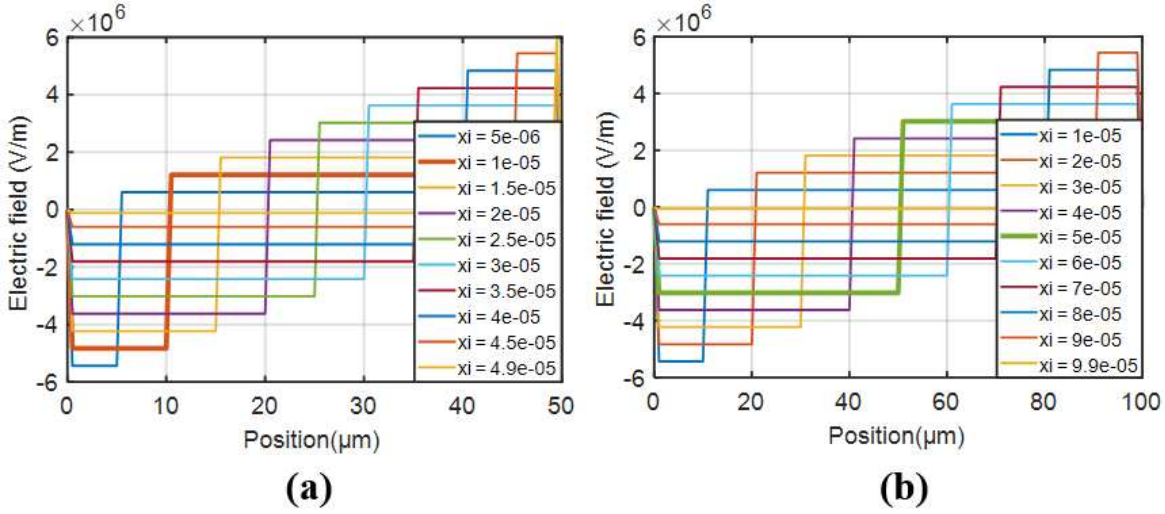


*Figure 2.11 Electric field values and distributions induced by the charge $Q_i$ placed at different positions $x_i$ with respect to the left electrode (x=0): (a) 50 µm-thick insulating sample, (b) 100 µm-thick insulating sample*
*The bold curves correspond to the charge positions from Figure 2.10.*

## 2.4.2.Results and analysis

Simulations of transient currents induced by thermally excited a 50 µm-thick sample with electrodes of quasi-nil thickness ($x_0$ = 0.1 nm) are presented in the following figures. For very short pulses (5 ns) of energies of 1 to 5 mJ, which induce temperature raises at the interface of 10 K to 50 K, current signals with amplitudes of microamperes to dozens of microamperes are obtained for the assumed fields of the order of several kV/mm. The amplitude of the signal depends of course on the position of the space charge: it decreases when the charge position moves toward the counter electrode, as the electric field encountered by the thermal wave at its strongest amplitude decreases, and the zone of higher field, placed at the end of sample, is subjected to a low or nil thermal excitation; but even when the space charge is close to the counter electrode, the current response is still high.

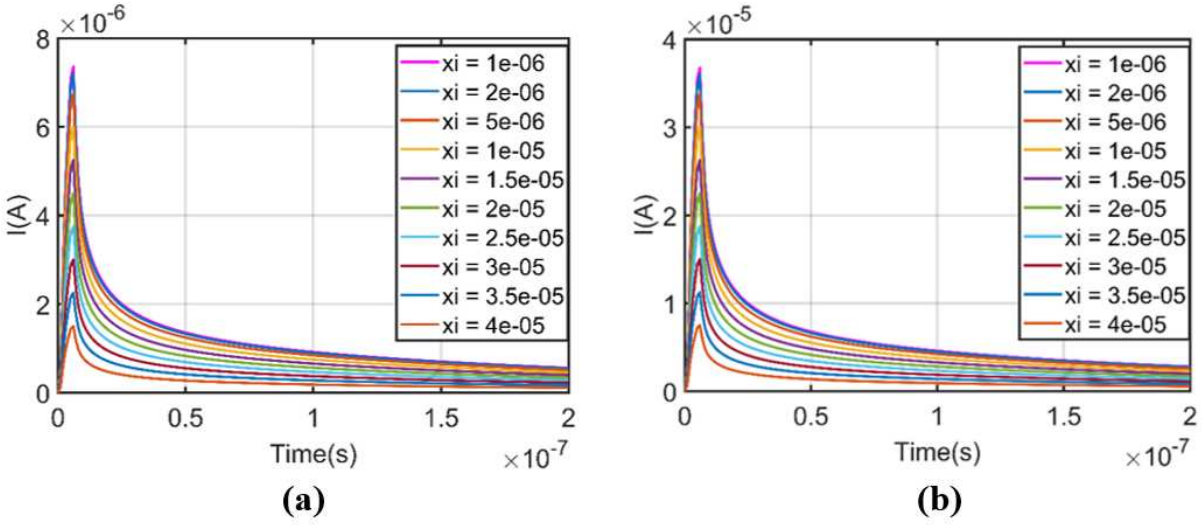


*Figure 2.12 Simulated thermal pulse current responses in a 50µm-thick sample for $t_{pulse}$=5 ns: (a) Q=1 mJ, (b) Q=5 mJ*

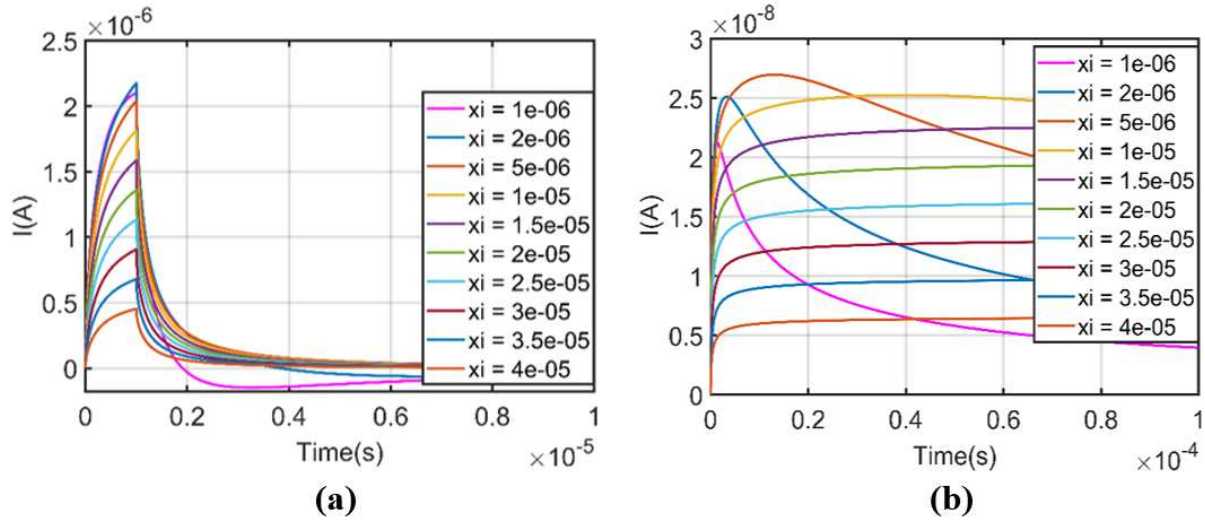


*Figure 2.13 Simulated thermal pulse current responses in a 50µm-thick sample for Q = 5 mJ and: (a) $t_{pulse}$ = 1 µs, (b) $t_{pulse}$ = 0.1 ms*

Measuring signals with such values is not a problem for the current amplifiers available today on the market, but, as the bandpass of most transimpedance amplifiers do not exceed 20 MHz for a gain of $10^5$ and several MHz at the most for higher gains, attention should be paid to the short-pulse current signals, which possess high dynamics and short durations. Longer pulses increase the duration of the transient signal, thus working around this problem (Figure 2.13). If the pulse energy is also increased, the amplitude of the current signal can be kept above the dozens of microamperes. For instance, passing from 5 mJ to 32 mJ of absorbed energy during 1 µs would raise the maximum temperature increase in the sample by a factor of 6.4 (*i.e.*, from 3.7 to 23.7 K, Table 2.2). The current amplitude would increase by the same factor, *i.e.* to almost 15 µA with respect to the value from Figure 2.13, with a temperature raise not affecting the electrical state of the sample. However, this is made on the expense of the resolution, which decreases when the pulse width increases.

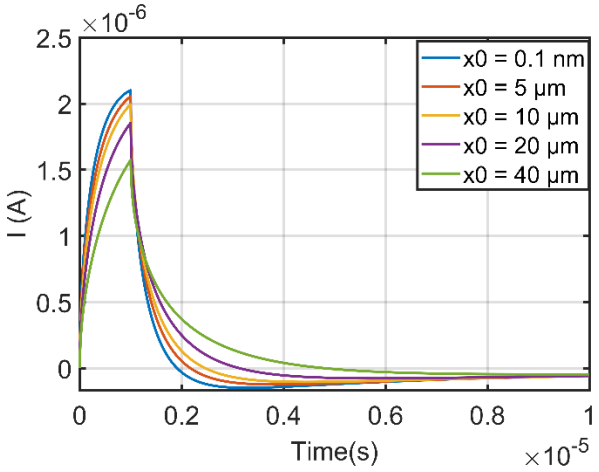


*Figure 2.14 Influence of the semicon electrode thickness $x_0$ on the thermal pulse current response for a 50 µm-thick sample when the charge is placed at the interface ($x_i$=0), $t_{pulse}$ = 1 µs and Q = 5 mJ*

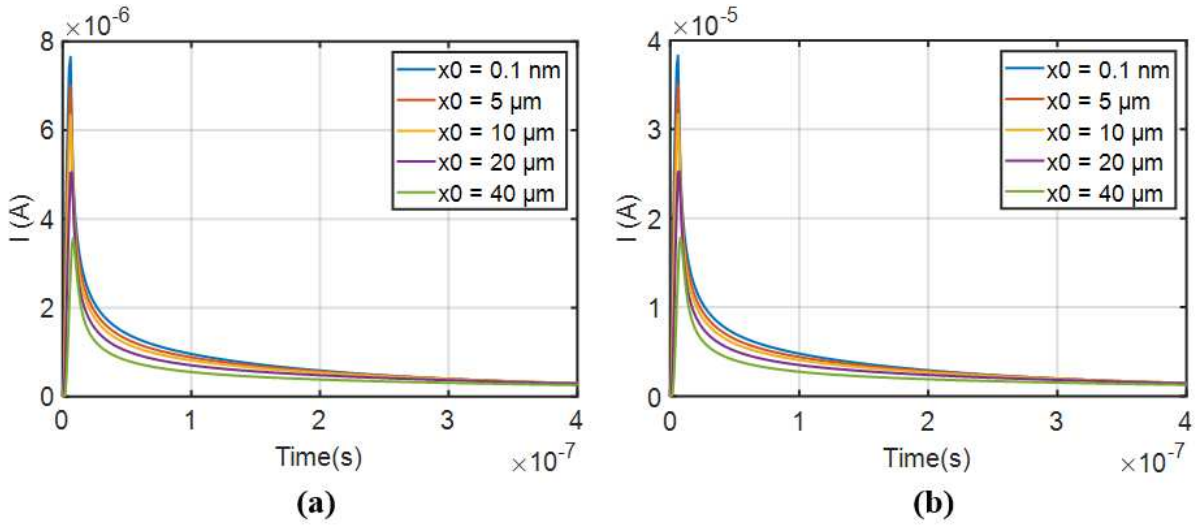


*Figure 2.15 Influence of the semicon electrode thickness $x_0$ on the thermal pulse current response for a 50 µm-thick sample when the charge is placed at the interface ($x_i$=0), $t_{pulse}$=5 ns and: (a) Q = 1 mJ, (b) Q = 5 mJ*

When a semicon electrode of thickness up to 40 µm is present, the current amplitude obviously decreases (Figure 2.14 - Figure 2.15). The decrease is more important for shorter (Figure 2.15) than for longer ones (Figure 2.14). However, even for a semicon thickness of 40 µm, the signal stays in the same order of magnitude as the one corresponding to a sample with a semicon electrode of 0.1 nm. The current response is thus still measurable (even with temperature variations well below 1 K (Figure 2.5 (b) corresponding to the thermal stimulus used for calculating the current from Figure 2.14)), and should allow to determine the semicon/insulator interface field, particularly if pulses of durations greater than 1 µs are used in these conditions.

It is to note that this analysis also holds for 100-µm thick samples, as the main result of doubling the sample thickness is the division by two of its capacitance and, consequently, of the current amplitude (Eq 1.57), without affecting its dynamics, considering the pulse durations. In contrast, voltage responses are not proportional to the capacitance of the sample (Eq 1.56), so a voltage signal would be the same whatever the sample thickness, provided that the thermally scanned zone is the same in terms of field and thermal properties (which is the case here). (Whether the real signals are voltage of current signals will depend on the signal duration, the amplifier and the measuring circuit). Simulated voltage signals are presented in the following figures.

Figure 2.16 - Figure 2.17 herein after show that, even for low energy pulses (1 mJ), voltage amplitudes higher than the millivolt are to be expected. This is particularly interesting as, for measuring such amplitudes, gains of $10^3$ to $10^4$, for which the dynamics of the illustrated signals are less a problem, are sufficient. Indeed, state-of-the-art instrumentation amplifier provide, at such gains, bandwidths higher than 80 MHz [167], which are suitable for measuring signals from Figure 2.16 - Figure 2.19. Considering the performance of such devices, even signals with comparable dynamics but lower than those presented here (for example, issued by the application of lower thermal stimuli) should be measurable and processable.

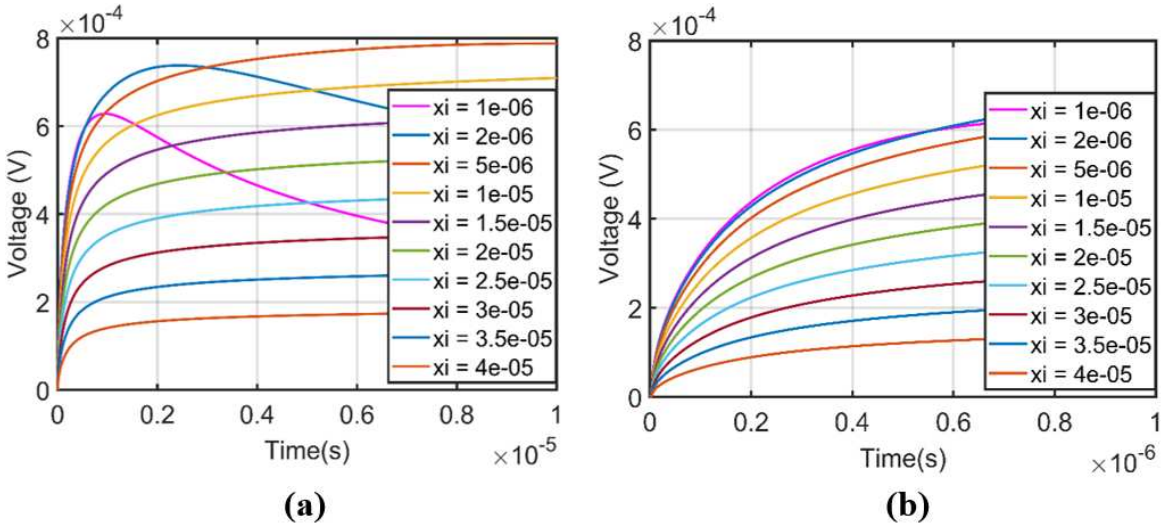


*Figure 2.16 Simulated thermal pulse voltage response for Q=1 mJ and $t_{pulse}$=5 ns and zoom in area of the first microsecond*

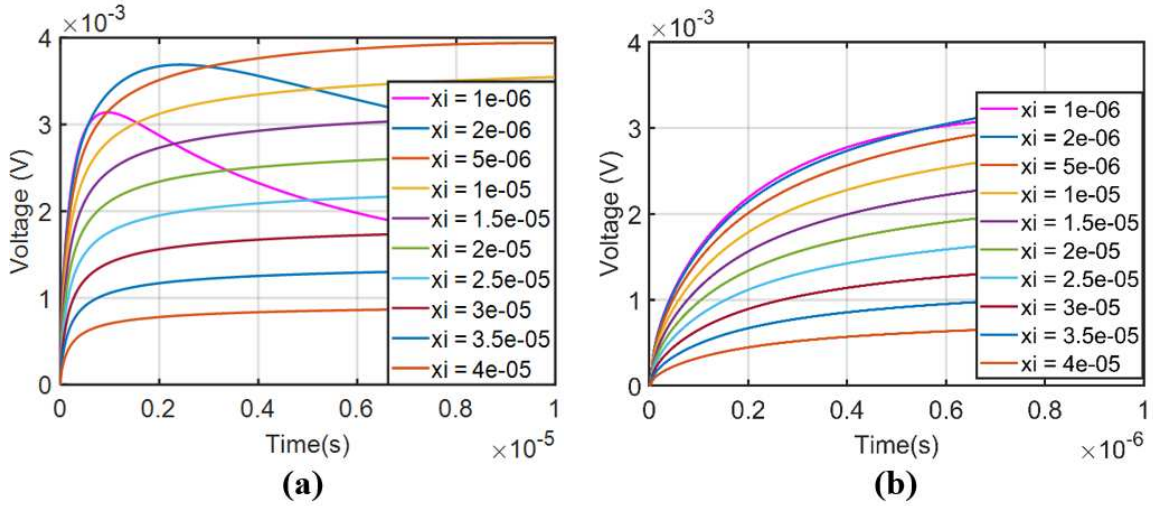


*Figure 2.17 Simulated thermal pulse voltage response for Q = 5 mJ, $t_{pulse}$=5 ns and zoom in the area of the first microsecond*

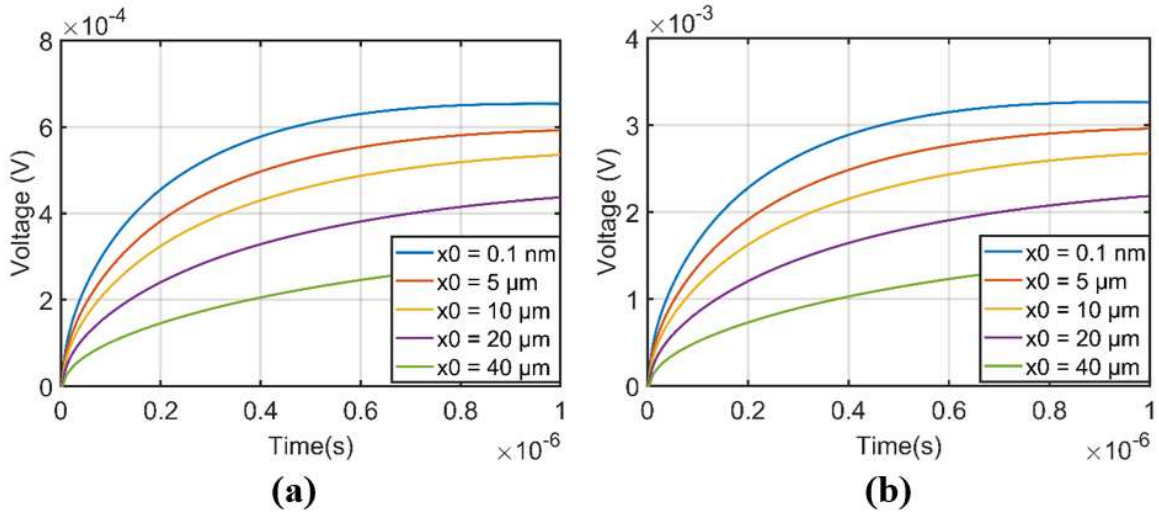


*Figure 2.18 Influence of the semicon electrode thickness $x_0$ on the thermal pulse voltage response for $t_{pulse}$=5 ns and: (a) Q = 1 mJ, (b) Q = 5 mJ*

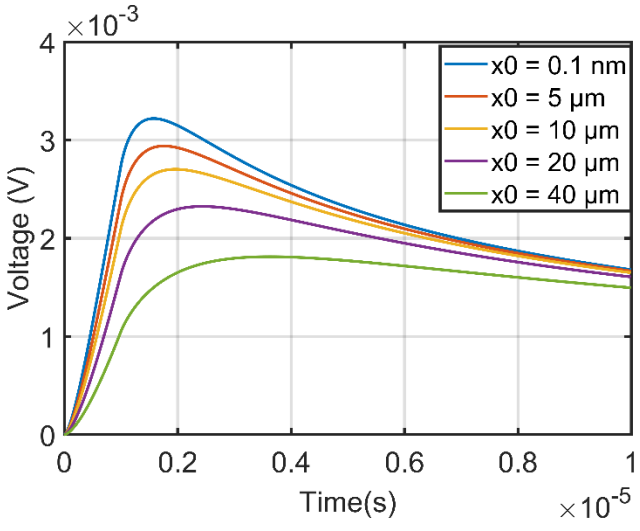


*Figure 2.19 Influence of the semicon electrode thickness $x_0$ on the thermal pulse voltage response when $t_{pulse}$=1 µs and Q=5 mJ*

As far as the thickness of the semicon is concerned, the results from Figure 2.18 - Figure 2.19 lead to the same conclusions as for the current signals analysed previously, *i.e.* the electric field at the semicon/insulator interface may be reachable, provided that enough energy is absorbed by the sample.

Finally, it is to note that much more in-depth analysis can be made using the presented thermal and electrical modelling (or by expanding it to take into account a gaussian form of the stimulus, as proposed, for instance, in [166] and in many other publications), but we have limited our study to the essentials required by the objective of the thesis.

## 2.5. Conclusions

Thermal and electrical simulations concerning polyethylene samples of thicknesses of several dozens of microns excited with heat pulses of different energies (0.1 mJ to several hundreds of mJ) and durations (5 ns to 0.1 ms) have been presented in this chapter.

The thermal simulations allowed to approach the temperature raises and distributions in the samples with the applied thermal stimuli. They have shown that temperature increases of several degrees to several dozens of degrees can be generated with such excitations, with respect to the energy absorbed by the sample and to the pulse duration. It came out that, in the studied conditions, the penetration depth of the heat stimulus allowing to expect reasonably accurate resolutive results is in the range of one micron to several dozens of microns.

The electrical simulations put into focus that fields in the kV/mm range should induce transient electrical responses measurable with state-of-the-art instrumentation, particularly in voltage mode, where amplitudes of the millivolt order and above can be expected. This strongly suggest that direct measurements of the electric field at the interface of the considered samples are at reach, even for thermal excitations with energies below the milli joule. An experimental setup, the obtained results and their analysis are the subject of the following chapter.

# Chapter 3:
# Experimental Results

# 3.1. Introduction

After having presented simulations supporting the feasibility of space charge measurements with thermal pulses on medium thickness samples, the present chapter is dedicated to the experimental work done on such samples to simultaneously measure the surface temperature and the space charge signal in order to assess the interface fields.

First, the samples and the associated electrodes, which served both as temperature sensors and as contacts for the space charge signal, are presented. The measurement cell and the acquisition circuit are then described and examples of acquired signals are illustrated and discussed. The procedure set up for decoupling charge and temperature responses from the primary signals is presented, followed by a qualitative analysis aimed to underline, in particular, the responses of the interfaces.

The last part of the chapter is concerned with a detailed analysis of the measured signals, by considering the entire acquisition chain, allowing to determine the temperature distribution across the samples and the amplitude of the interface fields.

# 3.2. Samples

## 3.2.1. Materials, structures and dimensions

In order to be as close as possible to the structure of insulators used in power cables by keeping the thickness as low as possible, the experimental work was made on 50, 100 and 160 µm-thick polyethylene samples. The structure of the samples is presented in the diagrams from Figure 3.2 and Figure 3.1.

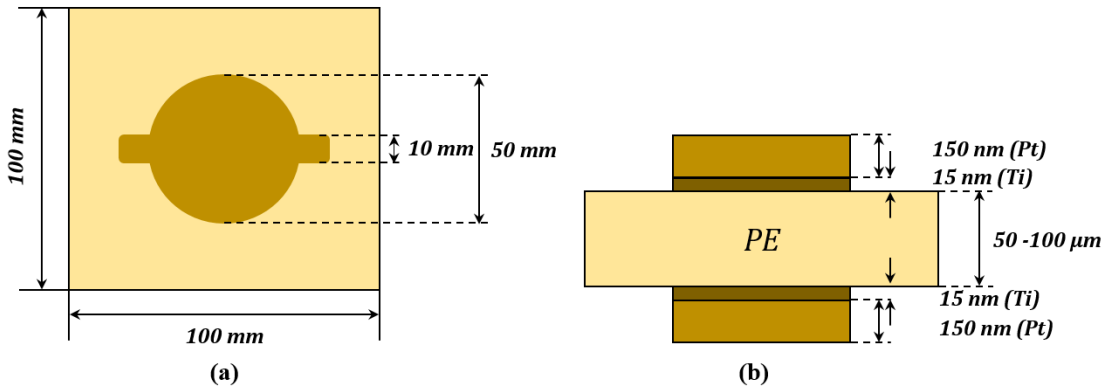


*Figure 3.1 Structure of the Pt-coated LDPE samples*

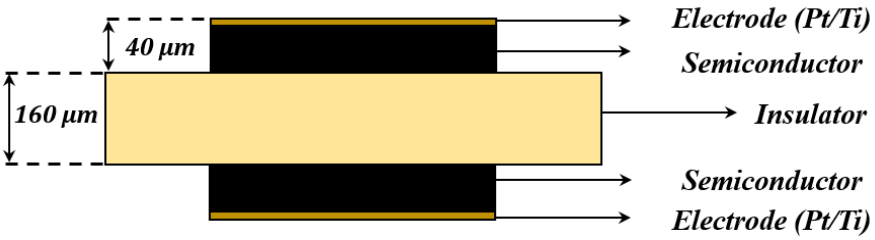


*Figure 3.2 Structure of the carbon-black XLPE samples with Pt layers for the surface temperature measurements*

As the experimental work was made by using a Nd:YAG laser operating at 1064 nm, it is preferable that the electrode material is as much absorbent as possible at this wavelength. Fig. 3.3 shows the wavelength dependence of reflectivity of several materials. It comes out that platinum (Pt) has, in the concerned wavelength range, the lower reflectivity with respect to other metals that could be considered for the electrode manufacturing, such as Ag, Au or Al.

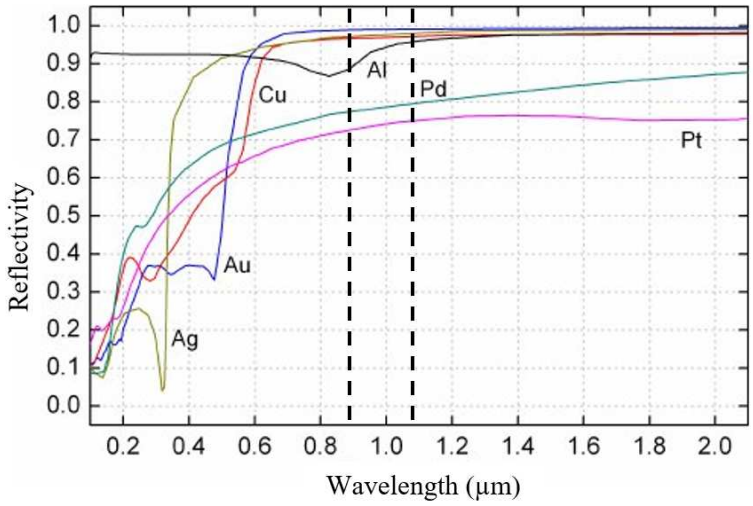


*Figure 3.3 Reflectivity versus wavelength of various typical metals at normal incidence (Φ=0) [168]*

On the other hand, the electrodes must also serve as temperature sensors. Pt is a widely used metal for manufacturing temperature sensors, particularly because it exhibits an almost linear temperature / resistivity dependence. Its coefficient of variation of the resistivity with temperature ($3.92 * 10^{-3} K^{-1}$) is high enough to obtain measurable variation of the resistance, even for low temperature changes. It is also chosen for its stability over time and its resistance to oxidation. For all these reasons, Pt has been chosen as the material to be used for the electrodes.

The 50 µm and the 100 µm-thick samples were commercially available Low Density Polyethylene (LDPE) 100 mm-wide square films purchased from GoodFellow. On each side, they have been coated with metallic electrodes in form of discs of 50 mm in diameter provided with 10 mm x 10 mm extensions to allow additional contacts in order to measure the variation of the electrode resistance during the experiment. As this variation is proportional to the temperature raise, *i.e.* $\Delta R_e(t) = R_e \alpha \Delta T(t)$ (where $R_e$ is the initial value of the electrode

resistance, $\Delta R_e$ its variation with the temperature variation $\Delta T$ and $\alpha$ the coefficient of variation of the electrode material with temperature), the temperature variation $\Delta T(t)$ during the experiment can be extracted directly from the data $\Delta R_e(t)$. A direct measurement of the surface temperature can therefore be obtained, allowing to determine precisely the temperature distribution across the sample $\Delta T(x, t)$ without the need of knowing the exact form and energy of the thermal excitation and, above all, the real absorbance of the electrode, which is very difficult to estimate. Such an improvement of the knowledge of the thermal stimulus allows to significantly increase the confidence in estimating the field in the sample, which is one of the contributions of this work.

The 160 µm samples were 100 mm – wide discs made of cross linked polyethylene (XLPE) co-molded with a carbon black semi-conducting compound, of the same composition as those of HVDC cables. The thickness of the semi-conductor compound (commonly called "semicon") was 40 µm.

The Pt electrodes have been deposited on both sides of the LDPE samples (directly on the insulator) and on the XLPE samples provided with carbon-black electrodes, on top of these semiconducting layers, in order to monitor the surface temperature.

### 3.2.2. Electrodes / Temperature sensors

There are different types of deposition technologies available on the market, such as magnetron sputtering, thermal evaporation, atomic layer deposition, electron beam evaporation etc. Electrode deposition was made by electron beam evaporation, which was found to be the most appropriate after comparisons with sputtering.

Electron beam (e-beam) evaporation is time-tested deposition method for generating dense, and coating high purity. A current is initially transmitted through a tungsten filament during an e-beam evaporation process, causing Joule heating and electron emission. Figure 3.4 (a) illustrates the schematic diagram and Figure 3.4 (b) represents the e-beam chamber. To speed the freed electrons towards the crucible containing the material to be deposited, a high voltage is provided between the filament and earth. A high magnetic field concentrates the electrons into a unified beam and, upon arrival, the energy of this electron beam is transmitted to the deposition material, enabling it to evaporate and deposit onto the substrate. During evaporation, a partial pressure of a reactive gas, such as oxygen or nitrogen, can be added to the chamber to reactively deposit non-metallic layers.

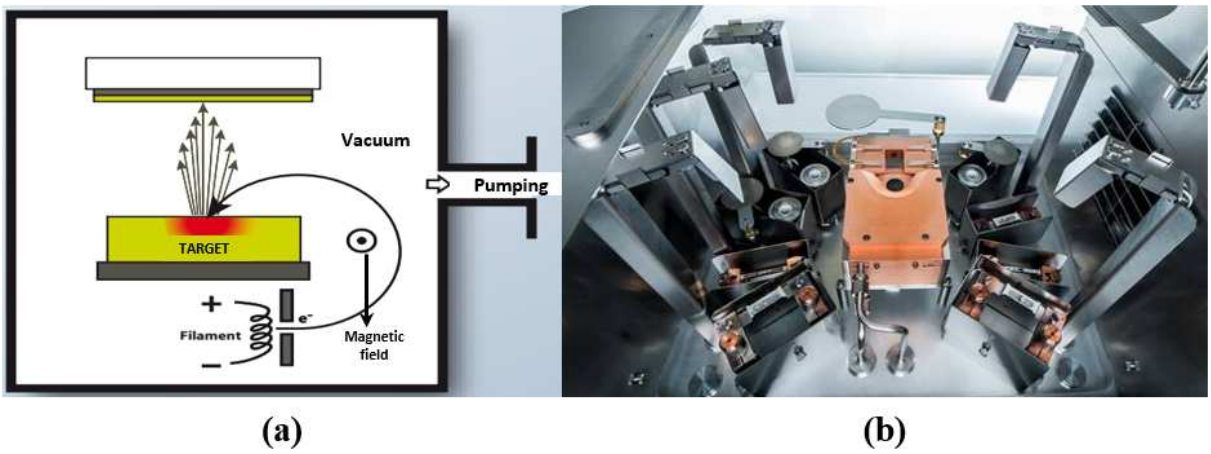


*Figure 3.4 (a) Diagram of the e-beam evaporation process, (b) E-beam thermal evaporator chamber*

There are several advantages of the e-beam evaporation technique over other methods. When compared to the sputtering technique, one can control the temperature that is applied to the sample, which is very important for very thin samples of the order of the μm. The e-beam source can heat materials to significantly greater temperatures than a resistive boat or crucible heater can. This enables extremely fast deposition and evaporation of high-temperature materials and refractory metals like tungsten, tantalum and graphite when compared to sputtering or resistive thermal evaporation. Water cooling of the crucible closely restricts the electron beam heating to the region inhabited by the source material, preventing any undesirable contamination from neighbouring components. Films produced by electron beam evaporation can better retain the purity of the source material. The e-beam evaporation device used in our case was an Oerlikon Univex 350, which can deposit metals such as Au, Pt, Pd, Ti, Cr.

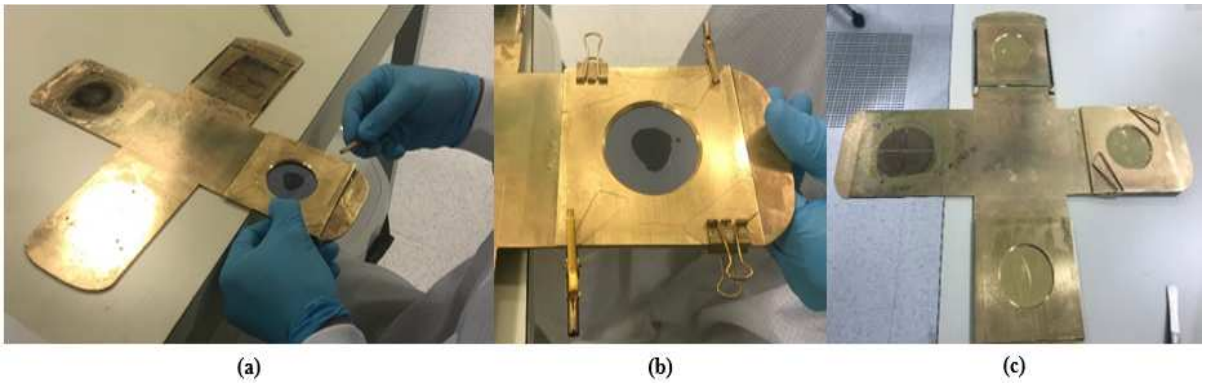


*Figure 3.5 Steps taken to make the electrode deposition*

The preparation of the samples was made in the following way:

- The sample is cleaned with ethanol. The use of solvents like acetone was avoided because they might change the properties of the sample.
- Silicon wafers are placed on the plate of the depositing device and oil is applied on the silicon wafer. The oil is specifically applied on the area where the deposition of the electrode will be made, as shown in the Figure 3.5.

- The sample is placed on the silicon wafer, then the mask with the shape of the electrode is placed on the sample and clipped on both ends.
- Once the sample has been clipped on the plate, it is placed inside the depositing device.
- A secondary vacuum is made in the deposition chamber (several hours).
- After the pumping process, an electrode is deposited on one face of the sample. Once the electrode deposition completed, the sample is removed from the chamber, returned and cleaned with alcohol, then the same procedure is followed in order to deposit an electrode on the other face of the sample.

The use of oil (Fomblin 701) was needed to avoid overheating of the samples, which may occur when they are in contact with the sample holder.

Before deposing the Pt layer, which has a thickness of 150 nm, in order to obtain an homogeneous layer with respect to the possibilities of the deposition device, a titanium (Ti) 15nm-thick layer was deposited directly on the sample to provide good adhesion.

This procedure allowed to obtain uniform Pt electrodes with resistances of several dozens of ohms. The electrodes are extremely thin and considerably more thermally diffusive than the rest of the sample. By taking into account the thermal conductivity of Pt ($\lambda_{Pt} = 72\ W/mK$), its density ($\rho_{Pt} = 21450\ kg/m^3$), its specific heat ($Cp_{Pt} = 133\ J/kgK$) and the thickness of the Pt layer ($e$ =150 nm), the time thermal constant of an electrode is:

$$\tau_{th} = \frac{1}{\lambda_{Pt}} \rho_{Pt} e^2 Cp_{Pt} = 8.91 * 10^{-10} s \cong 1\ ns$$

which is low enough to consider that the heated electrode thermalizes prior to heat actually starting to diffuse inside the insulator, acting as a heat source.

## 3.3. Experimental setup

### 3.3.1. Instrumental chain and measurement cell

The experimental setup used for generating the thermal pulse, holding the sample and acquiring the temperature and charge signals is shown in Figure 3.6.

The thermal pulses are delivered by a 1064 nm, 5 ns, 400 mJ Nd: YAG laser. The laser beam is deflected to the measurement cell by a non-completely opaque mirror, behind which is placed a photo diode which allows to detect the moment when the laser beam comes out from the laser. A beam expander and a concave lens are placed in front of the measurement cell, allowing to expand the 8 mm-wide laser beam to the diameter of the electrode of the sample. The sample is placed in the measurement cell, specially designed and manufactured for the experiments (Figure 3.7).

The body of the measurement cell is a cylindrical box made of aluminum to allow electromagnetic shielding. An opening of a diameter equal to the one of the electrode is made on one of the cell basis to allow the laser beam to light the electrode. The sample rests on an

insulating plate on which the necessary contact system is made and which contains the components needed to reduce the noise and to decouple the high frequency signals generated by the thermal excitation from the low frequency components and to allow measuring the temperature and the charge signals.

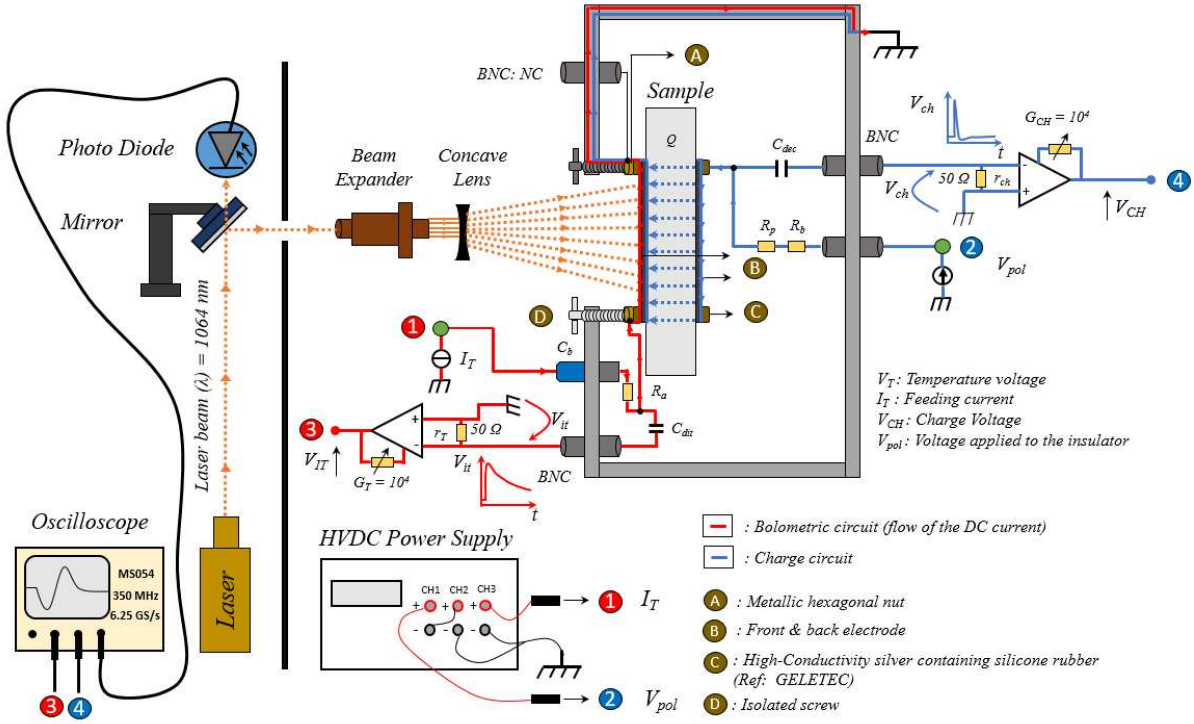


*Figure 3.6 Schematic diagram of the experimental setup using TPM*

The connections to the electrode are made through 500 µm-thick high-conductivity silver-containing silicone rubber pads, as shown in Figure 3.7. Such pads are placed both on the front and back faces of the sample to provide good connections with the measurement circuit. In Figure 3.7 (b), we can see the inside part of the test cell, where we can observe the hexagonal nut which will be eventually in contact with the pads placed between the sample and the nut. The external part of the test cell is connected to 2 different amplifiers, one for the temperature measurement on the front face and another one for the charge measurement on the back, as shown in Figure 3.7 (c) and (d).

The used amplifiers are DHPCA-100 models from Femto. The gain set for the measurements was $10^4$, for which the input impedance is of the device is 50 Ω and its upper cut-off frequency 80 MHz. To preserve the bandwidth and noise performance, the source capacitance was kept as low as possible by using short cables.

A low voltage highly stabilized power supply was used to generate the current $I_T$ fed to the front face electrode (thermally excited electrode), which acts as a sensor for the surface temperature measurement. The voltage drop across the electrode is noted $V_{it}$ before amplification and $V_{IT}$ after amplification. The temperature measurement circuit is coloured in red on Figure 3.6. The sense of $I_T$ can be reverted.

A high voltage low ripple power supply is used to apply an external dc voltage to the sample to make possible both voltage-off and voltage-on bipolar measurements, particularly for calibration reasons. The dc voltage is decoupled at the input of the back face amplifier from the transient (charge) signals. The value of the dc current is limited through protection resistances. The charge measurement circuit is coloured in blue in Figure 3.6.

The outputs of the photodiode and of the two wideband amplifiers are connected to a high-speed oscilloscope [169], which is pre-triggered and allows to measure simultaneously the photo-diode "start" signal, the temperature signal and the charge signal.

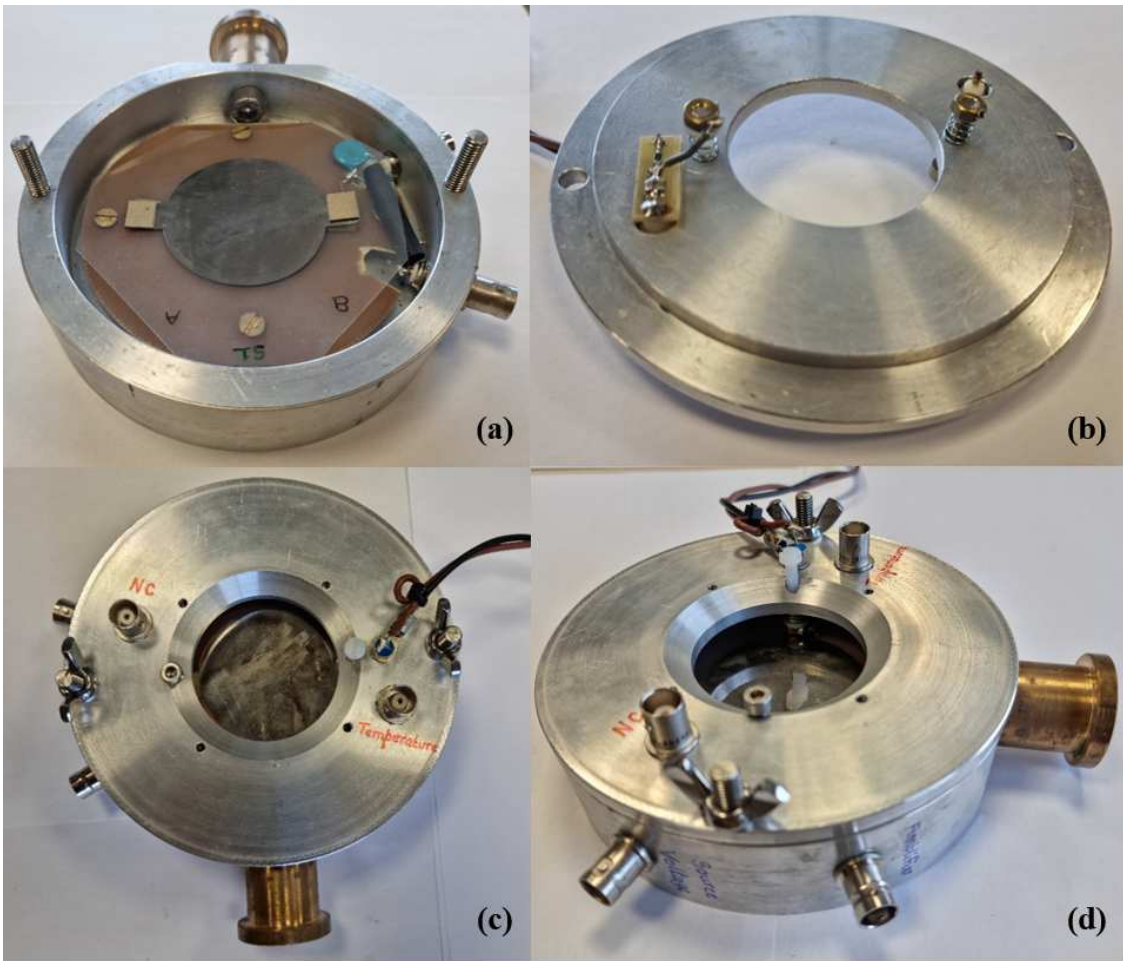


*Figure 3.7 Test cell and details*

## 3.3.2. Conditioning circuit

The equivalent diagram of the temperature measurement circuit is shown in the Figure 3.8. The decoupling capacitor $C_{dit}$ prevents the dc current $I_T$ to be fed to the amplifier, reduces the circuit inductance and low frequency components. Its value of 440 nF has been chosen so the time constant $r_T\ C_{dit}$ (where $r_T$ is the input resistance of the current amplifier) is higher enough than the useful measurement time which is of the order of the µs, *i.e.* $r_T\ C_{dit} = 50\ \Omega * 440\ ns =$

22 µs, so for $t < 22$ µs this capacitor can be considered as short-circuited. $R_a$ is an adaptation resistance, so of value close to that of the electrode resistance ($R_e \cong 30\ \Omega$ to $50\ \Omega$).

As for the temperature measurement circuit, the charge measurement circuit (shown at the upper right part of Figure 3.6) contains a decoupling capacitor $C_{dec}$, which can withstand a voltage up to 2 kV to isolate the input of the measurement amplifier from the dc current of the high voltage source and to eliminate low frequency components. The value of $C_{dec}$ was set to overcome the sample capacitance $C_e$ by an order of magnitude, *i.e.* $C_{dec} = 10\ nF$ as the thinnest sample has a capacitance of 800 pF.

$R_p$ is a dc current limiting protection resistance which should also avoid the HF components to pass through the power supply instead of the amplifier. For $R_p = 1$ MΩ, one has $I_{pol} = V_{pol}/R_p = 1$ mA (dc) for $V_{pol} = 1$ kV, which is much lower than the 25 mA delivered to the temperature circuit.

For a frequency of 100 MHz (of the order of the bandpass), the reactance of the decoupling capacitors reads $1/(\omega C_{dec})_{min} = 0.16\ \Omega$, and for a time of 1 µs ($f_{min} = 1$ MHz) corresponding to the duration of the charge signal, $1/(\omega C_{dec})_{max} = 150\ \Omega$, both values being much lower than the value of $R_p$ (1 MΩ). Therefore, at high frequencies the capacitor $C_{dec}$ short-circuits $R_p$, so the signal "flows" into the charge amplifier.

The time constant $R_p C_e$ would be of 0.8 ms for a 800 pF sample, which means that the capacitor charges in less than 1 ms. The time constant of the measurement is $r_c C_e = 4$ ns for the same value of the sample capacitance, meaning that the rise time of the signal should be greater than this value.

A small resistance $R_b = 1$ kΩ has been added in series with $R_p$ hopefully for reducing noise coming from the power supply, but its use was rather few efficient.

The table below recall the signification of each element from the circuit and its value, as well as the meaning of the indicated voltages and currents from Figure 3.6 and Figure 3.8.

*Table 3.1 Components of the measurement circuit*

| *Component* | *Values* | *Significance* |
|---|---|---|
| $C_e$ | 50 µm : 800 pF | Sample capacitance |
| | 100 µm : 400 pF | |
| | 160 µm : 240 pF | |
| $R_e$ | 30 – 50 Ω | Electrode Resistance |
| $R_a$ | 47 Ω | Adaptation resistance |
| $C_b$ | 10 nF | Anti-noise cylindrical capacitor |
| $R_{pb}$ ($R_p$+ $R_b$) | 1 MΩ + 1 kΩ | Current limitation resistance |
| $C_{dec}$ | 10 nF | Decoupling capacitor for the charge signal |
| $C_{dit}$ | 440 nF | Decoupling capacitor for the temperature signal |
| $r_c$ | 50 Ω | Input resistance of the charge signal amplifier |
| $r_T$ | 50 Ω | Input resistance of the temperature signal amplifier |

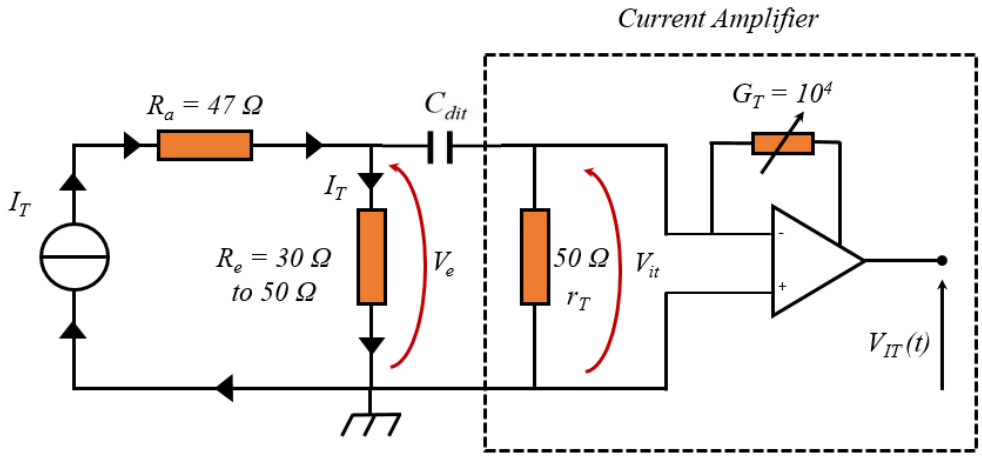


*Figure 3.8 Diagram of the temperature measurement circuit*

*Table 3.2 Significance of notations used for measurements*

| *Notation* | *Significance* |
|---|---|
| $I_T$ | Temperature sensor (front face electrode) feeding current |
| $V_{it}$ | Voltage drops across the front face electrode before amplification |
| $V_{IT}$ | Voltage drops across the front face electrode after amplification |
| $V_{ch}$ | Voltage drops across the sample before amplification (“charge” signal) |
| $V_{CH}$ | Voltage drops across the sample after amplification (“charge” signal) |
| $V_{pol}$ | DC voltage applied across the sample (“polarization” voltage) |
| $G_T$ | Gain of the amplifier of the temperature measurement circuit |
| $G_{ch}$ | Gain of the amplifier of the charge measurement circuit |

### 3.3.3. Measurement protocol

Before any measurement campaign, tests have been performed to quantify the noise level and to exclude the possibility of artefacts. A first test is made without connecting the power supply, a second measurement with connection to the power supply and a third measurement by masking the electrode of the sample from the laser. This allows to fully validate that the subsequent measurement results are generated by the electric field in the sample and are not affected by external phenomena.

A measurement campaign starts in voltage-off conditions ($V_{pol} = 0$) and without any current fed to the electrode ($I_T = 0$). The second step consists in setting ascending positive values for the current fed to the electrode ($I_T > 0$) and, for each value, varying the voltage $V_{pol}$ applied to the sample, starting from 0 V to several hundreds of volts (up to $\pm 1000\ V$), by alternating polarities. Between two polarities, the sample is set at 0 V for several minutes. In a third step, negative values of the electrode feeding current are set ($I_T < 0$), and the procedure described in step two is repeated. This protocol allows, as it will be shown in the next sections, to decouple

temperature and charge signals, which are measured simultaneously, but which inherently act one on the other because of the measurement circuit and conditions. Every recorded signal is the mean of 16 successive measurements, in order to reduce noise.

## 3.4. Primary results

Typical examples of transient voltages $V_{IT}$ measured across an electrode of a sample when thermally excited in volt-off conditions ($V_{pol} = 0$) are shown in Figure 3.9.

Each signal corresponds to the response of the same electrode to which different values of current $I_T$ (between 0 and 25 mA, positive and negative) were fed. As it can be seen, the amplitude of the measured signal increases with the increase of the feeding current, and the polarity of the signal switches with the polarity switch of the feeding current. The increase of the amplitudes of $V_{IT}$ and $I_T$ are almost perfectly proportional (up to several percent), particularly for the lower and middle values of $I_T$. This illustrates well a quasi-linear dependence $V_{IT} = k\Delta R_e I_T$, showing that in this case non-linearities due to the components of the measurement circuit are small. The coefficient $k$ is not necessarily equal to 1; a complete analysis of the circuit is needed to determine it, and the thermoelectric effect must also be eliminated.

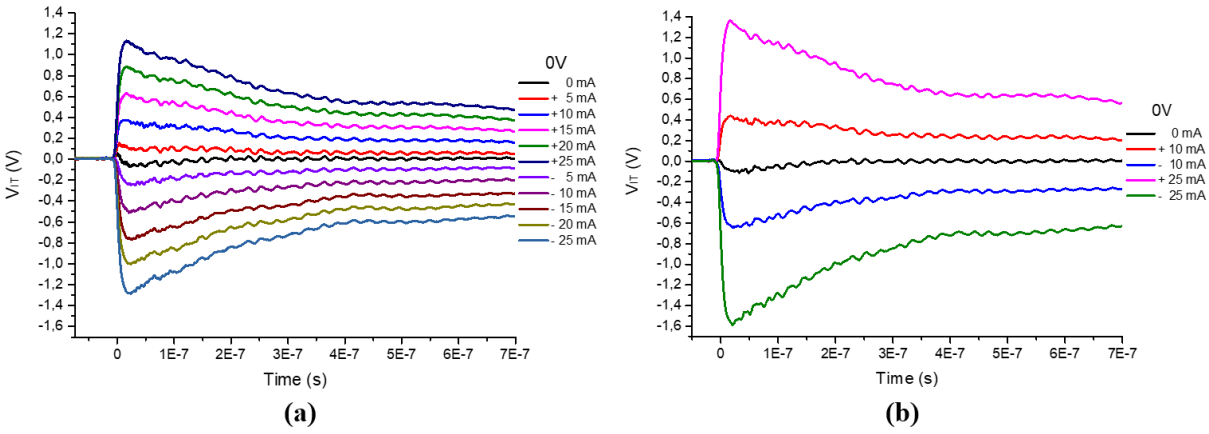


*Figure 3.9 Primary temperature signals measured without applying voltage for different currents( $I_T$) fed to the electrode(a) 50 µm-thick sample ($R_e$=30 Ω), (b) 100 µm-thick sample ($R_e$=53 Ω)*

In Figure 3.10, examples of temperature signals measured while different voltages are applied to 50 µm and 100 µm samples are presented. These data show that the amplitude of the temperature signal varies with the voltage applied to the sample. This means that the measured response is not entirely due to the variation of the electrode resistance, otherwise the curves obtained for a given value of the feeding current $I_T$ should superpose, whatever the voltage applied to the sample. A contribution of the "charge" part is therefore present in these signals and must be eliminated in order to retrieve the "pure" temperature signals.

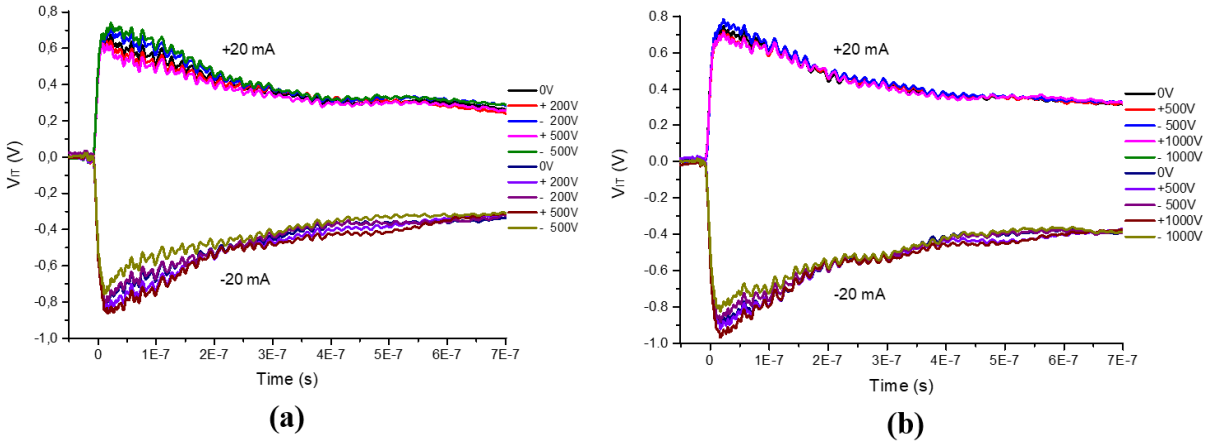


*Figure 3.10 Primary temperature signals measured on samples submitted to different voltages and fed with an electrode current of +/- 20mA: (a) 50 µm-thick sample ($R_e$=56 Ω), (b) 100 µm-thick sample ($R_e$=39 Ω)*

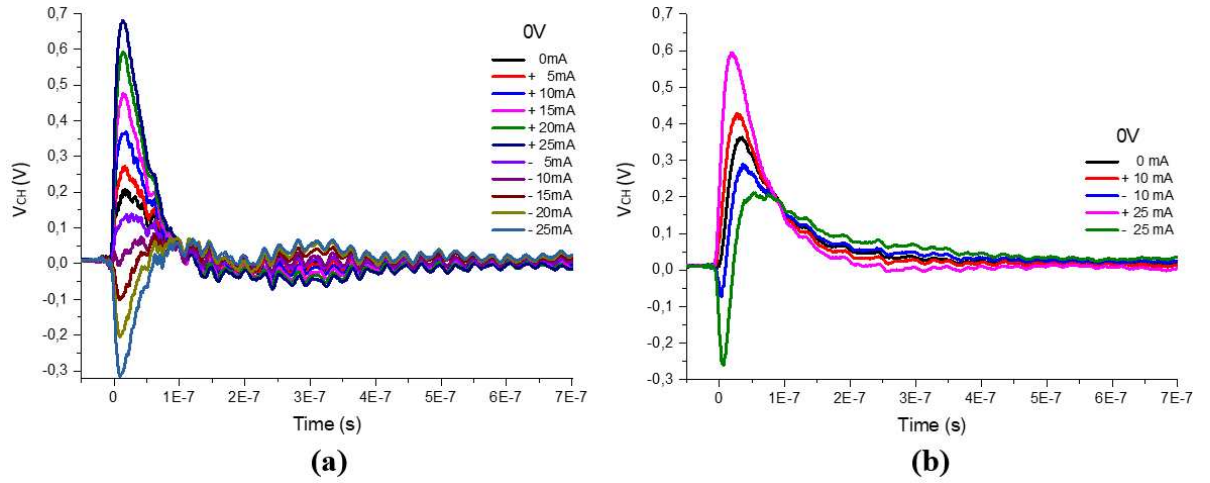


*Figure 3.11 Primary charge signals measured without applying voltage on a: (a) 50 µm-thick sample ($R_e$=30 Ω), (b) 100 µm-thick sample ($R_e$=53 Ω)*

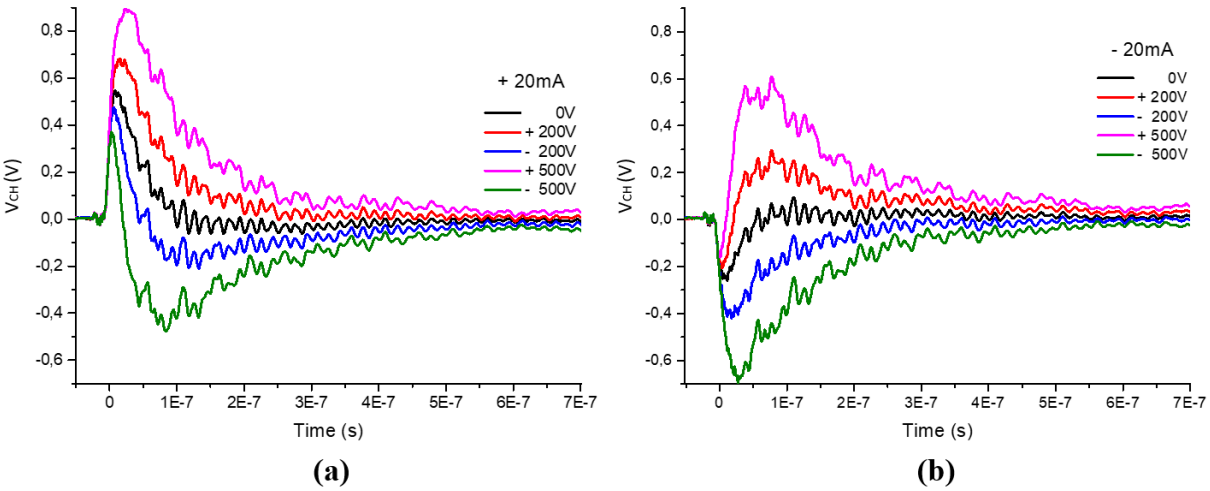


*Figure 3.12 Primary charge signals measured on a 50 µm-thick sample submitted to different voltages for feeding currents of +/- 20mA ($R_e$=56 Ω)*

In the same way, the "space charge" responses in volt-off conditions measured on the same 50 µm-thick sample and illustrated in Figure 3.11 (a) are almost proportional to the feeding current $I_T$. This indicates a mostly linear contribution of the "temperature" circuit, otherwise all the curves from this figure would superpose.

Examples of "charge" signals obtained on a 50 µm-thick sample under different applied voltages and by reverting the sense of the feeding current $I_T$ are shown in the Figure 3.12. The amplitude variation of the responses follows well the variations of the applied voltage as expected (as no significant space charge is injected in the sample under this stress). However, the volt-off signal is reverted when the sense of the bolometric current $I_T$ is reverted, and the shape and the amplitudes of the signals are affected by the change of the sign of $I_T$, which would not happen if there was no contribution of the temperature circuit to these responses.

Typical responses measured on 100 µm-thick samples are also presented in Figure 3.13. As it can be seen, they exhibit the same behaviour as the ones of the 50 µm-thick sample and thus allow to draw the same conclusions. It is interesting to observe, already at this stage, that the temperature responses measured on the 50 µm and the 100 µm-thick samples, even if they look close, are not identical for the same $I_T$, even if the laser pulse is the same. Taking apart the influence of the electrode resistance $R_e$, this underlines that the variation of the surface temperature of a sample is characteristic to the said sample and cannot be extrapolated a priori from one sample to another, putting into forces the importance of performing simultaneous charge/temperature measurements if high accuracy is desired.

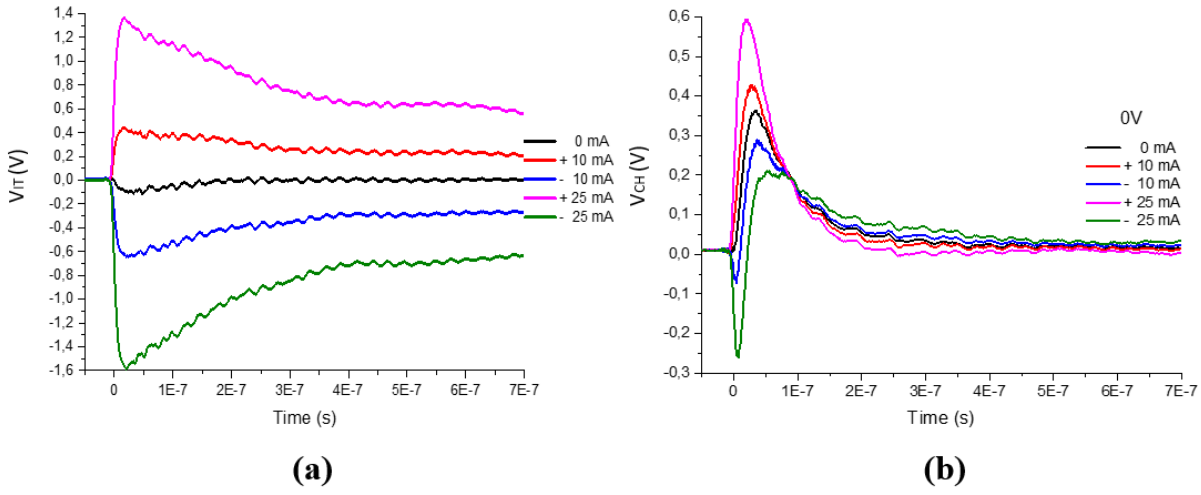


*Figure 3.13 Primary signals measured on a 100 µm-thick sample in volt-off conditions: (a) Temperature signals ($R_e$=53 Ω), (b) Charge signals*

To conclude, from the observations of the measured signals, it comes out that, both for $V_{IT}$ and $V_{CH}$, the acquired responses are a sum of contributions of temperature and charge signals, because the "temperature" and the "charge" circuits are coupled through the sample itself, as it can be seen from Figure 3.6. Thus, they have to be decoupled in order to be fully exploited.

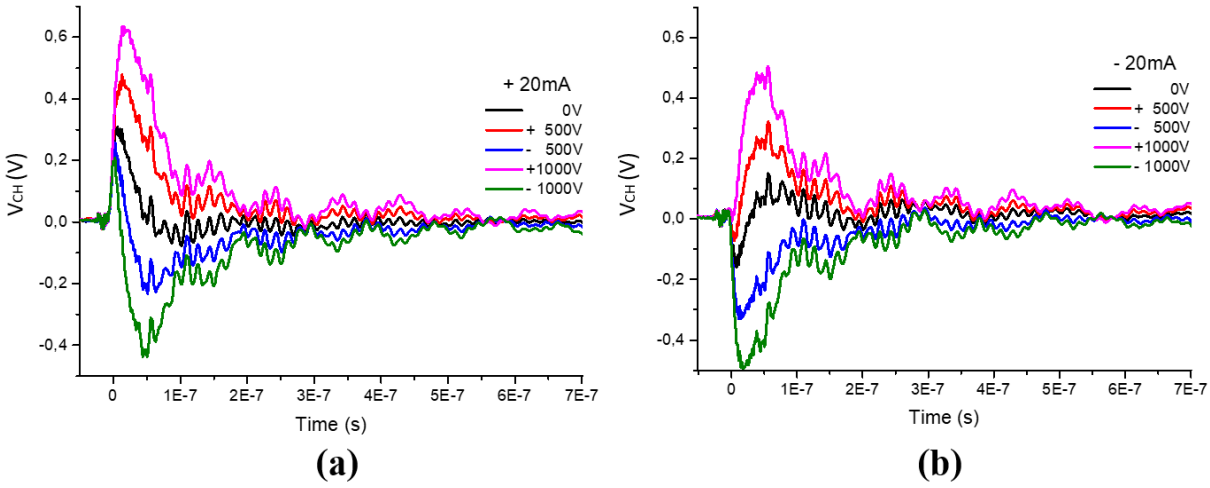


*Figure 3.14 Primary charge signals measured on a 100 µm-thick sample for a feeding current of +/- 20mA ($R_e$=39 Ω) for different applied voltage*

# 3.5. Decoupling and analysis of temperature and charge signals

## 3.5.1. Temperature signals

### *3.5.1.1. Decoupling procedure*

The voltage $V_{IT}$ measured across the sample is the result of the variation of the electrode resistance with temperature (bolometric effect $V^*_{I_T}$), of the thermoelectric (Seebeck) effect $V_S$ and of the "charge" circuit coupling $V_{chc}$:

$$V_{IT} = V^*_{I_T} + V_S + V_{chc} \qquad Eq\ 3.1$$

$$V_{IT} = \frac{k\Delta R_e I_T}{\Delta T}\Delta T + \frac{k\Delta V_{IT}}{\Delta T}\Delta T + V_{chc} \qquad Eq\ 3.2$$

with $k$ depending on the elements of the measurement circuit.

As the two last terms do not depend on the feeding current $I_T$, the bolometric contribution $V^*_{I_T}$ can be isolated by making the difference between the signal $V^+_{I_T}$, acquired with a positive feeding current ($I_T > 0$), and the signal $V^-_{I_T}$, acquired with a negative feeding current ($I_T < 0$) of the same value as the positive one:

$$V^*_{I_T} = \frac{V^+_{I_T} - V^-_{I_T}}{2} = k\Delta R_e I_T \qquad Eq\ 3.3$$

### *3.5.1.2. Qualitative analysis*

Results of the above operation applied to temperature signals acquired on 50 µm and 100 µm-thick samples are presented in Figure 3.15. It comes out that the performed operation eliminates the non-bolometric components as expected, as the curves corresponding to the feeding currents

of 10 mA and 20 mA superpose very well (at the reproducibility limit of the measurements), and proportionality is observed between the amplitudes of the signals measured at 10 mA and 20 mA. The performed operation also has a smoothing effect. It is also interesting to see that the non-bolometric effects are very small on the 50 µm-thick sample, but more important on the 100 µm-thick one, as witnessed by the signals measured for $I_T = 0$ mA, which cannot obviously be decoupled as there are no "- 0 mA" signals (Figure 3.15 (b)).

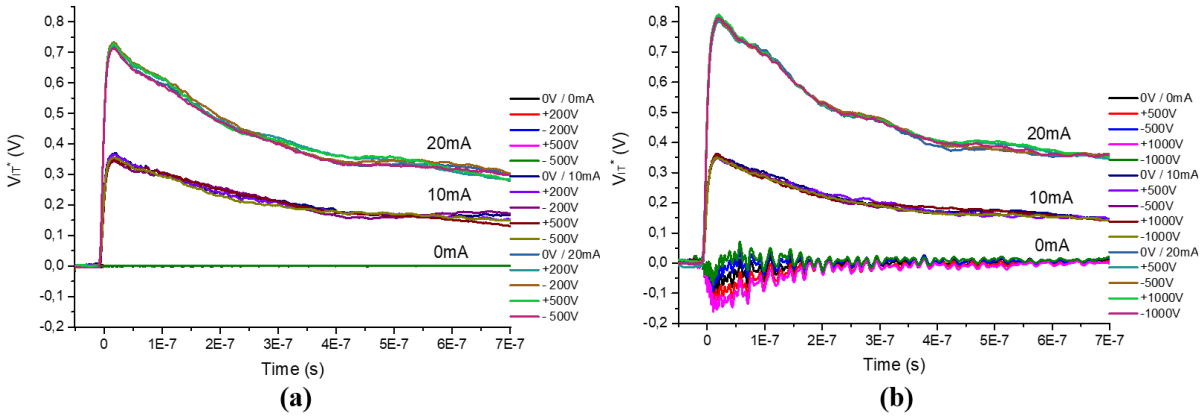


*Figure 3.15 Bolometric signals measured on a: (a) 50 µm-thick sample ($R_e$=56 Ω), (b) 100 µm-thick sample ($R_e$=39 Ω)*

## 3.5.2. Charge signals

### *3.5.2.1. Decoupling procedure*

The signal $V_{ch}$, measured by the amplifier connected to the back (non-thermally excited) electrode of the sample, depends simultaneously on the effect of the feeding current $I_T$, on the effect of the space charge $Q$ contained in the sample and on that of the voltage $V_{pol}$ applied across the sample.

If the voltage $V_{pol}$ is low enough to prevent charge injection in the sample during the measurement, the contributions of $Q$ and $V_{pol}$ are superposable, so it can be written:

$$V_{CH}(Q,\ I_T, V_{pol}) = V_{CH}(Q) + V(I_T) + V_{CH}(V_{pol}) \qquad Eq\ 3.4$$

where $V(I_T)$ is the contribution from the positive or negative bolometric current, $V_{CH}(Q)$ is the contribution of the space charge contained in the sample and $V_{CH}(V_{pol})$ the one of the voltage applied to the sample. As the contributions of positive or negative bolometric currents should be opposite, this component can be eliminated by taking half of the sum of the signals measured with a positive and a negative $I_T$:

$$V^*_{CH}(Q, V_{pol}) = \frac{V_{CH}(I_T^+)+V_{CH}(I_T^-)}{2} \qquad Eq\ 3.5$$

$$V^*_{CH}(Q, V_{pol}) = \frac{V_{CH}(Q)+V_{CH}(I_T^+)+V_{CH}(V_{pol})+V_{CH}(Q)+V_{CH}(I_T^-)+V_{CH}(V_{pol})}{2} \qquad Eq\ 3.6$$

Since the response $V_{CH}(I_T^+)$ and that of its opposite current $V_{CH}(I_T^-)$ are equal and opposite, we get:

$$V_{CH}^*(Q, V_{pol}) = V_{CH}(Q) + V_{CH}(V_{pol}) \qquad Eq\ 3.7$$

Let us put:

$$V_{CH}^{*+} = V_{ch}^*(Q, V_{pol}^+) = V_{CH}(Q) + V_{CH}(V_{pol}^+) \qquad Eq\ 3.8$$

$$V_{CH}^{*-} = V_{ch}^*(Q, V_{pol}^-) = V_{CH}(Q) + V_{CH}(V_{pol}^-) \qquad Eq\ 3.9$$

Thus, the space charge response $V_{CH}(Q) = V_{CH}^*(Q, V_{pol} = 0)$ can be either measured directly or computed from voltage-on signals, as $V_{CH}(V_{pol}^+) = -V_{CH}(V_{pol}^-)$:

$$V_{CH}(Q) = \frac{V_{CH}^{*+} + V_{CH}^{*-}}{2} = \frac{V_{CH}(Q) + V_{CH}(V_{pol}^+) + V_{CH}(Q) + V_{CH}(V_{pol}^-)}{2} \qquad Eq\ 3.10$$

Calibration signals $V_{CHpol} = V_{CH}^*(Q = 0, V_{pol})$ can also be obtained, either by subtracting the measured charge signal $V_{CH}^*(Q, V_{pol} = 0)$ from the measured voltage-on signal, or by making the difference of signals measured for positive and negative voltages of the same amplitude (keeping in mind that $V_{CH}(V_{pol}^+) = -V_{CH}(V_{pol}^-)$):

$$V_{CHpol} = \frac{V_{CH}^{*+} - V_{CH}^{*-}}{2} = \frac{V_{CH}(Q) + V_{CH}(V_{pol}^+) - V_{CH}(Q) - V_{CH}(V_{pol}^-)}{2} \qquad Eq\ 3.11$$

The signals obtained with Eq 3.11 are thus proportional to the applied voltage (and thus to the field $V_{pol}/d$) and can be used, after calculating the temperature across the sample, to determine the coefficient of variation of the sample capacitance.

### *3.5.2.2. Qualitative analysis*

#### *3.5.2.2.1. LDPE samples with Pt electrodes*

The curves $V_{CH}^*$, determined by processing the measured charge signals in order to eliminate the bolometric components as indicated by Eq 3.5, are illustrated in Figure 3.16 for a 50 µm and 100 µm sample. It comes out that the procedure is efficient, as the signals corresponding to a given voltage (positive or negative) completely superpose, whatever the value of the bolometric current.

This is also true for the signal $V_{CH.pol}$ related only to the application of the voltage (Figure 3.17 and Figure 3.18). Indeed, in Figure 3.17 it can be seen that, these decoupled signals are strictly proportional to the applied voltage. In Figure 3.18, where the quantities $V_{CH}^{*+} - V_{CH}(0)$ and $V_{CH}^{*-} - V_{CH}(0)$ have been plotted, it can be seen that the values for the same voltage amplitude superpose, showing the perfect symmetry between a signal obtained under a positive voltage and its counterpart obtained under a negative one.

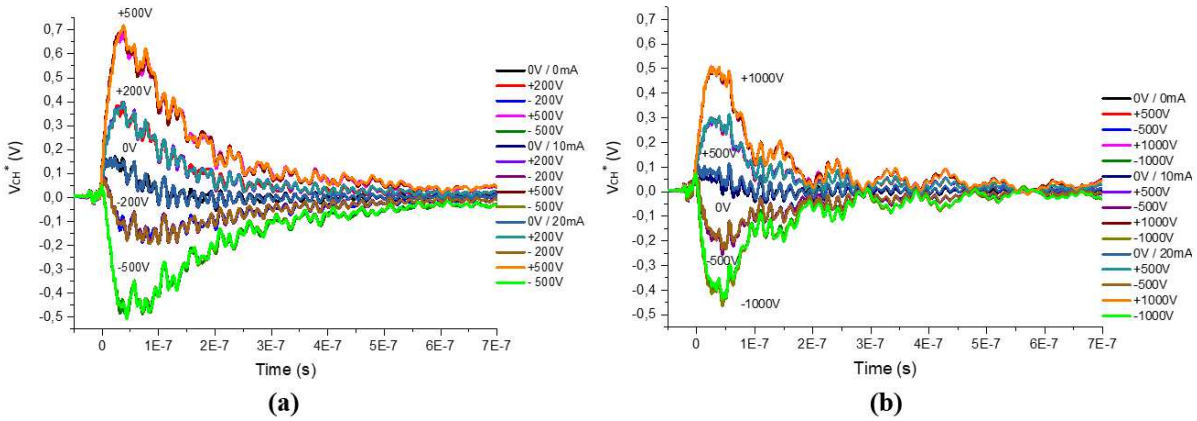


*Figure 3.16 Charge signals issued by a (a) 50 µm-thick sample ($R_e$=56 Ω), (b) 100 µm-thick sample ($R_e$=39 Ω)*

Signals related to the charge contained in sample of 50 µm and 100 µm or, more precisely, only to their internal fields, are presented in Figure 3.19 and Figure 3.20. First, it can be seen that the decoupling procedure presented in the previous section works well, as the signals decoupled from the responses measured at different voltages perfectly superpose on the voltage-off signals.

The dynamics and the shape of the signals seems practically independent on the sample capacitance, which, taking into account that the capacitance differ only by a factor of two, is in accordance with the pre-calculations from section 3.3.2, but which also suggests that the temperature penetrates in the sample only on a very limited depth.

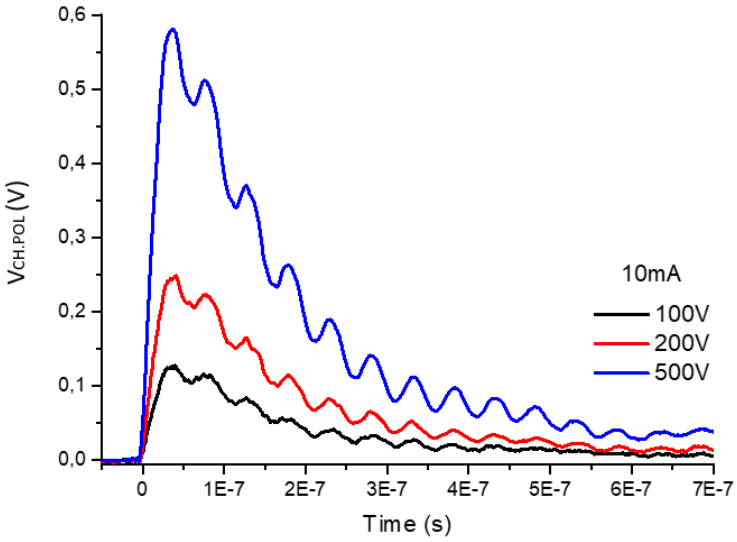


*Figure 3.17 Charge signals related to low field polarization in a 50 µm-thick sample*

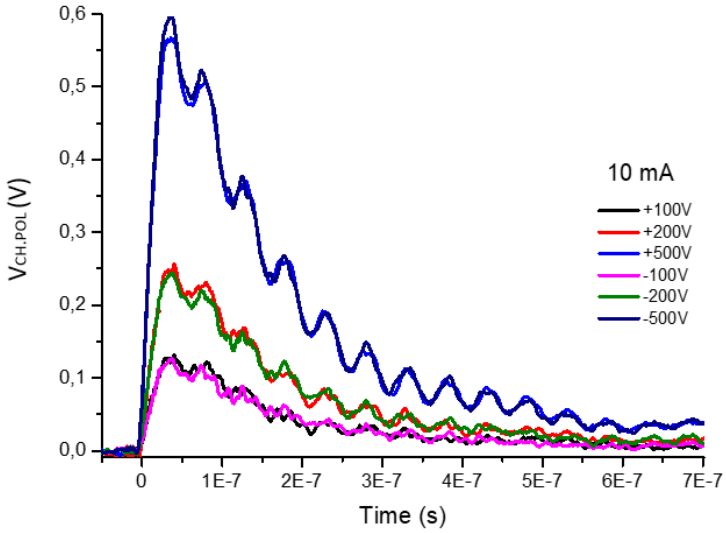


*Figure 3.18 Illustration of the symmetry of charge signals when positive and negative voltages are applied to a 50 µm-thick sample*

If we assume that the temperature diffuses in the sample mainly on a distance of several microns, these signals should be directly related to the field at the interface between the electrode and the insulator. By considering the values of the calibration voltages from Figure 3.17 and Figure 3.18 (*i.e.*, several hundreds of millivolts for applied fields $E_{app} = V_{pol}/d$ of several kV/mm), it can be concluded that the internal fields at the interfaces are of the order of several kV/mm on an average width of several µm. These data also show that the interfaces are not identical, as the values of the signals can be multiplied by a factor of 2 between the two faces of the same sample (by considering the close variations of the temperature during the thermal excitation). This is not so peculiar if we take into consideration that these are low-grade, commercially-available LDPE samples, for which the surface states are not well-controlled. However, these results show clearly that it is possible to assess directly such sample interfaces with a TPM setup, which was one of the aims of this work.

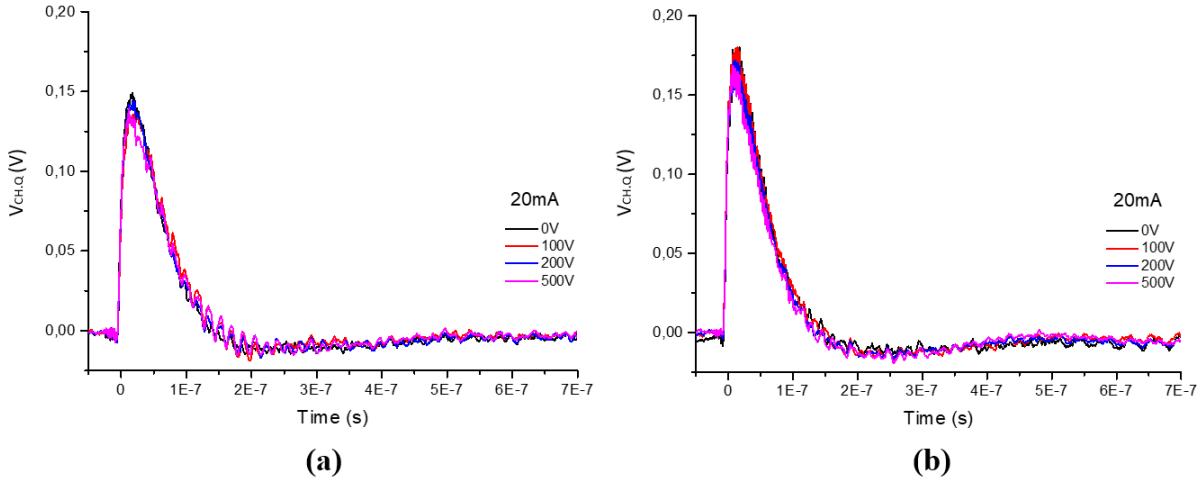


*Figure 3.19 Signals related to the internal field in a 50 µm-thick sample (a) Face A, (b) Face B*

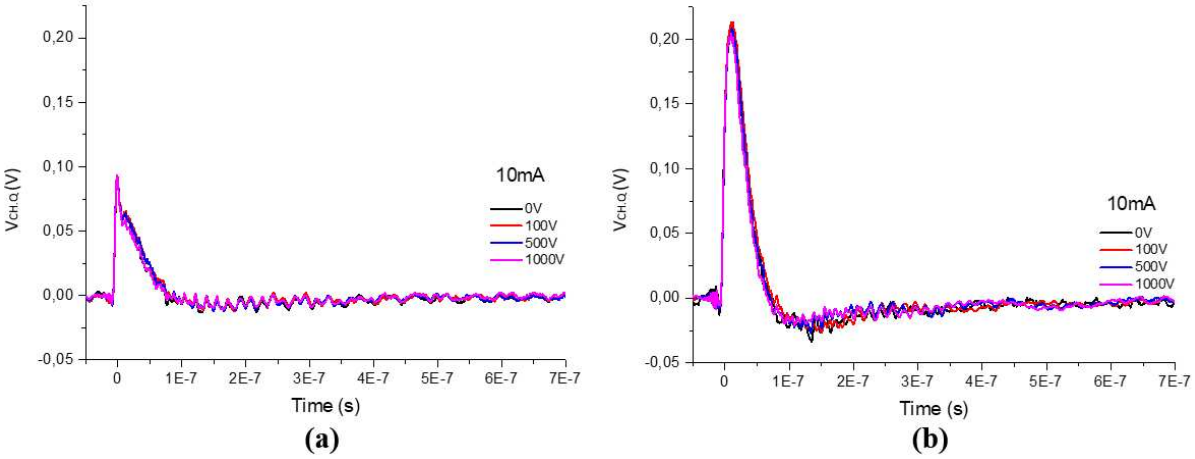


*Figure 3.20 Signal related to the internal field in a 100 µm-thick sample (a) Face A, (b) Face B*

#### *3.5.2.2.2. XLPE samples coated with carbon-black electrodes and Pt electrodes*

The results obtained on XLPE samples coated with the carbon-black semi-conducting electrodes (on top of which the Pt layers have been deposited for temperature measurements, Figure 3.2) are very different. Typical charge signals measured in volt-off and under several positive and negative voltages are presented in Figure 3.21.

One may notice two sharp successive peaks of opposite signs, as opposed to the single peak observed on the "classical" LDPE samples discussed earlier. The amplitude of these peaks are also higher than in the case of the samples without semi-conducting layers. The shape of the signals of the samples coated with semi-conducting layers is the same on the two faces, suggesting that, as for the case of the LDPE samples without semicon electrodes, they are characteristic of the interface scanned by the thermal wave.

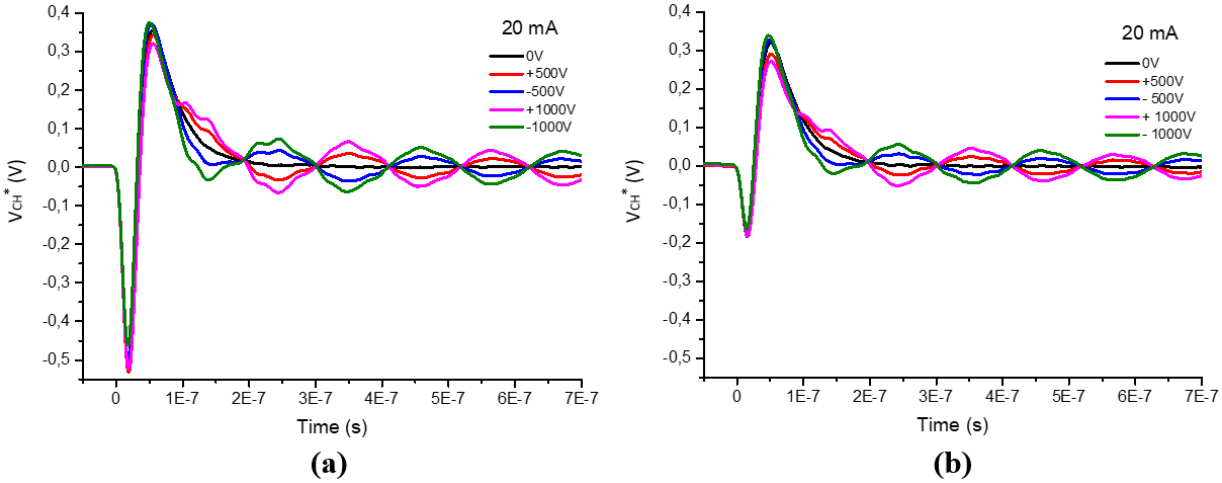


*Figure 3.21 Charge signals issued from a 160 µm-thick sample with semicon electrodes: (a) Face A ($R_e$=58 Ω), (b) Face B ($R_e$=55 Ω)*

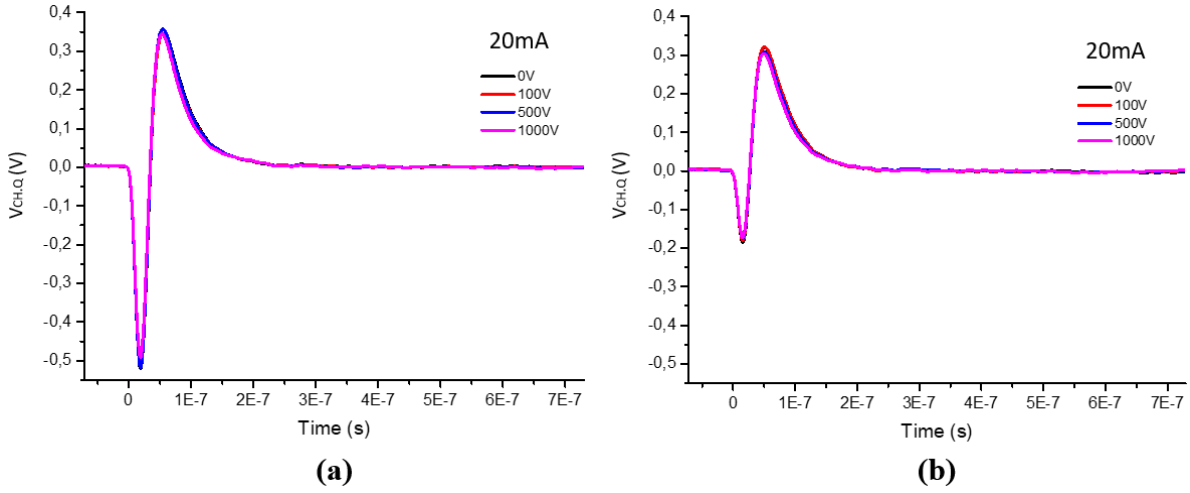


*Figure 3.22 Signals related to the interface field in a 160 µm-thick sample with semicon electrodes: (a) Face A ($R_e$=58 Ω), (b) Face B ($R_e$=55 Ω)*

Some oscillations are observed on the signals, which are probably related to stationary phenomena induced by elasto-electric coupling between the applied field and the charge in the sample. Such phenomena are also observed, at a lesser extent, on the 50 µm and 100 µm sample. Even if they impair aesthetically the charge signals, they are not an obstacle to the signal treatment, because the processing described in section 3.5.2.1 allows to completely eliminate them, as it can be seen from Figure 3.19 and Figure 3.22.

Another important difference observed between the semicon-coated samples and the others is the behaviour of the charge signals when a voltage $V_{pol}$ is applied. Indeed, in contrast with the results from Figure 3.16, where the amplitude of the signals increase proportionally to the applied voltage, the amplitude of the signals measured on the semicon-coated sample does practically not change, whatever the applied voltage (Figure 3.21). As the proportional increase of the signal amplitude with the voltage $V_{pol}$ is directly linked to the increase of the internal field in the sample by $V_{pol}/d$, this suggests that the region scanned by the thermal wave is a region where the field does not vary, even when the voltage applied to the sample increases. As the power source supplied well the set voltages, without any sign of significant increase of the conduction current which could have been related to a defect or breakdown of the samples, it came out clearly that the insulating XLPE layer of the samples withstood fine the applied voltages, so the field $E_{app} = V_{pol}/d$ was actually applied across the insulator. In turn, the field across the semi-conducting layers is practically zero whatever the applied voltage, due to the very small resistivity of this layers. This leads to the conclusion that the responses observed on the semicon-coated XLPE sample are due to the interface fields between the Pt layer and the semicon layer, which would not vary if no injection occurs between the two materials when an electric stress is applied to the sample, which is certainly the case for the fields applied to the samples used in this work.

In order to verify this assumption, we have characterized with the same experimental set-up two 100 µm-thick layers of carbon-black semiconducting compound similar to the one used for the XLPE sample. One of the semi-conducting samples was coated with an Au electrode on one

side and with a Pt electrode on the other. A second semi-conducting was characterized as it was, without any metallic deposit.

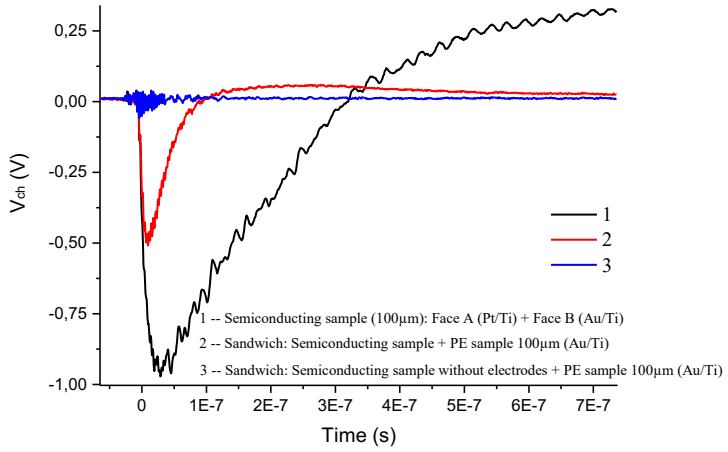


*Figure 3.23 Primary charge signal measured on the semiconducting samples in volt-off conditions*

Figure 3.23 shows the results of experiments made in volt-off conditions on the semi-conducting sample with metallic electrodes and on 'sandwiches' made with each of the two semi-conducting samples and a 100 µm thick LDPE "classical" sample.

As it can be seen, when the sample made of semi-conducting compound is hit by the thermal pulse, it issues a high TPM response (curve 1). When an insulating sample is placed under the semi-conducting one, the signal decreases (curve 2) because of the decrease of the overall capacitance of the "sandwich" (the capacitance of the insulating sample is placed in series with that of the semiconducting one). An experiment made on a "sandwich" composed of a semi-conducting sample without metallic electrodes on top of an insulating sample issues no TPM response (curve 3).

Taking into account the results of these complementary measurements, it can be concluded without any doubt that the signals from Figure 3.21 and Figure 3.22 are images of the electric field at the interface between the metallic layer of Pt used as electrode/bolometer and the semiconducting compound with which the XLPE samples are coated, and not of the interface between the semicon and the insulator, or of the field across the insulator. This means that the amount of heat provided to the surface of the sample is not sufficient to make the temperature vary significantly beyond the 40 µm which constitute the semicon layer, *i.e.* to excite the insulating layer. This may be regarded as a drawback at the first sight, particularly if the targeted region is the semicon/insulator interface. However, the study of this region can be at reach by diminishing the thickness of the semicon and by increasing the power of the heat pulse, as discussed in the simulation chapter.

On the other hand, these experiments demonstrate, for the first time, the ability of directly measuring, through a thermal method, the field at the interface between a metal and a semiconductor, or in the bulk of a semiconducting material. This is an original and notable result, as despite previous non resolutive results obtained on MOS structures (ex. [169]), it is not clear at what extent measurements on such structures were feasible because of supposed thermal effects leading to charge displacement in low resistive media. This work proves that

the principle of a thermal method is applicable to low resistive media and their interfaces, which, taking into account the high sensitivity of the thermal methods with respect to others, could trigger interesting developments in the future.

### 3.5.3. Conclusion

The measurements, procedures, analysis and validations presented in this section showed that and how pure bolometric, charge-dependent and calibration signals can be extracted from the responses acquired on 50, 100 and 160 µm thick polyethylene samples coated with metallic and semi-conducting electrodes. It has thus been shown that signals directly depending on the metal/semicon and metal/insulator interface fields can be obtained simultaneously with temperature signals, directly linked to the variation of the electrode resistance with temperature. In the following section, combinations of these data will be used to determine the surface temperature, the volume temperature and the interface fields.

## 3.6. In-depth signal analysis. Determination of temperature distributions and of interface fields

### 3.6.1. General considerations

Obtaining a direct relationship between the measured then decoupled voltage $V^*_{I_T}$ and the temperature variation at electrode $\Delta T$, *i.e.* determining the coefficient $k'$ from $V^*_{I_T} = k\Delta R_e I_T = k'\Delta T I_T$, needs first to determine the coefficient $k$, which depends on the elements present in the equivalent circuit of the experimental set up (Figure 3.24).

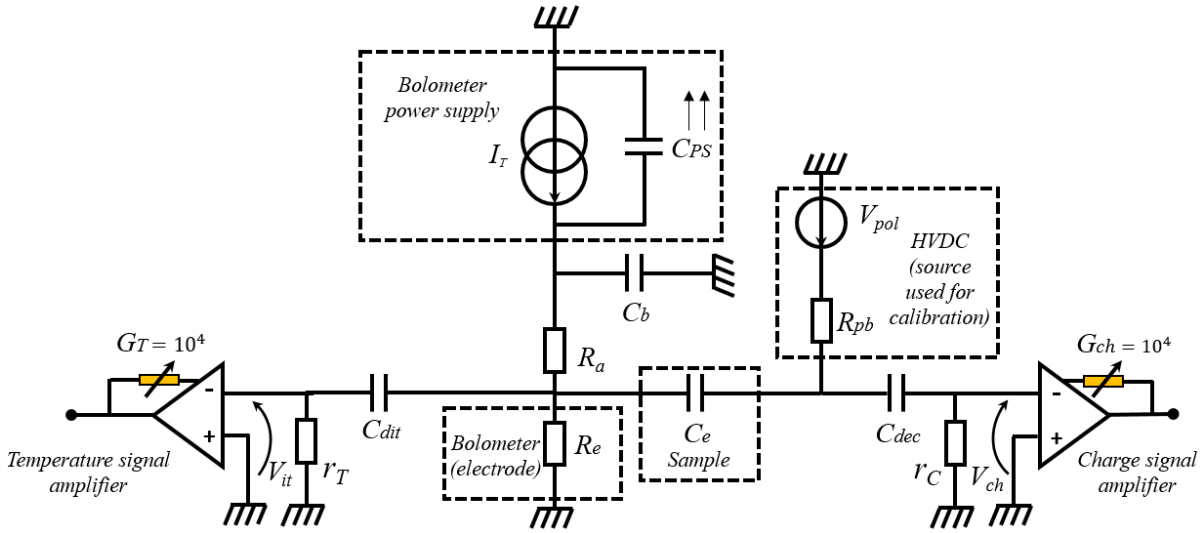


*Figure 3.24 Electrical diagram of temperature and charge measurement circuit*

In the same way, obtaining the dependence between the value $V_{TPM}$ of the real voltage variation at the electrodes of the sample with respect to the measured then decoupled voltage $V_{CH}^{*}$ requires a detailed high-frequency analysis of the measurement circuit.

For high frequencies (*i.e.,* during the transient corresponding to the thermal step signals, $t < 10^{-6}s$), the electrical diagram of the measurement circuit can be simplified as follows:

- The capacitance $C_{PS}$ of the dc power supply of the temperature sensor (front electrode) is very large and short-circuits the power source at high frequencies, so during the measurement this power source can be removed from the circuit.
- $r_T C_{dit} = 50\Omega * 440nF = 22\ \mu s$, so below 22 µs the capacitor $C_{dit}$ is short-circuited and can be removed from the circuit.
- $C_e \ll C_{dec}$ (the maximum value of the sample capacitance is 800 pF for a 50 µm sample vs 440 nF), hence $C_{dec}$ can be removed from the circuit.
- $C_b || C_{PS}$, which tends to ∞, so $C_b = 10\ nF$ is short circuited and can be removed from the circuit.
- There is no current flowing through $R_{pb}$ of the calibration circuit, so $R_{pb}$ can be removed.
- $R_e$ varies to $\delta R_e$ during the measurement, so we can add in the circuit a high frequency voltage source of value $I_T \delta R_e$, created by the variation of the resistance $R_e$.
- The sample gives rise to the TPM voltage $V_{TPM}$ during the measurement, so a source of voltage $V_{TPM}$ is added in the circuit.

With these simplifications, the high-frequency equivalent diagram of the circuit becomes:

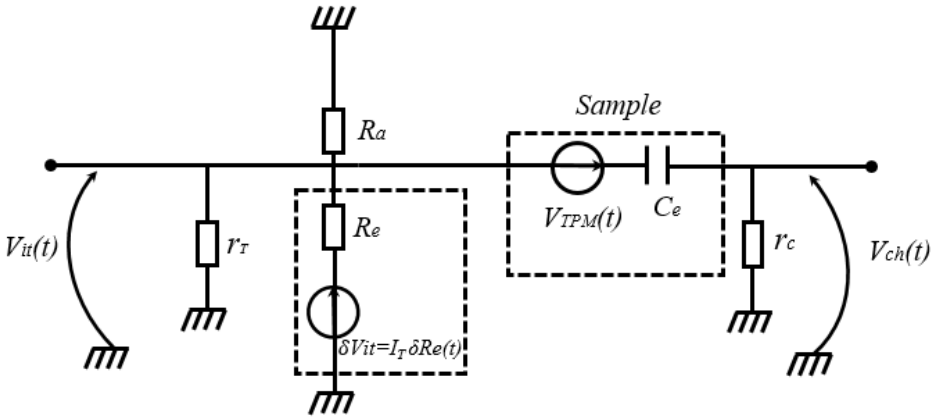


*Figure 3.25 Simplified equivalent circuit at high frequencies*

The dependencies $V_{ch} = f(V_{TPM}, \delta R_e)$ and $V_{it} = f(V_{TPM}, \delta R_e)$ can be obtained in the Laplace domain from analysing the circuit with the superposition principle. Then, the dependency $V_{TPM} = f(\mathrm{V}_{\mathrm{ch}}^{*})$ and $\delta V_{it} = f(\mathrm{V}_{\mathrm{IT}}^{*})$ can be calculated by using the decoupling procedure and the inverse Laplace transform.

### 3.6.2. Expressions of the temperature and charge signals with respect to the measured signals and the components of the conditioning circuit

In the virtue of the superposition principle, let us first set $I_T = 0$. In this case, the equivalent circuit can be re-drawn as in Figure 3.6:

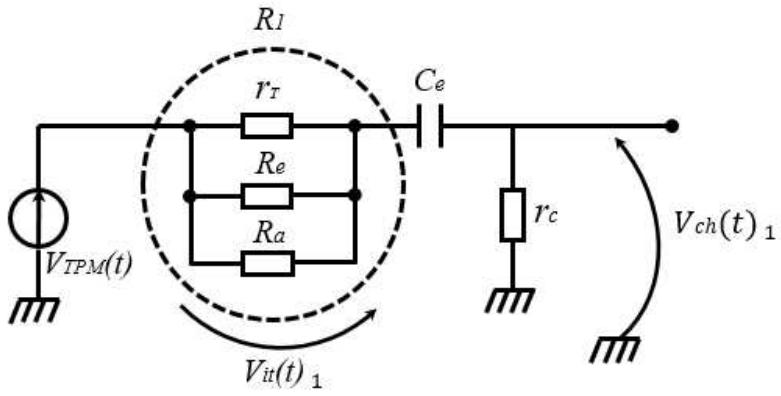


*Figure 3.26 Equivalent circuit when $I_T = 0$*

In the Laplace domain we have:

$$V_{ch}(p)_1 = \frac{r_c}{r_c + R_1 + \frac{1}{C_e p}} V_{TPM}(p) \qquad \textit{Eq 3.12}$$

$$V_{it}(p)_1 = -\frac{R_1}{r_c + R_1 + \frac{1}{C_e p}} V_{TPM}(p) \qquad \textit{Eq 3.13}$$

When $V_{TPM} = 0$, the equivalent circuit becomes the one from Figure 3.27:

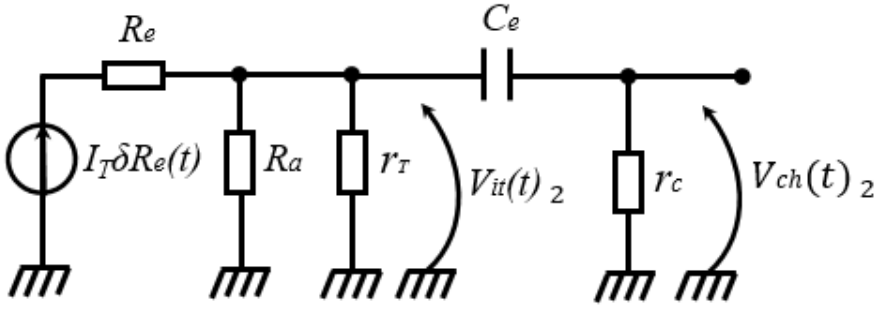


*Figure 3.27 Equivalent circuit when $V_{TPM}$=0*

$$V_{it}(p)_2 = \frac{R_a || r_T || \left(\frac{1 + r_c C_e p}{C_e p}\right)}{R_a || r_T || \left(\frac{1 + r_c C_e p}{C_e p}\right) + R_e} I_T \delta R_e(p) \qquad \textit{Eq 3.14}$$

$$V_{ch}(p)_2 = \frac{r_c}{r_c + \frac{1}{C_e p}} V_{it}(p)_2 \qquad \textit{Eq 3.15}$$

where the sign "||" is used to denote circuit elements placed in parallel. Substituting Eq 3.14 in Eq 3.15, we get:

$$V_{ch}(p)_2 = \frac{R_a||r_T||\left(\frac{1+r_cC_ep}{C_ep}\right)}{R_a||r_T||\left(\frac{1+r_cC_ep}{C_ep}\right)+R_e} * \left(\frac{r_cC_ep}{r_cC_ep+1}\right) * I_T\delta R_e(p) \qquad \textit{Eq 3.16}$$

The superposition principle gives:

$$V_{ch}(p) = V_{ch}(p)_1 + V_{ch}(p)_2 \qquad \textit{Eq 3.17}$$

$$V_{it}(p) = V_{it}(p)_1 + V_{it}(p)_2 \qquad \textit{Eq 3.18}$$

By substituting Eq 3.12 and Eq 3.16 in Eq 3.17 and similarly Eq 3.13 and Eq 3.14 in Eq 3.18, one gets:

$$V_{ch}(p) = \frac{r_c}{r_c+R_1+\frac{1}{C_ep}}V_{TPM}(p) + \frac{R_a||r_T||\left(\frac{1+r_cC_ep}{C_ep}\right)}{R_a||r_T||\left(\frac{1+r_cC_ep}{C_ep}\right)+R_e} * \left(\frac{r_cC_ep}{r_cC_ep+1}\right) * I_T\delta R_e(p) \qquad \textit{Eq 3.19}$$

$$V_{it}(p) = -\frac{R_1}{r_c+R_1+\frac{1}{C_ep}}V_{TPM}(p) + \frac{R_a||r_T||\left(\frac{1+r_cC_ep}{C_ep}\right)}{R_a||r_T||\left(\frac{1+r_cC_ep}{C_ep}\right)+R_e}I_T\delta R_e(p) \qquad \textit{Eq 3.20}$$

In order to eliminate the contributions of $V_{TPM}$ in the expression of $V_{\mathrm{it}}$ and of $I_T$ in the expression of $V_{TPM}$, we perform the following operations:

$${V_{it}}^*(p) = \frac{V_{it}(p)_{(I_T>0)} - V_{it}(p)_{(I_T<0)}}{2} \qquad \textit{Eq 3.21}$$

$$V_{ch}^*(p) = \frac{V_{ch}(p)_{(I_T>0)} + V_{ch}(p)_{(I_T<0)}}{2} \qquad \textit{Eq 3.22}$$

From the above two equations we obtain, for the temperature signal:

$${V_{it}}^*(p) = \frac{R_a||r_T||\left(\frac{1+r_cC_ep}{C_ep}\right)}{R_a||r_T||\left(\frac{1+r_cC_ep}{C_ep}\right)+R_e}\delta V_{it} \qquad \textit{Eq 3.23}$$

where $\delta V_{\mathrm{it}} = I_T\delta R_e$, the $V_{TPM}$ term disappears after the subtraction. For the charge signal:

$$V_{ch}^*(p) = \frac{r_cC_ep}{(r_c+R_1)C_ep+1}V_{TPM}(p) \qquad \textit{Eq 3.24}$$

Similarly for the temperature equation, the term $I_T\delta R_e$ disappears because $I_T$ changes sign.

It comes out from above that:

$$V_{TPM}(p) = \frac{(r_c+R_1)C_ep+1}{r_cC_ep}{V_{ch}}^*(p) \qquad \textit{Eq 3.25}$$

$$V_{TPM}(p) = \left(\frac{1}{r_cC_ep} + \frac{(r_c+R_1)}{r_c}\right){V_{ch}}^*(p) \qquad \textit{Eq 3.26}$$

$$V_{TPM}(p) = \frac{1}{r_cC_e}\frac{1}{p}{V_{ch}}^*(p) + \frac{(r_c+R_1)}{r_c}{V_{ch}}^*(p) \qquad \textit{Eq 3.27}$$

In order to obtain $V_{TPM}(\mathrm{t}) = f\left(V_{ch}^{*}(t)\right)$, we apply the Laplace transform to the previous equation.

As:

$$L^{-1}\{af(p)\} = aL^{-1}\{f(p)\} = af(t) \qquad \textit{Eq 3.28}$$

$$L^{-1}\left\{\frac{f(p)}{p}\right\} = \int_0^t f(t)dt \qquad \textit{Eq 3.29}$$

we get:

$$V_{TPM}(t) = \frac{1}{r_c C_e}\int_0^t V_{ch}^{*}(t)dt + \frac{(r_c+R_1)}{r_c}V_{ch}^{*}(t) \qquad \textit{Eq 3.30}$$

$$V_{TPM}(t) = \frac{1}{r_c C_e}\int_0^t V_{ch}^{*}(t)dt + \left(1+\frac{R_1}{r_c}\right)V_{ch}^{*}(t) \qquad \textit{Eq 3.31}$$

The real TPM voltage signal is thus the sum of two terms which contain the measured then decoupled charge signal $V_{ch}^{*}$. It is to note that, with this calculation procedure, we do not have to worry about whether the signal is a voltage or current response.

Let us now determine $\delta V_{it}(t) = f({V_{it}}^{*}(t))$. From Eq 3.23, we have:

$$\delta V_{it}(p) = \frac{R_a||r_T||\left(\frac{1+r_c C_e p}{C_e p}\right)+R_e}{R_a||r_T||\left(\frac{1+r_c C_e p}{C_e p}\right)}{V_{it}}^{*}(p) \qquad \textit{Eq 3.32}$$

$$\delta V_{it}(p) = \frac{R_2||\left(\frac{1+r_c C_e p}{C_e p}\right)+R_e}{R_2||\left(\frac{1+r_c C_e p}{C_e p}\right)}{V_{it}}^{*}(p) \qquad \textit{Eq 3.33}$$

where $R_2 = R_a||r_T = \frac{r_T R_a}{r_T+R_a}$, then

$$\delta V_{it}(p) = \frac{\frac{R_2\left(\frac{1+r_c C_e p}{C_e p}\right)}{R_2+\frac{1+r_c C_e p}{C_e p}}+R_e}{\frac{R_2\left(\frac{1+r_c C_e p}{C_e p}\right)}{R_2+\frac{1+r_c C_e p}{C_e p}}}{V_{it}}^{*}(p) \qquad \textit{Eq 3.34}$$

$$\delta V_{it}(p) = \frac{R_2(1+r_c C_e p)+R_e(R_2 C_e p+1+r_c C_e p)}{R_2(1+r_c C_e p)}{V_{it}}^{*}(p) \qquad \textit{Eq 3.35}$$

$$\delta V_{it}(p) = \left(\frac{R_2+R_e}{R_2}\right)\frac{\left[1+\left(\frac{R_2 r_c}{R_2+R_e}+\frac{R_2 R_e}{R_2+R_e}+\frac{R_e r_c}{R_2+R_e}\right)C_e p\right]}{1+r_c C_e p}{V_{it}}^{*}(p) \qquad \textit{Eq 3.36}$$

$$\delta V_{it}(p) = a\frac{1+bp}{1+cp}{V_{it}}^{*}(p) \qquad \textit{Eq 3.37}$$

where $a = \left(\frac{R_2+R_e}{R_2}\right), b = \left(\frac{R_2 r_c}{R_2+R_e}+\frac{R_2 R_e}{R_2+R_e}+\frac{R_e r_c}{R_2+R_e}\right)C_e, c = r_c C_e$. By re-arranging Eq 3.37, we get:

$$\delta V_{it}(p) = a\frac{1+bp+cp-cp}{1+cp}{V_{it}}^{*}(p) \qquad \textit{Eq 3.38}$$

$$\delta V_{it}(p) = aV_{it}{}^{*}(p) + \underbrace{\frac{(b-c)p}{1+cp}} V_{it}{}^{*}(p) \qquad \textit{Eq 3.39}$$

By dividing the numerator and the denominator of the second half of the above equation by $c$, we get:

$$\delta V_{it}(p) = aV_{it}{}^{*}(p) + \frac{(b-c)}{c} p \frac{1}{\frac{1}{c}+p} V_{it}{}^{*}(p) \qquad \textit{Eq 3.40}$$

It is known that:

$$L^{-1}[af(p)] = a\, f(t) \qquad \textit{Eq 3.41}$$

$$L^{-1}[pf(p)] = \frac{df(t)}{dt} \qquad \textit{Eq 3.42}$$

$$L^{-1}\left[\frac{f(p)}{\frac{1}{c}+p}\right] = e^{-\frac{t}{c}} * f(t) \qquad \textit{Eq 3.43}$$

where * denotes the convolution product, defined as:

$$f(t) * g(t) = \int_{-\infty}^{\infty} f(\tau) g(t-\tau) d\tau, \text{ or:} \qquad \textit{Eq 3.44}$$

$$f(t) * g(t) = \int_{-\infty}^{\infty} f(t-\tau)\, H(t-\tau) g(\tau) d\tau \qquad \textit{Eq 3.45}$$

with $H(t)$ Heaviside's function : $H(t) = 0$ if $t \leq 0$ and $H(t) = 1$ if $t > 0$; hence, $H(t-\tau) = 1$ for $t > \tau$ and $H(t-\tau) = 0$ for $t \leq \tau$.

From Eq 3.40, we have:

$$\delta V_{it}(t) = L^{-1}[\delta V_{it}(p)], \textit{ i.e.}: \qquad \textit{Eq 3.46}$$

$$\delta V_{it}(t) = aV_{it}{}^{*}(t) + \frac{(b-c)}{c} \frac{d}{dt}\left[e^{-\frac{t}{c}} H(t) * V_{it}{}^{*}(t)\right] \qquad \textit{Eq 3.47}$$

$$\delta V_{it}(t) = aV_{it}{}^{*}(t) + \left(\frac{b}{c} - 1\right) \frac{d}{dt} \int_{-\infty}^{\infty} e^{-\frac{t-\tau}{c}} H(t-\tau) V_{it}{}^{*}(\tau) d\tau \qquad \textit{Eq 3.48}$$

The derivative reads:

$$\frac{d}{dt}\left[e^{-\frac{t-\tau}{c}} H(t-\tau)\right] = -\frac{1}{c} e^{-\frac{t-\tau}{c}} H(t-\tau) + e^{-\frac{t-\tau}{c}} \delta(t-\tau) \qquad \textit{Eq 3.49}$$

where $\delta(t-\tau)$ is Dirac's function. By substituting Eq 3.49 in Eq 3.48 we get:

$$\delta V_{it}(t) = aV_{it}{}^{*}(t) + \left(\frac{b}{c} - 1\right) \int_{-\infty}^{\infty} \left[-\frac{1}{c} e^{-\frac{t-\tau}{c}} H(t-\tau) + e^{-\frac{t-\tau}{c}} \delta(t-\tau)\right] V_{it}{}^{*}(\tau) d\tau \qquad \textit{Eq 3.50}$$

$$\delta V_{it}(t) = aV_{it}{}^{*}(t) + \left(\frac{b}{c} - 1\right) \left[\begin{array}{c} \int_{-\infty}^{\infty} \left(-\frac{1}{c} e^{-\frac{t-\tau}{c}} H(t-\tau)\right) V_{it}{}^{*}(\tau) d\tau \\ + \int_{-\infty}^{\infty} \left(e^{-\frac{t-\tau}{c}} \delta(t-\tau)\right) V_{it}{}^{*}(\tau) d\tau \end{array}\right] \qquad \textit{Eq 3.51}$$

If $t \to \tau$, $e^{-\frac{t-\tau}{c}} = 1$, then

$$\int_{-\infty}^{\infty} e^{-\frac{t-\tau}{c}} \delta(t-\tau)\, {V_{it}}^*(\tau) d\tau = \int_{-\infty}^{\infty} \delta(t-\tau) {V_{it}}^*(\tau) d\tau \qquad \textit{Eq 3.52}$$

The value of $\delta(t-\tau) = 1$, only when $t = \tau$ or else

$$\int_{-\infty}^{\infty} \delta(t-\tau) {V_{it}}^*(\tau) d\tau = {V_{it}}^*(t) \qquad \textit{Eq 3.53}$$

Substituting Eq 3.53 in Eq 3.51, we get:

$$\delta V_{it}(t) = a {V_{it}}^*(t) + \left(\frac{b}{c} - 1\right) {V_{it}}^*(t) + \left(\frac{b}{c} - 1\right) \int_{-\infty}^{t} \left(-\frac{1}{c} e^{-\frac{t-\tau}{c}}\right) {V_{it}}^*(\tau) d\tau \quad \textit{Eq 3.54}$$

Since ${V_{it}}^*(\tau) = 0$ for $\tau < 0$, the lower bound of the integral can be set to 0, and thus we obtain:

$$\delta V_{it}(t) = \left(a + \frac{b}{c} - 1\right) {V_{it}}^*(t) - \frac{1}{c}\left(\frac{b}{c} - 1\right) \int_{0}^{t} e^{-\frac{t-\tau}{c}} {V_{it}}^*(\tau) d\tau \qquad \textit{Eq 3.55}$$

For example, with the known values for a 100 µm-thick sample without semicon ($C_e = 400$ pF, $R_e = 50\ \Omega$, $R_a = 50\ \Omega$, $r_T = 50\ \Omega$), the following numerical values occur:

$$R_1 = r_T || R_a || R_e \cong r_T/3 \cong 50\ \Omega/3 \cong 17\ \Omega$$

$$R_2 = r_T || R_a \cong r_T/2 \cong 50\ \Omega/2 \cong 25\ \Omega$$

$$(r_c + R_1)/r_c = (50 + 17)/50 = 1.33$$

$$a = (R_2 + R_e)/R_2 = (25 + 50)/25 = 3$$

$$b = \left(\frac{R_2 r_c}{R_2 + R_e} + \frac{R_2 R_e}{R_2 + R_e} + \frac{R_e r_c}{R_2 + R_e}\right) C_e = (17 + 17 + 33)\Omega \times 400\ \text{pF} = 27\ \text{ns}$$

$$c = r_c C_e = 50\ \Omega \times 400\ \text{pF} = 20\ \text{ns}$$

$$b/c - 1 = 27/20 - 1 = 0.35$$

$$a + b/c - 1 = 3 + 27/20 - 1 = 3.35$$

$$(1/c)(b/c - 1) = (1/(20 \times 10^{-9}))(27/20 - 1) = 17.5 \times 10^{-6}\text{s}^{-1}$$

One may note that if ${V_{it}}^*(t)$ does not vary a lot, since $(b/c - 1) \cong 0.1(a + b/c - 1)$, the 2nd term does not account for more than 10 % compared to the first one. This means that in such conditions the bolometric voltage is practically proportional to the measured one.

## 3.6.3. Temperature across the sample

### *3.6.3.1. Surface Temperature*

#### *3.6.3.1.1. Equations*

In order to obtain the temperature, the measured/decoupled signal ${V_{it}}^*(t)$ is inserted into equation (Eq 3.55) and the signal $\delta V_{it}(t)$ is calculated. This signal is then divided by the gain

of the amplifier ($10^4$) to obtain the value $\Delta V_{it}(t)$, which is proportional to the variation of the electrode's resistance $\Delta R_e$ and to the feeding current $I_T$:

$$\Delta V_{it} = \Delta R_e I_T \qquad \textit{Eq 3.56}$$

The resistance of the electrode $R_e$ varies with temperature $T$ after the law:

$$R_e(T) = R_e(T_0)[1 + \alpha_{Pt}(T - T_0)] = R_e(T_0)(1 + \alpha_{Pt}\Delta T) \qquad \textit{Eq 3.57}$$

where $T_0$ is the initial temperature of the electrode (20°C), $\alpha_{Pt}$ the coefficient of variation of the sensitivity of Pt with the temperature ($3.92 * 10^{-3}\mathrm{K}^{-1}$) and $\Delta T = T - T_0$ the temperature variation.

The previous equation can also be written as:

$$R_e(T) - R_e(T_0) = R_e(T_0)\alpha_{Pt}\Delta T \qquad \textit{Eq 3.58}$$

$$\Delta R_e(T) = R_e(T_0)\alpha_{Pt}\Delta T \qquad \textit{Eq 3.59}$$

By combining Eq 3.56 and Eq 3.59, one has:

$$\Delta T = \frac{\Delta V_{it}}{I_T R_e(T_0)\alpha_{Pt}} \qquad \textit{Eq 3.60}$$

In this way, the curve $\Delta T(t)$ of the variation of the temperature of the excited electrode can be obtained with several calculations made with the acquired $V_{it}{}^*(\mathrm{t})$ curve.

#### *3.6.3.1.2. Results and analysis*

The variations of the surface temperature when thermally excited are shown in Figure 3.28 for 50 µm and 100 µm-thick LDPE samples bearing Pt electrodes in volt-off conditions. These results were obtained from the temperature signals using the expressions 3.55 and 3.60.

As it can be seen, the temperature of the excited electrode raises almost instantly when the pulse hits the sample, then starts to descend slowly, as expected taking into account the very short duration of the pulse (several ns). On the other hand, the temperature raises are very low, below 0.1 K. If we compare these results to the simulations from Chapter 2, it comes out that the real energy absorbed at the sample surface should be below 0.1 mJ, meaning that the energy really absorbed by the sample across the electrode is much smaller than that of the laser beam when it comes out from the source. This is due to the energy lost in the semi-transparent mirror and mostly in the beam expander which is used to increase the diameter of the spot to cover the whole electrode, and of course to the high reflectivity of the electrode. On the other hand, the diameter of the beam when it hits the measurement cell is slightly higher than the diameter of the electrode to ensure that the entire electrode is heated, which also diminishes the energy transferred to the electrode and thus the increase of the electrode temperature.

These experimental results confirm that even very small increases of the temperature allow to obtain fully measurable charge responses, witnessing the sensitivity of the thermal methods.

The results from Figure 3.28 also show that the temperature raise of the two electrodes, even if close, is not identical. It is clear that the energy transfer to the sample is affected by the absorbance of the two electrodes which may slightly differ (as does their resistance), and that the thermal interface between the electrode and the insulator is also likely to differ at least slightly, leading to differences in the absorption of heat by the sample.

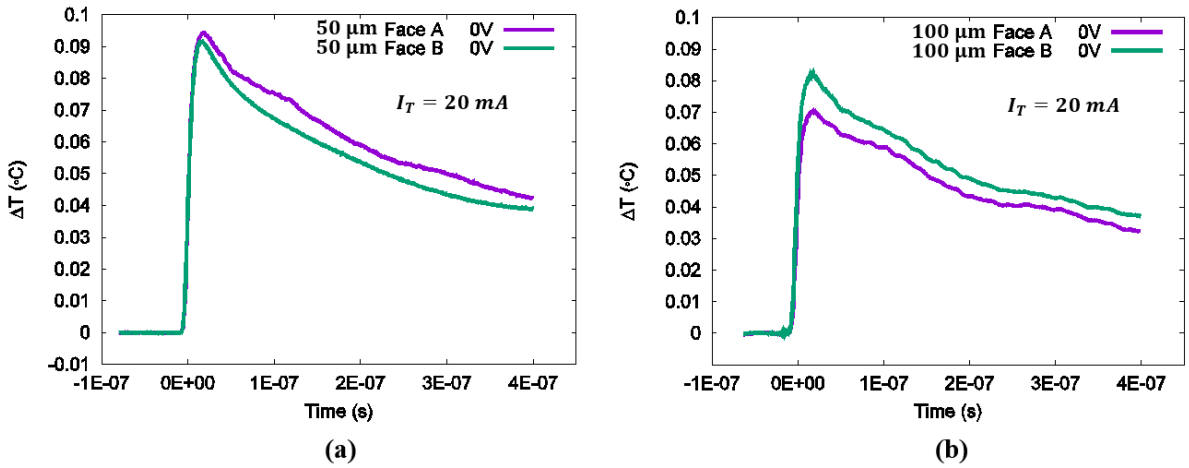


*Figure 3.28 Surface temperature variations of the thermally excited faces of 50 µm-thick (a) and 100 µm-thick (b)LDPE sample coated with Pt electrodes in volt-off conditions*

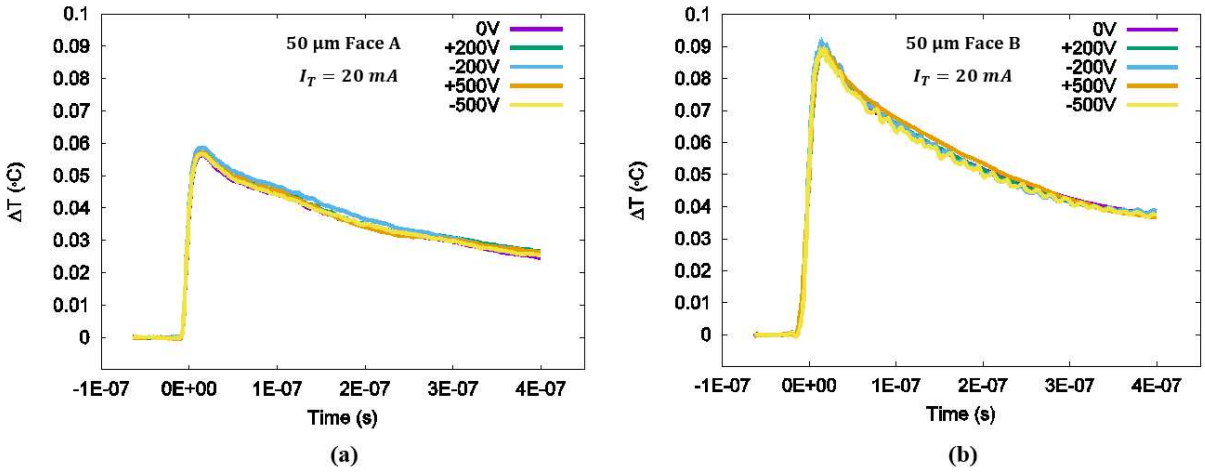


*Figure 3.29 Surface temperature variations of the thermally excited faces of a 50 µm-thick LDPE sample coated with Pt electrodes and submitted to different voltages: (a) Face A, (b) Face B*

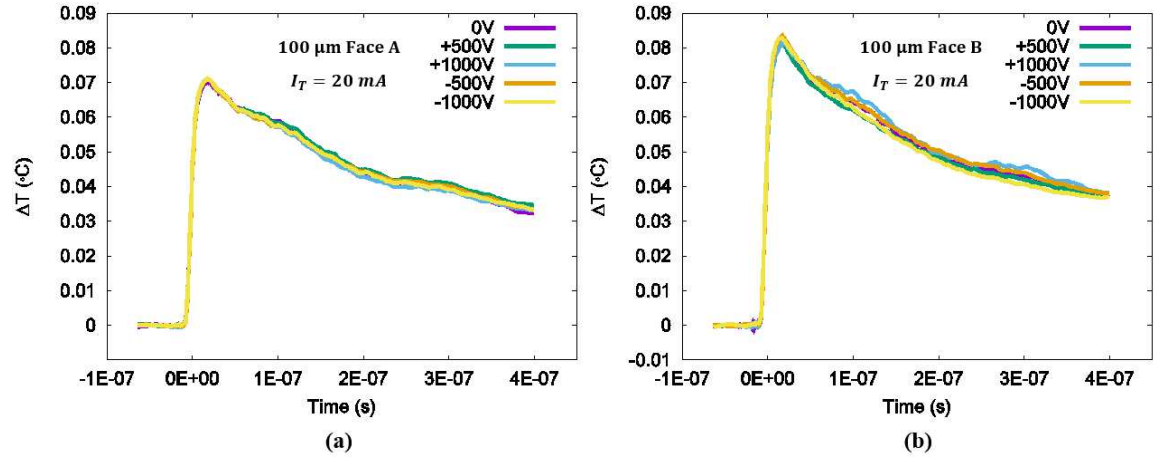


*Figure 3.30 Surface temperature variations of the thermally excited faces of a 100 µm-thick LDPE sample coated with Pt electrodes and submitted to different voltages: (a) Face A, (b) Face B*

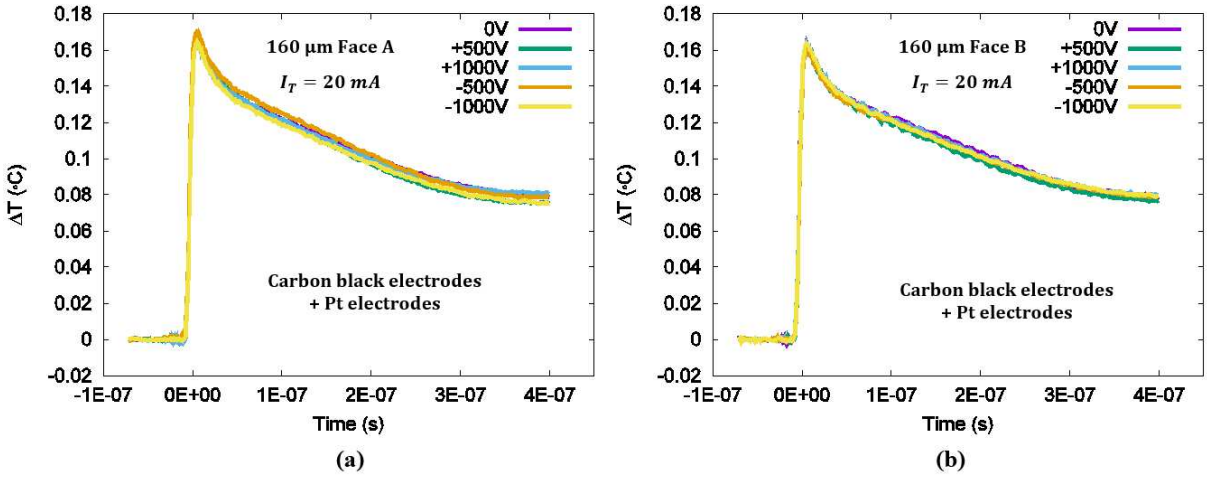


*Figure 3.31 Surface temperature variations of the thermally excited faces of a 160 µm-thick XLPE sample provided with semicon and Pt electrodes: (a) Face A, (b) Face B*

Variations of the surface temperature measured while positive and negative voltage of values between -1 kV and +1 kV are applied to samples of different thicknesses are illustrated in Figure 3.29 to Figure 3.31. They show superposable plots, proving as expected that the surface temperature measurements are not affected by the fact that the sample is polarized.

It is interesting to note that, if the temperature raises measured on the LDPE samples bearing only Pt electrodes are pretty close, in the range of 0.06 to 0.09 K, the raises are between 0.16 K and 0.18 K for the XLPE samples bearing semicon electrodes and the Pt electrodes, *i.e.* the temperature increase is multiplied by the factor of 2. This indicates that the heat transfer to the samples with semicon coatings is better and/or that the thermal resistance of the Pt/semicon interface is higher than that of the Pt/XLPE one.

In a general way, the performed measurements show temperature increases between 0.06 and 0.18 K, specific to each sample and to each electrode/face. The observed differences are obviously not a problem in terms of modelling or processing the acquired signals, as the real

temperature variation of the heated surface is measured each time, making unnecessary the knowledge of the beam energy and of the absorption coefficient of the surface (which is anyway very hard to determine), and allowing to make repeatability issues of a much smaller concern.

#### *3.6.3.2. Volume Temperature*

##### *3.6.3.2.1. Equations*

When a semi-infinite plane domain is heated on the surface by an energy per surface unit $q(t)$ [J/m$^2$], the temperature variation at the instant *t* at a depth *x* from the surface (of coordinate $x = 0$), obtained by solving the heat equation, reads [143]:

$$\Delta T(x,t) = q(t) * \frac{e^{\frac{-x^2}{4Dt}}}{M_v C_p \sqrt{\pi D t}} \qquad \textit{Eq 3.61}$$

where the operator * stands for the convolution product (Eq 3.44), *D* is the thermal diffusivity of the medium, $M_v$ its density and $C_p$ its specific heat. Thus, the surface temperature is given by:

$$\Delta T(x=0,t) = \Delta T_0(t) = q(t) * \frac{1}{M_v C_p \sqrt{\pi D t}} \qquad \textit{Eq 3.62}$$

As shown in [143], as the Laplace transform of $1/\sqrt{\pi t}$ is $1/\sqrt{p}$, with *p* the Laplace variable, *q(t)* can be obtained from (Eq 3.62) via the Laplace transform of:

$$q(p) = \Delta T_0(p)\, M_v C_p \sqrt{Dp} \qquad \textit{Eq 3.63}$$

which reads:

$$q(t) = M_v C_p \sqrt{\frac{D}{\pi t}} * \frac{\partial \Delta T_0(t)}{\partial t} \qquad \textit{Eq 3.64}$$

By inserting Eq 3.64 in Eq 3.61, it comes out:

$$\Delta T(x,t) = \sqrt{\frac{1}{\pi t}} * \frac{\partial \Delta T_0(t)}{\partial t} * \frac{e^{\frac{-x^2}{4Dt}}}{\sqrt{\pi t}} \qquad \textit{Eq 3.65}$$

which can be expressed for all $x > 0$, after some calculations, as:

$$\Delta T(x,t) = \Delta T_0(t) * \frac{x e^{\frac{-x^2}{4Dt}}}{2\sqrt{\pi D t^3}} \qquad \textit{Eq 3.66}$$

*i.e.*:

$$\Delta T(x,t) = \frac{1}{2\sqrt{\pi D}} \int_{-\infty}^{\infty} \Delta T_0(\tau) \frac{x e^{\frac{-x^2}{4D(t-\tau)}}}{\sqrt{(t-\tau)^3}} d\tau \qquad \textit{Eq 3.67}$$

for $\tau < t$, and as $t > 0$:

$$\Delta T(x,t) = \frac{1}{2\sqrt{\pi D}} \int_0^t \Delta T(x=0,\tau) \frac{x e^{\frac{-x^2}{4D(t-\tau)}}}{\sqrt{(t-\tau)^3}} d\tau \qquad Eq\ 3.68$$

#### *3.6.3.2.2. Results and analysis*

Figure 3.32 to Figure 3.37 present the temperature variations with time in the bulk of 50 µm and 160 µm-thick samples, computed by using the time variations of the measured temperatures at the excited electrodes $\Delta T(x=0,t)$ and Eq 3.68.

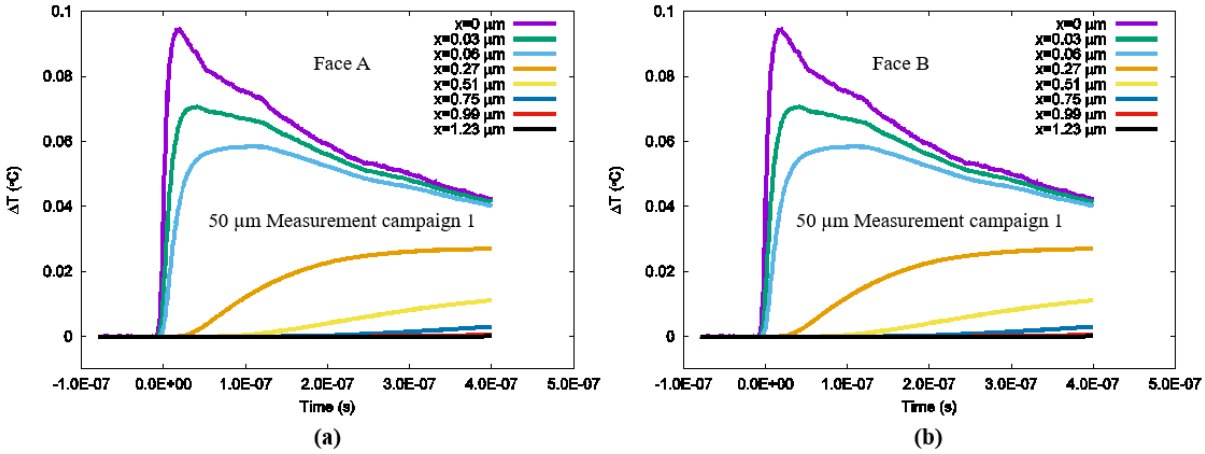


*Figure 3.32 Temperature variations with time at different depths from the excited electrodes of a 50 µm-thick LDPE sample: (a) Excitation applied to Face A, (b) Excitation applied to Face B. Measurement campaign 1. Volt-off conditions.*

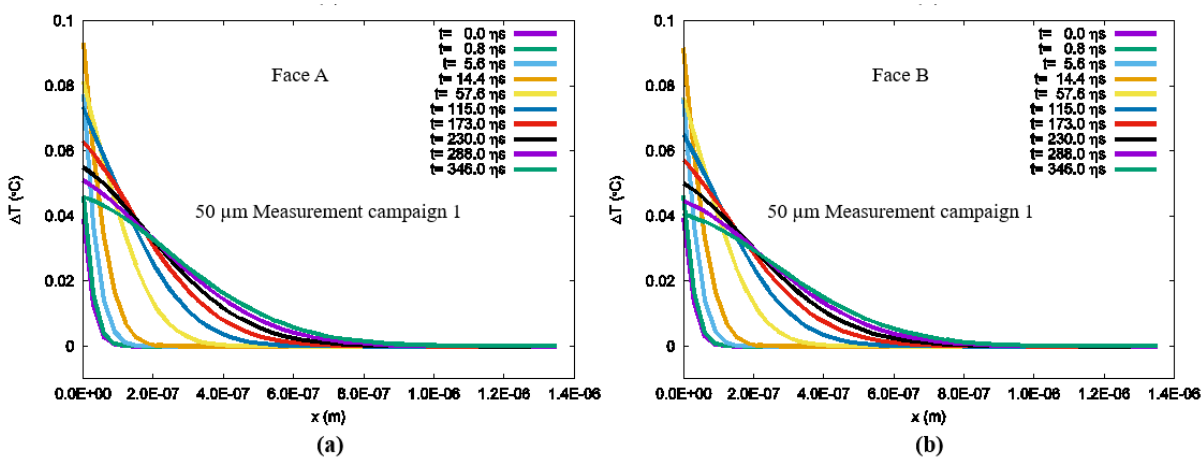


*Figure 3.33 Temperature distributions across a 50 µm-thick LDPE sample at different moments after thermal excitation of Face A (a) and Face B (b). Measurement campaign 1. Volt-off conditions.*

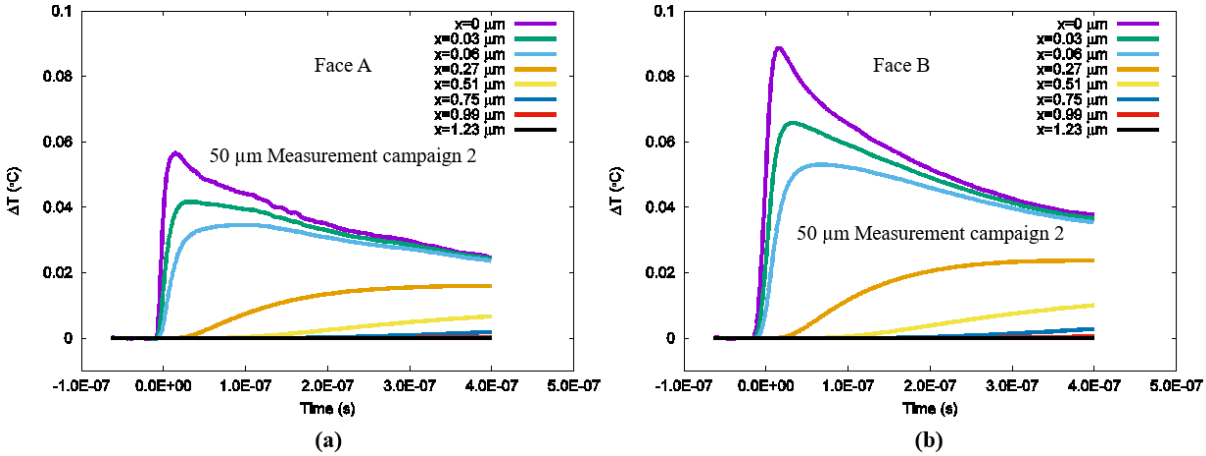


*Figure 3.34 Temperature variations with time at different depths from the excited electrodes of a 50 µm-thick LDPE sample: (a) Excitation applied to Face A, (b) Excitation applied to Face B. Measurement campaign 2. Volt-off conditions.*

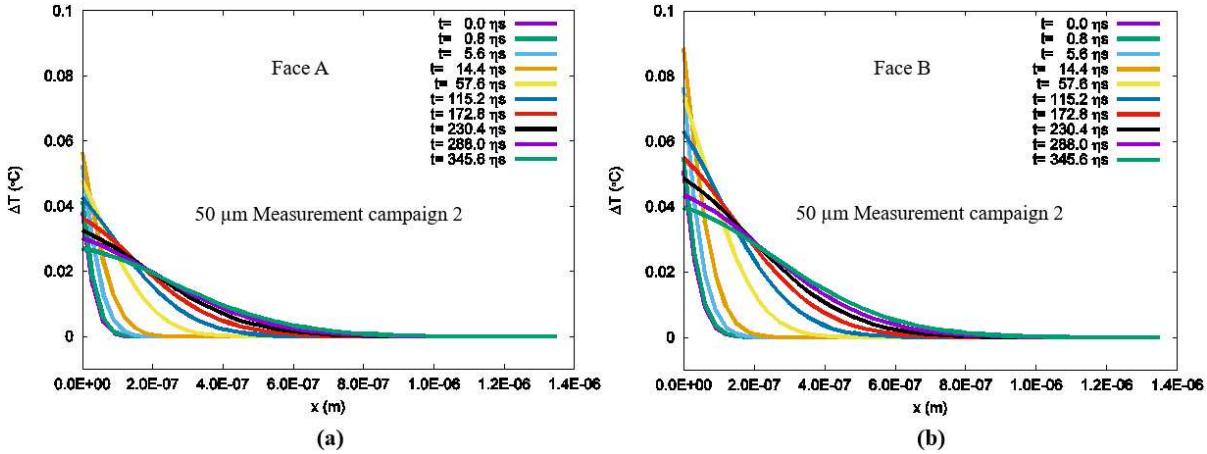


*Figure 3.35 Temperature distributions across a 50 µm-thick LDPE sample at different moments after thermal excitation of Face A (a) and Face B (b) of. Measurement campaign 2. Volt-off conditions.*

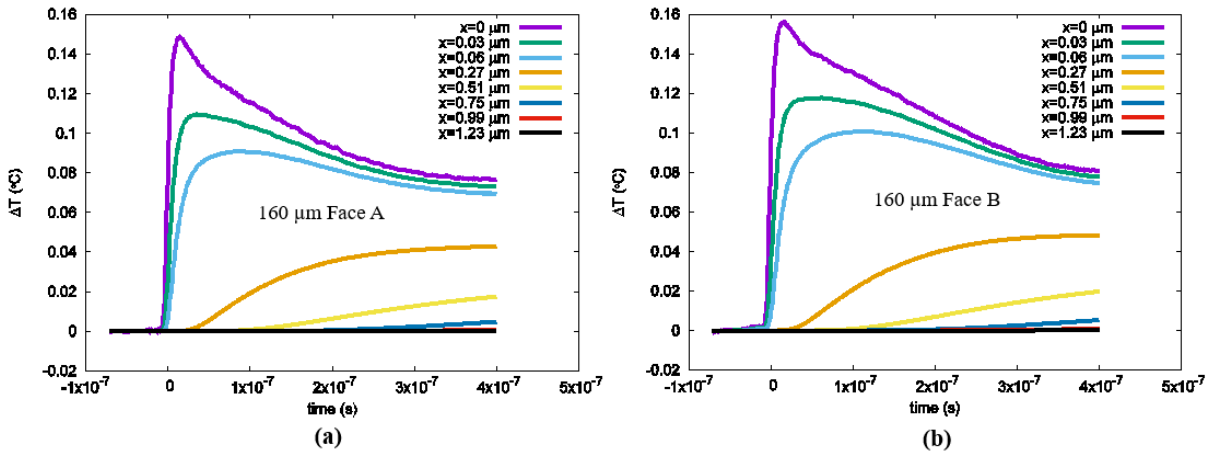


*Figure 3.36 Temperature variations with time at different depths from the excited electrodes of a 160 µm-thick XLPE sample provided with carbon-black electrodes:*
*(a) Excitation applied to Face A, (b) Excitation applied to Face B. Volt-off conditions.*

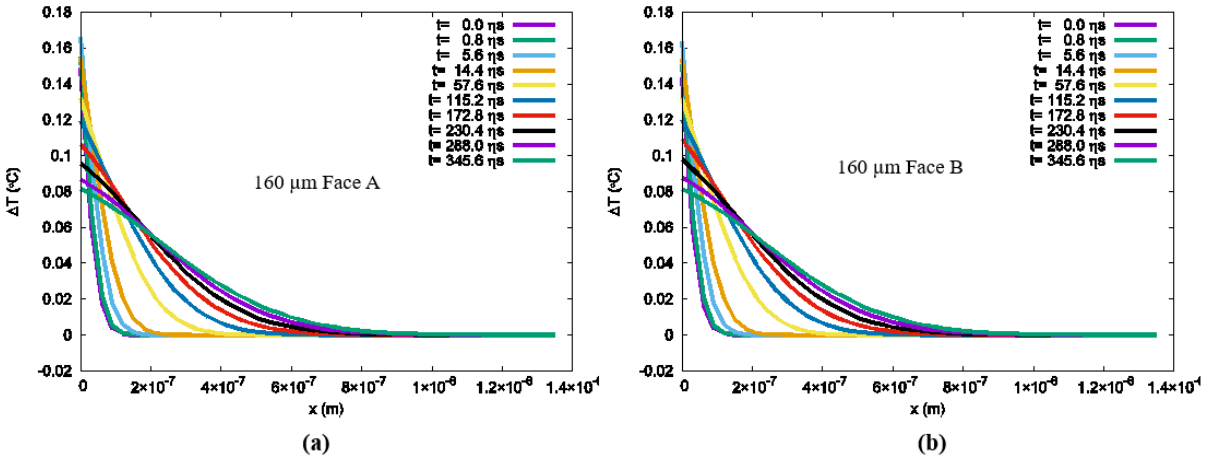


*Figure 3.37 Temperature distributions across a 160 µm-thick XLPE sample provided with carbon-black electrodes at different moments after thermal excitation of Face A (a) and Face B (b) of. Volt-off conditions.*

The figures show that most of the temperature variation in the sample bulk during the major part of the duration of the measured signals (*i.e.*, 0.5 µs) occurs mainly across the first µm. Indeed, the time variation of the temperature at 0.99 µm and 1.23 µm is almost nil during the first 0.5 µs (Figure 3.32, Figure 3.34 and Figure 3.36). Alternatively, the plots from Figure 3.33, Figure 3.35 and Figure 3.37 put into evidence that, after 0.346 µs, the temperature variation beyond 1.4 µm falls significantly, approaching practically zero, whatever the sample. In the same time, this allows to validate, as expected, the "semi-infinite" plane approach used for the determination of the temperature distribution, as during the measurement the temperature varies only for depth coordinates much smaller than the thickness of the samples (which is at least 50 µm).

In the case the XLPE samples provided with semicon electrodes, the temperature variation occurring at depths of no more than 1.4 µm during the measurement, as shown in Figure 3.37, it comes out that the thermal wave does certainly not cross the semicon thickness (30 µm) to reach the insulator, so the electric field present in the insulating thickness is not "scanned" by the thermal wave. Consequently, there is no contribution of the field across the insulation to the charge signal, which is due only to the field present on the 1 to 2 µm at the interface between the Pt layer and the semicon layer. This brings a supplementary confirmation that the charge signals issued by the samples with semicon electrodes are due to the field at the interface between the metal and the semicon, and not to the field at the semicon/insulator interface or in the bulk of the dielectric.

To synthesize, these results show that the temperature variation in the studied samples occurs only on a very limited depth of 1 to 2 µm near the thermally excited surface, so the charge signals are images of the interface fields, and there is practically no contribution of the bulk fields.

On another level, Figure 3.33 and Figure 3.35 corresponding to the same sample characterized at two different moments separated by several months, show different temperature distributions in the vicinity of Face A, whereas very similar repartitions are observed near Face B. This illustrates the evolution of the thermal absorption properties of one of the electrodes, while the

other did not evolve, underlining once more the interest of measuring systematically the electrode temperature simultaneously with the charge signal.

## 3.6.4. Determination of interface fields

### *3.6.4.1. Charge signals and dependence of the field across the sample*

Examples of TPM signals derived from the measured charge signals after obtaining the $V_{CH}^{*}$ quantities by using the decoupling procedure from Section 3.5 and Eq 3.30 are illustrated in Figure 3.38 and Figure 3.39.

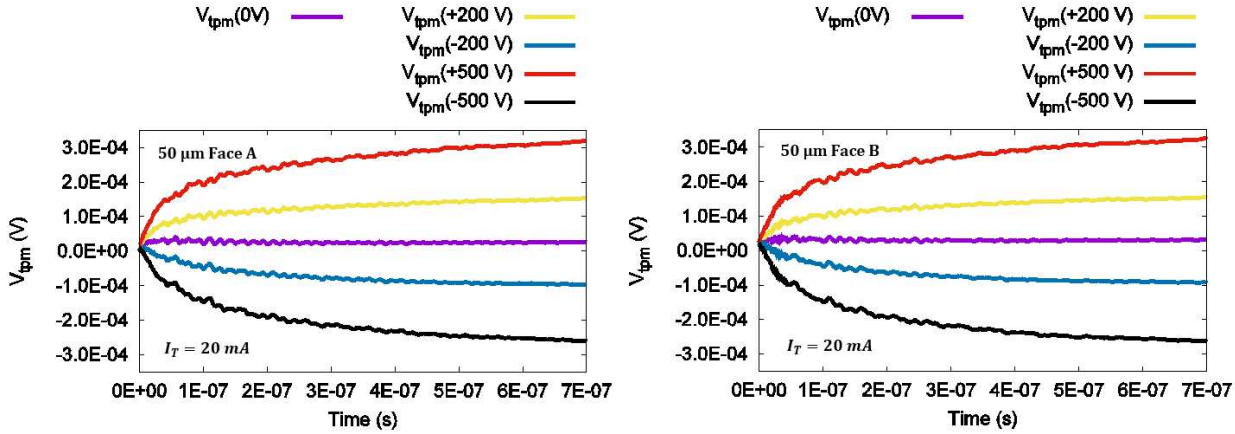


*Figure 3.38 Volt-on and volt-off TPM signals issued by a 50 µm sample: Thermal stimulus applied on Face A (a) and on Face B (b)*

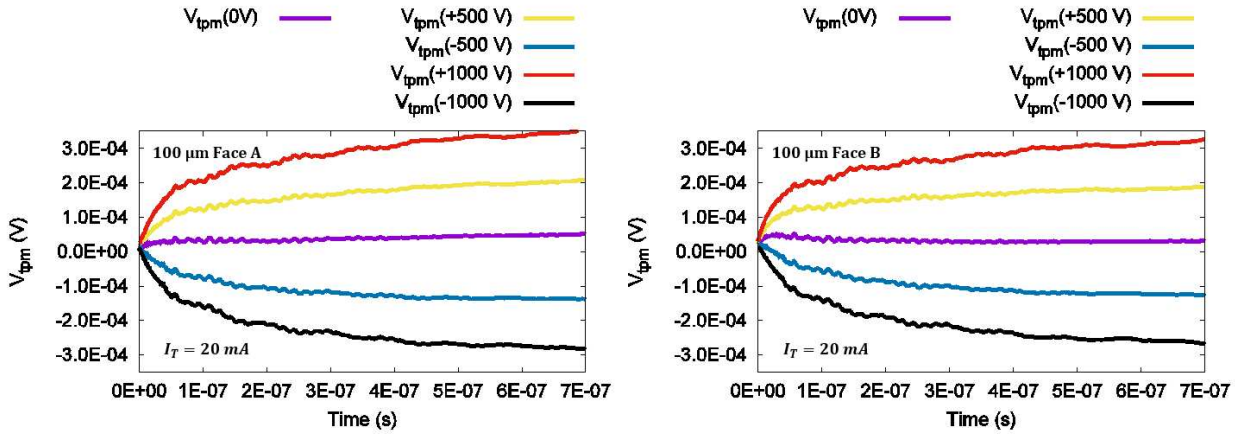


*Figure 3.39 Volt-on and volt-off TPM signals issued by a 100 µm sample: Thermal stimulus applied on Face A (a) and on Face B (b)*

Each signal is related to the distribution of the electric field across the sample $E(x)$ at the moment when it was acquired through the relationship 1.56, *i.e.*:

$$V_{TPM}(t) = -\alpha \int_0^d E(x)\,\Delta T(x,t)dx \qquad \textit{Eq 3.69}$$

where $\Delta T(x,t)$ is the spatio-temporal temperature distribution of the temperature across the sample, $\alpha$ the coefficient of variation of permittivity and abscissae of the thermally excited region (Eq 1.37 – Eq 1.38 and the explanations around them) and *d* the sample thickness ($x \in [0,d]$).

It is to note that $E(x)$ is the total field across the sample during the measurement. Thus, if the sample contains, in volt-off conditions, a residual field $E_{residual}(x)$, when a voltage $V_{pol}$ is applied to the sample, and if this applied voltage is low enough to prevent charge injection or detrapping of the charge already present in the sample, the theorem of superposition applies and the total field $E(x)$ in volt-on conditions under the voltage $V_{pol}$ reads:

$$E(x) = E_{residual}(x) + E_{pol}(x) \qquad \textit{Eq 3.70}$$

where $E_{pol}(x) = \frac{V_{pol}}{d}$ is the applied field. Consequently, Eq 3.70 can be written as:

$$V_{TPM}(t) = -\alpha \int_0^d \left[E_{residual}(x) + \frac{V_{pol}}{d}\right] \Delta T(x,t)dx$$

$$V_{TPM}(t) = -\alpha \int_0^d E_{residual}(x)\, \Delta T(x,t)dx - \alpha \int_0^d \frac{V_{pol}}{d}\, \Delta T(x,t)dx$$

$$V_{TPM}(t) = V_{TPM}(Q, V=0) + V_{TPM}\left(Q=0, V=V_{pol}\right) \qquad \textit{Eq 3.71}$$

The first term $V_{TPM}(Q, V=0)$ corresponds to the residual field, while the second $V_{TPM}\left(Q=0, V=V_{pol}\right)$ corresponds to the applied field, and as $\frac{V_{pol}}{d}$ is a constant, the second term is proportional to the temperature integral:

$$V_{TPM}\left(Q=0, V=V_{pol}\right) = -\alpha \frac{V_{pol}}{d} \int_0^d \Delta T(x,t)dx \qquad \textit{Eq 3.72}$$

This term can be isolated by subtracting the signal measured in volt-off conditions from the signal measured in volt-on conditions under a moderate applied field, after which one can obtain the coefficient $\alpha$, as all the other quantities from Eq 3.72 are measured ($V_{TPM}$ and $\Delta T$) or known ($V_{pol}$ and *d*). This coefficient can subsequently be used in Eq. 3.69, allowing to determine the residual field from the volt-off signal or from a volt-on signal under high field.

### *3.6.4.2. Calibration signals and determination of the coefficient α*

From Eq 3.71, it comes out that:

$$V_{TPM}\left(Q=0, V=V_{pol}\right) = V_{TPM}\left(Q, V=V_{pol}\right) - V_{TPM}(Q, V=0) \qquad \textit{Eq 3.73}$$

By replacing the left term with its expression from Eq 3.72, one gets:

$$-\alpha \left(\frac{V_{pol}}{d}\right) \int_0^d \Delta T(x,t)dx = V_{TPM}\left(Q, V=V_{pol}\right) - V_{TPM}(Q, V=0) \qquad \textit{Eq 3.74}$$

$$\alpha = -\frac{V_{TPM}(Q,V=V_{pol}) - V_{TPM}(Q,V=0)}{\left(\frac{V_{pol}}{d}\right)\int_0^T \Delta T(x,t)dx} \qquad Eq\ 3.75$$

Thus, by dividing the "calibration signal" $V_{cal} = V_{TPM}(Q = 0, V = V_{pol})$ by the factor from the above fraction, the value of $\alpha$ can be obtained. In Figure 3.40 and Figure 3.41, calibration and volt-off signals obtained on 50 µm and 100 µm LDPE samples are presented.

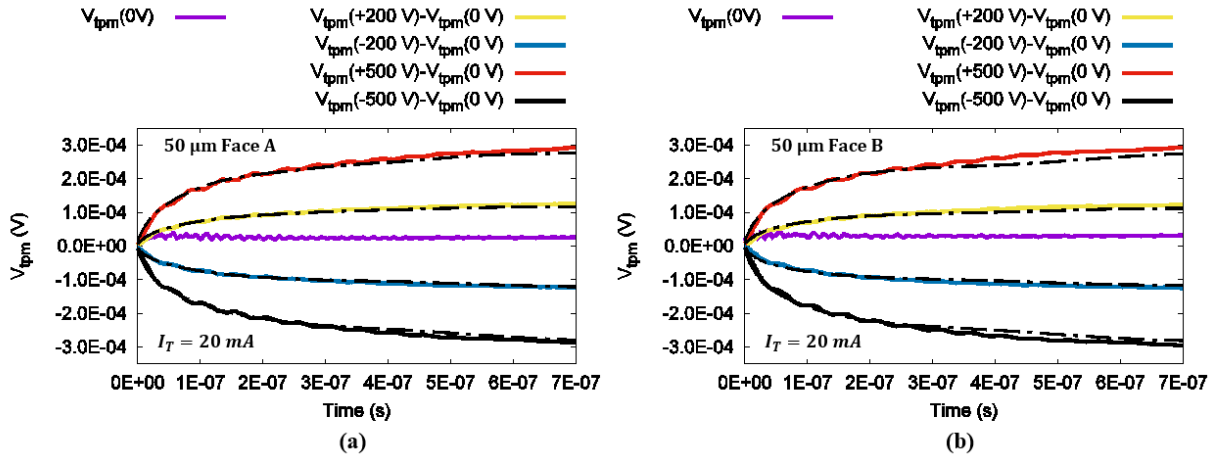


*Figure 3.40 Calibration signals and volt-off signals corresponding to a 50 µm sample: Stimulus applied on Face A (a) and on Face B (b). The dotted curves correspond to signals recalculated after determining the value of α.*

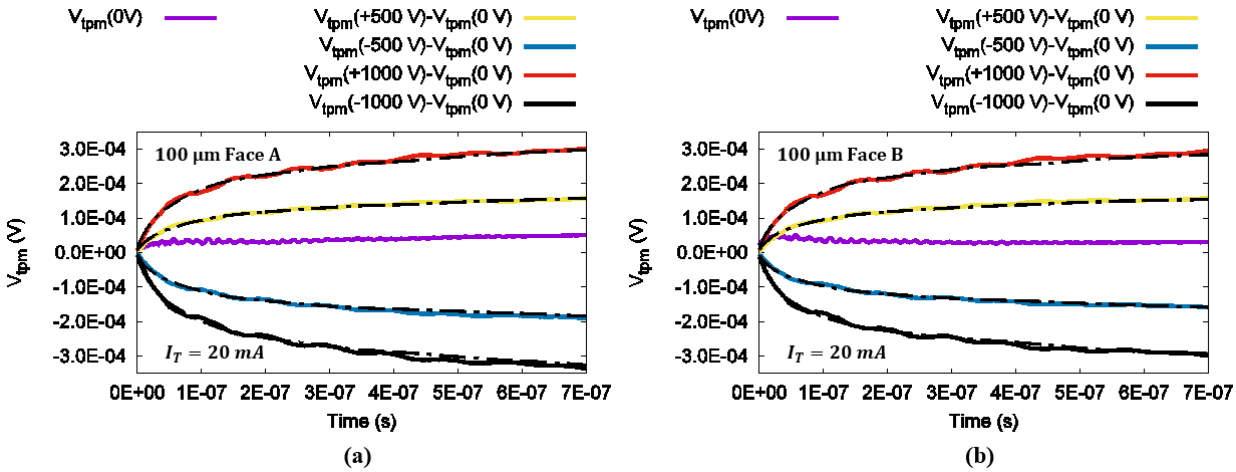


*Figure 3.41 Calibration signals and volt-off signals corresponding to a 100 µm sample: Stimulus applied on Face A (a) and on Face B (b). The dotted curves correspond the signals recalculated after determining the value of α.*

The calibration signals are almost perfectly proportional to the voltage amplitude and symmetrical when the voltage sign is reverted, so the hypothesis that the values of the applied field has no effect on the charge state of the studied sample is fully verified, and Eq. 3.75 can be used for determining $\alpha$. This gives, by taking into account that when a positive potential is applied to the electrode opposite to the excited one a negative field is seen by the thermal wave,

a value of $\alpha = 2.65 * 10^{-3}K^{-1}$ for a 50 µm-thick sample (with a small deviation of several % with respect to the voltage at which it has been determined, Table 3.3). The same value is obtained for 100 µm-thick samples. This underlines that the value of $\alpha$ is characteristic of the interface set up between the two materials (LDPE and Pt), which depends on their nature but also on the surface state and on the deposition process.

*Table 3.3 Coefficient α determined from different calibration signals issued by a 50 µm-thick LDPE sample with Pt electrodes*

| $V_{pol}$ | $\alpha$ | Mean value of $\alpha$ |
|---|---|---|
| + 200 V | $2.91 * 10^{-3}K^{-1}$ | $2.65 * 10^{-3}K^{-1}$ |
| - 200 V | $2.60 * 10^{-3}K^{-1}$ | |
| + 500 V | $2.40 * 10^{-3}K^{-1}$ | |
| - 500 V | $2.70 * 10^{-3}K^{-1}$ | |

### *3.6.4.3. Determination of interface fields*

The equation (Eq. 3.69) can be solved for determining the electric field distribution $E(x)$, as discussed in section 1.4.2.2.2. In order for the obtained field distributions to have a reasonable physical meaning, the homogeneity of the sample must be better than the expected resolution. In the case of the studied samples, the homogeneity in the thickness direction is more or less of the micron order, and the penetration depth of the thermal stimulus is in the same range (1-2 µm). Thus, even if the mathematical processing of the TPM signal is possible, the physical meaning of a field distribution deduced in these conditions may be debatable. However, in the first moments of the application of the thermal stimulus, when this latter is not much dampened, the stimulus acts like a wave and the thermal pulse signal is proportional to the encountered field, which allows to determine the interface field.

In other words, the mean value theorem can be used to obtain the interface field. Thus, for any couple of functions *f* and *g* of a real variable *x* which are continuous on an interval [*a*, *b*], with $a < b$, if *g* keeps a constant sign on [*a*, *b*], there is a real value of *x* namely $x_i \in [a, b]$ so as:

$$\int_a^b f(x)g(x)dx = f(x_i)\int_a^b g(x)dx \qquad \textit{Eq 3.76}$$

If we apply this theorem to the thermal pulse signal equation (Eq. 3.69), by putting $f(x) = E(x)$ and $g(x) = \Delta T(x,t)$, it comes out that at every instant *t* the value of $V_{TPM}(t)$ is the product of a particular value of the field $E(x_i)$ in the sample by the integral of the thermal stimulus:

$$V_{TPM}(t) = -\alpha E(x_i)\int_0^d \Delta T(x,t)dt \qquad \textit{Eq 3.77}$$

When $t \to 0$, $x_i \to 0$ (as the rest of the sample has not been thermally scanned yet) and the stimulus is few dampened, so the values of the signal at the beginning of the measurement give the values of the field near the interface.

In Figure 3.42 and Figure 3.43 has been plotted the quantity (for $t \leq 0.4$ µs):

$$E(x_i) = E(t) = \frac{V_{TPM}}{-\alpha \int_0^d \Delta T(x,t)dt} \qquad Eq\ 3.78$$

for 50 µm and 100 µm-thick LDPE samples with Pt electrodes. As it can be seen, this gives interface fields between 3 and 10 kV/mm, with respect to the sample and the excited interface. The obtained values are close whatever the sample thickness, so it can be concluded that they are characteristic of the material surface state and of the metal/insulator couple.

If we take into account the homogeneity of the sample (which is not exactly known, but believed to be more or less of the micron order) and the penetration depth of the temperature, which is of the micron order during the considered time, it is likely that these field values $E(t)$ are combinations of very localised fields at different locations on the surface and across the penetration depth. However, the obtained results prove that by a direct method the existence of electric fields of several kV/mm at the metal/insulator interface, in the absence of any previous electrical stress applied to the material (as the samples have never been stressed electrically, except by the application of the calibration voltages, which do not inject or detrap space charge). Such results can be cross-correlated with others obtained with longer pulses or with more bulk-oriented techniques, like the TSM, to obtain an extended domain of charge measurement from the vicinity of electrodes toward the bulk. On the other hand, these results clearly show that resolutions below the micron, accompanied by the values of the local field (and not only by distributions given in arbitrary units) are at reach on samples for which the structural homogeneity is below the micron scale.

The same quantity $E(t)$ is plotted in Figure 3.44 for a 160 µm-thick XLPE sample provided with semicon and Pt electrodes, *i.e.* corresponding to the interface between the Pt and the semicon. An inversion of the field is observed near both faces, in contrast with the results obtained at the Pt/LDPE interface, where there is no field reversal. This inversion is the image of a different charge distribution, with presumably an extension of a charge zone of a different sign in the semicon. This is a very interesting result but, as for the case of the Pt/LDPE interface, it is difficult to speculate further, as the homogeneity of the interface is not known but presumably not far from the penetration depth of the thermal wave. Nevertheless, it is clear that using this setup on highly homogeneous samples will help to approach much closer the interface phenomena.

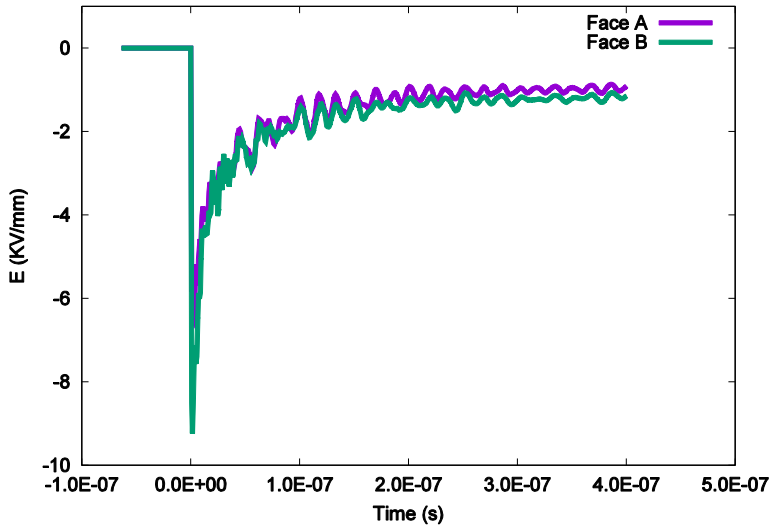


*Figure 3.42 Quantity E(t) as an image of the electric field at the interface zone of a 50 µm-thick LDPE sample with Pt electrodes*

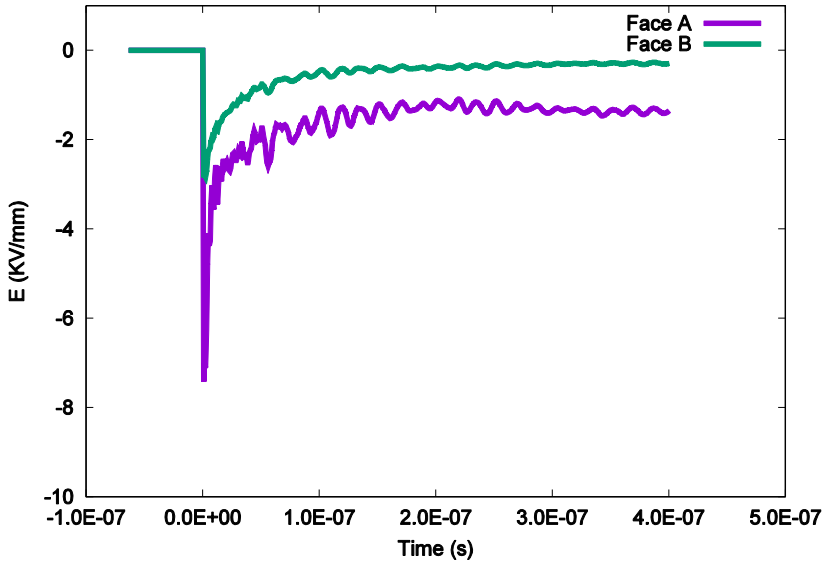


*Figure 3.43 Quantity E(t) as an image of the electric field at the interface zone of a 100 µm-thick LDPE sample with Pt electrodes*

Concerning the values of the field in this configuration, the curves from Figure 3.44 have been obtained by considering the α coefficient of the semicon of the same value as the one measured in LDPE, because it was not possible to obtain calibration signals for the semicon, as these signals did not vary when voltage was applied (section 3.5.2.2.2 and the analysis herein). It is therefore possible that the real values are lower than those from Figure 3.44 (as the $\alpha$ coefficient may be higher), but probably not much below the kV/mm. A more precise determination of the field values will require to adapt the calibration method or to use an alternative one to determine the $\alpha$ coefficient for low resistive materials like semicon.

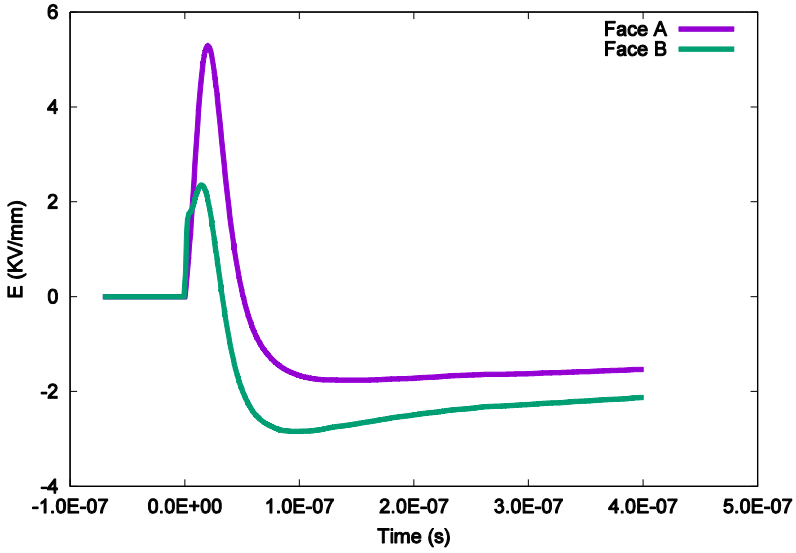


*Figure 3.44 Quantity E(t) as image of the electric field at the interface zone of a 160 µm-thick XLPE sample with semicon electrodes and Pt layers deposited on the semicon electrodes, i.e. at the Pt/semicon interface. A value of α equal to the one determined for LDPE has been considered.*

## 3.7. Conclusions

Experimental results obtained on LDPE and XLPE samples of thicknesses between 50 µm and 160 µm, thermally excited with 5 ns-width thermal pulses, were presented, modelled and discussed.

Transient voltage responses, depending on the temperature of the thermally excited surface and on the electric field distribution across such samples, have been measured simultaneously, by using thin metallic films both as electrical contacts (electrodes) and as temperature sensors. The temperature and charge measurement circuits being coupled through the sample itself, the acquired responses are sums of contributions of temperature signals, internal field signals and applied field signals. Therefore, procedures allowing to separate the different signals have been established and validated experimentally. An in-depth high frequency electrical analysis of the measurement circuit made it possible to extract, by considering the transfer functions and the decoupling procedures, accurate bolometric and electric field signals.

The temperature variation of the heated surface has thus been obtained experimentally from the bolometric response, which is directly proportional to the electrode temperature variation via the electrode resistance. The real temperature distributions across the samples during the thermal pulse measurement were then determined via the heat equation, showing temperature elevations well below the degree and penetration depths of the thermal stimulus of one to two microns in the conditions of the experiments. These results demonstrate experimentally that even very small temperature increases enable for fully measurable electric field responses, proving the sensitivity of thermal methods.

Using a calibration process based on the application of low electric fields (which were proven not to affect the electrical state of the samples) and the temperature distributions determined

during the related measurements, the coefficient of variation of permittivity and abscissae of the material was calculated. Through all these crossed experiments and procedures, we have proved that full access to the thermal and electrical parameters of the sample can be obtained at the moment of the space charge measurements, allowing to significantly increase the confidence in the electric field results to be extracted from the transient signal issued by the sample when excited by the heat pulse.

With the aid of the obtained temperature distributions and of the calibration signals, the values (of several kV/mm) and the images of the electric field at Pt/LDPE and Pt/semicon interfaces were determined from the electric field signals. These results demonstrate that it is possible to evaluate with a TPM setup not only metal/insulator interfaces but also interfaces between metals and low resistive media, which, given the high sensitivity of thermal methods, may lead to interesting technological prospects.

# Conclusions & Perspectives

The overstress of dielectrics is often due to the accumulation of electrical charges (space charges), which cause electric field distortions. In order to set up new materials and to optimize insulating structures, accurate measurements of these space charges are required.

The aim of this thesis was to contribute to the development of non-destructive space charge measurement techniques, to allow a better understanding of the establishment and evolution of space charge zones in materials and at interfaces, which are the weak points of insulating structures. In particular, the objective of the work was to assess the feasibility and the fallouts of the principle of the Thermal Pulse Method (TPM) for space charge measurements in medium thickness insulating samples, for a resolution as close as possible to the degree of homogeneity of the interfaces (in the micrometer range).

The issues involved in the development of HVDC networks and the problems of the dielectrics subjected to high fields have been first addressed. As thermal methods have better sensitivities and spatial resolutions near the excited surface of the characterized sample, the principle of the TPM was targeted. The use of the TPM is of interest particularly for determining interface fields, because the resolution of the TPM near the interface is the best of all techniques, and the non-contact mode of application of the stimulus is potentially a significant asset for characterizing samples under electro-thermal or other types of stress. In the same time, recent advances have demonstrated that temperature signals coming from the thermally excited electrode can be acquired concurrently with the space charge signal, hopefully allowing to gather more accurate information of the thermal stimulus, to increase the accuracy of the space charge measurements. These facets were the focus of the thesis.

The following elements can be highlighted from the presented work:

- The accomplished simulations and experiments allowed to confirm the applicability of the TPM on medium thickness insulating samples, in order to be able to characterize objects with structures and morphologies as close as possible to those that can be found in electrical engineering components. The use of pulses with durations of several nanoseconds and energies in the milli joule range and even below allows to scan micron-large depths, whereas wider stimuli of higher energies allow scanning thicknesses of several dozens of microns. Estimations of temperature raises and of TPM signals expected for different stimuli were given for internal fields in the range of the kV/mm in order to approach the limits of employment of the studied principle on insulating thicknesses of several dozens of microns.

- The experimental work, concerned with the simultaneous measurement, modelling and analysis of transient signals issued, on one hand, from the temperature variation of the thermally excited electrode used as a bolometer, and on the other hand from the response of the electric field across the sample, confirmed the imbrication of temperature, field and calibration signals, putting into focus the need for their decoupling. We have carried out an extended analysis by taking into account the entire measurement circuit, which made it possible to determine accurate expressions and separation processes for the bolometric and space charge responses.

- With the aid of the decoupling techniques and analysis tools, we were able to show that it is possible to go directly to the quantitative time evolution of the surface temperature, which we determined for each measurement, on several types of samples and interfaces. This allowed to obtain through direct measurements, not only qualitatively but also, for the first time, quantitatively, the real temperature distribution across the sample during the measurement of the electric field.

- The extraction of material parameters through a calibration protocol and the employment of the temperature distribution obtained with the bolometric measurements allowed to determine the quantitative values and the images of interface fields. These results obtained through a direct method, by considering for the first time the real temperature in the sample, confirmed that fields of several kV/mm can exist at the metal/polyethylene interface, even in the absence of a previous electrical conditioning.

- The use of the TPM on XLPE samples provided with semicon electrodes showed that the technique can be employed not only to measure the space charge in insulating materials and at their interfaces, but also for field measurements at metal/semicon interfaces. These results, that previous studies on MOS structures foreshadowed, and which were validated in this work by several methods, prove clearly that the principle of a thermal method is applicable to low resistive media and their interfaces.

It is to note that many conclusions drawn from this work are applicable to a large variety of thicknesses and materials. Thus, the above issues give leads for further work which, given the sensitivity of the thermal methods, should trigger interesting developments in the future.

As far as materials for HVDC are concerned, the simulations suggest that the use of wider pulses (of several microseconds or more) and of higher energies, which are available, for instance, with flash lamps, should allow to detect the field at semicon/insulator interfaces placed after semicon electrodes of several dozens of microns in thickness. On the other hand, the non-contact heating principle of the TPM could be used, with the associated analysis tools shown in this thesis, for monitoring samples while submitted to long-term ageing under thermo-electrical stress, to detect low variations of field at interfaces. Even for offline characterization, taking into account the low temperature raise needed to obtain TPM signals, the use of TPM alone or in complement to more bulk-oriented techniques (like the TSM) can be an interesting tool to have a complete image of the field distribution with a detailed insight into the interface areas.

The present study brought experimental data to support the fact that submicronic resolutions are clearly at reach, obviously on materials with a compatible degree of homogeneity. Thus, the use of the TPM on thinner materials (several microns and below) should allow to better characterize the interfaces, at a submicronic scale, to increase the knowledge of physical phenomena taking place at the interfaces under high fields. On another plan, measurements at such scale will certainly find applicability to biological material.

The applicability of the TPM to semiconducting materials put into evidence in this work can have fallouts in the electronics domain. Thus, such measurements can be used to obtain the real

field distributions at the metal/oxide and semiconductor/oxide interfaces, which are key points of the functioning and reliability of most of the today's electronic devices.

Through this work, we have attempted to make our contribution at the characterization and the understanding of phenomena occurring in the materials for use under high dc fields. This belongs to a framework of studies carried out jointly by scientists and industrialists to allow the increase of constraints in materials and systems and the reduction of their costs, in order to promote energy transition and industrial renewal.

# Résumé

La croissance industrielle des pays émergents et la nécessité d'agir fortement contre les facteurs de pollution demandent aujourd'hui une évolution de l'architecture des réseaux électriques pour répondre aux besoins du futur. Ainsi, on assiste à une augmentation continue du nombre d'installations de production d'énergie "propre" de forte puissance (hydraulique, solaire, éolienne) situées à des endroits de plus en plus éloignés des centres de consommation. Les réseaux de transport à haute tension, établis et développés depuis plus d'un siècle, sont le principal moyen d'acheminer l'énergie électrique, indispensable aux activités de la société, vers les utilisateurs. Pour accompagner cette transition énergétique et répondre aux besoins futurs, de nouveaux moyens de transport de l'énergie sont nécessaires.

L'énergie électrique est aujourd'hui transportée en grande partie par des réseaux en courant alternatif. Or, le développement des "super-grids", destinés à transporter cette énergie sur de très longues distances, est indissociable du développement d'équipements haute tension à courant continu (HTCC). Ainsi, au-delà d'une certaine distance, qui peut aller de quelques dizaines à plusieurs centaines de kilomètres, la transmission en courant continu est économiquement supérieure à la transmission en courant alternatif. De plus, le courant continu permet de connecter des réseaux non synchronisés ou ayant des fréquences différentes, via des stations de conversion basées sur l'électronique de puissance. Enfin, comme les effets capacitifs limitent l'utilisation des câbles à haute tension en courant alternatif à quelques dizaines de kilomètres, les réseaux en courant continu sont particulièrement bien adaptés à la transmission par câbles sous-marins et terrestres sur de très longues distances. Le transport d'électricité en HTCC est important dans le réseau électrique mondial actuel et le restera à l'avenir, notamment pour le transport d'électricité à haute tension, à grande capacité et sur de longues distances. Les prévisions prévoient une forte augmentation de la capacité (6 GW sur 3000 km au lieu de 2 GW sur 600 km aujourd'hui), d'où la nécessité de tripler les tensions actuelles. Pour cela, il est nécessaire de développer de nouveaux câbles et accessoires, avec des isolants polymères. Le principal obstacle à ce développement est lié à la mise au point de matériaux et de structures aux propriétés adaptées aux contraintes de la HTCC.

La fiabilité des systèmes du génie électrique où l'on rencontre des forts champs électriques continus et des températures élevées est liée à l'apparition et au développement de zones de charges électriques au niveau des couches diélectriques. La sur-sollicitation des isolants est souvent due à l'accumulation de ces charges (dites « charges d'espace » car réparties dans des espaces isolants), qui provoquent des distorsions du champ électrique, menant à un vieillissement prématuré et/ou au claquage.

Afin de mettre en place de nouveaux matériaux et d'optimiser les structures isolantes, des mesures précises des charges d'espace et des champs électriques qu'elles induisent sont nécessaires. La maîtrise de ces charges étant un élément clé pour la mise au point de systèmes d'isolation haute performance, leur mesure est indispensable à la conception, à la qualification et à la surveillance de tels systèmes, notamment en haute tension à courant continu.

Les interfaces constituant les points faibles des systèmes d'isolation, l'étude des champs aux interfaces est déterminante. D'autre part, une reproduction fidèle des phénomènes se produisant

en pratique nécessite que l'interface et la structure de l'isolant soient proches de celles d'un composant réel. Ces deux exigences peuvent être antagonistes, car des mesures à haute sensibilité/résolution nécessitent des films minces, tandis que la réalisation de structures proches de celles rencontrées en pratique dans des composants du génie électrique nécessite des couches semi-conductrices et isolantes plus épaisses, tant pour des raisons de représentativité que pour des raisons technologiques.

Le but de cette thèse a été de contribuer au développement de techniques de mesure non destructives, afin de permettre une meilleure compréhension de l'établissement et de l'évolution des zones de charges d'espace près des interfaces. En particulier, on s'est intéressé à la faisabilité et aux retombées du principe de la méthode de l'impulsion thermique (MIT) pour des mesures de charges d'espace dans des échantillons isolants d'épaisseur moyenne, pour une résolution aussi proche que possible du degré d'homogénéité des interfaces (de l'ordre du micromètre). Cette technique non-destructive consiste à exciter brièvement et faiblement l'objet d'essai avec une impulsion de chaleur, afin d'obtenir un signal transitoire dépendant de la répartition du champ électrique au voisinage de la zone excitée. Les méthodes à stimulus thermique ayant les meilleures sensibilités et résolutions spatiales, l'utilisation de la MIT est particulièrement intéressante pour la détermination des champs d'interface : sa résolution près de l'interface est la plus élevée de toutes les techniques, et le mode d'application sans contact du stimulus est potentiellement un atout important pour la caractérisation des échantillons soumis à des contraintes électrothermiques ou autres. Dans le même temps, des progrès récents ont démontré que les signaux de température provenant de l'électrode excitée thermiquement peuvent être acquis en même temps que le signal de charge d'espace, ce qui devrait permettre de recueillir des informations plus précises sur le stimulus thermique, afin d'augmenter la précision des mesures de charge d'espace. Ces facettes ont été au centre de la thèse.

Le présent travail a ainsi visé à étudier les possibilités offertes par cette technique non destructive a fort potentiel résolutif sur des échantillons polymères isolants d'épaisseurs moyennes (50 à 150 µm) munis de couches conductrices et semi-conductrices. En même temps, a été mise en œuvre une approche visant à augmenter la sensibilité et la résolution de la technique et à obtenir directement les valeurs des champs d'interface, en exploitant complètement la mesure simultanée de la température de l'interface et de la réponse due à la charge d'espace.

Cette thèse est divisée en trois chapitres. Le chapitre 1 présente d'abord un aperçu du sujet qui constitue la base du travail, en se concentrant sur les objectifs, les enjeux et les problématiques liés à l'utilisation des diélectriques solides dans les systèmes HTCC. Les principaux phénomènes liés à la charge rencontrés dans ces milieux (polarisation, injection, conduction et piégeage) sont ensuite discutés afin de mettre en évidence les mécanismes et les conséquences de la création de zones de charge d'espace dans les isolants polymères soumis à de fortes contraintes thermoélectriques. Les différentes techniques existantes pour la mesure de la répartition des charges d'espace sont ensuite décrites. Elles sont ensuite analysées par rapport aux objectifs du travail et une synthèse de toutes ces méthodes est proposée. Enfin, la MIT est discutée en détail.

Après avoir posé, dans le premier chapitre du manuscrit, les bases de la compréhension du sujet, l'analyse par simulation des différents problèmes connexes et la recherche de solutions sont abordées dans le deuxième chapitre. Pour approcher la variation surfacique et la distribution de la température en volume, nous avons réalisé une étude numérique sur des échantillons isolants de polyéthylène avec des épaisseurs de plusieurs dizaines de microns, dans des conditions cohérentes avec l'objectif de la thèse. Nous avons ainsi simulé la diffusion de la chaleur à travers des éprouvettes planes non revêtues et revêtues d'un compound semiconducteur polyéthylène/noir de carbone, soumises à des impulsions rectangulaires de chaleur sur une face, afin de déterminer les distributions de température et d'évaluer dans quelles conditions des signaux mesurables pourraient être obtenus sans affecter l'intégrité physique des éprouvettes.

Dans un premier temps, l'augmentation de la température de surface et la distribution de la température dans l'épaisseur ont été calculées pour déterminer la température maximale des échantillons et la profondeur de pénétration du stimulus thermique lorsque des impulsions de différentes énergies (0.1 mJ à plusieurs centaines de mJ) et durées (5 ns à 0.1 ms) sont utilisées, ainsi que pour estimer la quantité maximale de chaleur qui peut être apportée dans différentes conditions sans endommager le matériau. Les calculs ont montré que des augmentations de température de plusieurs degrés à plusieurs dizaines de degrés pouvaient être générées avec de telles excitations, en fonction de l'énergie absorbée par l'échantillon et de la durée des impulsions. Il en est ressorti que, dans les conditions étudiées, la profondeur de pénétration du stimulus thermique permettant d'espérer des résultats résolutifs raisonnablement précis est de l'ordre du micron à plusieurs dizaines de microns.

Des simulations électrothermiques ont ensuite été réalisées pour estimer les amplitudes et les dynamiques des signaux électriques transitoires susceptibles d'être générés par des échantillons contenant des champs électriques de plusieurs kV/mm, afin d'analyser leur mesurabilité avec une instrumentation de pointe et pour aider ensuite à l'interprétation des résultats expérimentaux. Ces simulations électriques ont mis en évidence que les champs dans la gamme des kV/mm devraient induire des réponses électriques transitoires mesurables avec une instrumentation de pointe, en particulier en mode tension, où des amplitudes de l'ordre du millivolt et au-delà peuvent être attendues. Ceci suggère fortement que des mesures directes du champ électrique à l'interface des échantillons considérés sont à portée de main, même pour des excitations thermiques avec des énergies inférieures au milli joule. Un dispositif expérimental, les résultats obtenus et leur analyse ont fait l'objet du chapitre suivant.

Le troisième chapitre du manuscrit est consacré aux résultats expérimentaux obtenus en appliquant des stimuli de type impulsion thermique de largeur 5 ns (obtenues avec un laser Nd :YAG de longueur d'onde 1064 nm) à des échantillons de polyéthylène d'épaisseurs de 50 µm à 160 µm. La première partie est consacrée à la préparation des échantillons, conformément aux exigences du travail expérimental et de la technologie disponible. Les échantillons et les électrodes, qui servent à la fois de capteurs de température et de contacts pour le signal de charge d'espace, sont d'abord décrits. La cellule de mesure et le circuit d'acquisition sont ensuite présentés, suivis d'illustrations, de discussions et de modélisations de signaux acquis.

Des réponses en tension transitoire, dépendant d'une part de la température de la surface excitée thermiquement, et d'autre part de la distribution du champ électrique à travers les échantillons, ont été ainsi mesurées simultanément. La mesure, la modélisation et l'analyse simultanées de signaux transitoires issus, d'une part, de la variation de température de l'électrode thermiquement excitée utilisée comme bolomètre, et d'autre part, de la réponse du champ électrique à travers l'échantillon, ont confirmé l'imbrication des signaux de température, de champ et de calibration, mettant en évidence la nécessité de leur découplage. Des procédures permettant de séparer les différents signaux ont alors été établies et validées expérimentalement. Une analyse électrique haute fréquence approfondie du circuit de mesure a permis d'extraire, en considérant les fonctions de transfert et les procédures de découplage, des signaux bolométriques et de champ électrique précis.

A l'aide des techniques de découplage et des outils d'analyse, il est montré qu'il est possible de passer directement à l'évolution temporelle quantitative de la température de surface, que nous avons déterminée pour chaque mesure, sur plusieurs types d'échantillons et d'interfaces. Ceci a permis d'obtenir par des mesures directes, non seulement qualitativement mais aussi, pour la première fois, quantitativement, la distribution réelle de la température à travers l'échantillon pendant la mesure du champ électrique.

La variation de température de la surface chauffée a ainsi été obtenue expérimentalement à partir de la réponse bolométrique, qui est directement proportionnelle à la variation de température de l'électrode via la résistance de l'électrode. Les distributions de température réelles à travers les échantillons pendant la mesure ont ensuite été déterminées via l'équation de la chaleur, montrant des élévations de température bien en dessous du degré et des profondeurs de pénétration du stimulus thermique d'un à deux microns dans les conditions des expériences. Ces résultats démontrent expérimentalement que même de très petites augmentations de température permettent d'obtenir des réponses de champ électrique entièrement mesurables, prouvant la sensibilité des méthodes thermiques.

En utilisant un processus d'étalonnage basé sur l'application de faibles champs électriques (dont on démontre qu'ils n'affectent pas l'état électrique des échantillons) et les distributions de température déterminées lors des mesures associées, le coefficient de variation de la permittivité et des abscisses du matériau a été calculé. A travers toutes ces expériences et procédures croisées, il est prouvé qu'un accès complet aux paramètres thermiques et électriques de l'échantillon peut être obtenu au moment des mesures de charge d'espace, permettant d'augmenter significativement la confiance dans les résultats de champ électrique à extraire du signal transitoire généré par l'échantillon lorsqu'il est excité par l'impulsion de chaleur.

L'extraction des paramètres du matériau par le protocole de calibration et l'utilisation de la distribution de température obtenue par les mesures bolométriques ont permis de déterminer les valeurs quantitatives et les images du champ électrique aux interfaces Pt/LDPE et Pt/semiconducteur. Ces résultats obtenus par une méthode directe, en considérant pour la première fois la température réelle dans l'échantillon, ont confirmé que des champs de plusieurs kV/mm peuvent exister à l'interface métal/polyéthylène, même en l'absence d'un conditionnement électrique préalable. Ils démontrent par ailleurs qu'il est possible d'évaluer

avec une configuration MIT non seulement des interfaces métal/isolant mais également des interfaces entre métaux et milieux faiblement résistifs. De tels résultats, que des études précédentes sur les structures MOS laissaient présager, et qui ont été validés dans ce travail par plusieurs voies, prouvent clairement que le principe d'une méthode thermique est applicable aux milieux à faible résistivité et à leurs interfaces, ce qui, compte tenu de la grande sensibilité des méthodes thermiques, confirme des perspectives technologiques intéressantes.

De nombreuses enseignements tirées de ce travail sont applicables à une grande variété d'épaisseurs et de matériaux. En ce qui concerne les matériaux pour la HTCC, les simulations suggèrent que l'utilisation d'impulsions plus larges (de plusieurs microsecondes ou plus) et d'énergies plus élevées, qui sont disponibles, par exemple, avec des lampes flash, devrait permettre de détecter le champ aux interfaces semi-conducteur/isolant placées après des électrodes semiconductrices de plusieurs dizaines de microns d'épaisseur. D'autre part, le principe de chauffage sans contact de la MIT pourrait être utilisé, avec les outils d'analyse associés présentés dans cette thèse, pour le suivi d'échantillons soumis à un vieillissement à long terme sous contrainte thermoélectrique, afin de détecter de faibles variations de champ aux interfaces. Même pour la caractérisation hors ligne, en tenant compte de la faible élévation de température nécessaire pour obtenir des signaux MIT, l'utilisation de la MIT seule ou en complément de techniques plus orientées vers le volume (comme la méthode de l'onde thermique - MOT) peut être un outil intéressant pour avoir une image complète de la distribution du champ avec un aperçu détaillé des zones d'interface.

La présente étude a apporté des données expérimentales pour soutenir le fait que des résolutions submicroniques sont clairement à portée de main sur des matériaux avec un degré d'homogénéité compatible. Ainsi, l'utilisation de la MIT sur des matériaux plus fins (quelque microns et moins) devrait permettre de mieux caractériser les interfaces, à une échelle submicronique, afin d'accroître la connaissance des phénomènes physiques se déroulant aux interfaces sous champs élevés. Dans un autre ordre d'idée, les mesures à cette échelle trouveront certainement une applicabilité aux matériaux biologiques.

L'applicabilité de la MIT aux matériaux semi-conducteurs mise en évidence dans ce travail peut avoir des retombées dans le domaine de l'électronique. Ainsi, de telles mesures peuvent être utilisées pour obtenir les distributions réelles de champ aux interfaces métal/oxyde et semi-conducteur/oxyde, qui sont des points clés du fonctionnement et de la fiabilité de la plupart des dispositifs électroniques actuels.

A travers ce travail, nous avons tenté d'apporter notre contribution à la caractérisation et à la compréhension des phénomènes se produisant dans les matériaux destinés à être utilisés sous des champs continus élevés. Ceci s'inscrit dans un cadre d'études menées conjointement par des scientifiques et des industriels pour permettre l'augmentation des contraintes dans les matériaux et les systèmes et la réduction de leurs coûts, afin de favoriser la transition énergétique et le renouveau industriel.

# Bibliography

[1] M. M. Mazzanti, Extruded cables for HVDC trans, John Wiley & Sons, 2013.

[2] C. Filloy-Corbrion, S. Hole, P. Notingher, S. Agnel, L. Berquez et D. Marty-Dessus, «Simultaneous measurement of surface temperature and space charge distribution with thermal pulse method,» chez *2016 IEEE International Conference on Dielectrics (ICD)*, 2016.

[3] M. Cembalest, «Eye on the market,» *J.P. Morgan, Annual energy paper,* 2018.

[4] M. Lampriere, «China's mega transmission lines,» *power-technology.com,* 2019.

[5] Z. Li et B. Du, «Polymeric insulation for high-voltage dc extruded cables: challenges and development directions,» *IEEE Electrical Insulation Magazine,* vol. 34, pp. 30-43, 11 2018.

[6] E. W. Kimbark, Direct current transmission, Wiley, 1971.

[7] R. L. Hauth, P. J. Tatro, B. D. Railing, B. K. Johnson, J. R. Stewart et J. L. Fink, «HVDC power transmission technology assessment,» Office of Scientific and Technical Information (OSTI), 1997.

[8] M. Bahrman et B. Johnson, «The ABCs of HVDC transmission technologies,» *IEEE Power and Energy Magazine,* vol. 5, pp. 32-44, 3 2007.

[9] D. Jovcic, High voltage direct current transmission: converters, systems and DC grids, WILEY, 2019.

[10] O. E. Oni, I. E. Davidson et K. N. I. Mbangula, «A review of LCC-HVDC and VSC-HVDC technologies and applications,» chez *2016 IEEE 16th International Conference on Environment and Electrical Engineering (EEEIC)*, 2016.

[11] Y. Zhang et Y. Li, «Current source converters and their control,» chez *Control of Power Electronic Converters and Systems*, Elsevier, 2018, pp. 115-140.

[12] C. C. Davidson et D. R. Trainer, «Innovative concepts for hybrid multi-level converters for HVDC power transmission,» chez *9th IET International Conference on AC and DC Power Transmission (ACDC 2010)*, 2010.

[13] R. Marquardt, «Modular multilevel converter: An universal concept for HVDC-networks and extended DC-bus-applications,» chez *The 2010 International Power Electronics Conference - ECCE ASIA -*, 2010.

[14] Y. Jiang-Hafner, H. Duchen, M. Karlsson, L. Ronstrom et B. Abrahamsson, «HVDC with voltage source converters - a powerful standby black start facility,» chez *2008 IEEE/PES Transmission and Distribution Conference and Exposition*, 2008.

[15] K. Friedrich, «Modern HVDC PLUS application of VSC in Modular Multilevel Converter topology,» chez *2010 IEEE International Symposium on Industrial Electronics*, 2010.

[16] J. Luo, J. Yao, D. Wu, C. Wen, S. Yang et J. Liu, «Application research on VSC-HVDC in urban power network,» chez *2011 IEEE Power Engineering and Automation Conference*, 2011.

[17] T. A. N. G. Guangfu, H. E. Zhiyuan et P. A. N. G. Hui, «R&D and application of voltage sourced converter based high voltage direct current engineering technology in China,» *Journal of Modern Power Systems and Clean Energy,* vol. 2, pp. 1-15, 2 2014.

[18] T. Lagier, P. Ladoux et P. Dworakowski, «Potential of silicon carbide MOSFETs in the DC/DC converters for future HVDC offshore wind farms,» *High Voltage,* vol. 2, pp. 233-243, 12 2017.

[19] D. Johannesson, M. Nawaz, K. Jacobs, S. Norrga et H.-P. Nee, «Potential of ultra-high voltage silicon carbide semiconductor devices,» chez *2016 IEEE 4th Workshop on Wide Bandgap Power Devices and Applications (WiPDA)*, 2016.

[20] J. Millan, P. Godignon, X. Perpina, A. Perez-Tomas et J. Rebollo, «A survey of wide bandgap power semiconductor devices,» *IEEE Transactions on Power Electronics,* vol. 29, pp. 2155-2163, 5 2014.

[21] A. B. Jørgensen, T. S. Aunsborg, S. Bęczkowski, C. Uhrenfeldt et S. Munk-Nielsen, «High-frequency resonant operation of an integrated medium-voltage SiC MOSFET power module,» *IET Power Electronics,* vol. 13, pp. 475-482, 2 2020.

[22] "Passivation layer for semiconductor devices". Patent US 2012/0217633 A1, 30 8 2012.

[23] M. Kosse, K. Juhre, M. Kuschel et D. Li, «Overview of development, design, testing and application of compact gas-insulated DC systems up to ± 550 kV,» *Global Energy Interconnection,* vol. 2, pp. 567-577, 12 2019.

[24] E. Volpov, «Dielectric strength coordination and generalized spacer design rules for HVAC/DC SF/sub 6/ gas insulated systems,» *IEEE Transactions on Dielectrics and Electrical Insulation,* vol. 11, pp. 949-963, 12 2004.

[25] J. Zhong, B. Zhang, Y. Guo, Z. Wang, Y. Yao, H. Zhang et Y. Liu, «Gas and solid insulation in HVDC gas insulated switchgear,» chez *2017 IEEE Conference on Energy Internet and Energy System Integration (EI2)*, 2017.

[26] «High voltage direct current transmission: Proven technology for power exchange,» *Siemens AG—Power transmission and distribution: High voltage division, Erlangen, Germany,* 2003.

[27] T. Worzyk, Submarine power cables, Springer Berlin Heidelberg, 2009.

[28] R. Bartnikas et K. D. Srivastava, Power and Communication Cables: Theory and Applications Show Less, W. E. E. E. Press, Éd., IEEE Press Series on Power Engineering, 2000.

[29] E. P. R. I. R. N. 1008720, «DC Cable Systems with Extruded Dielectrics,» 12 2004.

[30] M. Jeroense, «HVDC, the next generation of transmission highlights with focus on extruded cable systems,» chez *2008 International Symposium on Electrical Insulating Materials (ISEIM 2008)*, 2008.

[31] H. G. M. G. R.Vogelsang, «Silicone technology for reliable performance of joints and terminations for high voltage polymer power cables,» *8th International Conference on Insulated Power Cables, Versailles, France,* 2011.

[32] G. C. Psarras, «Fundamentals of dielectric theories,» chez *Dielectric Polymer Materials for High-Density Energy Storage*, Elsevier, 2018, pp. 11-57.

[33] G. Blaise, «Microscopic and macroscopic description of the polarization of dielectric materials, the concept of polaron applied to the conduction and trapping of charges, Le vide, les couches minces,» 1992.

[34] P. Hedvig, Dielectric spectroscopy of polymers, Wiley, 1977.

[35] J. V. T. P. A. M. Steeman, Broadband dielectric spectroscopy, Springer Berlin Heidelberg, 2012.

[36] S. Zhao, «Contributions à l'évolution de la méthode de l'onde thermique pour la mesure des charges d'espace dans les structures isolantes pour les câbles HTCC,» *Thèse de doctorat, Université de Montpellier,* 2017.

[37] F.-C. Chiu, «A review on conduction mechanisms in dielectric films,» *Advances in Materials Science and Engineering,* vol. 2014, pp. 1-18, 2014.

[38] D. R. Lamb, Electrical conduction mechanisms in thin insulating films, Methuen, 1967.

[39] K. Weiser, «Current injection in solids. Murray A. Lampert and Peter Mark. Academic Press, New York, 1970. xiv, 354 pp. Electrical Science series,» *Science,* vol. 170, pp. 966-967, 1970.

[40] K. C. Kao, Dielectric Phenomena in Solids, Elsevier, 2004.

[41] K. C. Kao, W. Hwang et S.-I. Choi, «Electrical transport in solids,» *Physics Today,* vol. 36, pp. 90-90, 10 1983.

[42] A. B. Petrin, «Thermionic field emission of electrons from metals and explosive electron emission from micropoints,» *Journal of Experimental and Theoretical Physics,* vol. 109, pp. 314-321, 8 2009.

[43] L. A. Dissado et J. C. Fothergill, Electrical degradation and breakdown in polymers, IET, 1992.

[44] «Electron emission in intense electric fields,» *Proceedings of the Royal Society of London. Series A, Containing Papers of a Mathematical and Physical Character,* vol. 119, pp. 173-181, 5 1928.

[45] T.-H. Chiang et J. F. Wager, «Electronic conduction mechanisms in insulators,» *IEEE Transactions on Electron Devices,* vol. 65, pp. 223-230, 1 2018.

[46] C. Hamann et T. Frauenheim, «Electrical conduction mechanisms in solids,» *Berlin : Deutscher Verlag der Wissenschaften,* p. 290, 1988.

[47] J. Frenkel, «On pre-breakdown phenomena in insulators and electronic semi-conductors,» *Physical Review,* vol. 54, pp. 647-648, 10 1938.

[48] J. G. Simmons, «Poole-frenkel effect and schottky effect in metal-insulator-metal systems,» *Physical Review,* vol. 155, pp. 657-660, 3 1967.

[49] H. Schroeder, «Poole-frenkel-effect as dominating current mechanism in thin oxide films—An illusion?!,» *Journal of Applied Physics,* vol. 117, p. 215103, 6 2015.

[50] F.-C. Chiu, C.-Y. Lee et T.-M. Pan, «Current conduction mechanisms in Pr2O3/oxynitride laminated gate dielectrics,» *Journal of Applied Physics,* vol. 105, p. 074103, 4 2009.

[51] N. F. Mott, Electronic processes in non-crystalline materials, OXFORD UNIV PR, 2012.

[52] T. K. Kundu et J. Y.-m. Lee, «Thickness-dependent electrical properties of Pb(Zr, Ti)O3 thin film capacitors for memory device applications,» *Journal of The Electrochemical Society,* 2000.

[53] J. Y. M. Lee et P. C. Juan, The application of highdielectric-constant and ferroelectric thin filmsin integrated circuit technology, vol. 4, American Scientific Publishers, 2009.

[54] M. Unge, C. Tornkvist et T. Christen, «Space charges and deep traps in polyethylene &#x2014 Ab initio simulations of chemical impurities and defects,» chez *2013 IEEE International Conference on Solid Dielectrics (ICSD)*, 2013.

[55] V. Griseri, «Polyimide used in space applications,» chez *Polyimide for Electronic and Electrical Engineering Applications*, IntechOpen, 2021.

[56] R. Bartnikas, «Performance characteristics of dielectrics in the presence of space charge,» *IEEE Transactions on Dielectrics and Electrical Insulation,* vol. 4, pp. 544-557, 1997.

[57] R. W. Greaves, E. P. Fowler, A. Goodings et D. R. Lamb, «The direct piezoelectric effect in extruded polyethylene,» *Journal of Materials Science,* vol. 9, pp. 1602-1608, 10 1974.

[58] N. H. Ahmed et N. N. Srinivas, «Review of space charge measurements in dielectrics,» *IEEE Transactions on Dielectrics and Electrical Insulation,* vol. 4, pp. 644-656, 1997.

[59] M. S. Khalil, «International research and development trends and problems of HVDC cables with polymeric insulation,» *IEEE Electrical Insulation Magazine,* vol. 13, pp. 35-47, 11 1997.

[60] J. C. Fothergill, «The coming of Age of HVDC extruded power cables,» chez *2014 IEEE Electrical Insulation Conference (EIC)*, 2014.

[61] T. B. CIGRE, «Recommendations for testing DC extruded cable systems for power transmission at a rated voltage up to 500 kV,» 2012.

[62] T. B. CIGRE, «Dielectric testing of gasinsulated HVDC systems,» 2021.

[63] C. Eoll, «Theory of stress distribution in insulation of high-voltage DC cables: Part I,» *IEEE Transactions on Electrical Insulation,* Vols. %1 sur %2EI-10, pp. 27-35, 3 1975.

[64] C. Eoll, «Theory of stress distribution in insulation of high-voltage DC cables Part II,» *IEEE Transactions on Electrical Insulation,* Vols. %1 sur %2EI-10, pp. 49-54, 6 1975.

[65] J.-m. Yang, X. Wang, C.-j. Zheng, H. Zhao et Q.-q. Lei, «DC conduction properties of SiOinf2/inf/LDPE nanocomposite,» chez *2012 IEEE 10th International Conference on the Properties and Applications of Dielectric Materials*, 2012.

[66] P. Notingher, S. Agnel et A. Toureille, «Thermal step method for space charge measurements under applied dc field,» *IEEE Transactions on Dielectrics and Electrical Insulation,* vol. 8, pp. 985-994, 2001.

[67] P. Notingher, A. Toureille, S. Agnel et J. Castellon, «Determination of Electric Field and Space Charge in the Insulation of Power Cables With the Thermal Step Method and a New Mathematical Processing,» *IEEE Transactions on Industry Applications,* vol. 45, pp. 67-74, 1 2009.

[68] P. Notingher, S.Hole, L. Berquez et G.Teyssedre, «An insight Iinto space charge mesaurements,» *ISNPEDADM,* 2015.

[69] J. Turnhout, «Thermally stimulated discharge of polymer electrets,» *Polymer Journal,* vol. 2, pp. 173-191, 3 1971.

[70] Y. Zhang, F. Zheng, Z. An et X. Zhang, «Research on space charge in insulating and functional dielectrics at Tongji University,» *IEEE Electrical Insulation Magazine,* vol. 28, pp. 14-25, 5 2012.

[71] G. R. G. Raju, «Conduction and thermally stimulated discharge currents in aramid paper,» *IEEE Transactions on Electrical Insulation,* vol. 27, pp. 162-173, 1992.

[72] C. L. Gressus, F. Valin, M. Henriot, M. Gautier, J. P. Duraud, T. S. Sudarshan, R. G. Bommakanti et G. Blaise, «Flashover in wide-band-gap high-purity insulators: Methodology and mechanisms,» *Journal of Applied Physics,* vol. 69, pp. 6325-6333, 5 1991.

[73] H. Gong, C. L. Gressus, K. H. Oh, X. Z. Ding, C. K. Ong et B. T. G. Tan, «Charge trapping on different cuts of a single-crystalline -SiO2,» *Journal of Applied Physics,* vol. 74, pp. 1944-1948, 8 1993.

[74] B. Vallayer, G. Blaise et D. Treheux, «Space charge measurement in a dielectric material after irradiation with a 30 kV electron beam: Application to single-crystals oxide trapping properties,» *Review of Scientific Instruments,* vol. 70, pp. 3102-3112, 7 1999.

[75] H. J. Wintle, «Analysis of the scanning electron microscope mirror method for studying space charge in insulators,» *Journal of Applied Physics,* vol. 86, pp. 5961-5967, 12 1999.

[76] F. Mady, R. Renoud, C. Attard, J. Bigarré, J.-P. Ganachaud et P. Hourquebie, «Interpretation method for mirror experiments based on a Monte Carlo charge implantation model,» *The European Physical Journal Applied Physics,* vol. 20, pp. 41-53, 10 2002.

[77] R. Coelho, L. Levy et D. Sarrail, «Charge decay measurements and injection in insulators,» *Journal of Physics D: Applied Physics,* vol. 22, pp. 1406-1409, 9 1989.

[78] B. A. Roland Coelho, Les diélectriques: Propriétés diélectriques des matériaux isolants, H. S. Publications, Éd., 1993.

[79] V. Adamec et J. H. Calderwood, «The interpretation of potential decay on the surface of a charged dielectric specimens,» *Journal of Physics D: Applied Physics,* vol. 20, pp. 803-804, 6 1987.

[80] P. Llovera et P. Molinie, «New methodology for surface potential decay measurements: application to study charge injection dynamics on polypropylene films,» *IEEE Transactions on Dielectrics and Electrical Insulation,* vol. 11, pp. 1049-1056, 2004.

[81] P. Molinie, «Measuring and modeling transient insulator response to charging: the contribution of surface potential studies,» *IEEE Transactions on Dielectrics and Electrical Insulation,* vol. 12, pp. 939-950, 2005.

[82] A. S. Friedrich Kremer, Broadband Dielectric Spectroscopy, Springer Berlin Heidelberg, 2002.

[83] E. H. Nicollian et J. R. Brews, MOS (metal oxide semiconductor) physics and technology, John Wiley & Sons, 2002.

[84] M. Kohno, T. Kitajima, H. Okada, S. Hirae et T. Sakai, «Noncontact measurement of sodium ions in silicon oxide,» *Japanese Journal of Applied Physics,* vol. 41, pp. 2266-2275, 4 2002.

[85] S. Hole, T. Ditchi et J. Lewiner, «Non-destructive methods for space charge distribution measurements: what are the differences?,» *IEEE Transactions on Dielectrics and Electrical Insulation,* vol. 10, pp. 670-677, 8 2003.

[86] T. Takada, T. Maeno et H. Kushibe, «An electric stress-pulse technique for the measurement of charges in a plastic plate irradiated by an electron beam,» *IEEE Transactions on Electrical Insulation,* Vols. %1 sur %2EI-22, pp. 497-501, 8 1987.

[87] T. Takada, «Acoustic and optical methods for measuring electric charge distributions in dielectrics,» chez *1999 Annual Report Conference on Electrical Insulation and Dielectric Phenomena (Cat. No.99CH36319)*, 1999.

[88] G. Ala, M. Caruso, V. Cecconi, S. Ganci, A. Imburgia, R. Miceli, P. Romano et F. Viola, «Review of acoustic methods for space charge measurement,» chez *2015 AEIT International Annual Conference (AEIT)*, 2015.

[89] G. Rizzo, P. Romano, A. Imburgia et G. Ala, «Review of the PEA Method for Space Charge Measurements on HVDC Cables and Mini-Cables,» *Energies,* vol. 12, p. 3512, 9 2019.

[90] K. Kumaoka, T. Kato, H. Miyake et Y. Tanaka, «Development of space charge measurement system with high positionalal resolution using pulsed electro acoustic method,» chez *Proceedings of 2014 International Symposium on Electrical Insulating Materials*, 2014.

[91] P. Laurençeau, G. Dreyfus et J. Lewiner, «New principle for the determination of potential distributions in dielectrics,» *Physical Review Letters,* vol. 38, pp. 46-49, 1 1977.

[92] G. D. P. Laurenceau et J. Lewiner, «Une méthode nouvelle de détermination de la distribution spatiale des potentiels dans les diélectriques,» *C. R. Acad. Sc., Paris,* vol. Vol. 283, pp. 135-138, 1976.

[93] J. Lewiner, S. Hole et T. Ditchi, «Pressure wave propagation methods: a rich history and a bright future,» *IEEE Transactions on Dielectrics and Electrical Insulation,* vol. 12, pp. 114-126, 2 2005.

[94] S. HoIe, «Recent developments in the pressure wave propagation method,» *IEEE Electrical Insulation Magazine,* vol. 25, pp. 7-20, 2009.

[95] G. M. Sessler, J. E. West, R. Gerhard-Multhaupt et H. Seggern, «Nondestructive Laser Method for Measuring Charge Profiles in Irradiated Polymer Films,» *IEEE Transactions on Nuclear Science,* vol. 29, pp. 1644-1649, 12 1982.

[96] G. M. Sessler, J. E. West et G. Gerhard, «High-resolution laser-pulse method for measuring charge distributions in dielectrics,» *Physical Review Letters,* vol. 48, pp. 563-566, 2 1982.

[97] G. M. Sessler et A. Berraissoul, «LIPP investigation of piezoelectricity distributions in PVDF poled with various methods,» *Ferroelectrics,* vol. 76, pp. 489-496, 12 1987.

[98] G. M. Sessler, «Charge distribution and transport in polymers,» *IEEE Transactions on Dielectrics and Electrical Insulation,* vol. 4, pp. 614-628, 1997.

[99] X. Wu, G. Chen, A. E. Davies, R. N. Hampton, S. J. Sutton et S. G. Swingler, «Space charge measurements in polymeric HV insulation materials,» *IEEE Transactions on Dielectrics and Electrical Insulation,* vol. 8, pp. 725-730, 2001.

[100] F. Fukuyoshi, D. Gotoh, Y. Tanaka, T. Takada, R. Watanabe, N. Tomita et R. Liu, «Observation of charge accumulation process in electron beam irradiated polymers using pressure wave propagation

method,» chez *Proceedings of 2005 International Symposium on Electrical Insulating Materials, 2005. (ISEIM 2005).*, 2005.

[101] L. Cheng, L. Zhong, Y. Zhang, S. Tan et J. Chen, «A Piezo-PWP method for charge measurement of the cell suspension,» chez *2009 IEEE 9th International Conference on the Properties and Applications of Dielectric Materials*, 2009.

[102] H. T. Van, J.-L. Auge et P. Rain, «Study of the generation of the pressure pulse in the laser induced pressure pulse method: Optimization of the process,» chez *2010 10th IEEE International Conference on Solid Dielectrics*, 2010.

[103] Z. Fei-Hu, Z. Ye-Wen, W. Chang-Shun, L. Ji-Xiao et X. Zhong-Fu, «Piezo-PWP and PEA methods for measuring space charge in solid dielectric,» *Acta Physica Sinica,* vol. 52, p. 1137, 2003.

[104] W. Eisenmenger et M. Haardt, «Observation of charge compensated polarization zones in polyvinylindenfluoride (PVDF) films by piezoelectric acoustic step-wave response,» *Solid State Communications,* vol. 41, pp. 917-920, 3 1982.

[105] W. Eisenmenger, M. Haardt and K. Holdik, *Observation of charge compensated polarization zones in Polyvinylidenefluoride (PVDF) by piezoelectrically generated pressure step wave (PPS) response,* Universität Stuttgart, 1982.

[106] M. Haardt et W. Eisenmenger, «High resolution technique for measuring charge and polarization distributions in dielectrics by piezoelectrically induced pressure step waves (PPS),» chez *Conference on Electrical Insulation & Dielectric Phenomena - Annual Report 1982*, 1982.

[107] A. Toureille et J. P. Reboul, «The thermal-step-technique applied to the study of charge decay in polyethylene thermoelectrets,» chez *6th International Symposium on Electrets,(ISE 6) Proceedings.*, 1988.

[108] A. Cherifi, M. A. Dakka et A. Toureille, «The validation of the thermal step method,» *IEEE Transactions on Electrical Insulation,* vol. 27, pp. 1152-1158, 1992.

[109] A. Toureille, J.-P. Reboul et P. Merle, «Détermination des densités de charge despace dans les isolants solides par la méthode de londe thermique,» *Journal de Physique III,* vol. 1, pp. 111-123, 1 1991.

[110] S. Bauer, «Method for the analysis of thermal-pulse data,» *Physical Review B,* vol. 47, pp. 11049-11055, 5 1993.

[111] A. Cernomorcenco et P. Notingher, «Application of the thermal step method to space charge measurements in inhomogeneous solid insulating structures: A theoretical approach,» *Applied Physics Letters,* vol. 93, p. 192903, 11 2008.

[112] M. Abou-Dakka, S. S. Bamji et A. T. Bulinski, «Space-charge distribution in XLPE by TSM, using the inverse matrix technique,» *IEEE Transactions on Dielectrics and Electrical Insulation,* vol. 4, pp. 314-320, 6 1997.

[113] M. A. Dakka, S. S. Bamji et A. T. Bulinski, «Precision of the inverse matrix technique for space charge measurement with the thermal step method,» chez *1999 Annual Report Conference on Electrical Insulation and Dielectric Phenomena (Cat. No.99CH36319)*, 1999.

[114] R. L. Peterson, G. W. Day, P. M. Gruzensky et R. J. Phelan, «Analysis of response of pyroelectric optical detectors,» *Journal of Applied Physics,* vol. 45, pp. 3296-3303, 8 1974.

[115] R. E. Collins, «Distribution of charge in electrets,» *Applied Physics Letters,* vol. 26, pp. 675-677, 6 1975.

[116] R. E. Collins, «Analysis of spatial distribution of charges and dipoles in electrets by a transient heating technique,» *Journal of Applied Physics,* vol. 47, pp. 4804-4808, 11 1976.

[117] G. M. Sessler, J. E. West, D. A. Berkley et G. Morgenstern, «Determination of Spatial Distribution of Charges in Thin Dielectrics,» *Physical Review Letters,* vol. 38, pp. 368-371, 2 1977.

[118] A. S. DeReggi, C. M. Guttman, F. I. Mopsik, G. T. Davis et M. G. Broadhurst, «Determination of charge or polarization distribution across polymer electrets by the thermal pulse method and fourier analysis,» *Physical Review Letters,* vol. 40, pp. 413-416, 2 1978.

[119] F. I. Mopsik et A. S. DeReggi, «Numerical evaluation of the dielectric polarization distribution from thermal-pulse data,» *Journal of Applied Physics,* vol. 53, pp. 4333-4339, 6 1982.

[120] S. B. Lang, A. S. DeReggi, F. I. Mopsik et M. G. Broadhurst, «Preexisting polarization and influence of electrode materials on PVF2electrets as determined by thermal pulse and pyroelectric methods,» *Journal of Applied Physics,* vol. 54, pp. 5598-5602, 10 1983.

[121] F. I. Mopsik et A. S. DeReggi, «Poling behavior of polyvinylidene fluoride at room temperature,» *Applied Physics Letters,* vol. 44, pp. 65-67, 1 1984.

[122] R. Gerhard-Multhaupt et Z.-F. Xia, «Determination of temperature distribution in single- and double-side metallized electret films,» *IEEE Transactions on Electrical Insulation,* vol. 24, pp. 517-522, 6 1989.

[123] G. F. L. Ferreira et R. Gerhard-Multhaupt, «Derivation of response equations for the nondestructive probing of charge and polarization profiles,» *Physical Review B,* vol. 42, pp. 7317-7321, 10 1990.

[124] R. E. Collins, «Measurement of charge distribution in electrets,» *Review of Scientific Instruments,* vol. 48, pp. 83-91, 1 1977.

[125] N. Hozumi, J. Tanaka, A. S. D. Reggi et N. Nagusrinivas, «Space charge induced in stressed polyethylene,» chez *Conference on Electrical Insulation and Dielectric Phenomena*, 1989.

[126] T. Suzuki, S. Katakai, M. Kanaoka et Y. Sekii, «DC characteristics of cable insulating materials,» chez *Proceedings of the 3rd International Conference on Conduction and Breakdown in Solid Dielectrics*, 1989.

[127] S. Aryal et A. Mellinger, «Two-and three-dimensional analysis of polarization profiles in electret materials with thermal pulses,» chez *2011 Annual Report Conference on Electrical Insulation and Dielectric Phenomena*, 2011.

[128] A. Mellinger, R. Singh, M. Wegener, W. Wirges, R. F. Suairez, S. B. Lang, L. F. Santos et R. Gerhard-Multhaupt, «High-resolution three-dimensional space-charge and polarization mapping with thermal pulses,» chez *12th International Symposium on Electrets*, 2005.

[129] R. E. Collins, «Practical application of the thermal pulsing technique to the study of electrets,» *Journal of Applied Physics,* vol. 51, pp. 2973-2986, 6 1980.

[130] R. E. Collins, «The thermal pulsing technique applied to polymer electrets,» *Ferroelectrics,* vol. 33, pp. 65-74, 6 1981.

[131] A. S. DeReggi, «Effects of the measuring circuit on broadband piezo and pyroelectric measurements,» *IEEE Transactions on Dielectrics and Electrical Insulation,* vol. 1, pp. 146-152, 2 1994.

[132] B. Salamé et S. Holé, «Elasto-electric coupling for direct electric field distribution measurement in semiconductor structures,» *Journal of Applied Physics,* vol. 120, p. 175702, 11 2016.

[133] R. V. Churchill, Fourier series and boundary value problems, McGraw-Hill Book Company, Inc., New York and London, 1941, p. ix+206.

[134] C. P. B. W. J. Parker et G. L. Abbott, «Flash method of determining thermal diffusivity, heat capacity, and thermal conductivity,» *Journal of Applied Physics,* pp. 1679-1684, 1961.

[135] M. G. Broadhurst, G. T. Davis, J. E. McKinney et R. E. Collins, «Piezoelectricity and pyroelectricity in polyvinylidene fluoride—A model,» *Journal of Applied Physics,* vol. 49, pp. 4992-4997, 10 1978.

[136] A. S. De Reggi, M. G. Broadhurst, G. T. Davis et F. I. Mopsik, «Measurement of space charge fields in polymers,» chez *Conference on Electrical Insulation & Dielectric Phenomena — Annual Report 1987*, 1987.

[137] S. B. Lang, «Laser intensity modulation method (LIMM): Experimental techniques, theory and solution of the integral equation,» *Ferroelectrics,* vol. 118, pp. 343-361, 6 1991.

[138] G. F. L. Ferreira, «On the deconvolution of heat-pulse-like signals,» *Journal of Applied Physics,* vol. 66, pp. 4924-4927, 11 1989.

[139] H. J. Coufal, R. K. Grygier, D. E. Horne et J. E. Fromm, «Pyroelectric calorimeter for photothermal studies of thin films and adsorbates,» *Journal of Vacuum Science &amp Technology A: Vacuum, Surfaces, and Films,* vol. 5, pp. 2875-2889, 9 1987.

[140] B. Ploss, R. Emmerich et S. Bauer, «Thermal wave probing of pyroelectric distributions in the surface region of ferroelectric materials: A new method for the analysis,» *Journal of Applied Physics,* vol. 72, pp. 5363-5370, 12 1992.

[141] B. Ploss, «Probing of pyroelectric distributions from thermal wave and thermal pulse measurements,» *Ferroelectrics,* vol. 156, pp. 345-350, 6 1994.

[142] S. Bauer, «Direct evaluation of thermal-pulse, thermal-step, and thermal-wave results for obtaining charge and polarization profiles,» chez *Proceedings of 8th International Symposium on Electrets (ISE 8)*, 1994.

[143] C. Corbrion, S. Hole, P. Notingher, S. Agnel, L. Berquez et D. Marty-Dessus, «Temperature profile estimation for high spatial resolution space charge measurement with thermal pulse methods,» chez *2017 International Symposium on Electrical Insulating Materials (ISEIM)*, 2017.

[144] C. Corbrion et S. Hole, «Interface charge effect measurement in 2-m-thick polypropylene sample under voltage with thermal method,» chez *2020 IEEE 3rd International Conference on Dielectrics (ICD)*, 2020.

[145] C. Filloy-Corbrion, C. Boue, E. Géron, T. Ditchi, J. Lucas, S. Hole, P. Notingher, S. Agnel, D. Marty-Dessus, L. Berquez et G. Teyssedre, «Surface temperature measurement for space charge distribution measurements with thermal methods,» *IEEE Transactions on Dielectrics and Electrical Insulation,* vol. 22, pp. 1506-1511, 6 2015.

[146] C. Alquie, C. L. Tolra, J. Lewiner et S. B. Lang, «Comparison of polarization distribution measurement by the LIMM and PWP methods,» *IEEE Transactions on Electrical Insulation,* vol. 27, pp. 751-757, 1992.

[147] S. B. Lang et D. K. Das-Gupta, «A technique for determining the polarization distribution in thin polymer electrets using periodic heating,» *Ferroelectrics,* vol. 39, pp. 1249-1252, 10 1981.

[148] S. B. Lang et D. K. Das-Gupta, «A new technique for determination of the spatial distribution of polarization in polymer electrets,» *Ferroelectrics,* vol. 60, pp. 23-36, 10 1984.

[149] S. B. Lang et D. K. Das-gupta, «Complex polarization distributions in PVDF samples,» *Ferroelectrics,* vol. 55, pp. 151-154, 4 1984.

[150] S. B. Lang et D. K. Das-Gupta, «Laser-intensity-modulation method: A technique for determination of spatial distributions of polarization and space charge in polymer electrets,» *Journal of Applied Physics,* vol. 59, pp. 2151-2160, 3 1986.

[151] J. L. Franceschi et V. Haas, «Laser thermoacoustic modulation for space charge measurement,» *Applied Physics Letters,* vol. 70, pp. 2236-2237, 4 1997.

[152] J. L. Franceschi, D. Marty-Dessus, C. Biellmann, L. Berquez et M. Mousseigne, «Profils de charges d'espace dans les isolants polymers minces par une méthode d'excitation thermoque avec laser focalisé,» chez *Conference of the French Society of Electrostatics SFE*, 2000.

[153] J. M. Reboul, «Simultaneous space charge and TSDC measurements on polarized polymer,» *IEEE Transactions on Dielectrics and Electrical Insulation,* vol. 13, pp. 1016-1022, 10 2006.

[154] S. B. Lang, «Laser intensity modulation method (LIMM) : review of the fundamentals and a new method for data analysis,» *IEEE Transactions on Dielectrics and Electrical Insulation,* vol. 11, pp. 3-12, 2 2004.

[155] Rayleigh, «XXXI. Investigations in optics, with special reference to the spectroscope,» *The London, Edinburgh, and Dublin Philosophical Magazine and Journal of Science,* vol. 8, pp. 261-274, 10 1879.

[156] Dagher, Hole et Lewiner, «A preliminary study of space charge distribution measurements at nanometer spatial resolution,» *IEEE Transactions on Dielectrics and Electrical Insulation,* vol. 13, pp. 1036-1041, 10 2006.

[157] S. Hole, «Resolution of direct space charge distribution measurement methods,» *IEEE Transactions on Dielectrics and Electrical Insulation,* vol. 15, pp. 861-871, 2008.

[158] S. Sakai, M. Ishida, M. Date et T. Furukawa, «Changes in photo-induced pyroelectric transients during polarization reversal in VDF-TrFE copolymers,» chez *[1991 Proceedings] 7th International Symposium on Electrets (ISE 7)*, 1991.

[159] A. Imburgia, P. Romano, M. Caruso, F. Viola, R. Miceli, E. Riva Sanseverino, A. Madonia et G. Schettino, «Contributed Review: Review of thermal methods for space charge measurement,» *Review of Scientific Instruments,* vol. 87, p. 111501, 2016.

[160] A. Imburgia, R. Miceli, E. R. Sanseverino, P. Romano et F. Viola, «Review of space charge measurement systems: acoustic, thermal and optical methods,» *IEEE Transactions on Dielectrics and Electrical Insulation,* vol. 23, pp. 3126-3142, 10 2016.

[161] P. Notingher, S.Hole, L. Berquez et G.Teyssedre, «An insight into space charge mesaurements,» *ISNPEDADM,* 2015.

[162] L. Hamidouche, E. Geron et S. Hole, «Electro-Acoustic Reflectometry, a new method toward very high spatial resolution space charge measurements,» chez *2016 IEEE International Conference on Dielectrics (ICD)*, 2016.

[163] L. Hamidouche, E. Geron et S. Hole, «Electro-acoustic reflectometry: Reaching high spatial resolution and high sensitivity for space charge measurements,» chez *2017 International Symposium on Electrical Insulating Materials (ISEIM)*, 2017.

[164] L. Hamidouche, «Spectroscopie micro-onde pour la mesure des charges d'espace à haute résolution spatiale dans les isolants en couche mince,» *Thèse de doctorat, Sorbonne Université,* 2018.

[165] M. G. Broadhurst, A. S. DeReggi, G. T. Davis et F. I. Mopsik, «Charging behavior of polyethylene and ionomers,» chez *Conference on Electrical Insulation & Dielectric Phenomena — Annual Report 1987*, 1987.

[166] S. S. Hegde, P. Notingher et J.-C. Laurentie, «Considerations on using Thermal Pulses for Space Charge Measurements in Medium Thickness Insulating Samples,» chez *2021 IEEE Conference on Electrical Insulation and Dielectric Phenomena (CEIDP)*, 2021.

[167] «DHPCA-100 Variable Gain High Speed Current Amplifier DataSheet,» 2019.

[168] M. Fabian, E. Lewis, T. Newe et S. I. Lochmann, «Novel multimode fibre-cavity for ring-down experiments,» chez *2009 IEEE Sensors*, 2009.

[169] «Series 5 MSO -Mixed Signal Oscilloscope Datasheet,» 2021.

[170] S. Baudon, «Etude de l'influence des contraintes appliquées sur l'évolution des propriétés diélectriques des couches minces isolantes dans les composants semi-conducteurs de puissance,» *Thèse de doctorat, Université Montpellier 2,* 2013.